Hot Molecular Line Lists for Extrasolar Planets and Industry

Emma Jane Barton
Research Degree: Physics and Astronomy
University College London

Principle Supervisor
Prof. Jonathan Tennyson

Secondary Supervisor
Prof. Giovanna Tinetti

August 23, 2016

Preface

I Emma Jane Barton confirm that the work presented in this thesis is my own. Where information has been derived from other sources, I confirm that this has been indicated in the thesis.

Acknowledgements

This thesis would not have been possible without the support and guidance of my principle supervisor Jonathan Tennyson and my secondary supervisor Giovanna Tinetti. It has been a privilege to work with the ExoMol and exoplanet groups at University College London. In particular I would like to thank Christian Hill and Sergey Yurchenko from the ExoMol group and Marco Rocchetto and Ingo Waldmann from the exoplanet group for helpful discussions.

This research was supported by a grant from Energinet.dk project N. 2013-1-1027, by UCL through the Impact Studentship Program and the European Research Council under Advanced Investigator Project 267219.

My work has greatly benefited from a number of external collaborations, namely with Alexander Fateev and Sønnik Clausen from Danish Technical University, Alain Campargue and Serge Béguier from Université Grenoble Alpes, Nina Lavrentieva and Anna Dudaryonok from V. E. Zuev Institute of Atmospheric Optics and Peter Bernath and Daniel Frohman from Old Dominion University. I would also like to thank Iouli Gordon, Larry Rothman, Robert Gamache and Ryan Garland for helpful discussions, Vincent Boudon for providing his empirical data for the methane project, the Kitt Peak data centre for giving open access to data recorded at the observatory and Catherine de Bergh for measuring high quality infra-red spectra of ammonia before I was born.

I am grateful for having the opportunity to participate in ORBYTS, a science outreach educational program associated with the Twinkle Space Mission. Many thanks to Clara Sousa-Silva, Shelia Smith, Tim Morris, Jon Barker, Fawad Sheikh, summer students Richard Stones and Saajan Sujanani, Highams Park School, Researchers in Schools, Twinkle Space Mission and my outstanding team of sixth formers, Menghan Liu, Tom Farnell, Alex Goring, Megan Sturgeon and Georgia White. Financial support was provided by the Nuffield Foundation and the UK Science, Technology and Facilities Council.

Finally over the past few years I have received a lot of emotionally and financial support from my friends and family for which I am enormously appreciative. I would like to thank my parents Wendy and John Barton, my grandparents Ray and Delia Barton and Ron and Janet Livesey, my brother James, my wonderful friends Abi Rollinson, Yan Kay Ho, Hongorzul Davaapil, James Coughtrey, Maire Gorman and Laura Mckemmish, and my caring boyfriend Ron Gourley for helping me through my research degree. I could not have done it without them.

Abstract

This research is a composite of projects which have individually contributed new results to their respective subjects, whilst collectively contributing to the updating of the ExoMol database to include pressure broadening. This research also represents a successful collaboration between academia and industry.

A combination of empirical and *ab initio* methods were used to compute accurate ro-vibrational line lists for sodium chloride and potassium chloride and refine line lists for carbon monosulphide.

Hot line lists for hydrogen chloride, formaldehyde, ammonia and methane were assessed by comparison to high resolution laboratory spectra at temperatures relevant to industrial spectral studies and extrasolar planets.

Hot and room temperature Fourier transform infrared spectra of ammonia have been analysed using a variational line list available from ExoMol and, where available, experimental energy levels. Over 5000 new line assignments have been made, providing over 3000 new experimental energies in the range 500 - 11,000 cm^{-1}. In addition, an analysis of a room temperature spectrum in the region 9000 - 10,400 cm^{-1} has been started.

A combined analysis of assigned high resolution experimental spectra of methane available from peer reviewed sources using the MARVEL algorithm has been started. It is intended that the resulting compilation of verified experimental ro-vibrational energies will aid the analysis of hot methane spectra in the region 1000 - 6300 cm^{-1}.

Custom built pressure and temperature dependent absorption cross sections for water, carbon monoxide, carbon dioxide and ammonia were generated using ExoMol and HITEMP line lists for new spectral retrieval code τ-REx, to facilitate the unbiased analysis of extrasolar planetary spectra.

Finally, the data requirements and challenges related to data usage of these separate projects are used to inform the implementation of pressure broadening in the ExoMol database.

This thesis lays out the motivation and background for the current work, details the present results and reviews avenues for further work.

Contents

List of Tables

List of Figures

List of Publications

This Work

E. J. Barton, C. Chui, S. Golpayegani, S. N. Yurchenko, J. Tennyson, D. J. Frohman and P. F. Bernath (2014) *ExoMol molecular line lists V: The ro-vibrational spectra of NaCl and KCl* Monthly Notices of the Royal Astronomical Society, **442**, 1821

I. P. Waldmann, G. Tinetti, M. Rocchetto, **E. J. Barton**, S. N. Yurchenko and J. Tennyson (2015) *Tau-REx I: A next generation retrieval code for exoplanetary atmospheres* The Astrophysical Journal, **802**, 107

E. J. Barton, S. N. Yurchenko, J. Tennyson, S. Clausen and A. Fateev (2015) *High-resolution absorption measurements of NH_3 at high temperatures: 500 - 2100 cm^{-1}* Journal of Quantitative Spectroscopy and Radiative Transfer, **167**, 126

G. Paulose, **E. J. Barton**, S. N. Yurchenko and J. Tennyson (2015) *ExoMol Molecular Line Lists XII: Line Lists for 8 isotopes of CS* Monthly Notices of the Royal Astronomical Society, **454**, 1931

I. P. Waldmann, M. Rocchetto, G. Tinetti, **E. J. Barton**, S. N. Yurchenko and J. Tennyson (2015) *Tau-Rex II: Retrieval of emission spectra* The Astrophysical Journal, **813**, 13

A. Tsiaras, M. Rocchetto, I. P. Waldmann, O. Venot, R. Varley, G. Morello, M. Damiano, G. Tinetti, **E. J. Barton**, S. N. Yurchenko and J. Tennyson (2016) *Detection of an atmosphere around the super-Earth 55 Cancri e* The Astrophysical Journal, **820**, 99

E. J. Barton, S. N. Yurchenko, J. Tennyson, S. Béguier and A. Campargue (2016) *A near infrared line list for NH_3: Analysis of a Kitt Peak spectrum after 35 years* Journal of Molecular Spectroscopy, **325**, 7

J. Tennyson, S. N. Yurchenko, A. F. Al-Refaie, **E. J. Barton**, K. Chubb, P. J. Coles, R. S. Diamantopoulou, M. Gorman, C. Hill, L. Lodi, L. K. McKemmish, Y. Na, A. Owens, O. L. Polyansky, T. Riviln, C. Sousa-Silva, D. S. Underwood, A. Yachmenev

and E. Zak (2016) *The ExoMol database: molecular line lists for exoplanet and other hot atmospheres* Journal of Molecular Spectroscopy Special Issue, *in press*

E. J. Barton, C. Hill, S. N. Yurchenko, J. Tennyson, A. S. Dudaryonok and N. N. Lavrentieva (2016) *Pressure-dependent water absorption cross-sections for exoplanets and other atmospheres* Journal of Quantitative Spectroscopy and Radiative Transfer, *in preparation*

E. J. Barton, S. N. Yurchenko, J. Tennyson, S. Clausen, A. Fateev (2016) *High-resolution absorption measurements of NH_3 at high temperatures: 2100 - 5500 cm^{-1}* Journal of Quantitative Spectroscopy and Radiative Transfer, *in preparation*

E. J. Barton, O. L. Polyansky, S. N. Yurchenko, J. Tennyson, S. Civis, S. Béguier, A. Campargue, P. F. Bernath (2016) *The NH_3 spectrum from 9000 - 10,400 cm^{-1}* Journal of Molecular Spectroscopy, *in preparation*

E. J. Barton, V. Boudon, M. Liu, T. Farnell, A. Goring, M. Sturgeon, G. White, R. Stones, S. Sujanani, J. Tennyson, S. N. Yurchenko, A. G. Császár, T. Furtenbacher, C. Sousa-Silva (2016) *MARVEL analysis of the measured high-resolution spectra of $^{12}CH_4$* Journal of Quantitative Spectroscopy and Radiative Transfer, *in preparation*

E. J. Barton, S. N. Yurchenko, J. Tennyson, S. Clausen and A. Fateev (2016) *High-resolution absorption measurements of CH_4 at high temperatures: 1000 - 6300 cm^{-1}* Journal of Quantitative Spectroscopy and Radiative Transfer, *in preparation*

C. Sousa-Silva, **E. J. Barton**, K. Chubb, L. McKemmish, J. Tennyson (2016) *ORBYTS: When can students start performing original research?* Science Education, *in preparation*

Other Publications

E. J. Barton, S. N. Yurchenko, J. Tennyson (2013) *ExoMol line lists - II. The rovibrational spectrum of SiO* Monthly Notices of the Royal Astronomical Society, **434**, 1469

G. Tinetti et al. (2015) *The EChO science case* Experimental Astronomy, **40**, 329

Acronyms, Constants and Units

Table 1: Acronyms used in this work.

Acronym	Meaning
NIST	National Institute of Standards and Technology
SI	International System of Units
UCL	University College London
DTU	Danish Technical University
BOA	Born Oppenheimer Approximation
BOB	Born Oppenheimer Breakdown
PEC	Potential Energy Curve
PES	Potential Energy Surface
DMC	Dipole Moment Curve
DMS	Dipole Moment Surface
EMO	Expanded Morse Oscillator
MLR	Morse Long Range
MLJ	Morse Lennard-Jones
ILS	Instrument Line Shape
FT	Fourier Transform
FTS	Fourier Transform Spectroscopy
FTIR	Fourier Transform InfraRed
BB	Black Body
SB	Single Beam
q-HGC	quartz High temperature Gas-flow Cell
FWHM	Full Width Half Maximum
NIDL	Normal Intensity Distribution Law
ORBYTS	Original Research By Young Twinkle Students
MARVEL	Measured Active Rotation-Vibration Energy Levels
UV	Ultraviolet
EH	Effective Hamiltonian
RMS	Root Mean Squared
MCT	Mercury Cadmium Telluride
obs. - calc.	Observed minus calculated

Table 2: Constants used in this work. Values taken from NIST (Mohr et al. (2014)).

Symbol	Name	Value
c_2	Second radiation constant	$1.43877736(83) \times 10^{-2}$ m K
k	Boltzmann constant	$1.38064852 \times 10^{-23}$ J K^{-1}
h	Planck's constant	$6.62607004 \times 10^{-34}$ J s^{-1}
$\hbar$	Planck's constant / 2π	$1.054571800 \times 10^{-34}$ J s^{-1}
c	Speed of light	2.99792458×10^{8} m s^{-1}

Table 3: Units used in this work. Written with reference to NIST (NIST (2009)).

Symbol	Name	Description	SI equivalent
μm	Microns	Unit of length	1 μm = 1×10^{-6} m
cm^{-1}	Wavenumbers	Unit of energy	1 cm^{-1}= 1.98630×10^{-23} J
Å	Angstroms	Unit of length	1 Å= 1×10^{-10} m
D	Debye	Unit of electric dipole moment	1 D = 3.335641×10^{-30} C m
°C	Degrees Celsius	Unit of temperature	0 °C = 273.15 K
atm	Atmospheres	Unit of pressure	1 atm = 101,325 Pa
bar	Bar	Unit of pressure	1 bar = 100,000 Pa
Torr	Torr	Unit of pressure	1 Torr = $\frac{101,325}{760}$ Pa

Chapter 1

Introduction

The properties of gaseous environments whether astrophysical, for example stellar atmospheres, or terrestrial, such as smoke stacks, can be determined through the study of spectra. A spectrum is a measure of electromagnetic-radiation (light) as a function of wavelength. The position, intensity and shape of features in a spectrum is characteristic of the physical conditions and composition of the environment the light has traversed.

To interpret a spectrum an observer might employ one or more line lists. A line list is a list of parameters describing the appearance of a particular atom, ion or molecule's spectrum. This may include the central position of spectral features, also known as lines, their intensity, which is dependent on abundance and temperature, and shape, commonly provided as a line width which is dependent on temperature, pressure and other factors which influence line broadening.

The purpose of a line list is to identify atomic, ionic and molecular lines in spectra, and to use their strength and shape to deduce the physical conditions of the environment. This is done by modelling or measuring the behaviour of atoms, ions or molecules under specific conditions to produce an experimental or theoretical line list. If the position, strength and shape of experimental or theoretical lines match the observed lines it can be inferred that the composition and physical conditions used in the experiment or model apply to the source of the observed lines.

Line lists are compiled in spectroscopic databases such as ExoMol (Tennyson & Yurchenko (2012); Tennyson et al. (2016)) or HITRAN (Rothman et al. (2013)) and applied by users of the databases to the study of, for example, astronomical objects.

This work consists of several projects focused towards one of two applications that require molecular line lists, industrial spectral studies and characterisation of extrasolar planetary atmospheres. These applications have molecules, temperatures and pressure of interest in common, the advantage being that results from each project could be used for either application. In addition, the data requirements and challenges related to data usage for each project are used to inform the updating of the ExoMol database to include pressure broadening.

1.1 Industry

Many industrial processes involve the gasification or combustion of reactants, products or fuel. Monitoring the conditions, gas mixing and chemical reactions in these processes is imperative to ensure efficiency and compliance with environmental standards. Spectroscopy provides a means of doing this through the *in situ* measurement of gas temperature and composition, though the result is highly dependent on the quality of reference data (Fateev & Clausen (2012)).

For this reason, a collaboration has been established between the Optical Diagnostics Group at Danish Technical University (DTU) and the ExoMol group at University College London (UCL), to combine high resolution spectra measured at elevated temperatures and empirically-tuned *ab initio* methods to produce suitable line lists for modelling important molecules in combustion or gasification processes.

The molecules of interest in the present work are sodium chloride (NaCl), potassium chloride (KCl), hydrogen chloride (HCl), ammonia (NH_3), methane (CH_4) and formaldehyde (H_2CO). The presence of chloride containing molecules increases the corrosive nature of combustion gases (Yang et al. (2014), Kear (2007)), while excess NH_3, used as a reagent to reduce emissions of nitrogen oxides, can cause fouling of downstream components and create maintenance and operational issues for power plants (Carnegie (2011)). Regulations have been put in place to reduce the emission of CH_4 from industrial sources due to its role in global warming (EPA (2014a)). Natural gas systems are amongst the largest industrial sources for this pollutant (EPA (2015)). H_2CO concentrations have to be minimised in industrial emissions as it is a very toxic compound and a known carcinogen (Zhang et al. (2009)).

The aims of this work were to calculate comprehensive line lists for NaCl and KCl, validate hot HCl, H_2CO and CH_4 line lists for smoke stack conditions and to increase the number of assigned lines and experimentally known energy levels of NH_3 and CH_4.

These molecules are also of interest in the context of extrasolar planetary atmospheres. NaCl and KCl are expected to be present in super-Earth atmospheres (Schaefer et al. (2012)) and may form in the observable atmosphere of known object GJ 1214 b (Kreidberg et al. (2014)). HCl is likely to be the other main chlorine-containing species in extrasolar planets as it is a known component of Venus' mesosphere (Vandaele et al. (2008)). NH_3 and CH_4 are present in the atmospheres of solar system giant planets (Woodman et al. (1977); Encrenaz (1990)) and late T-type dwarf stars (Canty et al. (2015)) suggesting that they are likely to be present in the atmospheres of extrasolar giant planets (Sudarsky et al. (2003)). In fact CH_4 has been detected in the atmospheres of Jupiter sized planets HD 189733 b (Swain et al. (2008)) and HR 8799 b (Barman et al. (2015)). The presence of H_2CO in a extrasolar planetary atmosphere could indicate that the planet is undergoing the stages of pre-life (Neveu et al. (2013)). Illuminating an 'early-Earth' type molecular gas mix with UV radiation results in a considerable amount of H_2CO. This should be observable in the atmosphere, before it is deposited in the pre-biotic oceans (Neveu et al. (2013)).

1.2 Extrasolar Planets

The following section was written with reference to Pater & Lissauer (2013) and Seager (2008).

The developing field of extrasolar planetary science entices many researchers with the prospect of answering fundamental questions about planetary systems in our galaxy and beyond, including the most popular, do they harbour life? A vital step in this process is the characterisation of extrasolar planets and extrasolar planetary systems, but before this they must be found.

The first confirmed detection of extrasolar planets were the two companions to pulsar PSR B1257+12 (Wolszczan & Frail (1992)). Pulsars are a type of variable star that emit radio waves which appear as regular pulses to an observer on Earth. Periodic variation in the arrival time of these pulses that cannot be attributed to other factors, such as the motion of the Earth around the sun, may indicate the presence of planets. The first planet detected around a main sequence star was the famous 51 Peg b (Mayor & Queloz (1995)). A host star will move around the centre of gravity of its system, which is offset from the centre of the star by the gravitational pull of the orbiting planets. This radial motion manifests as varying Doppler shifts in the spectral lines of the star. The amplitude of radial velocity variations of the host star is proportional to the size of the planets and position of the planets in the system. Therefore using radial velocity variation to detect extrasolar planets can provide planetary mass and orbital period, inclination and eccentricity. Since 1995 various extrasolar planet detection techniques have emerged. The most rewarding has been transit photometry. If a planet passes in front of its host star with respect to Earth, the disk of the planet blocks out a fraction of the starlight resulting in an observed dip in stellar brightness. The depth of this dip is proportional to the area of the planetary disk, and hence provides a planetary radius. In addition, since the orbit normal must be nearly 90° for the transit to be observed, limits on the orbital inclination and distance between the star and the planet can also be derived. Over 2300 planets have been confirmed using this technique so far and there are many more possible transit observations waiting to be analysed (Batalha et al. (2013)). A more modest number of around 16 and 50 planets each have been detected using microlensing and direct imaging methods respectively (Giannini & Lunine (2013); Schmidt et al. (2016)). Microlensing is a consequence of Einstein's general theory of relativity. Light from a distant star that passes a more massive object (a lens) between the source and the observer is bent, typically by a small angle. This focuses the light from the source, resulting in a peak in the observed light curve of the background star. If the lensing star has planetary companions this will produce additional, smaller peaks in the light curve. From these characteristic peaks the mass ratio and projected separation of the planets and the host star may be derived. As implied by the name, direct imaging is a direct method of detecting extrasolar planets by taking an image of the system. In order to image planets, the light from the star must be blocked out as the star is several orders of magnitude brighter than the planets. Other successful techniques for detecting extrasolar planets include transit

timing variations and eclipse timing variations, variations in the period of planet-star or star-star systems that betray the presence of additional objects, and astrometry, observing the wobble induced in the motion of a host star projected onto the plane of the sky induced by orbiting planets.

There are now a number of techniques for characterising extrasolar planetary atmospheres including direct imaging, phase curves and transit spectroscopy (Crossfield (2015); Madhusudhan et al. (2014)). A planetary spectrum can be constructed from several direct images taken at different wavelengths. However the extraordinary amount of work required to generate just one of these images with current facilities makes this technique a real challenge (Matsuo et al. (2011)). The properties of clouds in a extrasolar planetary atmosphere can be investigated using thermal phase curves, variation in the apparent thermal emission of the planet with its orbital phase (Muñoz & Isaak (2015)). They can also be used to put constraints on the atmospheric circulation (Selsis et al. (2011); Snellen et al. (2009)). Transit spectroscopy, the technique of importance for this work, has two components, transmission and emission. When a planet passes in front of its host star, primary transit, the starlight is filtered through the planetary atmosphere. Atoms, ions and molecules in the atmosphere will introduce small variations in the observed flux which can be measured as a function of wavelength to produce a transmission spectrum for the planet. The emission spectrum on the other hand can be observed when the planet passes behind its host star, secondary transit. In principle, a measurement of the star alone, during transit, can be subtracted from a measurement of the star and planet combined, prior to or preceding transit, to extract the planetary signal. Retrieving physical properties, such as temperature, pressure and composition from observed transmission or emission spectra can be achieved by generating a library of synthetic spectra for different physical conditions, then using some 'goodness-of-fit' parameter to match the observations to the best model. This is known as atmospheric retrieval (see for example Hollis et al. (2014)).

The interpretation of atmospheric spectra of extrasolar planets through inverse atmospheric retrieval modelling has become the industry standard (Waldmann et al. (2015a)). This requires the generation of numerous atmospheric spectral models with different compositions, temperatures and pressures. Therefore model generation needs to be as efficient as possible. A component of model generation is the input of multiple temperature and pressure dependent molecular line lists. These line lists can be very large and contain a lot of information, thence the format in which they are handled requires careful consideration. A balance must be found between compacting the line lists, to minimise computation time, and keeping the line lists as complete as possible, to preserve spectroscopic features in the data. The aim of this work was to compute temperature and pressure dependent molecular data suitable for extrasolar planetary spectral retrieval. The main challenge here is the treatment of pressure broadening, due to the overall lack of information on the pressure broadening of molecular lines by relevant species (Hedges & Madhusudhan (2016)).

Lessons learnt will also be useful for industrial spectral studies because *in situ* measurements of gas temperature and composition requires rapid model generation analogous to extrasolar planet spectral retrieval and accurate pressure broadening

information.

1.3 Additional Work

Although not high on the priority list in the context of extrasolar planetary atmospheres or industrial spectral studies, carbon monosulfide (CS) is an important molecule for other applications. It is present in several astrophysical environments, notably interstellar clouds (Shi et al. (2011); Bilalbegovic & Baranovic (2015)), and plays a role in the formation of aerosols, in particular carbonyl sulphide (OCS), in the Earth's troposphere (Li et al. (2013)). The aim of this work was to refine line lists for CS using a technique which demonstrates a useful feature of ExoMol format. Also the final line lists were used to investigate a limitation of LEVEL, a computer program for solving the radial Schrödinger equation of diatomics (LeRoy (2007)), which may have implications for other similar programs.

1.4 This Thesis

This work represents a successful collaboration between academia, specifically extrasolar planetary research, and industry. On the industrial side the aim is to monitor the concentrations of certain species in combustion and gasification processes, while on the extrasolar planetary side the aim is to characterise the atmospheres of planets outside of our solar system. Both can be done spectroscopically, though the result is highly dependent on the quality of reference data. As it happens industrial environments, such as smoke stacks, and extrasolar planetary atmospheres have molecules, temperatures and pressures in common. Hence work to improve or validate reference data for those molecules, temperatures and/or pressures would be beneficial for both applications. This is the theme of the current work.

The structure of this thesis is as follows. The background is reviewed in Chapter 2 and the methods and theory are explained in Chapters 3 to 5. Chapters 6 to 10 detail the results of individual projects while Chapter 11 presents the update to ExoMol format culminating from this work. Finally all results and conclusions are summarised in Chapter 12, avenues for future work are also discussed here.

Chapter 2

Background

2.1 Spectroscopic Databases

2.1.1 Sources of Molecular Data

There are numerous sources of molecular data including archives, catalogues and databases. The most complete library of published astronomical catalogues and data tables is the CDS catalogue, provided by VizieR (F. Ochsenbein et al. (2000)). Sometimes referred to as the 'catalogue of catalogues' it provides access to over 13,000 sources of molecular data and is used by many research groups to backup their results.

Molecular datasets can also be found in archives. For example the Kitt Peak Archive (NSO Digital Archive) provides free access to laboratory and other spectra measured at the observatory (NSO (2004)).

Databases are developed and populated by research groups for specialised applications. To name a few, HITRAN (Rothman et al. (2013)) and GEISA (Jacquinet-Husson et al. (2011)) provide data for molecules of importance in the atmospheres of Earth and other solar system planets. For the most part the data are only suitable for use at ambient temperature. JPL (Pickett et al. (1998)) and CDMS (Müller et al. (2005)) catalogues comprise of comprehensive lists of submillimeter, millimetre, microwave, and, in the case of CDMS, far-infrared transitions. The databases are complementary to one another and are aimed towards the cool interstellar medium. HITEMP (Rothman et al. (2010)), the analogues database to HITRAN, TheoReTS (Rey et al. (2016a)) and ExoMol (Tennyson & Yurchenko (2012)), to which this work is contributing, all focus on providing line lists suitable for modelling high temperature environments.

TheoReTS and ExoMol endeavour to provide complete and comprehensive lists of transitions while HITEMP first uses importance sampling to reduce the volume of data such that it may be supplied in HITRAN format (see Data Formats Section 2.1.2). Importance sampling is the removal of lines with an intensity below a set threshold (discussed further in Section 10.1.1). Currently HITEMP is limited to five species, though an expansion is planned, and TheoReTS only considers highly symmetric species while ExoMol aims to include all molecules of planetary importance.

Overall, even with the impending expansion of HITEMP, ExoMol provides complete data sets for the largest number of molecules. Although the molecules and temperatures considered by ExoMol are chosen on the basis of their importance in extrasolar planetary atmospheres, in practice the line lists are also useful for other applications that require data for elevated temperatures, including industrial spectral studies.

2.1.2 Data Formats

Molecular line lists may be represented in various ways. A format widely adopted by the community of spectroscopists that use molecular line lists is HITRAN format, most recently updated in 2004 (Rothman et al. (2005)). The format is all inclusive, every piece of information required to generate a line list for given physical conditions is provided in a single file. As useful as this sounds, it becomes a problem for large datasets. The ExoMol line lists can contain millions (for example AlO, Patrascu et al. (2015)) or even billions (for example NH_3, Yurchenko et al. (2011a)) of individual transitions. Indeed the largest to date (SO_3, Underwood et al. (2016b)) contains 21 billion lines. In order to distribute the data Tennyson et al. (2013) developed a uniform but flexible format for the line lists which separates the data into a list of energy levels (a states file), a list of allowed energy level pairings (a transitions file), and a partition function. The latter is required to calculate line intensities. The ExoMol format has since been updated to include more information (Tennyson et al. (2016)), including pressure broadening parameters (this work, see Chapter 11), but the collective size of the files is still considerably smaller than if the line lists were represented in HITRAN format.

Hill et al. (2013) also developed a procedure to reduce the size of the line lists based on the use of cross sections. Line lists are discrete, describing the position and strength of each line individually, while cross sections are continuous, describing the total absorption as a function of wavenumber for a single temperature and pressure. Cross sections are computed by first splitting the spectral range into sections or wavenumber bins. The contributions to absorption from spectral lines within each bin are summed to give a 'total' absorption for that bin, which is attributed to the central wavenumber of the bin (see Section 3.3 for more details). As such the size and resolution of a cross section set is defined by the bin spacing. ExoMol calculates high resolution cross sections, whereby the molecular data is reduced to a more manageable size but on a fine enough grid (bin spacing) such that spectroscopic features in the data are preserved. The reduction in the size of the line lists from multiple file representation to cross sections is considerable. However cross sections are inflexible and only apply to the temperature and pressure for which they have been calculated, so line lists are still preferable.

2.2 Molecules of Interest

2.2.1 Atmospheric Species

In the context of extrasolar planetary atmospheres, every molecule known to exist in gaseous form could potentially be of interest, as in general we simply do not know what they are made of. However a reasonable starting point would be the constituents of solar system planetary atmospheres.

ExoMol aims to provide line lists for all molecules expected to be of importance in the atmospheres of extrasolar planets. Line lists computed as part of the ExoMol project are summarised in Table 2.1. Line lists generated by members of the ExoMol team and co-workers though not explicitly for the ExoMol project are summarised in Table 2.2. The methodology used to generate the line lists, ExoMol (described in Chapter 3) or theoretical (*ab initio*) is indicated.

Presently only H_2O, CO_2, CO, CH_4 and more tentatively HCN have actually been detected. First detections are reported in Tinetti et al. (2007); Swain et al. (2009b, 2008, 2009a); Tsiaras et al. (2016) more comprehensive lists of references can be found in recent reviews such as Madhusudhan et al. (2016); Crossfield (2015); Madhusudhan et al. (2014); Bailey (2014). However this may change upon the launch of new space missions or the opening of new ground-based facilities so it is best to be prepared.

2.2.2 Chlorides

NaCl and KCl are important astrophysical species as they are simple, stable molecules containing atoms of relatively high cosmic abundance. Na, K and Cl are the 15th, 20th and 19th most abundant elements in the interstellar medium (Caris et al., 2004). In fact NaCl could be as abundant as the widely-observed SiO molecule (Cernicharo & Guelin, 1987).

The importance of NaCl and KCl spectra has motivated a number of laboratory studies, for example Rice & Klemperer (1957), Honig et al. (1954), Horiai et al. (1988), Uehara et al. (1989), Uehara et al. (1990) and Clouser & Gordy (1964). The most recent and extensive research on both KCl and NaCl spectra has been performed by Ram et al. (1997), who investigated infrared emission lines of $Na^{35}Cl$, $Na^{37}Cl$ and $^{39}K^{35}Cl$, Caris et al. (2004), who measured microwave and millimetre wave lines of $^{39}K^{35}Cl$, $^{39}K^{37}Cl$, $^{41}K^{35}Cl$, $^{41}K^{37}Cl$ and $^{40}K^{35}Cl$, and Caris et al. (2002), who recorded microwave and millimetre wave lines of $Na^{35}Cl$ and $Na^{37}Cl$.

Dipole moment measurements have been carried out by Leeuw et al. (1970) for $Na^{35}Cl$ and $Na^{37}Cl$, Wachem & Dymanus (1967) for $^{39}K^{35}Cl$ and $^{39}K^{37}Cl$, and Hebert et al. (1968) for $^{39}K^{35}Cl$, $Na^{35}Cl$ and $Na^{37}Cl$.

The only theoretical transition line lists for these molecules prior to this work are catalogued in the CDMS database. They were constructed using data reported in Caris et al. (2002), Clouser & Gordy (1964), Uehara et al. (1989) and Leeuw et al. (1970) for NaCl, and Caris et al. (2004), Clouser & Gordy (1964) and Wachem & Dymanus (1967) for KCl. The lists are limited to $v = 4$, $J = 159$ and do not include a list for $^{41}K^{37}Cl$. v and J indicate the rotational and vibrational excitation of the

Table 2.1: Datasets created by the ExoMol project and included in the ExoMol database (Tennyson et al. (2016)).

Molecule	$N_{\rm iso}$	$T_{\rm max}$	$N_{\rm lines}$	Name	Reference
BeH	1	2000	16 400	Yadin	Yadin et al. (2012)
MgH	3	2000	10 354	Yadin	Yadin et al. (2012)
CaH	1	2000	15 278	Yadin	Yadin et al. (2012)
SiO	5	9000	254 675	EJBT	Barton et al. (2013)
HCN/HNC	2[a]	4000	399 000 000	Harris	Barber et al. (2014)
CH_4	1	1500	9 819 605 160	YT10to10	Yurchenko & Tennyson (2014)
NaCl	2	3000	702 271	Barton	This work (Chapter 6)
KCl	4	3000	1 326 765	Barton	This work (Chapter 6)
PN	2	5000	142 512	YYLT	Yorke et al. (2014)
PH_3	1	1500	16 803 703 395	SAlTY	Sousa-Silva et al. (2015)
H_2CO	1	1500	10 000 000 000	AYTY	Al-Refaie et al. (2015)
AlO	4	8000	4 945 580	ATP	Patrascu et al. (2015)
NaH	2	7000	79 898	Rivlin	Rivlin et al. (2015)
HNO_3	1	500	6 722 136 109	AlJS	Pavlyuchko et al. (2015)
CS	8	3000	548 312	JnK	Paulose et al. (2015); This work (Chapter 6)
CaO	1	5000	21 279 299	VBATHY	Yurchenko et al. (2016b)
SO_2	1	2000	1 300 000 000	ExoAmes	Underwood et al. (2016a)
H_2O_2	1	1500	20 000 000 000	APTY	Al-Refaie et al. (2016)
H_2S	1	2000	115 000 000	AYT2	Azzam et al. (2016)
SO_3	1	800	21 000 000 000	UYT2	Underwood et al. (2016b)
VO	1	5000	270 000 000	VOMYT	McKemmish et al. (2016)

$N_{\rm iso}$ Number of isotopologues considered;
$N_{\rm lines}$ Number of lines: value is for the main isotope;
$T_{\rm max}$ Maximum temperature for which the line list is complete;
[a] A line list for $H^{13}CN/HN^{13}C$ due to Harris et al. (2008) is also available.

Table 2.2: Datasets not created as part of the ExoMol project but included in the ExoMol database (Tennyson et al. (2016)).

Molecule	N_{iso}	T_{max}	N_{lines}	Name	Reference	Methodology
H_3^+	2[a]	4000	3 070 571	NMT	Neale et al. (1996)	ExoMol
H_2O	2[b]	3000	505 806 202	BT2	Barber et al. (2006)	ExoMol
NH_3	2[c]	1500	1 138 323 351	BYTe	Yurchenko et al. (2011a)	ExoMol
HeH^+	4	10000	1 431	Engel	Engel et al. (2005)	Ab initio
HD^+	1	12000	10 119	CLT	Coppola et al. (2011)	Ab initio
LiH	1	12000	18 982	CLT	Coppola et al. (2011)	Ab initio
LiH^+	1	12000	332	CLT	Coppola et al. (2011)	Ab initio
ScH	1	5000	1 152 827	LYT	Lodi et al. (2015)	Ab initio

N_{iso} Number of isotopologues considered;
N_{lines} Number of lines: value is for the main isotope;
T_{max} Maximum temperature for which the line list is complete;
[a] There is a H_2D^+ line list available from Sochi & Tennyson (2010);
[b] The VTT line list for HDO due to Voronin et al. (2010b) is also available;
[c] There is a $^{15}NH_3$ line list due to Yurchenko (2015).

system (see Section 3.1).

Comprehensive line lists for four stable isotopologues of HCl ($H^{35}Cl$, $H^{37}Cl$, $D^{37}Cl$ and $D^{37}Cl$) have recently been provided by Li et al. (2013a,b). These are made available in HITRAN (Rothman et al. (2013)).

2.2.3 Carbon Monosulfide

The numerous astronomical detections of CS and the importance of the molecule in our own atmosphere has motivated copious laboratory studies. Experimentally the CS spectrum has been studied in wavelength regions ranging from the microwave to the ultraviolet (UV). A pioneering study was carried out by Crawford & Shurcliff (1934) whom discovered the main $A\ ^1\Pi$ - $X\ ^1\Sigma^+$ transition in the visible. Additional electronic transitions in the visible to near UV have been investigated by, for example, Bell et al. (1972), Cossart et al. (1977) and Stark et al. (1987).

Mockler & Bird (1955) made the first measurements of rotational lines for the $^{12}C^{32}S$, $^{12}C^{33}S$, $^{12}C^{34}S$ and $^{13}C^{32}S$ isotopomers in the microwave region. Transitions in this region have also been observed by, for example, Lovas & Krupenie (1974). Early work in the millimetre wave region began with measurements of rotational $^{12}C^{32}S$ and $^{12}C^{34}S$ lines by Kewley et al. (1963), later extended by Bogey et al. (1982) who additionally observed $^{13}C^{32}S$. Bogey et al. (1981) also presented a study of the millimetre spectrum of rarer isotopologues $^{12}C^{33}S$,$^{12}C^{36}S$, $^{13}C^{33}S$ and $^{13}C^{34}S$. More recent work in the region has been carried out by Ahrens & Winnewisser (1999) ($^{12}C^{32}S$, $^{12}C^{34}S$, $^{12}C^{33}S$, $^{13}C^{32}S$, $^{12}C^{36}S$, $^{13}C^{33}S$, $^{13}C^{34}S$), Kim & Yamamoto (2003) ($^{12}C^{32}S$, $^{12}C^{34}S$) and Gottlieb et al. (2003) ($^{12}C^{32}S$, $^{12}C^{34}S$, $^{12}C^{33}S$, $^{13}C^{32}S$).

The first study in the infra-red region was performed by Todd (1977) who measured the $v = 2$ - 0 vibrational band of the main isotope while Todd & Olson (1979) and Yamada & Hirota (1979) measured several $\Delta v = 1$ bands of $^{12}C^{32}S$, $^{12}C^{33}S$, $^{12}C^{34}S$ and $^{13}C^{32}S$. The resulting molecular parameters were later refined by Winkel et al. (1984) and Burkholder et al. (1987). Winkel et al. (1984) measured many $\Delta v = 2$ bands for vibrational levels up to $v = 8$ while Burkholder et al. (1987) obtained high resolution measurements of the 1 - 0 band, and 2 - 1 band for the main isotope, of $^{12}C^{33}S$, $^{12}C^{34}S$ and $^{13}C^{32}S$ for J up to 41, 28, 32 and 28 respectively. $\Delta v = 1$ bands up to $v = 9$ - 8 for the main isotope were later measured by Ram et al. (1995). The most recent research on CS infra-red spectra has been performed by Uehara et al. (2015), who reported $\Delta v = 1$ transitions of $^{13}C^{32}S$ up to $v = 5$ - 4. Additionally they measured $\Delta v = 1$ transitions of $^{12}C^{32}S$ up to $v = 7$ - 6 to a higher accuracy than Ram et al. (1995).

Using the vibration-rotation and pure rotation data on this molecule available to them, Coxon & Hajigeorgiou (1992) derived a spectroscopic potential energy curve (PEC) (see Section 3.1) that reproduced all the input experimental data within experimental error. Paulose et al. (2015) employed this spectroscopic curve as starting point, as well as a theoretical dipole moment curve (DMS) (see Section 3.1) from Pineiro et al. (1987) to calculate comprehensive line lists for all stable isotopologues of CS ($^{12}C^{32}S$, $^{12}C^{33}S$, $^{12}C^{34}S$, $^{12}C^{36}S$, $^{13}C^{32}S$, $^{13}C^{33}S$, $^{13}C^{34}S$, $^{13}C^{36}S$).

Post-calculation a large portion of the weak transitions had to be removed from the line lists as a result of work done by Li et al. (2015), Medvedev (2012) and Medvedev et al. (2015). Li et al. (2015) recently presented a new line list for the main isotopologue of CO with rigorous validation of the calculated parameters, including intensities. The authors found that certain predicted intensities did not obey the Normal Intensity Distribution Law (Medvedev (2012)). Simply put this law dictates that transition intensities should decrease in a linear fashion for an increasing change in energy. Medvedev et al. (2015) investigated this problem and proposed the cause to be inadequate precision employed in the calculation of the line list. As such the problem did not only apply to the CO line list of Li et al. (2015), but to many line lists calculated using the same numerical methods. This includes the present line lists for CS, NaCl and KCl.

2.2.4 Ammonia

A considerable amount of work, over 140 experimental studies, has been done on the NH_3 spectrum. Recent work includes high (Zobov et al. (2011); Hargreaves et al. (2011, 2012b) and this work) and low (Cermák et al. (2014); Cacciani et al. (2014)) temperature studies in various spectral regions. A comprehensive compilation of measured NH_3 rotational and ro-vibrational spectra can be found in a recent MARVEL study (Al Derzi et al. (2015)).

The MARVEL (measured active rotation-vibration energy levels) algorithm (Furtenbacher et al. (2007); Furtenbacher & Császár (2012)) simultaneously analyses all available assigned and labelled experimental lines, thus yielding the associated energy levels (see Section 4.4.1). The recent study for NH_3 analysed 29,450 measured

transitions and yielded 4961 accurately-determined energy levels which mostly lie below 7000 cm^{-1} (Al Derzi et al. (2015)).

The most complete experimental line lists for regions 740 - 2100 cm^{-1} and 1650 - 4000 cm^{-1} are those constructed by Hargreaves et al. (2011, 2012b) who supplemented their own hot (up to 1400 °C) emission line measurements with lines from HITRAN. The region 4000 - 11,000 cm^{-1} is covered by the band model parameters of Irwin et al. (1999), though these are only designed to be used at temperatures below 300 K. There are also copious sources of line measurements and quantum assignments for the region 0 - 7000 cm^{-1} collated in HITRAN.

A number of variational line lists are available for NH_3 (Yurchenko et al. (2009, 2011a); Huang et al. (2011b)). The line list employed by this work is BYTe (Yurchenko et al. (2011a)), which is a variationally computed line list for hot NH_3 that covers the range 0 - 12,000 cm^{-1}. BYTe is expected to be fairly accurate for all temperatures up to 1500 K (1226 °C). However there is motivation to improve BYTe which, in particular, is known to be less accurate for higher wavenumber transitions (Huang et al. (2011a,b); Sung et al. (2012)).

2.2.5 Methane

The experimental and theoretical work on the CH_4 spectrum is extensive. A compilation of measured CH_4 rotational and ro-vibrational spectra is presented in Chapter 9. An overview is given below.

The energy levels of methane are structured in groups of close lying energy levels called polyads (Boudon et al. (2006)). A visual representation of the first ten polyads of CH_4 is shown in Figure 2.1. The polyads, P_n where $n = 0, 1, 2, 3...$, are numbered with increasing energy. CH_4 is a highly symmetric species with a symmetric charge distribution and hence no permanent dipole. Molecules with no permanent dipole moment do not have a dipole allowed rotational spectrum (Tennyson (2011)).

However due to centrifugal distortion, CH_4 has a weak rotational spectrum belonging to the ground state monad. This has been observed by various studies, most recently by Boudon et al. (2010) and Sanzharov et al. (2012) using high intensity synchrotron radiation combined with an Fourier transform infra-red spectrometer at the AILES beamline of SOLEIL.

The dyad is well understood, with many high resolution studies providing detailed information for this region. In particular Champion et al. (1989) measured line positions near 7 μm ($\approx$ 1426 cm^{-1}) with a precision of 0.00006 cm^{-1}.

A comparatively high number of experimental studies pre-2010 have focused on the pentad. This has included measurement of high accuracy line positions (Albert et al. (2009)), line intensities (Fejard et al. (2000)), pressure broadened widths (Pine (1992)) and observation of forbidden lines (Tarrago et al. (1975)).

The octad, and lower polyads, were the subject of a global analysis in 2009 that obtained very accurate reproductions of the measured line positions employed in the fit (of the order 10^{-3} cm^{-1}, Albert et al. (2009)). Since this analysis, new assignments for the octad region have been reported by Daumont et al. (2013).

A considerable amount of post-2009 work has gone into improving the understanding of the tetradecad and icosad regions. Recent measurements include Nikitin et al. (2014) for the tetradecad and Zolot et al. (2013) for the icosad, while Nikitin et al. (2016) and Rey et al. (2016b) have presented detailed analyses for these regions.

Experimental studies for higher polyads are few in number, though include measurements in the triacontad (Béguier et al. (2015); Boursier et al. (2006)), tetracontad (Béguier et al. (2015); Pierre et al. (1980)), pentacontakaipentad (Boraas et al. (1994); Campargue et al. (1995)) and heptacontad (Campargue et al. (1991)).

The number of interacting levels within each polyad increases with polyad number, resulting in a very complex spectrum (Albert et al. (2009)). Consequently many of the experimental measurements are made at room or colder temperatures. However high temperature measurements have been reported by Hilico et al. (1993), Nassar & Bernath (2003) and Hargreaves et al. (2012a) for example. Several experimental studies are compiled in the HITRAN database, as detailed by Brown et al. (2013).

Numerous ro-vibrational line lists are available for CH_4. Experimental line lists include partial lists constructed by Campargue et al. (2013) (WKLMC) and Nikitin et al. (2015) (GOSAT-2014) for room temperature or colder applications, and Hargreaves et al. (2012a) and Nassar & Bernath (2003) for high temperature applications. There are also a number of empirical line lists, a notable example is the list produced by Béguier et al. (2015) for the 9000 - 10,400 cm^{-1} region. This was constructed to fill a gap in HITRAN coverage.

On the theoretical side, high temperature line lists have been computed by Yurchenko & Tennyson (2014), Yurchenko et al. (2016a), Rey et al. (2014) and Warmbier et al. (2009). The line list employed in this work is YT10to10 (Yurchenko & Tennyson (2014)) which covers the spectral range 0 - 10,000 cm^{-1} and is expected to be suitable for all temperatures up to 1500 K. Although sufficient for the purposes of this work (see Chapter 7), this line list has now been extended to higher temperatures (2000 K) and a number of predicted line positions have been improved by replacing calculated energies with empirical ones (Tennyson et al. (2016); Yurchenko et al. (2016a)).

2.3 Applications

2.3.1 Industrial Spectral Studies

In biomass, alkali metals and other problem compounds in the context of corrosion are often present in a form susceptible to vaporisation (Miles et al. (1995)). Gases containing chlorine (Cl_2), HCl, NaCl and KCl may cause corrosion directly, by accelerating the oxidation of metal alloys, or indirectly, by influencing other corrosion mechanisms such as chloride deposition (Nielson et al. (2000)). KCl is the dominant chloride in biomass combustion (Nielson et al. (2000)) though the other chlorides are no less of a concern. In fact the presence of HCl and Cl_2 can increase corrosion rates by some 40% (Kear (2007)). There is a need to monitor corrosion rates in power plants, particularly for straw-firing plants where the corrosion rates are higher (Montgomery et al. (2010)).

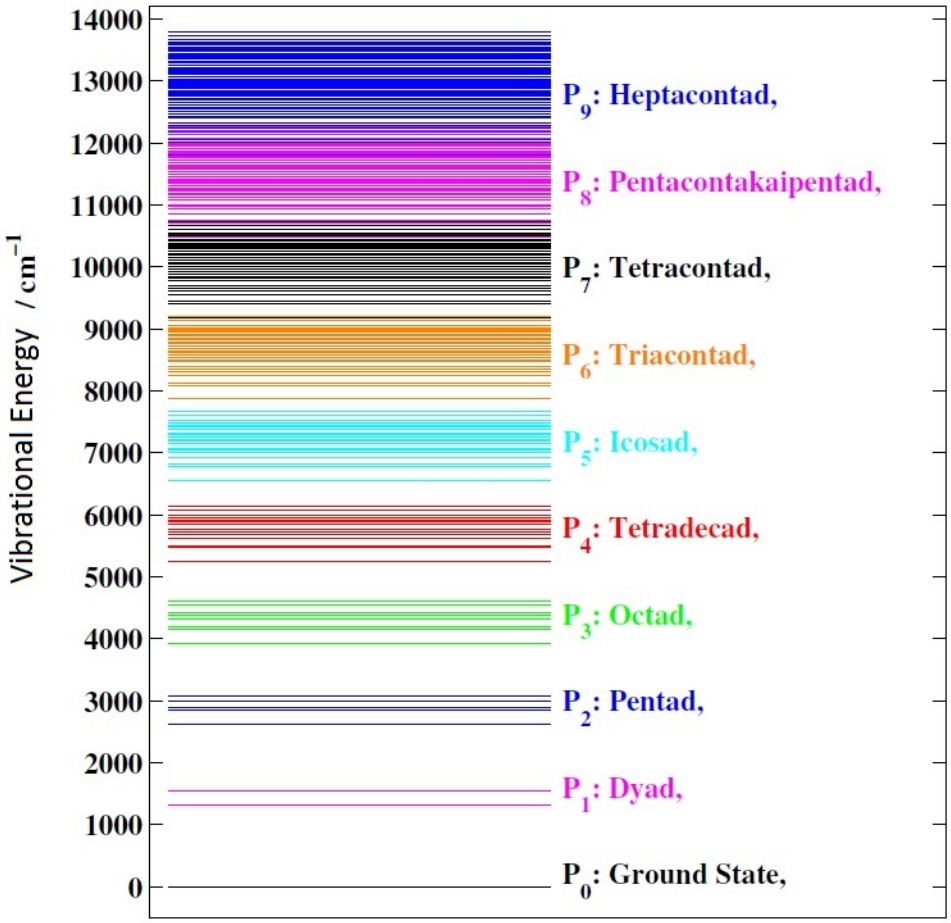

Figure 2.1: First ten vibrational polyads of methane (modified Figure 1 from Albert et al. (2009)).

Nitrogen oxides (NOx) are highly reactive gases and products of fuel combustion that have been linked to adverse effects on the environment and human health (EPA (2014b)). One method of controlling NOx emissions is Selective Catalytic Reduction (SCR) by NH_3. A by-product of this process is unreacted NH_3, referred to as 'ammonia slip' (Staudt (2000)). Ammonia slip reacts with sulphur compounds to produce ammonium sulphates which can cause fouling and corrosion of downstream components (Knight (2008)). Ammonia slip can also result in the contamination of fly ash, a residue generated by combustion. This leads to problems when recycling or disposing of the ash (Knight (2008)). There is motivation to closely monitor ammonia slip in power plants so as to optimise the manner in which facilities are operated to enhance income at a lower risk (Staudt (2000)).

The most important anthropogenic greenhouse gas, aside from CO_2, is CH_4 (Boucher et al. (2009)). The concentration of CH_4 in the atmosphere has increased by nearly a factor of three since pre-industrial times, and the impact on global warming is exacerbated by the oxidation of CH_4 in the troposphere and upper stratosphere which ultimately produces CO_2 (Boucher et al. (2009)). The exact causes of the increase in concentration of global atmospheric methane are still a source of debate (Nisbet et al. (2014)), although leaks from systems utilising natural gas (which consists largely of methane) are considered to be a major contributor (Brandt et al. (2014)). Monitoring of CH_4 emissions from industrial sources is required to inform management and policy decisions.

The economic impact of formaldehyde is considerable. The industrial sectors that use the chemical or produce goods containing it, reportedly account for around 500 billion dollars of the annual US gross national product (Zhang et al. (2009)). Applications include rock wool insulation and the manufacture of pressed wood products (Fré et al. (2004)). Unfortunately formaldehyde is extremely toxic, and occupational exposure has been linked to leukaemia (Zhang et al. (2009)). It is therefore vital to take steps, such as the minimisation of formaldehyde emissions from smoke stacks (Fré et al. (2004)), to protect human health.

2.3.2 Extrasolar Planetary Atmospheres

The characterisation of extrasolar planetary atmospheres has become a major component of extrasolar planetary research. To date several studies have used transit spectroscopy to probe the atmospheres of extrasolar planets for example Hot Jupiter WASP-19b (Mandell et al. (2013), Bean et al. (2013)), Hot Neptune GJ 436b (Pont et al. (2008), Knutson et al. (2014)) and Super Earth GJ 1214b (Croll et al. (2011), Bean et al. (2010), Kreidberg et al. (2014) and others). Transit spectroscopy is the observation of transiting planets in the combined light of the planet-star system. The signal from the planet can, in theory, be extracted from the combined observations by subtracting the stellar contribution. A transmission spectrum is obtained by observing the primary transit, when the planet passes in front of the star, while an emission spectrum is obtained by observing the secondary transit, when the planet passes behind the star (Seager (2008)).

Once the planetary signal has been extracted, the temperatures, pressures and

abundances of molecules in the atmosphere may be 'retrieved' by producing models for a variety of hypothesised compositions and physical conditions and comparing to the observations. This is inverse atmospheric retrieval modelling (Hollis et al. (2014)).

Existing retrieval codes include CHIMERA (Line et al. (2013)), a statistically robust suite of extrasolar atmospheric retrieval algorithms, and NEMISIS (Irwin et al. (2008)), a full planetary atmosphere radiative transfer and retrieval code that specifically employs k-correlated coefficients. K-correlated coefficients are calculated from absorption cross sections by transforming from wavenumber integration to an integration over cumulative probability. Using these coefficients in place of cross sections saves computation time but can lead to blurring in the data. (Fu & Liou (1992)).

A code from the extrasolar planet group at UCL, to which this work contributes, is τ-REx, a next generation retrieval code for extrasolar planetary atmospheres (Waldmann et al. (2015a,b)). It differentiates itself from existing codes in the literature through five unique approaches:

1. Optimised use of the ExoMol line lists (this work, see Chapter 10),
2. Unbiased prior selection of atmospheric constituents,
3. Use of two independent algorithms to fully sample the likelihood space,
4. Iterative parameter and model selection to ensure models are not over- or under-complete,
5. Scalability to cluster computing.

This code was recently used to retrieve the spectrum of super-Earth 55 Cancri e (Tsiaras et al. (2016)). The retrieval implied an atmosphere dominated by hydrogen and helium with molecular features that could be attributed to hydrogen cyanide (Tsiaras et al. (2016)).

Chapter 3

Methods and Theory I - Molecular Data

This Chapter was written with reference to Tennyson (2011).

ExoMol combines theoretical (*ab initio*) and semi-empirical methods to compute comprehensive molecular line lists (Tennyson & Yurchenko (2012)). Figure 3.1 presents a schematic of the ExoMol methodology described below. In summary energy states are calculated and labelled (Section 3.1.1), then allowed energy state pairings (selection rules) are applied and transition probabilities determined (Section 3.1.2), together these form the core line list. If required the line list may be refined by applying corrections, fitting to experiment or replacing calculated energies with experimental ones (Section 3.1.3).

Line lists are supplemented with additional information, such as the temperature dependent partition function and, if available, pressure broadening parameters. This information is required to model the molecular spectra for different physical conditions (Section 3.2).

ExoMol also provides absorption cross sections (Section 3.3) generated from the line lists (Hill et al. (2013)).

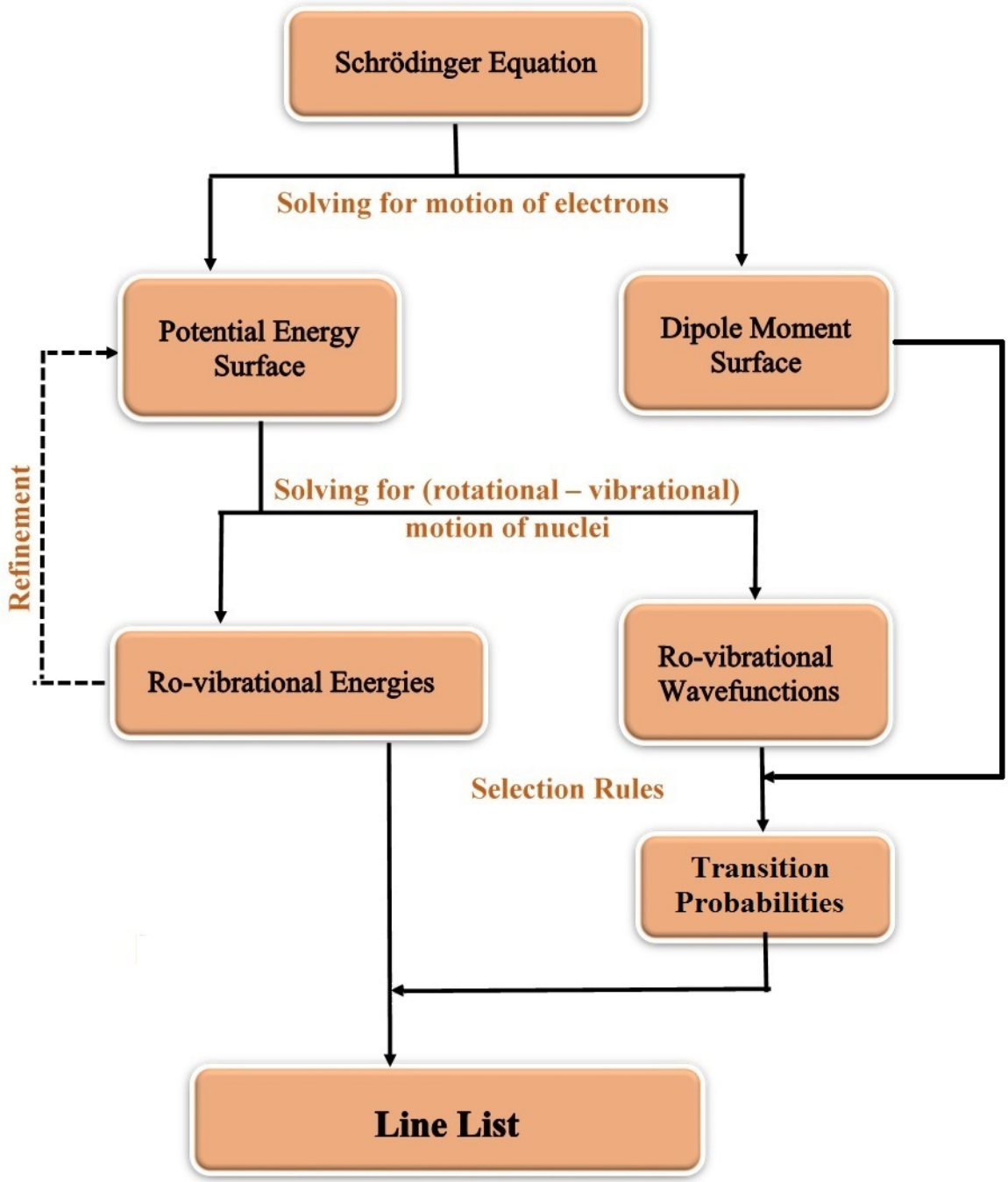

Figure 3.1: Schematic of the ExoMol methodology.

3.1 Line List

In this work lines lists are computed for closed-shell diatomics in their ground electronic states using program LEVEL, a computer program for solving the radial Schrödinger equation for energy states of diatomics (LeRoy (2007)). Closed-shell indicates that the outermost electronic shell of the molecule is fully populated. The theory is described below.

3.1.1 Energy States

Energy levels or states are calculated by solving the radial time-independent Schrödinger equation for the system:

$$\hat{H}\psi = E\psi \tag{3.1}$$

An equation of the form $A\underline{x} = \lambda\underline{x}$ may be solved by diagonalising matrix A. This involves determining the eigenvectors $\underline{x}$ and results in a matrix with diagonal entries equal to the eigenvalues λ.

First the Born-Oppenheimer Approximation (BOA, Born & Oppenheimer (1927)) is applied. This separates the nuclear and electronic wavefunction on the basis that the motions of the nuclei and electrons can be treated separately because, relative to the electrons, the nuclei are essentially stationary. The molecular wavefunction ψ is then approximately expressed as the product of the nuclear ψ_N and electronic ψ_e wavefunctions:

$$\psi \approx \psi_N \times \psi_e \tag{3.2}$$

and the molecular Schrödinger equation is separated into its electronic:

$$\hat{H}_e\psi_e(R) = V(R)\psi_e(R) \tag{3.3}$$

and nuclear:

$$\hat{H}_N\psi_N = E\psi_N \tag{3.4}$$

components. The electronic Schrödinger equation is solved first and for different nuclear configurations, giving the electronic potential V as a function of inter-nuclear distance R or the potential energy curve (PEC) for the molecule.

There are multiple solutions per nuclear configuration, in other words multiple PECs per molecule, one for each electronic state. This work considers only the lowest-lying (ground) states of closed-shell diatomics. Figure 3.2 gives the PEC for the ground electronic state of SiO as an example.

A PEC can be represented by turning points, values of $V(R)$ and R, or an empirical analytical function. There are numerous analytical representations of PECs. Those relevant to this work are given below. The functions differ mainly by how they model long-range behaviour (see Figure 3.3) and are written in terms of a series expansion $\beta(R)$ of radial variable $y_p^{eq}(R)$ with coefficients β_i.

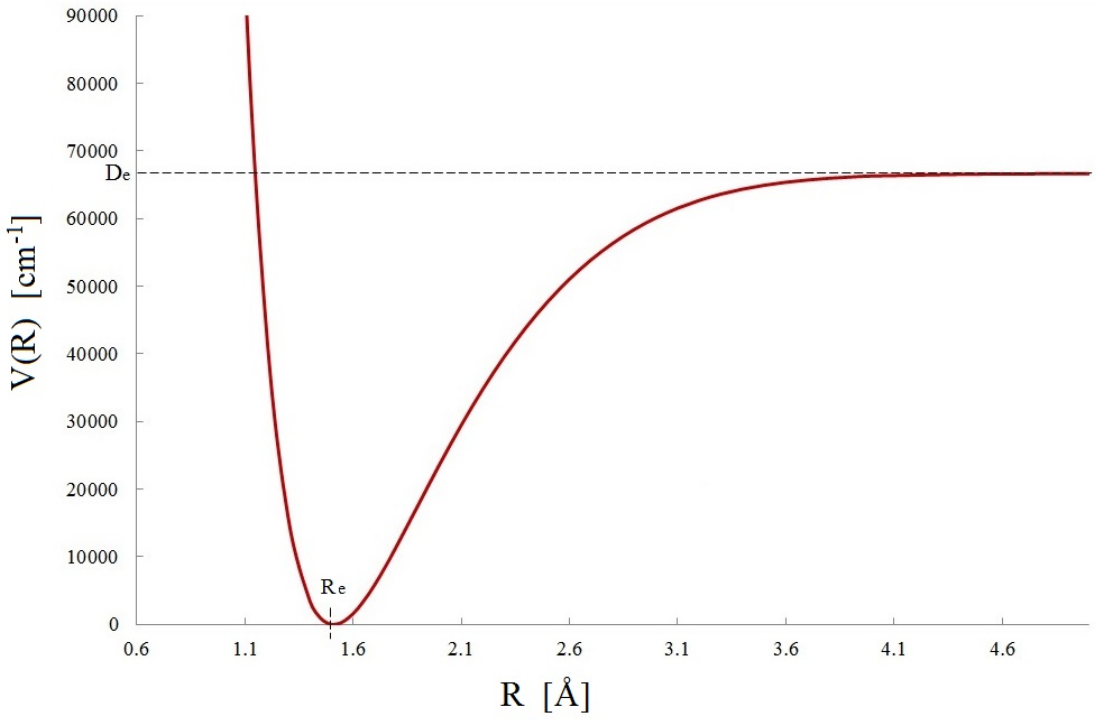

Figure 3.2: Potential energy curve for the lowest-lying state of a diatomic (SiO Barton et al. (2013)), where D_e is the dissociation energy and R_e is the equilibrium internuclear distance.

Expanded Morse Oscillator (EMO) from LeRoy (2011):

$$V_{EMO}(R) = D_e \left[1 - e^{-\beta(R)(R-R_e)}\right]^2, \tag{3.5}$$

where

$$\beta(R) = \beta_{EMO}(y_p^{eq}(R)) = \sum_{i=0}^{N_\beta} \beta_i y_p^{eq}(R)^i, \tag{3.6}$$

and

$$y_p^{eq}(R) = \frac{R^p - R_e^p}{R^p + R_e^p} \tag{3.7}$$

D_e is the dissociation energy, R_e is the equilibrium internuclear distance, p is selected as a small positive integer.

Morse Long Range (MLR) from LeRoy (2011):

$$V_{MLR}(R) = D_e \left[1 - \frac{u_{LR}(R)}{u_{LR}(R_e)} e^{-\beta(R) y_p^{eq}(R)}\right]^2, \tag{3.8}$$

where

$$\beta(R) = \beta_{MLR}(y_p^{eq}(R)) = y_p^{eq}(R)\beta_\infty + \left[1 - y_p^{eq}(R)\right] \sum_{i=0}^{N_\beta} \beta_i y_p^{eq}(R)^i, \tag{3.9}$$

in which $\beta_\infty = \lim_{r\to\infty}\beta(R) = \ln\left(2D_e/u_{LR}(R_e)\right)$ and

$$y_p^{eq}(R) = \frac{R^p - R_e^p}{R^p + R_e^p} \tag{3.10}$$

$$u_{LR}(R) = \frac{C_m}{R^m} + \frac{C_n}{R^n} \tag{3.11}$$

If C_n in Equation (3.11) equals zero, Equation (3.8) yields a Morse Lennard-Jones (MLJ) (LeRoy (2007)). D_e is the dissociation energy, R_e is the equilibrium internuclear distance, p, m and n are selected as small positive integers and C_m and C_n are constants chosen to give physical long range behaviour.

The PEC V(R) is incorporated into the nuclear Hamiltonian $\hat{H}_N$. The nuclear Schrödinger equation describes all motion of the nuclei and can be separated into an equation for internal motion (rotation-vibration) and translational motion (the motion of the whole system through space). The latter is separated off, as the energy of this motion gives a continuum that would otherwise obscure the quantised spectrum of ro-vibrational energy states. This leaves:

$$\hat{H}_N \psi_N = \left[-\frac{\hbar^2}{2\mu}\nabla^2 + V(R)\right] \psi_N = E\psi_N \tag{3.12}$$

where μ is the reduced mass given by:

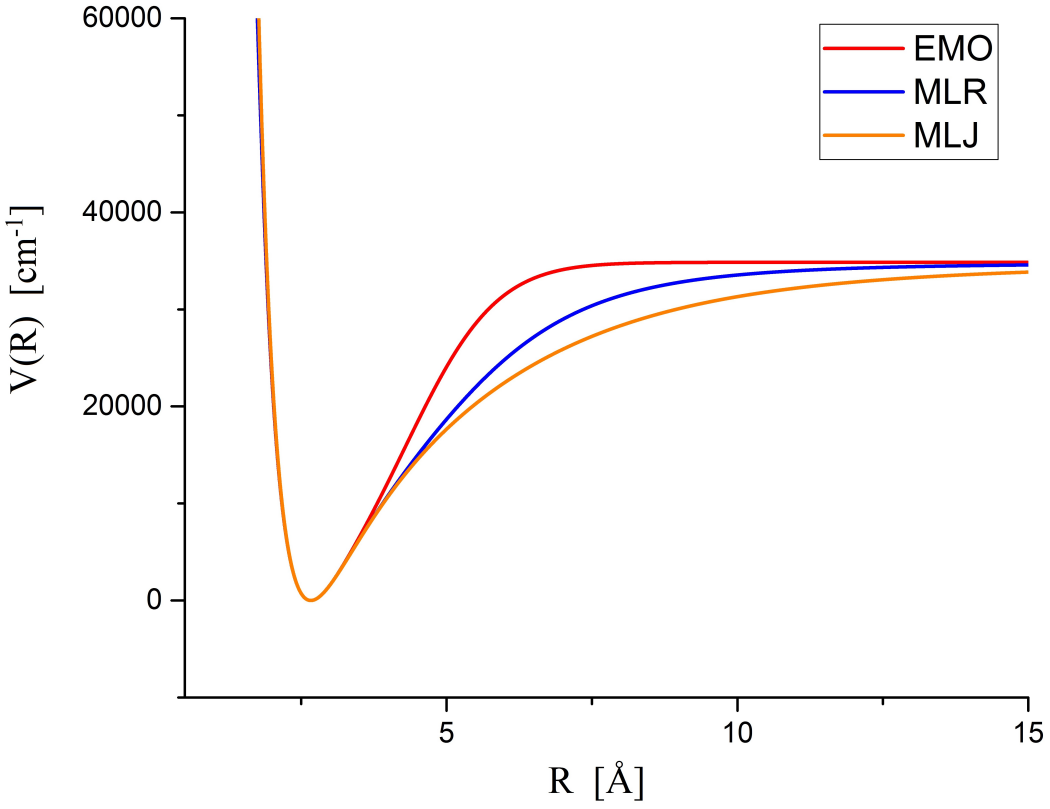

Figure 3.3: Comparison of three analytical functions used to represent potential energy curves: Expanded Morse Oscillator (EMO), Morse Long Range (MLR) and Morse Lennard-Jones (MLJ).

$$\mu = \frac{m_1 \times m_2}{m_1 + m_2} \tag{3.13}$$

where m values refer to the atomic mass of each particle.

The solutions to this equation are discrete ro-vibrational energy states (Figure 3.4). Each energy state is specified by two quantum numbers, total angular momentum J (rotational motion) and normal mode v (vibrational motion). Both quantum numbers take positive integer values starting from zero. The energy states also have a degeneracy due to rotational and nuclear spin (S) angular momentum. The projection of J onto the molecular axis, M_J, can take values $M_J = -J, -J+1, ..., 0, ..., J-1, J$, in other words there are $2J+1$ possible values of M_J giving a rotational state degeneracy of $2J+1$. The same applies to nuclear spin. The total energy state degeneracy is the product of rotational degeneracy, g_J and nuclear spin degeneracy g_S, $g_{tot} = (2J+1) \times (2S+1)$.

The results are compiled in a .states file (Tennyson et al. (2013), Tennyson et al. (2016)). This file has four compulsory columns:

1. state counting number i (i = 1,2,3...),
2. state energy E in cm^{-1},
3. total state degeneracy g_{tot} and
4. total angular momentum quantum number J.

These are followed by optional columns, in this case vibrational normal mode quantum number v. An example is presented in Table 3.1.

Table 3.1: Extract from the start of a ExoMol .states file for a diatomic (SiO Barton et al. (2013))

i	E	g_{tot}	J	v
1	0.000000	1	0	0
2	1.448467	3	1	0
3	4.345384	5	2	0
4	8.690712	7	3	0
5	14.484267	9	4	0
6	21.726203	11	5	0
7	30.416042	13	6	0

i: State counting number;
E: State energy in cm^{-1};
g: State degeneracy;
J: State rotational quantum number;
v: State vibrational quantum number.

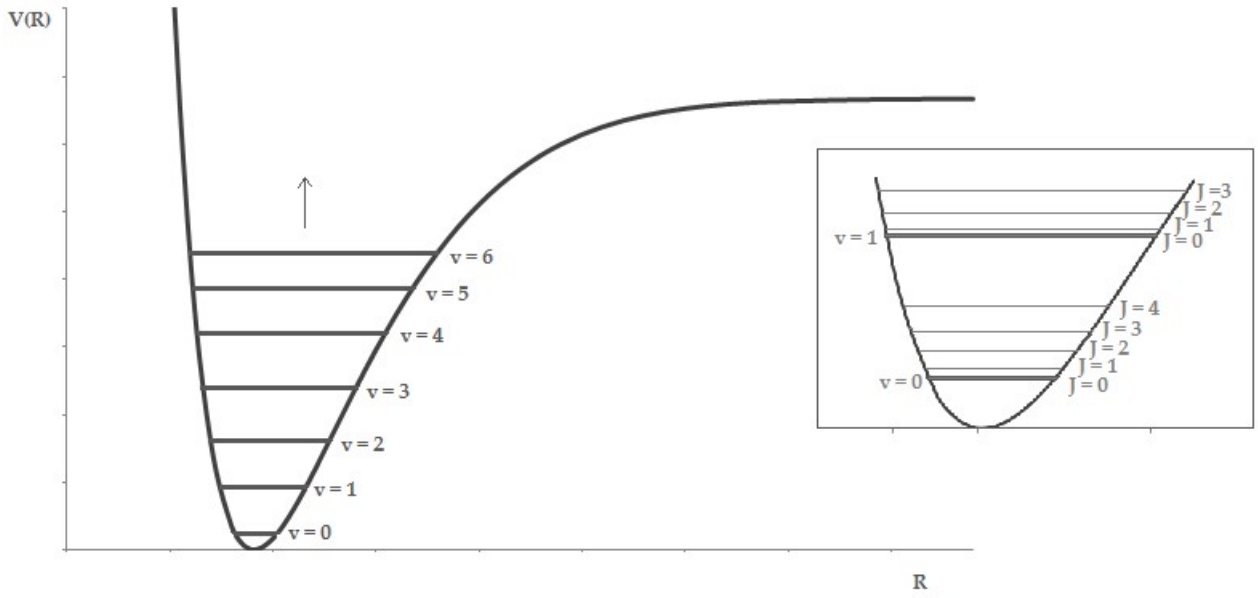

Figure 3.4: Bound ro-vibration energy levels on a ground state potential energy curve for a diatomic.

3.1.2 Transitions

Transitions occur between energy states (Section 3.1.1). States are coupled according to dipole selection rules which relate to the energy state quantum numbers. For the closed shell diatomics considered in this work the only selection rule is $\Delta J = \pm 1$.

In a spectrum, transitions manifest as lines of depleted (absorption) or excess (emission) intensity with respect to the background. The position of each line in the spectrum is expressed in wavenumbers and calculated by simple subtraction of the lower state energy from the upper state energy. The strength (and shape) of each line is dependent on many factors including temperature, pressure and molecular abundance. In order to supply flexible line lists ExoMol provides transition probabilities, which are independent of these factors, and additional information, such as the temperature dependent partition function, which can be combined to model the molecular spectrum for different physical conditions.

The transition probability is represented by the Einstein A Coefficient, A_{if}, which is the number of transitions per second from excited state i to lower state f. This is given by (Tennyson et al. (2004)).

$$A_{if} = \frac{64\pi^4}{3c^3h}\tilde{\nu}^3 \frac{S(f-i)g'_{tot}}{2J'+1} \tag{3.14}$$

where $\tilde{\nu}$ is the line position in wavenumbers, $'$ indicates upper state and $S(f-i)$ is the line strength. $S(f-i)$ is derived from the molecular dipole moment $\mu_m(R)$ and the wavefunctions of states i and f:

$$S(f-i) = |\langle \psi_i | \mu_m(R) | \psi_f \rangle|^2 \tag{3.15}$$

The molecular dipole moment can be thought of as the mathematical product of charge and position vector summed over all charged particles. The dipole moment as a function of internuclear distance is represented by a dipole moment curve (DMC). Figure 3.5 gives the dipole moment curve of SiO as an example.

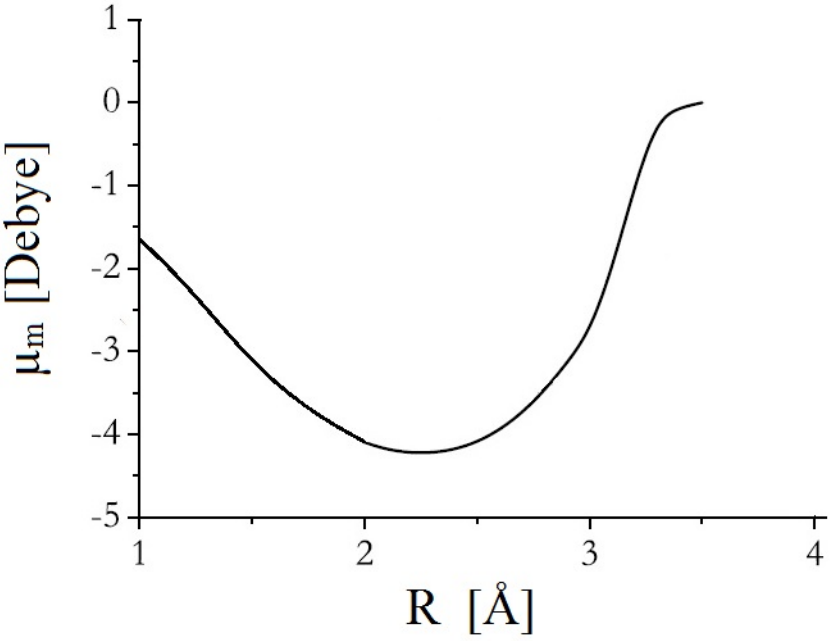

Figure 3.5: Dipole Moment Curve for a diatomic with a permanent dipole (SiO Barton et al. (2013))

The paired energy states and transition probabilities are compiled in a .trans file (Tennyson et al. (2013), Tennyson et al. (2016)). This file contains three compulsory columns:

1. upper state counting number i (i = 1,2,3...),
2. lower state counting number f (f = 1,2,3...) and
3. Einstein A coefficient (s^{-1}).

An example is presented in Table 3.2.

Table 3.2: Extract from the start of a ExoMol .trans file for a diatomic (SiO Barton et al. (2013))

i	f	A_{if}
2	1	3.0103e-06
3	2	2.8899e-05
4	3	1.0450e-04
5	4	2.5686e-04
6	5	5.1309e-04
7	6	9.0018e-04
8	7	1.4453e-03
9	8	2.1753e-03

i: Upper state counting number;
f: Lower state counting number;
A_{if}: Einstein A coefficient in s^{-1}.

3.1.3 Refinement

The BOA assumes the PEC does not change under isotopic substitution. Any shift represents a breakdown in the approximation but not a necessary consequence of separating electronic and nuclear motions (Bunker (1968)). It has become common for combined isotope studies to include atomic-mass-dependent Born-Oppenheimer Breakdown (BOB) correction terms. These corrections are applied to the PEC in the nuclear motion Hamiltonian.

For an isotope α of a diatomic A-B, where $\alpha = 1$ indicates the reference isotope and m_A and m_B are the respective atomic masses, the nuclear Hamiltonian may be written (LeRoy et al. (2006)):

$$\hat{H}_N = -\frac{\hbar^2}{2\mu}\frac{d^2}{dR^2} + \left[V(R) + V_{ad}^{(\alpha)}\right] - \frac{J(J+1)\hbar^2}{2\mu R^2}\left[1 + g^{(\alpha)}(R)\right] \tag{3.16}$$

The mass-dependent adiabatic correction function $V_{ad}(R)$ is equivalent to the difference between the potentials for isotope α and the reference species:

$$V_{ad}^{(\alpha)}(R) = \frac{m_A^{(\alpha)} - m_A^{(1)}}{m_A^{(\alpha)}}\hat{S}_{ad}^{A}(R) + \frac{m_B^{(\alpha)} - m_B^{(1)}}{m_B^{(\alpha)}}\hat{S}_{ad}^{B}(R) \tag{3.17}$$

While the mass-dependent non-adiabatic correction function $g(R)$ is given by:

$$g^{(\alpha)}(R) = \frac{m_A^{(1)}}{m_A^{(\alpha)}}\hat{R}_{na}^{A}(R) + \frac{m_B^{(1)}}{m_B^{(\alpha)}}\hat{R}_{na}^{B}(R) \tag{3.18}$$

For the analytical potential functions relevant to this work, the atom dependent radial BOB correction functions, $\hat{S}(R)$ and $\hat{R}(R)$ are given by:

$$\hat{S}_{ad}^{A/B}(R) = y_p(R, R_e)u_\infty^{A/B} + [1 - y_p(R, R_e)] \sum_{i=0}^{N} u_i^{A/B} y_p(R, R_e)^i \tag{3.19}$$

$$\hat{R}_{na}^{A/B}(R) = y_p(R, R_e)t_\infty^{A/B} + [1 - y_p(R, R_e)] \sum_{i=0}^{N} t_i^{A/B} y_p(R, R_e)^i \tag{3.20}$$

where

$$y_p(R, R_e) = \frac{R^p - R_e^p}{R^p + R_e^p} \tag{3.21}$$

The PEC may also be refined by fitting to experiment. This can be achieved by performing a 'direct potential fit' to measured line positions. This is the procedure employed by the program used in this work, DPotFit (LeRoy et al. (2006)), described here. A direct potential fit involves comparing eigenvalue differences calculated from the nuclear Schrödinger equation based on some analytic PEC, to observed line positions and minimising the squares of the differences between them by adjusting the expansion parameters of the analytical potential. Minimising the squares of the residuals is known as least-squares fitting.

As measured line positions may have very different magnitudes and absolute uncertainties, it is appropriate to perform a weighted fit where each data point has a weight w_i defined by its uncertainty u_i:

$$w_i = \left(\frac{1}{(u_i)}\right)^2 \tag{3.22}$$

Fits of this type are very non-linear, due to the functional form of the PEC, and are quick to diverge. A good method to ensure convergence is to begin by fitting line positions of transitions between lower energy states to a potential model with only a few expansion parameters. Once a converged fit for the restricted data set and model is obtained, the range of input data and the number of expansion parameters in the model can be extended until the whole data set in included and an optimum fit is achieved.

The quality of a fit yielding predicted line positions y_i^{calc} is quantified with respect to the uncertainty of the input line positions y_i^{obs} by the dimensionless root mean squared (RMS) deviation:

$$DRMSD = \bar{dd} = \left[\frac{1}{N}\sum_{i=1}^{N}\left(\frac{y_i^{calc} - y_i^{obs}}{u_i}\right)^2\right]^{\frac{1}{2}} \tag{3.23}$$

or standard deviation:

$$DSE = \bar{\sigma_f} = \vec{dd}\sqrt{\frac{N}{N-M}} \tag{3.24}$$

where M is the number of PEC expansion parameters and N is the number of input data points.

A 'good' fit will yield DRMSD and DSE values close to unity as, for example, a $\bar{dd}$ value of 2 indicates that on average the results y_i^{calc} disagree with the input data y_i^{obs} by 2 times the experimental uncertainty u_i.

It is also possible to refine predicted line positions post-calculation. ExoMol format rather helpfully separates energy states and allowed transitions into separate files (Tennyson et al. (2013), Tennyson et al. (2016)). Hence it is possible for calculated energies compiled in the .states file to be replaced with experimentally derived energies. This in principle provides experimental accuracy within the experimental range whilst maintaining the predictive power of the model, provided care is taken to maintain energy state separations outside the experimental range (see Barber et al. (2014) for example).

3.1.4 Note on Quantum Numbers

Part of the process of producing molecular line lists is assigning labels to energy states which (ideally) have some physical meaning. For example, the energy states of the ground state diatomics considered in this work are assigned two labels which relate to the vibrational and rotational motion of the molecule, v and J.

Although this work does not produce line lists for more complex systems, this work does assign upper and lower state labels to measured transitions of NH_3 and derived experimental energies of CH_4 by comparison to existing line lists BYTe (NH_3 Yurchenko et al. (2011a)) and YT10to10 (CH_4 Yurchenko & Tennyson (2014)). The quantum number conventions employed by this work for NH_3 (see Table 3.3) and CH_4 (see Table 3.4) are described below.

Table 3.3: NH_3 quantum numbers recommended by Down et al. (2013)

Label	Definition
v_1	Symmetric stretch vibrational normal mode
v_2	Symmetric bend vibrational normal mode
v_3	Asymmetric stretch vibrational normal mode
v_4	Asymmetric bend vibrational normal mode
L_3	Asymmetric stretch vibrational angular momentum
L_4	Asymmetric bend vibrational angular momentum
L	$L_3 + L_4$
J	Total rotational angular momentum
K	Projection of J onto the molecular axis
i	Inversion mode
Γ_{rot}	Symmetry of rotational wavefunction
Γ_{vib}	Symmetry of vibrational wavefunction
Γ_{tot}	Symmetry of total wavefunction

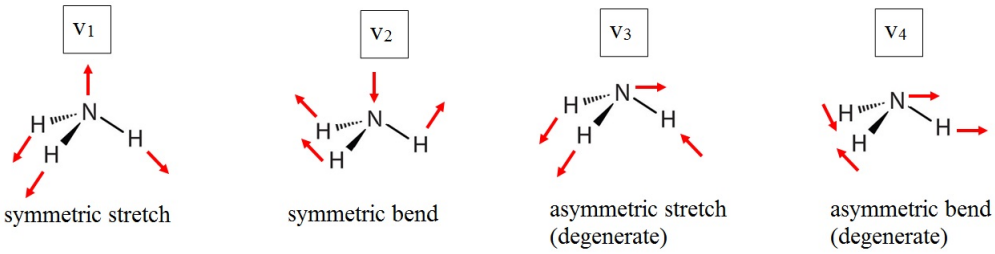

Figure 3.6: Normal modes of vibration of the ammonia molecule.

v_i relate to normal mode vibrational motion (Figure 3.6: NH_3, Figure 3.7: CH_4) and take positive integer values starting from zero. L_i are additional labels for de-

Table 3.4: CH_4 quantum numbers employed by Yurchenko & Tennyson (2014)

Label	Definition
v_1	Symmetric stretch vibrational normal mode
v_2	Symmetric bend vibrational normal mode
v_3	Asymmetric stretch vibrational normal mode
v_4	Asymmetric bend vibrational normal mode
L_2	Symmetric bend vibrational angular momentum
L_3	Asymmetric stretch vibrational angular momentum
L_4	Asymmetric bend vibrational angular momentum
M_3	Multiplicity Index for v_3, L_3
M_4	Multiplicity Index for v_4, L_4
J	Total rotational angular momentum
K	Projection of J onto the molecular axis
Γ_{rot}	Symmetry of rotational wavefunction
Γ_{vib}	Symmetry of vibrational wavefunction
Γ_{tot}	Symmetry of total wavefunction
$N_{\Gamma_{\text{tot,J}}}$	Counting number for $\Gamma_{\text{tot,J}}$

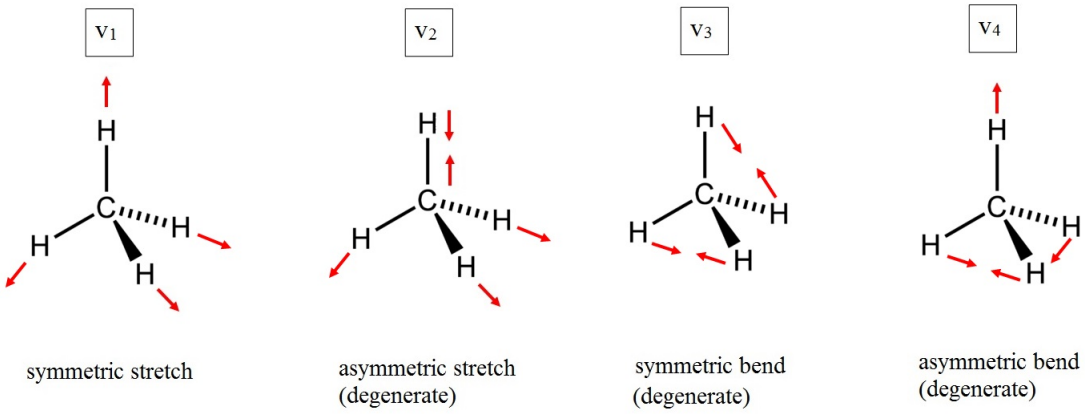

Figure 3.7: Normal modes of vibration of the methane molecule.

Figure 3.8: Inversion motion of the ammonia molecule.

generate modes relating to vibrational angular momentum where $L_i = v_i, v_i - 2, 0(1)$. For NH_3 $L = L_3 + L_4$ and for CH_4 $M_i \leq L_i$ is a multiplicity index used to count states within a given v_i, L_i set. J and K relate to rotational motion, both take integer values starting from zero but $K \leq J$. Γ_{xxx} are symmetry labels for the rotational, vibrational and total wavefunctions and span $A_1', A_1'', A_2', A_2'', E', E''$ for NH_3 and A_1, A_2, E, F_1, F_2 for CH_4. CH_4 additionally has a counting number $N_{\Gamma_{\text{tot,J}}}$ to count states with a given total symmetry and J. This is required because it is often not possible to uniquely define CH_4 quantum numbers (Yurchenko & Tennyson (2014)). The final NH_3 label is i, the inversion symmetry, this relates to the fact NH_3 can undergo an umbrella motion (inversion) illustrated in Figure 3.8. i can either by symmetric $i = s$ or 0 or $+$, or asymmetric $i = a$ or 1 or $-$.

3.2 Supplementary Data

In addition to the core line list additional information is required for modelling molecular spectra at different temperatures and pressures.

The molecular partition function (Section 3.2.1) is needed for calculating line intensity as a function of temperature, while modelling line shapes as a function of temperature and pressure calls for line profile functions and widths (Section 3.2.2).

3.2.1 Partition Function and Line Intensity

The partition function is related to the population P of molecular levels with energy E. For a system in thermodynamic equilibrium, this is adequately represented by a Boltzmann temperature distribution:

$$P = \frac{g_{ns} g_J}{Q(T)} \exp^{-\frac{E}{kT}} \tag{3.25}$$

where T is temperature in units K, g_{ns} is nuclear spin degeneracy, g_J is the rotational state degeneracy and $Q(T)$ is the partition function that ensures the sum over all populations is unity:

$$Q(T) = g_{ns} \sum_{i=0}^{n} g_J \exp\left(-\frac{E}{kT}\right) \tag{3.26}$$

The .pf file has two mandatory fields:

1. temperature in K and
2. partition function value.

An example partition function file is shown in Table 3.5. For ease of use partition functions values for a range of temperatures are fitted to a series expansion in the form of Vidler & Tennyson (2000):

$$\log_{10} Q(T) = \sum_{n=0}^{6} a_n \left[\log_{10} T\right]^n \tag{3.27}$$

Where the fitting parameters a_n can be used to compute the partition function for any given temperature within that range.

Line intensity, S_j, in units of cm/molecule is then given by:

$$S_j^a = \frac{A_{if}}{8\pi c} \frac{g'_{tot} \exp\left(-c_2 E''/T\right)}{\tilde{\nu}_0^2 Q(T)} \left(1 - \exp\left(-\frac{c_2 \tilde{\nu}_0}{T}\right)\right) \tag{3.28}$$

or:

$$S_j^e = \frac{A_{if}}{4\pi} \frac{g'_{tot} hc\tilde{\nu}_0}{Q(T)} \exp\left(-\frac{E'}{kT}\right) \tag{3.29}$$

Table 3.5: Extract from the start of a ExoMol .pf file for a diatomic (SiO Barton et al. (2013))

T	Q(T)
5	5.15
10	9.94
15	14.73
20	19.53
25	24.33
30	29.13
35	33.93
40	38.73
45	43.53
50	48.33

T: Temperature in Kelvin;
Q(T): Partition function value.

for absorption or emission intensity respectively, where $\tilde{\nu}$ is the line position in wavenumbers, $'$ refers to the upper state and $''$ refers to the lower state involved in the transition (Tennyson et al. (2004)).

3.2.2 Thermal and Collisional Broadening

This section was written with reference to Hollas (2004), Atkins & de Paula (2006) and Peach (1981).

Motion of absorbing or emitting species with respect to the observer results in a shift in the line position due to the Doppler effect:

$$\tilde{\nu} = \tilde{\nu}_0 \left(1 + \frac{v_r}{c}\right) \tag{3.30}$$

where $\tilde{\nu}$ is the shifted line position, $\tilde{\nu}_0$ is the rest line position and v_r is the velocity of the absorber or emitter along the line of sight. Because the thermal motion of a sample of absorbers or emitters obeys a velocity distribution this results in line broadening.

A thermal or Doppler broadened line will exhibit a Gaussian profile:

$$f_G(\tilde{v}, \tilde{v}_{0;j}, \alpha_j) = \sqrt{\frac{\ln 2}{\pi}} \frac{1}{\alpha_j} \exp\left(-\frac{(\tilde{v} - \tilde{v}_{0;j})^2 \ln 2}{\alpha_j^2}\right) \tag{3.31}$$

centred on $\tilde{\nu}_0$ with a width α:

$$\alpha = \sqrt{\frac{2kT\ln 2}{m}} \frac{\tilde{\nu}_0}{c} \tag{3.32}$$

Line by line thermal broadened line widths can be determined using Eq. (3.31) and the molecular mass m in kg.

Frequent collisions between absorbers or emitters results in a distortion of energy states. This distortion changes the distribution of energy states of the absorber or emitter and hence the line positions of transitions between those states.

Variable collision rates and interaction times within a sample of absorbers or emitters results in line broadening.

A collisionally or pressure broadened line will exhibit a Lorentzian line shape:

$$f_L(\tilde{\nu}, \tilde{\nu}_{0;j}, \gamma_j) = \frac{\gamma_j}{\pi} \frac{1}{(\tilde{\nu} - \tilde{\nu}_{0;j})^2 + \gamma_j^2} \tag{3.33}$$

centred on ν_0 with width γ.

The width γ depends on several factors including temperature, pressure and number density and the particular species involved in the collisions. Energy state structure of the absorber or emitters and the intermolecular dynamics will change with species for example.

The availability of line by line pressure broadened widths is assessed as part of this work. A procedure and format for providing this information with the ExoMol line lists is also developed (see Chapter 11).

The shape of a line broadened by both thermal and collisional effects is modelled as a Voigt profile, which is a convolution of the Gaussian and Lorentzian profiles:

$$f_V(\tilde{\nu} - \tilde{\nu}_0) = \int_{-\infty}^{\infty} f_G(\tilde{\nu}' - \tilde{\nu}_0) f_L(\tilde{\nu} - \tilde{\nu}') d\tilde{\nu}' \tag{3.34}$$

Note that the profiles are normalised and in the limits $\alpha \gg \gamma$ and $\alpha \ll \gamma$ the Voigt profile reduces to a Gaussian or Lorentzian respectively. In this work the Voigt profile is evaluated using the following expression:

$$f_V(\tilde{\nu}, \tilde{\nu}_0, \alpha, \gamma) = \frac{1}{\sqrt{\pi}} \frac{\sqrt{\ln 2}}{\alpha} \text{wofz}\left(\frac{\tilde{\nu} - \tilde{\nu}_0}{\alpha} \sqrt{\ln 2} + i \frac{\gamma}{\alpha} \sqrt{\ln 2} \right) \tag{3.35}$$

where wofz is the scaled complex complementary error function, also known as the Fadeeva function. This is calculated using the Fadeeva package (Johnson (2012)).

3.3 Cross-sections

3.3.1 Calculation

The following was written with reference to Hill et al. (2013).

The current ExoMol cross sections are calculated on a linearly spaced wavenumber grid $\tilde{\nu}$ defining bins of width $\triangle\tilde{\nu}$. The cross-section for each bin is the sum of the contributions from individual lines:

$$\sigma_i = \sum_j \sigma_{ij} \tag{3.36}$$

where:

$$\sigma_{ij} = \frac{S_j}{\triangle\tilde{\nu}} \int_{\tilde{\nu}_i - \triangle\tilde{\nu}/2}^{\tilde{\nu}_i + \triangle\tilde{\nu}/2} f(\tilde{\nu} - \tilde{\nu}_0) d\tilde{\nu} \tag{3.37}$$

Note that when the line width is much narrower than $\triangle\tilde{\nu}$, this equation reduces to:

$$\sigma_{ij} = S_j f(\tilde{\nu} - \tilde{\nu}_0). \tag{3.38}$$

S_j is the line intensity in units of cm/molecule calculated from a line list (see Section 3.2.1). $f(\tilde{\nu} - \tilde{\nu}_0)$ is the line shape which could be a Gaussian, Lorentzian or Voigt (see Section 3.2.2).

For the purposes of this work a Voigt profile shall be employed when computing temperature and pressure dependent cross sections, even in cases where the Gaussian or Lorentzian components may dominate, to ensure consistency.

3.3.2 Interpolation

Cross sections are temperature and pressure dependent and can only be computed on a finite grid. However it is possible to interpolate between cross sections computed on a static temperature-pressure grid to obtain cross sections for intermediate temperatures and pressures.

To obtain cross sections at the desired temperature T, interpolation between cross sections computed for a higher temperature T_2 and a lower temperature T_1 may be performed linearly:

$$\sigma_i = \sigma_i(T_1) + m(T - T_1) \tag{3.39}$$

where:

$$m = \frac{\sigma_i(T_2) - \sigma_i(T_1)}{T_2 - T_1} \tag{3.40}$$

Or using a more accurate exponential model (Hill et al. (2013)):

$$\sigma_i = a_i e^{\frac{b_i}{T}} \tag{3.41}$$

where:

$$b_i = \left(\frac{1}{T_2} - \frac{1}{T_1}\right)^{-1} \ln\frac{\sigma_i(T_1)}{\sigma_i(T_2)} \tag{3.42}$$

and:

$$a_i = \sigma_i(T_1)e^{\frac{b_i}{T}} \tag{3.43}$$

To obtain cross sections at the desired temperature P, interpolation between cross sections computed for a higher temperature P_2 and a lower temperature P_1 may be performed linearly (see Chapter 10):

$$\sigma_i = \sigma_i(P_1) + m(P - P_1) \tag{3.44}$$

where:

$$m = \frac{\sigma_i(P_2) - \sigma_i(P_1)}{P_2 - P_1} \tag{3.45}$$

Chapter 4

Methods and Theory II - Fourier Transform Spectroscopy

This chapter was written with reference to Griffiths & de Haseth (2007).

4.1 Experiment

Section 4.1.1 describes the experimental set-up employed as part of this work while Sections 4.1.2 and 4.1.3 detail relevant theory.

4.1.1 Experimental Set-up

Measurements made as part of this work were performed using a quartz high-temperature gas-flow cell (q-HGC) (see Figure 4.1) validated for high resolution measurements at temperatures up to 500 °C in the ultra-violet (UV) and infrared (IR) regions by Grosch et al. (2013). This q-HGC has previously been used to measure absorption cross sections of various gases (e.g. SO_2) up to 500 °C (Grosch et al. (2013)).

The cell has three sections separated by flow windows, a fully heated central part and two partially heated buffer parts with interchangeable optical windows at the ends. The buffer parts compensate for heat losses at the ends of the sample cell so as to obtain a uniform temperature along the length of the central part where absorption measurements are performed. Temperature stability along the axis of the hot part of the cell has been verified using thermocouple measurements and determined to be better than ± 1.84 °C (Grosch et al. (2013)).

The sample gas (e.g. N_2 + NH_3) is preheated and fed into the middle part of the cell while the buffer parts are purged with carrier gas (e.g. N_2) or dry air taken from a purge generator. The two gas flows meet and form flow windows between the central and outer parts. Here a laminar flow sheet is established meaning the sample gas can not reach, or react with or form deposits on, the optical windows (Fateev & Clausen (2008)). The sample gas may still react with the internal surface of the gas cell. To minimise this the inner walls of the q-HGC are made from quartz. Further details on the q-HGC and its performance are given in Grosch et al. (2013). Bottles of

premixed N_2 + NH_3 (1%) and pure NH_3, were obtained from AirLiquid. The purity of the N_2 and NH_3 in the gas bottles was 99.1% with H_2O being the main impurity. High purity N_2 (99.998%) was used in reference measurements.

Figure 4.2 shows a principle scheme of the optical set up for the absorption measurements. An Aligent 660 Fourier transform infra-red (FTIR) spectrometer, linearised Mercury-Cadmium Telluride (MCT) detector and an external IR light source, which is like a Blackbody (BB) at 900 °C, was used in the measurements. The optical absorption path length, as confirmed by previous measurements Grosch et al. (2013), is defined by the flow windows and has a value of 33.25 cm.

Aligents ResolutionsPRO software (Aligent) calculates the single beam (SB) spectra from the measured interferograms at a nominal resolution of 0.09 cm^{-1} using Fast Fourier Transformation (FFT) and certain apodization functions (see Section 4.1.2). In accordance with the discussion in Alberti et al. (2015), measured wavenumbers were multiplied by a factor of 1.000059 to account for the linear wavenumber shift caused by beam divergence. The experimental uncertainties on absorbance measurements are estimated to be within 0.5% (Alberti et al. (2015)).

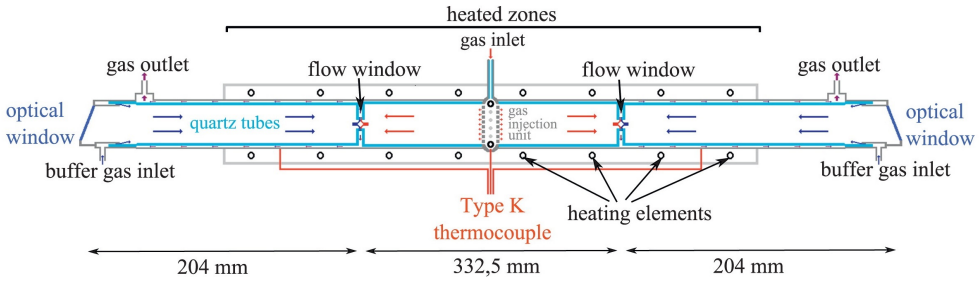

Figure 4.1: High temperature quartz gas flow cell (q-HGC) used in the experiments. The red arrows indicate the hot reactive gases, while the blue arrows show the colder buffer gas (Grosch et al. (2013)).

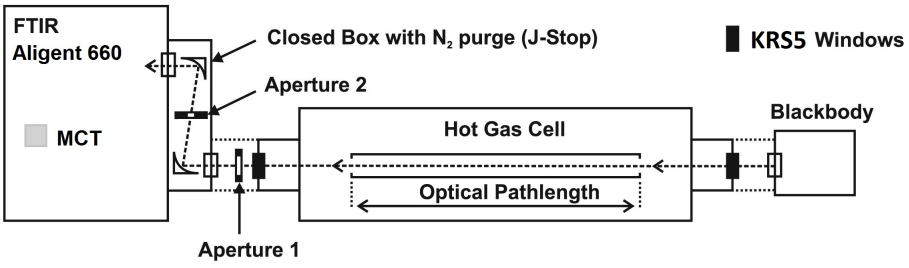

Figure 4.2: Experimental setup for the high-resolution measurements of NH_3 at high temperatures (Alberti et al. (2015)).

4.1.2 Michelson Interferometer

Inside the FTIR spectrometer is a Michelson interferometer, a simple schematic of this device is shown in Figure 4.3. Light from the source (BB) is partially reflected and partially transmitted by the beam splitter to the fixed and moving mirrors respectively. When the two beams return to the beam splitter they interfere and are once again partially reflected and partially transmitted to the detector or back to the source respectively.

The intensity of light reaching the detector I_{BEAM} is proportional to the difference in path length Δl between the beam splitter (BS) and fixed mirror (F), and the beam splitter and moving mirror (M):

$$\Delta l = 2(F \leftrightarrow BS - M \leftrightarrow BS) \equiv \delta \tag{4.1}$$

this is called the retardation δ. The variation in I_{BEAM} as a function of δ, known as an interferogram $I(\delta)$, is recorded The typical appearance of an interferogram is illustrated in Figure 4.4. The Fourier transform of the interferogram yields the spectral information $B(\tilde{\nu})$:

$$B(\tilde{\nu}) = \int_0^{+\infty} I(\delta)\cos 2\pi\tilde{\nu}\delta \; d\delta \tag{4.2}$$

As $I(\delta)$ is even, this integral may be re-written:

$$B(\tilde{\nu}) = 2\int_0^{+\infty} I(\delta)\cos 2\pi\tilde{\nu}\delta \; d\delta \tag{4.3}$$

where $\cos 2\pi\tilde{\nu}\delta$ is the phase angle. In practice additional terms need to be added to the phase angle to describe the actual measured interferogram. This may include corrections for the first sampling point being below $\delta = 0$ and wavenumber dependent phase lag introduced by electronic filters designed to remove high frequency noise from the interferogram. Figure 4.5 shows an example raw (SB) spectrum derived from an interferogram. Eq. (4.3) implies that, in principle, a spectrum from 0 to $+\infty$ (in cm^{-1}) could be measured at infinitely high resolution, although this would require δ to vary from 0 to $+\infty$ cm. In practice there is a maximum optical retardation, detonated Λ, that limits the best resolution, $\Delta\tilde{\nu}_{min}$, that could be obtained using this interferometer:

$$(\Delta\tilde{\nu}_{min}) = (\Lambda)^{-1} \tag{4.4}$$

Applying this restriction effectively multiplies the entire interferogram by a truncation function $D(\delta)$:

$$B(\tilde{\nu}) = \int_0^{+\infty} I(\delta)D(\delta)\cos 2\pi\tilde{\nu}\delta \; d\delta \tag{4.5}$$

The truncation function, also known as an apodization function, can take many forms. The two of importance to the current work are boxcar (un-weighted apodization function):

$$D(\delta) = \begin{cases} 1 & \text{if } -\Lambda \leq \delta \leq +\Lambda, \\ 0 & \text{otherwise.} \end{cases} \tag{4.6}$$

and triangular (weighted apodization function):

$$A(\delta) = \begin{cases} 1 - |\frac{\delta}{\Lambda}| & \text{if } -\Lambda \leq \delta \leq +\Lambda, \\ 0 & \text{otherwise.} \end{cases} \tag{4.7}$$

The Fourier transform of the product of two functions is the convolution of the Fourier transform of each function (Bracewell (2000)). Hence the effect of truncation is to convolve the true spectrum $B(\tilde{\nu})$ with the Fourier transform of the apodization function, also known as the instrument line shape function (ILS) $f(\tilde{\nu})$. The true spectrum is therefore distorted to an extent dependent on the ratio FWHM_{ILS} / $\text{FWHM}_{\text{true}}$ where FWHM is the full width half maximum of the ILS or true line shape respectively. The true line shape will be, for example, a Lorentzian. Weighted apodization is used to minimise the difference between the true spectrum and the measured spectrum.

Another factor limiting the resolution of the measured spectrum is beam divergence. Light from a BB source will spread out as it travels which affects how the light behaves inside the interferometer. Figure 4.6 illustrates a diverging beam passing through a Michelson interferometer. When the off-axis ray is out of phase with the on-axis ray, the fringe contrast at the detector disappears. The optical retardation at which this occurs defines the highest resolution obtainable with this set-up, as increasing δ further will add no more information to the interferogram.

In the current experimental set-up (Section 4.1.1) light exiting the gas-cell is focused into the spectrometer using two mirrors. The smaller the aperture the light is focused into, the higher the obtainable resolution, as this limits beam divergence between the aperture and the beam splitter. However a smaller aperture also means lower signal at the detector, due to beam divergence between the second focussing mirror and the aperture.

4.1.3 Calculating Experimental Absorption Spectra

The strategy for calculating experimental transmission spectra $\tau_{\text{exp}}(\tilde{\nu}, T)$ at a temperature T [K] and a line position $\tilde{\nu}$ [cm^{-1}] follows Evseev et al. (2012):

$$\tau_{\text{exp}}(\tilde{\nu}, T) = \frac{\mathbf{I}_{\text{gas+BB}} - \mathbf{I}_{\text{gas}}}{\mathbf{I}_{\text{ref+BB}} - \mathbf{I}_{\text{ref}}} \tag{4.8}$$

where $\mathbf{I}_{\text{gas+BB}}$ and $\mathbf{I}_{\text{gas}}$ are SB sample spectra (N_2 + NH_3 mixture) with and without signal from the BB and $\mathbf{I}_{\text{ref+BB}}$ and $\mathbf{I}_{\text{ref}}$ are SB reference spectra (pure N_2) with and without signal from the BB. The $\mathbf{I}_{\text{gas}}$ and $\mathbf{I}_{\text{ref}}$ have been measured by the blocking of the light by a beam-stopper at 23 °C. The absorption spectra are then calculated as:

$$A_{\text{exp}}(\tilde{\nu}, T) = \log_{10}\left[\frac{a_0}{a_1}\right] \tag{4.9}$$

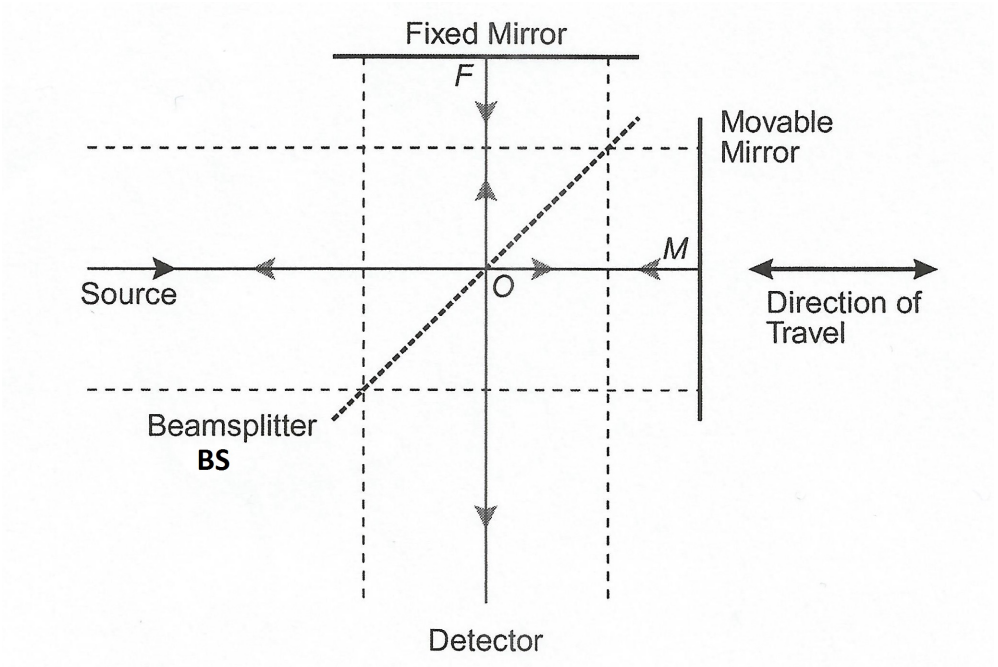

Figure 4.3: Schematic of a Michelson interferometer. Figure 2.1 in Griffiths & de Haseth (2007).

where a_0 ($= \mathbf{I}_{\text{ref+BB}} - \mathbf{I}_{\text{ref}}$) are the reference measurements and a_1 ($= \mathbf{I}_{\text{gas+BB}} - \mathbf{I}_{\text{gas}}$) are the sample measurements.

4.2 Modelling

To compare with an experimental line list, in other words retrieved line positions and intensities (see Figure 4.7), it is sufficient to compute a theoretical 'stick' spectrum. This is simply line positions and temperature dependent absorption intensities (see Eq. 3.33 in Section 3.2.1).

To compare with a Fourier transform absorbance spectrum (see Figure 4.8), a theoretical absorbance spectrum should be generated. This is done by the following steps.

Pressure-broadened absorption cross sections $\sigma(\tilde{\nu}, T)$ are calculated using a line list and partition function assuming a Voigt line shape (see Eqs. 3.28, 3.35 and 3.37). Pressure broadening parameters were taken from reference or estimated from the experimental spectrum. A transmittance spectrum is then calculated from the cross sections, taking into account absorption path length l [cm] and molecule concentration c [cm^{-3}]:

$$\tau_{\text{calc}}^{\text{true}}(\tilde{\nu}, T) = \exp\left(-\sigma(\tilde{\nu}, T) l c\right) \tag{4.10}$$

The transmittance spectrum is then convolved with the instrument line shape (ILS)

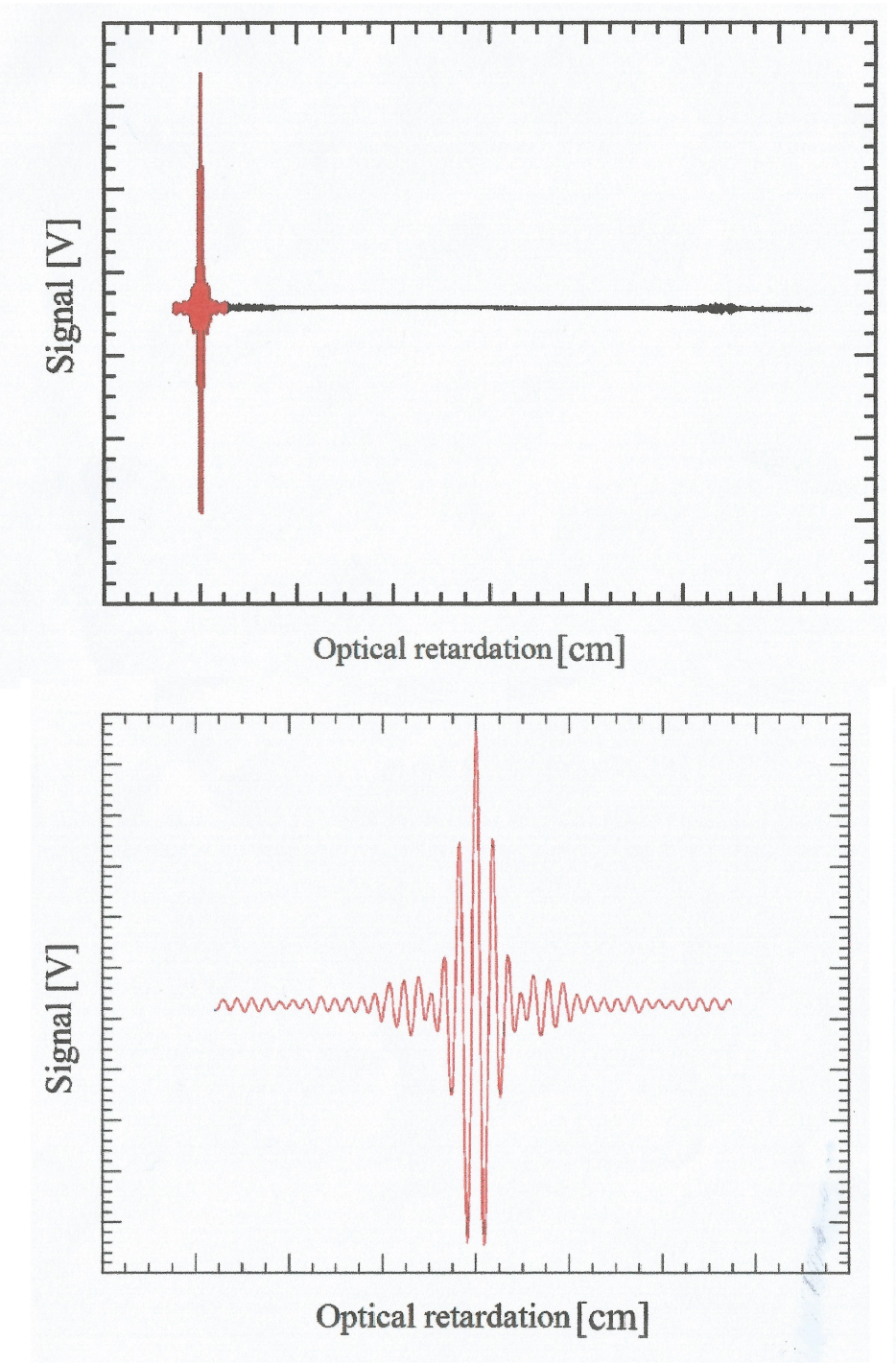

Figure 4.4: Arbitrary interferogram (upper), zoomed around the maximum signal level (lower).

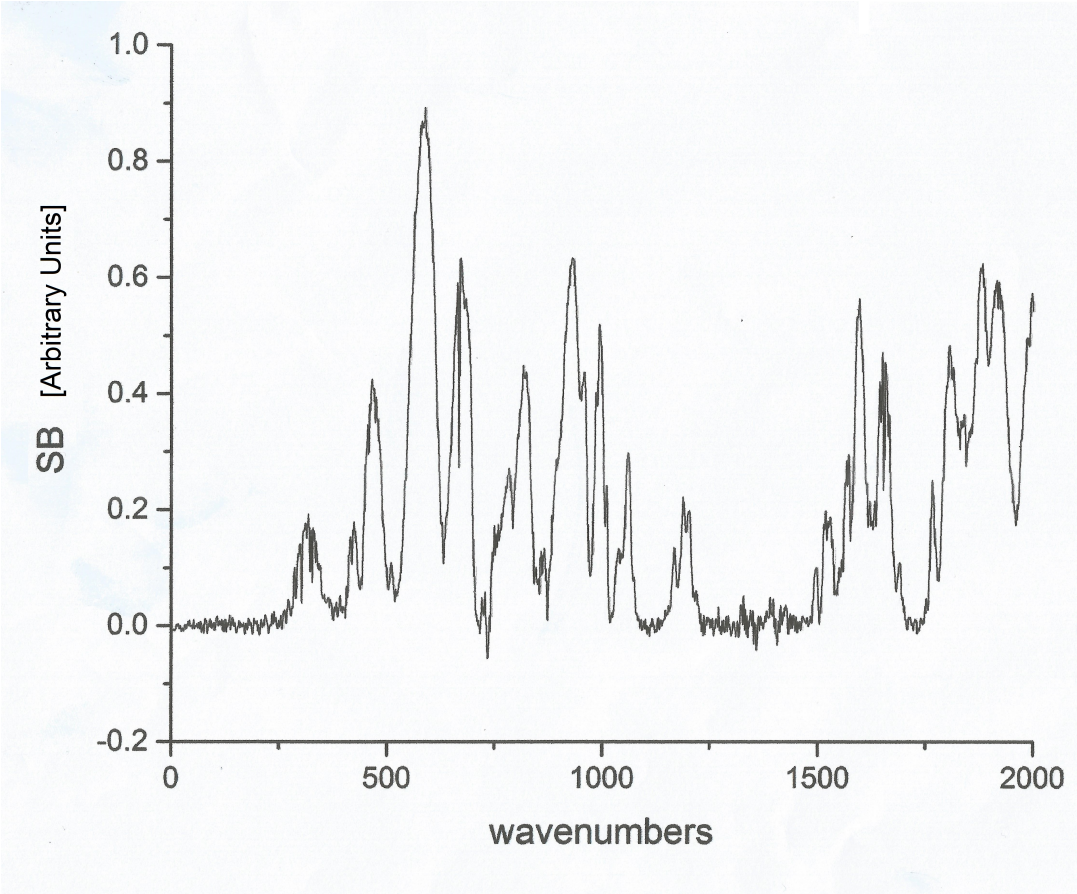

Figure 4.5: Single beam spectrum of N_2 at 200 °C measured as part of this work (see Chapter 7).

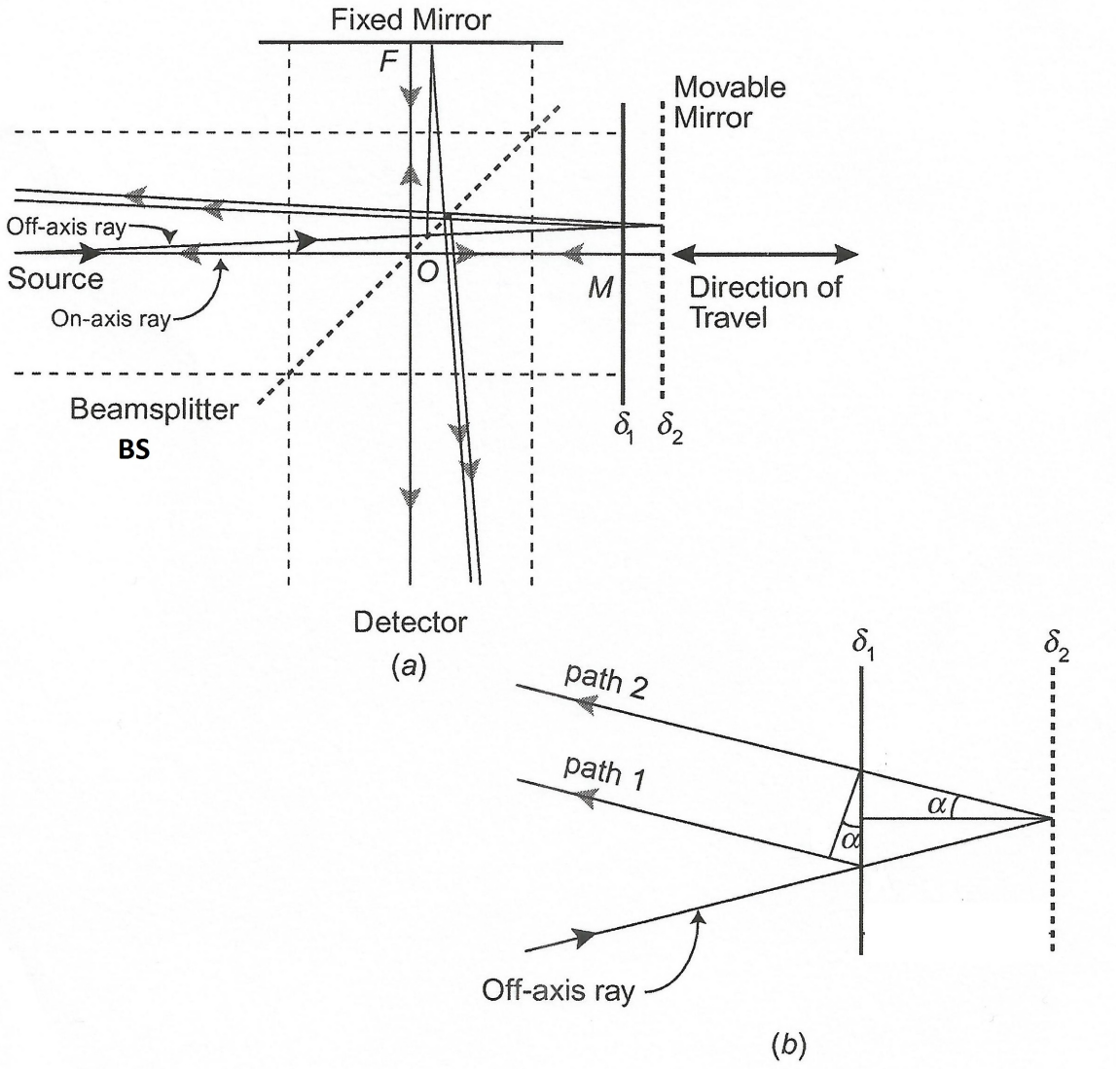

Figure 4.6: (a) Schematic of a diverging beam travelling through a Michelson interferometer. (b) Diverging beam striking the moving mirror. Path 1/2 refers to the beam at retardation $\delta_{1/2}$ respectively. Figure 2.14 in Griffiths & de Haseth (2007).

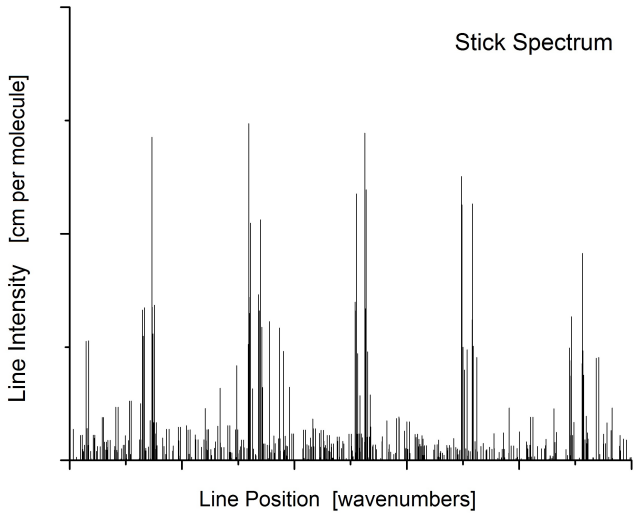

Figure 4.7: Plot of an arbitrary experimental line list or 'stick' spectrum.

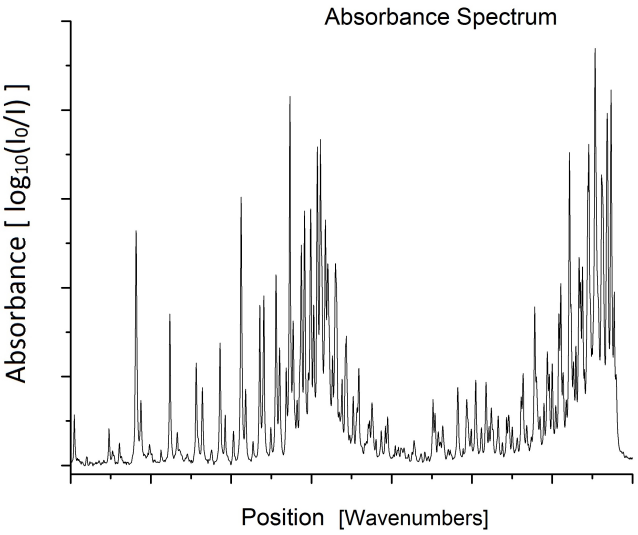

Figure 4.8: Plot of an arbitrary Fourier transform absorbance spectrum.

function $\Gamma(\tilde{\nu} - \tilde{\nu}_0)$:

$$\tau_{\text{calc}}^{\text{eff}}(\tilde{\nu}, T) = \int_0^{\infty} \tau_{\text{calc}}^{\text{true}}(\tilde{\nu}_0, T)\Gamma(\tilde{\nu} - \tilde{\nu}_0)d\tilde{\nu}_0 \tag{4.11}$$

For boxcar apodization, the ILS is a sinc function:

$$\Gamma(\tilde{\nu}) = \Lambda \text{ sinc}(\Lambda\pi\tilde{\nu}) = \Lambda\frac{\sin(\Lambda\pi\tilde{\nu})}{(\Lambda\pi\tilde{\nu})} \tag{4.12}$$

For triangular apodization, the ILS is a sinc^2 function:

$$\Gamma(\tilde{\nu}) = \Lambda \text{ sinc}^2(\Lambda\pi\tilde{\nu}) = \Lambda\frac{\sin^2(\Lambda\pi\tilde{\nu})}{(\Lambda\pi\tilde{\nu})^2} \tag{4.13}$$

where Λ is commonly termed the FTIR retardation (maximum optical retardation) and is generally defined as the inverse of the nominal resolution of the spectrometer. Finally the theoretical absorption spectrum is computed as:

$$A_{calc}(\tilde{\nu}, T) = \log_{10}\left[\frac{1}{\tau_{\text{calc}}^{\text{eff}}(\tilde{\nu}, T)}\right] \tag{4.14}$$

4.2.1 Note on the Beer-Lambert Law

An unknown concentration of an absorbing species can be determined by measuring the amount of light transmitted through a sample (transmittance T) and applying the Beer-Lambert Law. The Beer-Lambert Law is a linear relationship between the concentration of the absorbing species and its absorbance (A):

$$A = -\log_{10}(\text{T}) = \log_{10}\left(\frac{I}{I_0}\right) = \epsilon cl \tag{4.15}$$

where l is the absorption path length, c is the molecular concentration per unit volume and ϵ is the absorptivity of the sample. In the same way, the absorbance of a known amount of absorbing species can be derived using the Beer-Lambert Law. However the linearity of the Beer-Lambert Law can result in over- and under-estimates of the absorbance due to non-linear instrument and chemical effects.

4.3 Assignment Methods

This section was written with reference to Herzberg (1950), Herzberg (1991) and Hollas (2004).

It can be informative to assign upper and lower energy state labels to measured transitions, in other words specify which energy states are involved in the transition. This indicates the vibrational-rotational excitation of the system and can be used to derive experimental energies (see Section 4.4).

Observed transitions may be assigned labels by comparison to a line list, although assignment by line list comparison alone is highly dependent on the model used to compute the line list. More rigorous methods for determining upper and lower energy state assignments are described below. These can also be used to verify assignments made by line list comparison.

4.3.1 Trivial

If the upper and lower state energies are known from previous experimental studies, then an observed transition may be assigned by simple subtraction of the upper state energy from the lower state energy and matching the result to the observed line position. It is also necessary to compare the observed transition intensity to the predicted line intensity, from previous experimental measurements or a theoretical line list, to avoid false assignments.

Assignments made by this method are commonly termed 'trivial' (see for example Zobov et al. (2011), Polyansky et al. (1997a) or Zobov et al. (1999, 2005)).

4.3.2 Combination Differences

Vibrational bands have a particular structure which is direct result of the rotational selection rules. For the diatomics considered in this work, the rotation selection rule is $\Delta J = \pm 1$. For polyatomics, $\Delta J = 0$ transitions can also occur.

This means vibrational bands have two or three types of rotational transition or branches:

1. P - Branch: $J' = J''$ - 1
2. Q - Branch: $J' = J''$ (if $\Delta J = 0$ transitions are allowed)
3. R - Branch: $J' = J'' + 1$

These are typically referred to using the spectroscopic notation P(J''), Q(J'') or R(J''). Figure 4.10 illustrates P, Q and R rotational transitions between two arbitrary vibrational energy states while Figure 4.9 demonstrates the appearance of a vibrational band with P-, Q- and R- branches measured at high resolution.

Certain P, R and, if applicable, Q transitions in a single vibrational band share an upper energy level. For example consider a vibrational band with P, Q and R branches, lower vibrational state $v'' = 0$ and upper vibrational state $v' = 1$. The rotational P(2), R(0) and Q(1) transitions in this band all have an upper ro-vibrational state $v' = 1$, $J' = 1$. P and R transitions or P, Q and R transitions with the same upper energy state can be referred to as combination difference pairs or triplets. Combination difference pairs or triplets can be used to reliably assign experimental lines, provided the lower state energies are known, in one of two ways.

Firstly, if one transition from a PR pair or PQR triplet is known or assigned, from trivial assignment for example, the location of the other(s) can be predicted by subtracting the lower state energy for that transition from the upper state energy

derived (or known) from the assigned line. If the predicted line position(s) match an observed line position within the experimental uncertainty then the assignment(s) are confirmed, provided the observed intensity of all lines (reasonably) agree with predicted intensities.

Secondly, if each transition from a PR pair or PQR triplet is given a proposed assignment, by line list comparison for example, then the assignments can be checked by deriving upper state energies for each and comparing them. An upper state energy may be derived by adding the lower state energy, from previous experimental studies for example, to the observed line position. If the derived upper state energies agree within the experimental uncertainty, the assignments are confirmed.

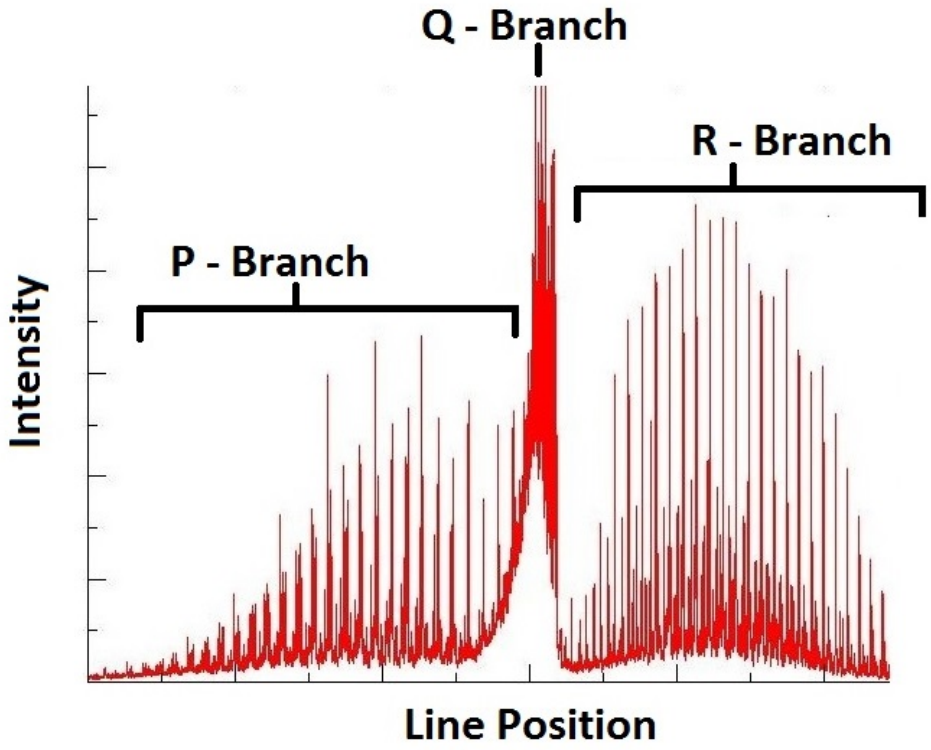

Figure 4.9: Synthetic high resolution spectrum demonstrating the appearance of a vibrational band with P, Q and R branches.

4.3.3 Method of Branches

Confirmed combination difference pairs or triplets, or trivial assignments, for the same vibrational band provide an expected observed minus calculated (Obs. - Calc.) line position difference for all lines in that band. This Obs. - Calc. difference can be used to correct the predicted line positions and hence make further assignments to the band by line list comparison. This is the method of branches (Polyansky et al.

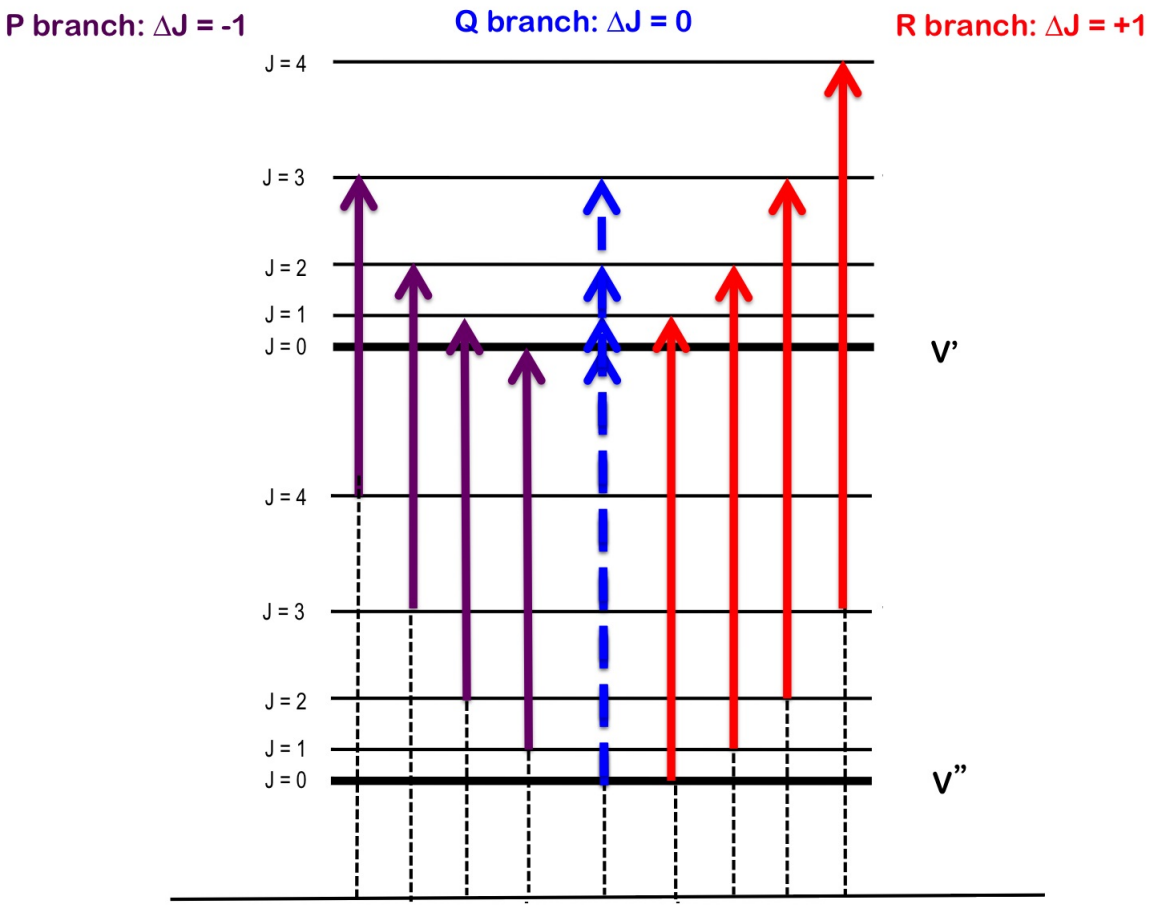

Figure 4.10: Energy level diagram illustrating P, Q and R rotational transitions between two arbitrary vibrational levels.

(1997b)), which exploits the systematic behaviour of variational calculations (ExoMol methodology) that give an overall band shift but largely preserve the rotational structure.

4.4 Retrieving Experimental Energies

Measured transitions can be used to extract energy state information for ionic, atomic or molecular systems.

Lower state energies, E_{low}, can be derived from line positions, $\tilde{\nu}$, and the ratio of line intensities, S/S_0, measured at different temperatures T and T_0 (Hargreaves et al. (2011, 2012b)). The ratio is given by:

$$\frac{S}{S_0} = \frac{Q(T)}{Q_0(T)} \exp\left(\frac{E_{\text{low}}}{kT_0} - \frac{E_{\text{low}}}{kT}\right) \left[\frac{1 - \exp\left(\frac{-h\tilde{\nu}}{kT}\right)}{1 - \exp\left(\frac{-h\tilde{\nu}}{kT_0}\right)}\right] \tag{4.16}$$

where S_0 and $Q_0(T)$ are the line intensity and partition function at reference temperature T_0 (typically 296 K). If this equation is rearranged:

$$\ln\left(\frac{SQR_0}{S_0Q_0R}\right) = \frac{E_{\text{low}}}{kT_0} - \frac{E_{\text{low}}}{kT} \tag{4.17}$$

where

$$R_0 = 1 - \exp\left(\frac{-h\tilde{\nu}}{kT_0}\right) \tag{4.18}$$

E_{low} can be extracted as the gradient of the intensity ratio plotted as a function of the reciprocal of temperature. Typically this method determines E_{low} with an accuracy of $\pm$ 1 - 2 cm^{-1}.

Once the lower state energy is known, an upper state energy can be derived by simply adding the lower state energy to the observed line position.

It is useful to assign labels to observed transition and derived energy such that different experimental works (and theoretical works) can be compared and the results can be used to refine theoretical models.

Another method of deriving experimental energies is through the use of spectroscopic networks. A spectroscopic network is a group of energy states linked by allowed ro-vibrational transitions.

If the lowest level within each spectroscopic network is measured, or estimated based on experimental and/or theoretical considerations, then the higher energies can, in principle, be extracted in turn from the observed transitions linking them to the lowest level and the linear relation between transitions and energy levels:

$$\tilde{\nu} = E_{upper} - E_{lower} \tag{4.19}$$

The MARVEL algorithm (Furtenbacher et al. (2007)) employs spectroscopic networks to obtain measured energy levels from uniquely assigned experimental ro-vibrational transitions.

4.4.1 MARVEL

The MARVEL algorithm is described in detail in the associated article (Furtenbacher et al. (2007)). An overview of the methodology and treatment of uncertainties is given below. A MARVEL analysis has five principle stages:

1. **Database creation:** compiling all available measured and assigned transitions with their uncertainties. Assignments must be unique, but not necessarily meaningful, otherwise MARVEL will be unable to differentiate between the associated energy levels.

2. **Spectroscopic network identification**: determining which energy levels belong to particular spectroscopic networks based on the assignments.

3. **Database pre-processing:** removing transitions from the database that are clearly incorrect. For example if three line positions with the same quantum numbers have been measured by three different sources, but one does not agree within the experimental uncertainties with the other two, that one has most likely been mis-assigned or incorrectly measured. Such a transition would be removed from the database in this step.

4. **Linear equation set up:** setting up equations describing the transitions, requested energy levels and the relationship between them, for each spectroscopic network.

5. **Linear equation solution:** Solving equations from step 4 and deriving uncertainties for the resulting energy levels using the uncertainties in the measured transitions (see below).

Treatment of uncertainties in step 5 requires careful consideration as there is no unique way to compute uncertainties in the derived energies, and the quoted uncertainties for the measured transitions may be unrealistic. Two analytical methods are used to determine the uncertainties for each MARVEL energy. The uncertainty, ϵ_j in energy level E_j can be computed as:

$$\epsilon_j^{(1)} = t\sqrt{A_{jj}^{-1}} \tag{4.20}$$

where matrix $\boldsymbol{A} = \boldsymbol{a}^T \boldsymbol{g}\boldsymbol{a}$,

$$a_{ij} = \begin{cases} -1, & \text{if } E_j \text{ is the lower level of the } i\text{th transition,} \\ +1, & \text{if } E_j \text{ is the upper level of the } i\text{th transition,} \\ 0 & \text{otherwise.} \end{cases} \tag{4.21}$$

and $g_i = 1 \,/\, \delta_i^2$, where δ_i is the uncertainty of the ith transition. For $t = 2$, ϵ_j^1 represents a $\sim$95% confidence limit. This equation holds if all the transitions were measured in an equally controlled way and the correctness of all uncertainties can be assured. As this is unlikely to be true in practice, the uncertainty can alternatively be computed as:

$$\epsilon_j^{(2)} = t\sqrt{(A^{-1})_{jj}\frac{\Sigma_i g_i \Delta_i^2}{N_t - N_l}} \tag{4.22}$$

where N_t is the number of transitions, N_l is the number of energy levels and Δ_i is the difference between the original measured line position, and the line position computed by subtracting the lower MARVEL derived energy from the upper one. Under favourable conditions, $\epsilon_j^{(1)} \approx \epsilon_j^{(2)}$. This condition can be achieved after suitable adjustment of the uncertainties in the measured line positions. MARVEL employs a robust weighting algorithm to iteratively adjust the uncertainty of measured transitions until the condition $\epsilon_j^{(1)} \approx \epsilon_j^{(2)}$ is fulfilled. The adjustment formula is given by (Watson (2003)):

$$g_i = \frac{1}{\delta_i^2 + \alpha\Delta_i^2} \tag{4.23}$$

where α is a positive number ($\alpha \leq 1/3$) chosen for the given problem.

Chapter 5

Methods and Theory III - Extrasolar Planet Spectroscopy

In this work absorption cross sections for use in extrasolar planet atmospheric retrieval (see Section 5.2) are computed (see Chapter 10). The following section, 5.1, describes how the cross sections are implemented in extrasolar planet atmospheric models.

5.1 Transit Spectroscopy

The following was written with reference to Pater & Lissauer (2013).

Transiting extrasolar planets provide a convenient geometry for the atmosphere of the planet to be probed (Figure 5.1). When the planet passes in front of the star, starlight is transmitted through the planetary atmosphere and the planetary signal can in theory be extracted by measuring the change in observed brightness due to molecules in the planetary atmosphere (transmission spectroscopy, Section 5.1.1). Just before the planet passes behind the star the thermal emission from the planet is observed combined with the stellar signal, the planetary signal can in theory be extracted by subtracting the observed light of the star alone from the observed light from the planet and star combined (emission spectroscopy, Section 5.1.2).

5.1.1 Transmission

The following was written with reference to Hollis et al. (2014), Waldmann et al. (2015a) and Liou (2002).

When a planet passes in front of a star (primary transit as shown in Figure 5.2) two things occur. Firstly it blocks out part of the stellar light leading to a dip in observed brightness (flux). If the star and planet are approximated as disks the magnitude of the dip, also known as the transit depth D_t, is proportional to the radius of the star R_* and planet R_P:

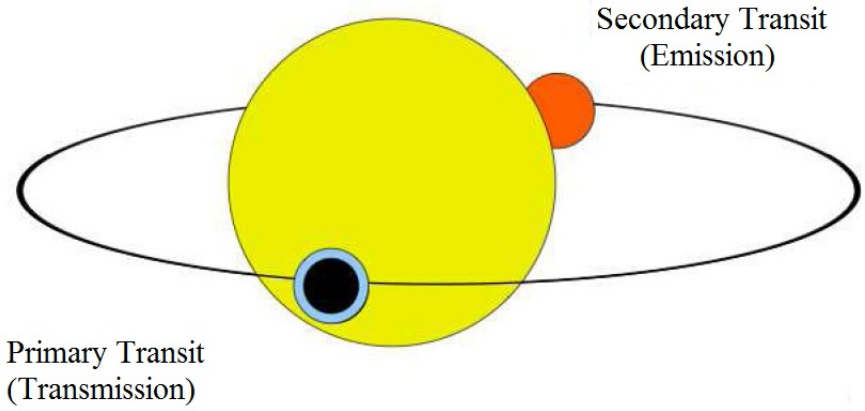

Figure 5.1: Diagram illustrating transit geometry

$$D_t = \frac{R_P^2}{R_*^2} \tag{5.1}$$

Secondly light is transmitted through part of the planetary atmosphere, specifically the terminator region, the part of the planet separating the dayside and nightside. Molecules in the atmosphere introduce small but measurable variation in the observed light. The transmission spectrum can be simulated using the following model.

When absorption and scattering of photons is the primary mechanism of energy transport in an atmosphere, the change in intensity dI_λ of radiation as it passes through the atmosphere along a path ds can be expressed as:

$$dI_\lambda = -I_\lambda \sigma_\lambda \rho ds \tag{5.2}$$

where ρ is the mass density of the material in kg m^3 and σ_λ is the mass extinction cross-section in m^2 kg^{-1} for radiation of wavelength λ. Rearranging for I_λ this equation becomes:

$$\frac{dI_\lambda}{\sigma_\lambda \rho ds} = -I_\lambda \tag{5.3}$$

from which the quantities optical path length u and optical depth τ can be defined as:

$$u = \int \rho ds \tag{5.4}$$

$$\tau_\lambda = \sigma_\lambda \int \rho ds = \sigma_\lambda u \tag{5.5}$$

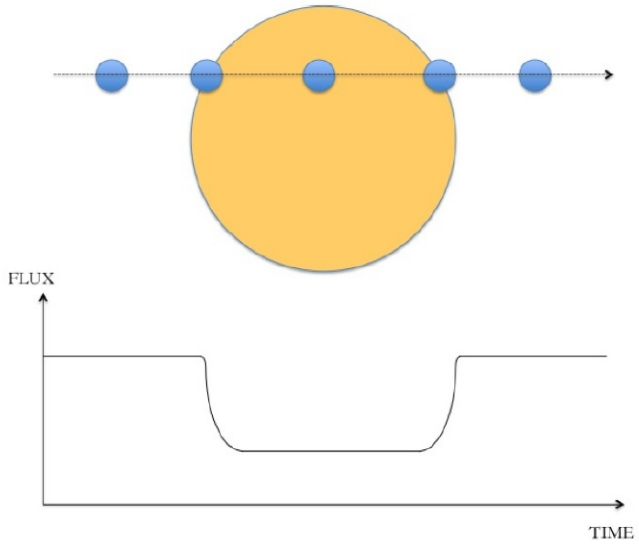

Figure 5.2: Diagram illustrating the primary transit geometry (Figure 1 in Hollis et al. (2014))

respectively. The radiative transfer equation can be solved for an altitude z by integrating along a vertical path from the top of the atmosphere z_∞:

$$I_\lambda(z) = I_\lambda(0) \exp\left(-\sigma_\lambda \int_z^{z_\infty} \rho dz\right) \tag{5.6}$$

The intensity at altitude z depends on the optical depth which in turn depends on the mass extinction cross section. If scattering is neglected for simplicity, this is the absorption cross section σ_i which is calculated from molecular line lists (see Section 3.2).

The optical depth also depends on the optical path length. The optical path is calculated according to the geometry shown in Figure 5.3 and also requires a knowledge of the quantity of each molecule i in the path. This is expressed as a fractional abundance of that molecule relative to all other molecules, or a dimensionless mixing ratio χ_i. The optical depth at an altitude z for a given molecule i with cross-section σ_i in m^2 is therefore given by:

$$\chi_i \tau_i(\lambda, z) = 2 \int_0^{l(z)} \sigma_i(\lambda) \chi_i(z') \rho_N(z') dl \tag{5.7}$$

where ρ_N is the total number density in m^3. The total depth for all molecules is then a sum of the contributions from individual molecules:

$$\tau(\lambda, z) = \sum_{i=1}^{N} \tau_i(\lambda, z) \tag{5.8}$$

By summing over all viewing paths this is converted to an equivalent atmospheric depth $A(\lambda)$:

$$A(\lambda) = 2\int_0^{z_{max}} (R_p + z)(1 - e^{-\tau(\lambda,z)})dz \tag{5.9}$$

Giving the total transit depth at that wavelength $D(\lambda)$:

$$D_t(\lambda) = \frac{R_P^2 + A(\lambda)}{R_*^2} \tag{5.10}$$

The variation in observed light introduced by molecules in the atmosphere can therefore be quantified by a conventional transit depth. A transmission spectrum can hence be constructed by plotting these transit depths as a function of wavelength.

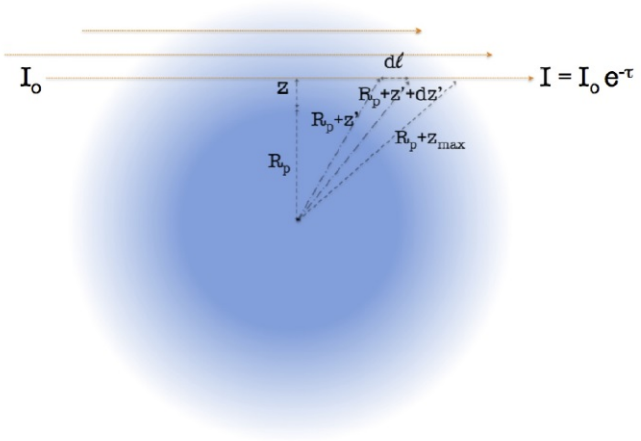

Figure 5.3: Geometry of a primary transit illustrating the paths of the stellar photons filtered through the planetary atmosphere (Figure 2 in Hollis et al. (2014))

5.1.2 Emission

The following was written with reference to Waldmann et al. (2015b) and Liou (2002).

When a planet passes behind a star (secondary transit) two things occur. Firstly, during transit, the observed brightness of the system is reduced as the contribution from the planet is no longer visible. Secondly, in the moments prior to and after transit, the thermal emission from the planet is observed combined with the stellar signal. Thermal emission from the planet can be simulated using the following model.

Assuming local thermodynamic equilibrium and no scattering occurs in the atmosphere, thermal radiation is given by:

$$\mu_i \frac{dI_\lambda(\tau, \mu_i)}{d\tau} = I_\lambda(\tau, \mu_i) - B_\lambda(T) \tag{5.11}$$

where B_λ is the Planck function at temperature T, τ is the optical depth, $I_\lambda(\tau, \mu_i)$ is the intensity per wavelength λ and $\mu_i = \cos\theta$ is the upward inclination. This is known as the Schwartzchild equation. As before the total optical depth for all molecules is the sum of the contributions from individual molecules:

$$\tau(\lambda, z) = \sum_{m=1}^{N} \tau_m(\lambda, z) \tag{5.12}$$

Here the optical depth at an altitude z for a given molecule m with cross-section σ_m in m^2 is given by:

$$\tau_m(\lambda, z) = \int_z^{z_\infty} \sigma_m(z')\chi_i(z')\rho_N(z')dz' \tag{5.13}$$

were χ_i (dimensionless) and ρ_N (m^3) are the column and number densities respectively. The radiation at the planetary surface (terrestrial planets) or defined surface pressure (gaseous planets) combined with integrated emission contributions from parallel layers of the atmosphere now provides an expression for the upward welling radiance:

$$I_\lambda(\tau, \mu_i) = I_\lambda(\tau_s) \exp^{-(\tau_s - \tau)/\mu_i} + \int_\tau^{\tau_s} B_\lambda(T_{\tau'}) \exp^{-(\tau' - \tau)\mu_i} \frac{d\tau'}{\mu_i} \tag{5.14}$$

where s refers to the surface of the planet. The monochromatic transmittance and its derivative are defined as:

$$\mathcal{T}_\lambda(\tau) = \exp^{-\tau}, \ \frac{\partial \mathcal{T}_\lambda(\tau)}{\partial \tau} = -\exp^{-\tau} \tag{5.15}$$

At the top of the atmosphere, where $\tau = 0$ and $z = \infty$, the total integrated radiation is hence given by:

$$I_\lambda(\tau = 0) = B_\lambda(T_s) \exp^{-\tau_s} + \int_{\tau_s}^{0} B_\lambda(T_\tau) \frac{\partial \mathcal{T}_\lambda(\tau)}{\partial \tau} d\tau \tag{5.16}$$

Finally the emission spectrum of the extrasolar planet is given by:

$$\frac{F_p}{F_*} = \frac{I_\lambda(\tau = 0)}{I_*} \times \left(\frac{R_p}{R_*}\right)^2 \tag{5.17}$$

with respect to the flux (F), radius (R) and intensity (I) of the planet (p) and/or star ($*$).

5.2 Atmospheric Retrieval

Atmospheric spectral retrieval is when physical conditions in an atmosphere, such as temperature, pressure and species abundance, are interpreted by fitting observations to model atmospheric spectra. The retrieval of species abundance in particular is dependent on putting a constraint on the product $\sigma_i \chi_i$ (see Eqs. 5.7 and 5.13). This is why it is important to have accurate cross sections σ_i.

This work is concerned with input molecular data for use in extrasolar planet atmospheric spectral retrieval code τ - REx (Waldmann et al. (2015a,b)), and the influence of factors such as resolution and pressure broadening on the forward model (simulated transmission and emission spectra described in Section 5.1)

5.2.1 τ - REx

τ - REx has a modular structure illustrated in Figure 5.4. The module relevant to this work is the 'Molecular + Atomic Line Lists' module, which is a library of temperature and pressure dependent absorption cross sections (see Chapter 10). The library is used by the program in two ways:

1. The 'Marple' module: Pre-selection of molecules, temperatures and pressures likely to be present in the observed transmission or emission spectra (see below).

2. The forward model: Generation of synthetic transmission or emission spectra (see Sections 5.1.1 and 5.1.2).

The 'Marple' module uses custom built facial-recognition software to identify likely compositions and physical conditions. Essentially the shape and strength of spectral features in the observed transmission or emission spectra are matched to the shape and strength of spectral features in the cross sections. This significantly reduces the parameter space that needs to be explored by the more computationally expensive minimisation routines in an objective manner.

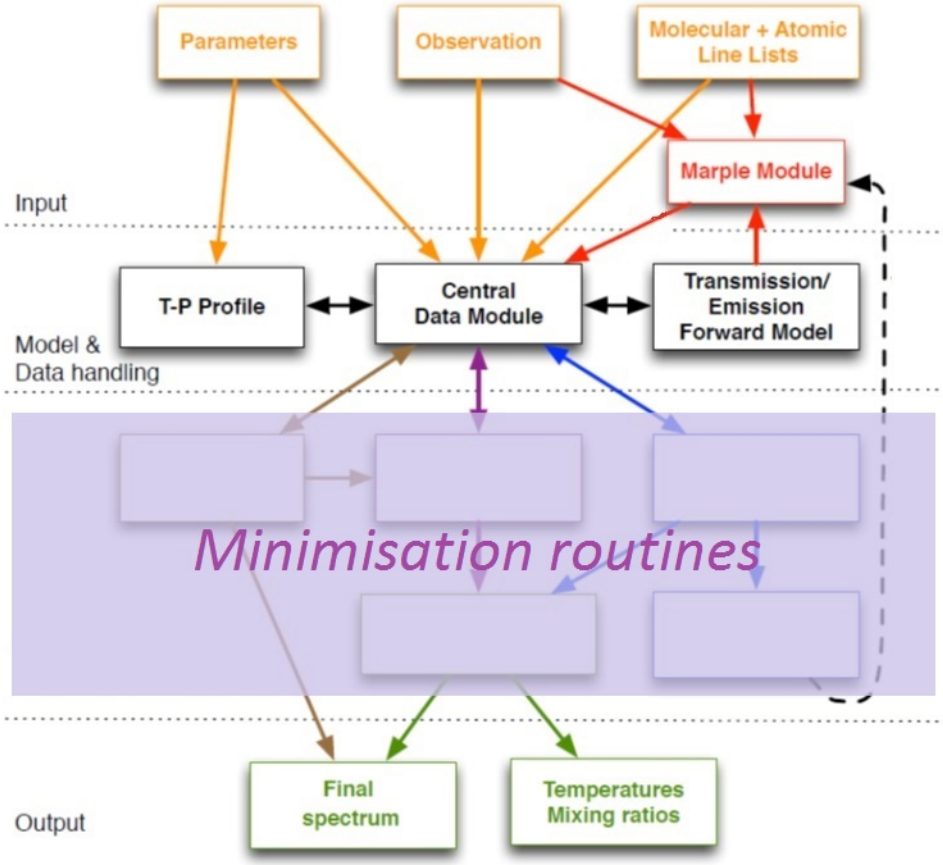

Figure 5.4: Modular design of the atmospheric retrieval code τ - REx (Waldmann et al. (2015a,b)).

Chapter 6

Calculating Diatomic Line Lists

6.1 The Ro-vibrational Spectrum of NaCl and KCl

The aim of this project was to compute hot line lists for NaCl and KCl. The nuclear motion Schrödinger equation allowing for BOB affects was solved for species XCl using program LEVEL (LeRoy (2007)). To initiate these calculations, program DPotFit (LeRoy et al. (2006)) was used to generate a refined PEC for each molecule by fitting *ab initio* curves to laboratory data. An *ab initio* PEC and DMC were determined for each molecule by Dr. Sergey Yurchenko using program MOLPRO (Werner et al. (2010)). The *ab initio* DMC grid points were used directly in LEVEL.

6.1.1 Spectroscopic Data

The most comprehensive and accurate sets of available laboratory measurements are the infra-red ro-vibrational emission lines of Ram et al. (1997) and the microwave rotational lines of Caris et al. (2002) and Caris et al. (2004) all of which were recorded at temperatures around 1000 °C, see Table 6.1. No electronic transition data appeared to be available. For KCl FTIR emission spectra measured by Ram et al. (1997) was re-analysed by Prof. Peter Bernath and Dr. Daniel Frohman of Old Dominion University, USA. Their new assignments for the ro-vibrational emission lines were used in place of those given by Ram et al. (1997) in this work.

6.1.2 Fitting the Potentials

The PECs were refined by fitting to the spectroscopic data identified in Table 6.1. However, extending the temperature range of the spectra requires consideration of highly excited levels and extrapolation of the PECs beyond the region determined by experimental input values. Hence, care needs to be taken to ensure that the curves maintain physical shapes outside the experimentally refined regions. In this context, a physical shape is assumed to be the shape of the *ab initio* curve. Multiple potential energy forms were tested, namely the EMO, MLR and MLJ potentials (see Section 3.1), to achieve an optimum fit to the experimental data whilst maintaining a physical curve shape. An optimum fit in this context was taken to be when the

Table 6.1: Summary of laboratory data used to refine the KCl and NaCl potential energy curves. Uncertainties are the maximum quoted uncertainty given in the cited papers.

Reference	Transitions	Frequency range (cm^{-1})	Uncertainty (cm^{-1})
Caris et al. (2002)	$\Delta v = 0$, $\Delta J = \pm 1$ $Na^{35}Cl$, $v = 0 - 5$, $J \leq 72$ $Na^{37}Cl$, $v = 0 - 4$, $J \leq 76$	6.6 – 31	6.7×10^{-6}
Caris et al. (2004)	$\Delta v = 0$, $\Delta J = \pm 1$ $^{39}K^{35}Cl$, $v = 0 - 7$, $J \leq 127$ $^{39}K^{37}Cl$, $v = 0 - 7$, $J \leq 129$ $^{41}K^{35}Cl$, $v = 0 - 6$, $J \leq 128$ $^{41}K^{37}Cl$, $v = 0 - 5$, $J \leq 131$	5.6 – 31	6.7×10^{-6}
Ram et al. (1997)	$\Delta v = 1$, $\Delta J = \pm 1$ $Na^{35}Cl$, $v = 0 - 8$, $J \leq 118$ $Na^{37}Cl$, $v = 0 - 3$, $J \leq 91$	240 – 390	0.005
Private Communication*	$\Delta v = 1$, $\Delta J = +1$ $^{39}K^{35}Cl$, $v = 0 - 6$, $J \leq 131$	240 – 390	0.005

* Prof. Peter Bernath and Dr. Daniel Frohman

measured line positions are reproduced within 0.01 cm^{-1} using the smallest number of expansion parameters. Data for multiple isotopologues were fitted simultaneously to ensure that the resulting curves are valid for all isotopologues. R_e and D_e were held constant in the fits, as the fits were found to be unstable otherwise.

For NaCl, BOB terms did not improve the quality of the fit and were not pursued. Of the 1370 lines used in the fit, 1060 were $Na^{35}Cl$ and 310 were $Na^{37}Cl$. The final potential was expressed as an EMO (see Eq. (3.5)), p was set to 3, N to 4, D_e to 34120.0 cm^{-1} (Huber & Herzberg (1979)) and R_e to 2.360796042 Å (Ram et al. (1997)). Parameters resulting from the fit are given in Table 6.2. The input experimental data were reproduced within 0.01 cm^{-1} and often much better than this.

Table 6.2: Fitting parameters used in the NaCl Extended Morse Oscillator potential, see Eq. (3.5) in Chapter 3. (Uncertainties are given in parenthesis in units of the last digit.)

N	β_i
0	0.8947078(17)
1	-0.287528(48)
2	0.00581(11)
3	-0.0278(14)
4	-0.0290(37)

For KCl, the fit to spectroscopic data was first attempted with the original lines

from Ram et al. (1997) and those from Caris et al. (2004). Although a fit was possible the resulting potential energy curves did not follow an *ab initio* shape and the input experimental data were only reproduced within 0.06 cm^{-1} at best. To give a few examples four fitted PECs are plotted in Figure 6.1. A fit to an MLR potential with one expansion parameter (pot 6) produced a curve shape closest to the *ab initio* potential but only reproduced input experimental data within 0.5 cm^{-1}. This residual was improved by increasing the number of expansion parameters, as shown in Table 6.3 for pot 6 (1 parameters), pot 7 (2 parameters), pot 5 (3 parameters) and pot 1 (4 parameters), but this did not improve the shape of the resulting curves, as illustrated in Figure 6.1.

As a much better fit had been achieved for NaCl, and the shape of the fitted curve for KCl proved very sensitive to the number of fitting parameters (Figure 6.1), it was suspected that Ram et al. (1997) had miss-assigned some of the KCl spectrum. Indeed it transpired that the KCl infra-red spectrum measured by Ram et al. (1997) was being re-analysed by Prof. Peter Bernath and Dr. Daniel Frohman and they advised against using the Ram et al. (1997) assignments. Taking that into account and considering the experimental data was limited to the transitions below $v = 4$ only ($\triangle v = 1$) the resulting band-head predictions from one fitted curve (pot 5) showed remarkably good agreement with the experimental values up to $v' - v'' =$ 11-12 (Table 6.4). On this basis Prof. Peter Bernath and Dr. Daniel Frohman agreed to collaborate and provide new assignments for the KCl infra-red spectrum such that an accurate KCl line list could be computed using ExoMol methods.

Table 6.3: Supplement to Figure 6.1. The second column reports the maximum observed minus calculated difference for experimental lines used in the fit.

Result	Residuals cm^{-1}	Number of Expansion Parameters	Notes
pot1	0.06	4	Best fit to Ram et al. (1997) lines
pot5	0.08	3	Best band-head predictions
pot7	0.1	2	
pot6	0.5	1	Curve shape closest to *ab initio*

As an intellectual exercise I attempted to re-assign the KCl spectrum myself. Using an *ab initio* starting potential I performed a fit only to the Caris et al. (2004) lines (rot). I then used PGOPHER (Western (2016)) to simulate the infra-red spectrum from the resulting line list. I discovered that the fitted line positions in each vibrational band were offset from the experimental line positions by a constant amount according to the respective band-head residuals (Table 6.5). By subtracting these residuals from the fitted line positions for each vibrational band I was able to construct my own set of assignments, a subset of which can be found in Table 6.6. My assignments agreed with those generated by Prof. Peter Berthan and Dr. Daniel Frohman. This demonstrates that empirically tuned line lists could be used to supplement conventional methods of assigning experimental spectra of diatomics.

The second fit to spectroscopic data was performed using the new lines generated

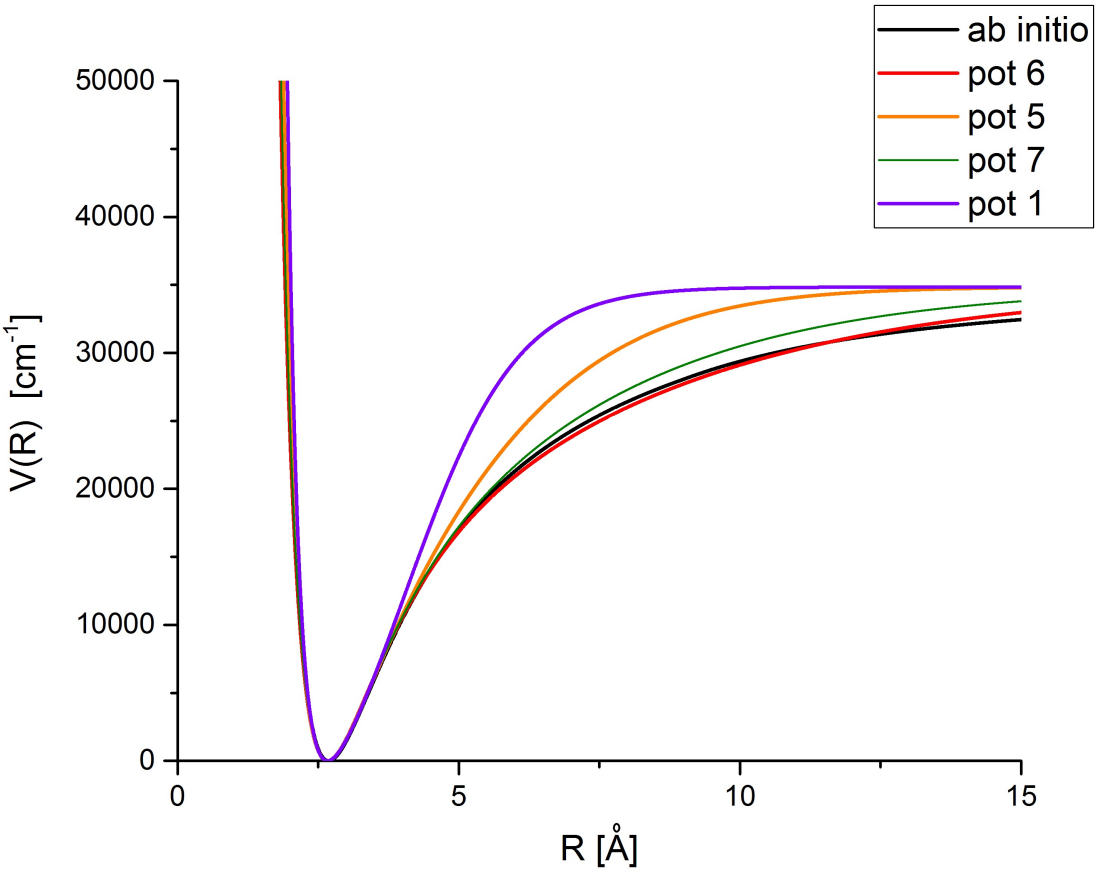

Figure 6.1: A sample of fitted KCl MLR potential energy curves (coloured lines) compared to the *ab initio* curve (black line). The fitted curves (assigned arbitrary names pot1, pot7, pot5 and pot6 for convenience) represent typical results from the first fit to Ram et al. (1997) and Caris et al. (2004) lines. Notes for each fitted curve are presented in Table 6.3

Table 6.4: Comparison of theoretically predicted $^{39}K^{35}Cl$ R-branch band-heads, in cm^{-1}, with laboratory measurements from Ram et al. (1997) and this work (pot5).

Band	Obs.	Calc.	Obs. - Calc.
1 – 0	296.702	296.613	0.089
2 – 1	294.181	294.100	0.081
3 – 2	291.680	291.607	0.073
4 – 3	289.201	289.134	0.067
5 – 4	286.742	286.676	0.066
6 – 5	284.303	284.236	0.067
7 – 6	281.884	281.821	0.063
8 – 7	279.488	279.417	0.071
9 – 8	277.110	277.030	0.080
10 – 9	274.752	274.675	0.077
11 – 10	272.414	272.326	0.088
12 – 11	270.012	270.068	-0.056

Table 6.5: Comparison of theoretically predicted $^{39}K^{35}Cl$ R-branch band heads, in cm^{-1}, with laboratory measurements from Ram et al. (1997) and this work (rot).

Band	Obs.	Calc.	Obs. - Calc.
1 – 0	296.702	296.065	0.637
2 – 1	294.181	293.537	0.644
3 – 2	291.680	291.026	0.654
4 – 3	289.201	288.531	0.670
5 – 4	286.742	286.053	0.689
6 – 5	284.303	283.592	0.711
7 – 6	281.884	281.148	0.736
8 – 7	279.488	278.720	0.768
9 – 8	277.110	276.309	0.801
10 – 9	274.752	273.916	0.836
11 – 10	272.414	271.539	0.875
12 – 11	270.012	269.189	0.823

Table 6.6: Sample of re-assigned Ram et al. (1997) $^{39}K^{35}Cl$ lines

Observed Line Position cm^{-1}	$v' - v''$	Assignment Ram et al. (1997) R/P(J'')	Obs.-Calc.	$v' - v''$	Assignment This Work R/P(J'')	Obs.-Calc.
288.988	4-3	R(129)	-0.023	3-2	R(90)	-0.009
289.003	4-3	R(130)	-0.034	4-3	R(129)	-0.008
286.906	4-3	R(94)	-0.021	3-2	R(72)	-0.004
286.807	4-3	R(93)	-0.027	No Line	No Line	No Line
286.703	4-3	R(92)	-0.037	5-4	R(136)	0.004
286.610	4-3	R(91)	-0.034	5-4	R(131)	-0.001
286.501	4-3	R(90)	-0.045	5-4	R(127)	-0.006

by Prof. Peter Bernath and Dr. Daniel Frohman and those in Caris et al. (2004). Centrifugal non-adiabatic BOB terms were included in the fit as they resulted in a reduction, by up to 50 percent, in the residuals obtained for high J's. Of the 549 lines used in the fit, 361 were $^{39}K^{35}Cl$, 82 were $^{39}K^{37}Cl$, 64 were $^{41}K^{35}Cl$ and 40 were $^{41}K^{37}Cl$. The final potential was expressed as an MLR (see Eq. (3.8) in Chapter 3), p was set to 2, N to 3, m to 2, n to 3, C_2 to 10000, C_3 to 13000000, D_e to 34843.15 cm^{-1} (Brewer & Brackett (1961)) and R_e to 2.6667253989 Å (Caris et al. (2004)). Constants C_2 and C_3 were implemented because the use of conventional constants C_6 and C_8 resulted in poor or no convergence giving completely non-physical curves (see discussion on avoided crossings below). Parameters resulting from this fit are given in Table 6.7. The input experimental data were reproduced within 0.01 cm^{-1} and often much better than this.

Table 6.7: Fitting parameters used in the KCl Morse Long Range potential, see Eq. (3.8) in Chapter 3. (Uncertainties are given in parenthesis in units of the last digit.)

N	β_i	t_j
0	-9.075210(10)	0.0
1	1.23590(85)	0.00030(12)
2	0.4859(22)	0.0
3	1.200(10)	0.0

The final curves, shown in Figure 6.4, follow the *ab initio* shape with the exception of regions 6-17 Å for KCl and 4.5-8 Å for NaCl. These regions are associated with the avoided crossings between Coulombic X^+-Cl and neutral X-Cl PECs which occur in the adiabatic representation of the ground electronic state (Giese & York (2004)). PECs calculated for ionic and covalent wavefunctions of X-Cl species in the BOA will 'cross' at some internuclear distance R_c (see Figure 6.2). This is because the properties of the system change with R. At short R the molecule is polar so it is ionic in nature, while at large R the system will eventually dissociate into neutral atoms, so it is covalent in nature. However the non-crossing rule for diatomics put forward by Hund (1927) and proved by von Newman & Wigner (1929) states that *"the potential energy curves of two electronic states with the same symmetry cannot cross"*. Hence the ionic and covalent curves in Figure 6.2 do not represent a true description of the system, in fact the best energies at any internuclear distance are obtained by mixing the ionic and covalent wavefunctions. At the crossing point, R_c, the new energies (which are closer to the true energies that the original ionic and covalent energies) 'split apart' and the curves no longer cross, this is called an avoided crossing (see Figure 6.3).

Without experimental data near dissociation, it is difficult to represent this accurately with DPotFit. Consequently, the line lists were limited to vibrational states lying below 20,000 cm^{-1} which do not sample these regions. This has consequences for the temperature range considered. Based on the partition sum, see Section 6.1.3, this range is 0 - 3000 K. Comparisons with observed frequencies for $Na^{35}Cl$ and $^{39}K^{35}Cl$ are given in Table 6.9 and Table 6.10. These demonstrate the accuracy of the fits.

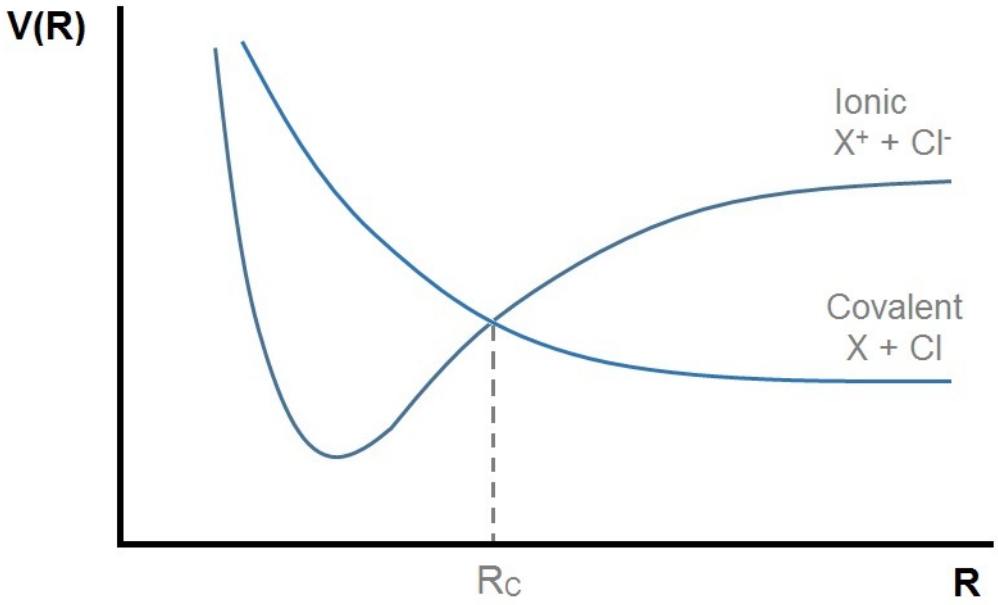

Figure 6.2: Sketch of the crossing of potential energy curves for ionic and covalent wavefunctions of X-Cl species.

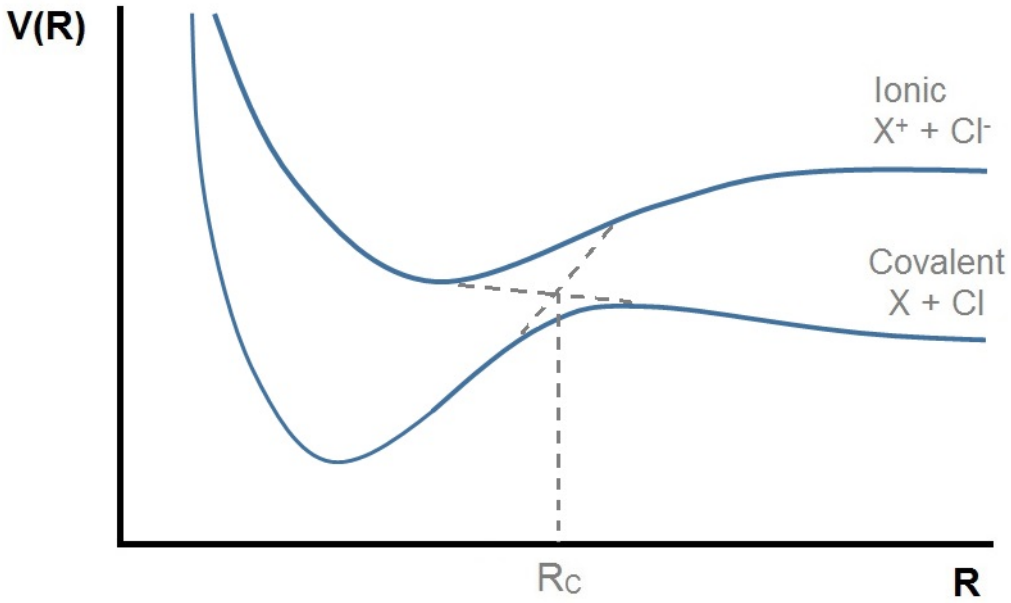

Figure 6.3: Sketch of the avoided crossing of potential energy curves for the mixed ionic and covalent wavefunctions of X-Cl species.

An important aim in refining a PEC is to also predict spectroscopic data outside the experimental range. This can be tested for KCl for which there are R-branch band-head measurements up to $v = 12$ (Ram et al. (1997)). The positions of these band heads, which are key features in any weak or low-resolution spectrum, are predicted to high accuracy, see Table 6.8.

Table 6.8: Comparison of theoretically predicted $^{39}K^{35}Cl$ R-branch band heads, in cm^{-1}, with laboratory measurements from Ram et al. (1997) and this work (final result).

Band	Obs.	Calc.	Obs.-Calc.
1 – 0	296.702	296.703	-0.001
2 – 1	294.181	294.182	-0.001
3 – 2	291.680	291.682	-0.002
4 – 3	289.201	289.203	-0.002
5 – 4	286.742	286.745	-0.003
6 – 5	284.303	284.306	-0.003
7 – 6	281.884	281.887	-0.003
8 – 7	279.488	279.489	-0.001
9 – 8	277.110	277.110	0.000
10 – 9	274.752	274.752	0.000
11 – 10	272.414	272.411	0.003
12 – 11	270.120	270.090	0.030

6.1.3 Partition Functions

The calculated energy levels, see Section 6.1.4, were summed in Excel to generate partition function values for a range of temperatures. The partition function is at least 95 per cent converged at 3000 K and much better than this at lower temperatures, therefore temperatures up to 3000 K were considered. Values for the parent isotopologues are compared to previous studies, namely Irwin (1981), Sauval & Tatum (1984) and Müller et al. (2005) in Table 6.11. As partition function values from this work are derived from many more energy levels that included in Müller et al. (2005) and from a direct sum over energy levels, rather that an analytical approximation as used by Irwin (1981) and Sauval & Tatum (1984), the results from this work are expected to be more accurate. For ease of use, the partition functions, $Q(T)$, were fitted to a series expansion of the form used by Vidler & Tennyson (2000) (see Eq. (3.26) in Section 3.2) with the values given in Table 6.12.

6.1.4 Line List Calculations

While sodium has only a single stable isotope, ^{23}Na, both potassium and chlorine each have two: ^{39}K (whose natural terrestrial abundance is about 93.25 per cent) and ^{41}K

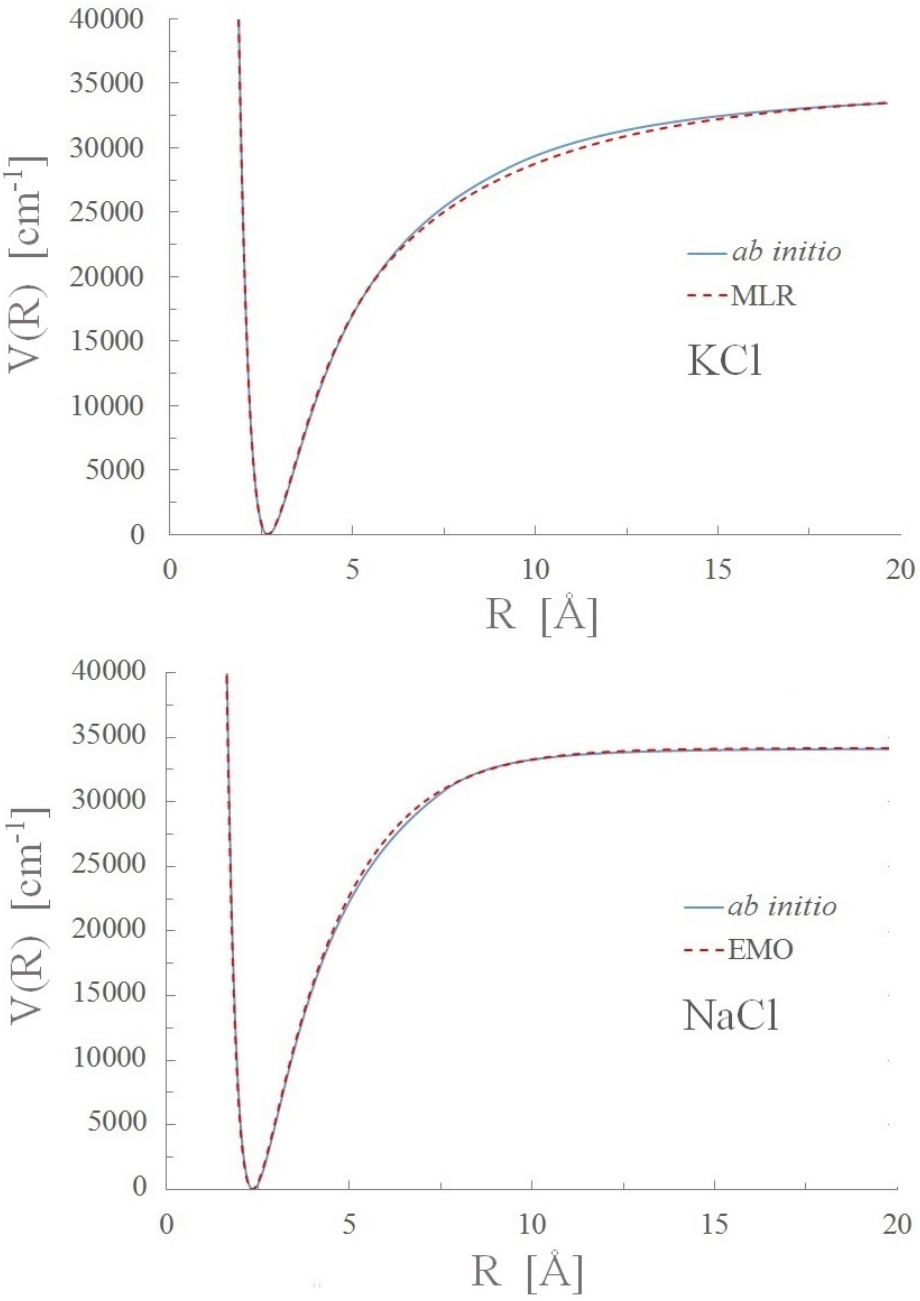

Figure 6.4: Comparison of *ab initio* and fitted ground electronic state potential energy curves for NaCl (right) and KCl (left).

Table 6.9: Comparison of theoretically predicted $Na^{35}Cl$ ro-vibrational wavenumbers, in cm^{-1}, with some of the laboratory measurements of Ram et al. (1997).

v'	J'	v''	J''	Obs.	Calc.	Obs.-Calc.
1	99	0	98	387.0444	387.0446	-0.0002
1	100	0	99	387.1219	387.1221	-0.0002
1	101	0	100	387.1950	387.1957	-0.0007
2	3	1	2	358.9248	358.9260	-0.0012
2	4	1	3	359.3419	359.3444	-0.0025
2	5	1	4	359.7587	359.7596	-0.0009
3	110	2	109	380.2722	380.2746	-0.0024
3	111	2	110	380.3014	380.3075	-0.0061
3	112	2	111	380.3372	380.3365	0.0007
4	28	3	27	361.3425	361.3429	-0.0004
4	29	3	28	361.6718	361.6730	-0.0012
4	31	3	30	362.3244	362.3230	0.0014
5	3	4	2	348.6060	348.6104	-0.0044
5	4	4	3	349.0193	349.0195	-0.0002
5	5	4	4	349.4289	349.4254	0.0035
6	114	5	113	369.5373	369.5406	-0.0033
6	115	5	114	369.5551	369.5562	-0.0011
6	117	5	116	369.5781	369.5758	0.0023
7	73	6	72	362.1649	362.1606	0.0043
7	74	6	73	362.3244	362.3276	-0.0032
7	75	6	74	362.4924	362.4910	0.0014
8	38	7	37	350.7058	350.7009	0.0049
8	39	7	38	350.9881	350.9876	0.0005

Table 6.10: Comparison of theoretically predicted $^{39}K^{35}Cl$ ro-vibrational wavenumbers, in cm^{-1}, with some of the laboratory data of Ram et al. (1997), as re-assigned by Prof. Peter Bernath and Dr. Daniel Froham.

v'	J'	v''	J''	Obs.	Calc.	Obs.-Calc.
1	102	0	101	294.9349	294.9347	0.0002
1	103	0	102	295.0173	295.0154	0.0019
1	104	0	103	295.0955	295.0941	0.0014
1	105	0	104	295.1729	295.1710	0.0019
2	43	1	42	284.5787	284.5795	-0.0008
2	49	1	48	285.6588	285.6551	0.0037
2	51	1	50	286.0004	286.0001	0.0003
2	52	1	51	286.1646	286.1700	-0.0054
3	121	2	120	291.1544	291.1554	-0.0010
3	122	2	121	291.2013	291.1992	0.0021
3	123	2	122	291.2433	291.2411	0.0022
3	126	2	125	291.3562	291.3555	0.0007
4	74	3	73	284.6069	284.6019	0.0050
4	75	3	74	284.7309	284.7300	0.0009
4	76	3	75	284.8579	284.8563	0.0016
4	78	3	77	285.1054	285.1036	0.0018
5	111	4	110	285.7192	285.7174	0.0018
5	113	4	112	285.8341	285.8375	-0.0034
5	114	4	113	285.8912	285.8947	-0.0035
5	116	4	115	286.0004	286.0037	-0.0033
6	73	5	72	279.6821	279.6817	0.0004
6	75	5	74	279.9388	279.9355	0.0033
6	76	5	75	280.0552	280.0598	-0.0047

Table 6.11: Comparison of $Na^{35}Cl$ and $^{39}K^{35}Cl$ partition functions

T(K)	This work	CDMS	Irwin (1981)	Sauval & Tatum (1984)
		$Na^{35}Cl$		
9.375	30.3338	30.3307	-	-
18.75	60.3352	60.3299	-	-
37.5	120.3556	120.3455	-	-
75	240.6984	240.6770	-	-
150	496.6455	496.5538	-	-
225	802.3712	802.1167	-	-
300	1173.0397	1172.5403	-	-
500	2506.9232	2505.0340	-	-
1000	8161.702	-	8204.6	8165.4
1500	17333.48	-	17409.8	16960.3
2000	30294.77	-	30370.1	29685.3
2500	47362.31	-	47324.9	46807.2
3000	68909.60	-	68530.1	68766.1
		$^{39}K^{35}Cl$		
9.375	51.1529	51.1495	-	-
18.75	101.9823	101.9724	-	-
37.5	203.6737	203.6504	-	-
75	409.1563	409.1053	-	-
150	876.2078	876.0902	-	-
225	1474.9611	1474.7618	-	-
300	2225.1732	2224.8905	-	-
500	5000.7402	5000.3352	-	-
1000	17102.33	-	17277.73	17112.5
1500	37064.68	-	37327.7	36147.1
2000	65580.22	-	65747.4	64142.9
2500	103489.55	-	103058.6	102212.0
3000	151831.71	-	149837.7	151368.0

Table 6.12: Fitting parameters used to fit the partition functions, see Eq. (3.26) in Section 3.2. Fits are valid for temperatures between 500 and 3000 K.

	$Na^{35}Cl$	$Na^{37}Cl$	$^{39}K^{35}Cl$	$^{39}K^{37}Cl$	$^{41}K^{35}Cl$	$^{41}K^{37}Cl$
a_0	35.528812	39.941335	71.922595	72.206029	74.926932	72.591531
a_1	-65.142353	-73.36368	-138.068267	-138.3407430	-143.689312	-139.093018
a_2	53.290409	59.6576584	114.1119477	114.10145500	118.474798	114.705511
a_3	-23.592248	-26.212185	-50.5270109	-50.41476400	-52.319838	-50.665015
a_4	6.036705	6.64133762	12.738250	12.68394200	13.1500522	12.740842
a_5	-0.8370958	-0.9113382	-1.7269110	-1.71634070	-1.7770609	-1.7230912
a_6	0.04887272	0.05266306	0.098186748	0.097426548	0.1007164997	0.0977526634

(6.73 per cent), and ^{35}Cl (75.76 per cent) and ^{37}Cl (24.24 per cent). Line lists were therefore calculated for two NaCl and four KCl isotopologues. Ro-vibrational states up to $v = 100$, $J = 563$ and $v = 120$, $J = 500$, respectively, and all transitions between these states satisfying the dipole selection rule $\triangle J = \pm 1$, were considered. High overtone transitions ($\triangle v > x$) were removed from the line lists post-calculation. This was due to a discovery by Medvedev et al. (2015) that the current version of program LEVEL significantly overestimates the intensities of high overtone transitions. Please refer to Section 6.2 for further details. The procedure described in Section 3.1 and above was used to produce line lists for two NaCl and four KCl isotopologues: Na^{35}Cl, Na^{37}Cl, ^{39}K^{35}Cl, ^{39}K^{37}Cl, ^{41}K^{35}Cl and ^{41}K^{37}Cl. The computed line lists are available from CDS and www.exomol.com.

Table 6.13: Summary of the original line lists.

	Na^{35}Cl	Na^{37}Cl	^{39}K^{35}Cl	^{39}K^{37}Cl	^{41}K^{35}Cl	^{41}K^{37}Cl
Maximum v	100	100	120	120	120	120
Maximum J	557	563	500	500	500	500
Number of lines	4734567	4763324	7224331	7224331	7224331	7224331

6.1.5 Results

The original line lists (before removal of high overtone transitions, see Section 6.2) computed for all isotopologues considered are summarized in Table 6.13. Each line list contained around 4 million transitions for NaCl and 7 million for the heavier KCl isotopologues. The final line lists (summarised in Table 6.25) contain around 700,000 lines for NaCl and 1.3 million lines for KCl. Each line list is therefore, for compactness and ease of use, presented in ExoMol format. Extracts from the start of the Na^{35}Cl and ^{39}K^{35}Cl files are given in Table 6.14, Table 6.16, Table 6.15 and Table 6.17. They can be downloaded from the CDS via http://cdsweb.u-strasbg.fr/cgibin/qcat?J/MNRAS/. The line lists and partition functions can also be obtained from www.exomol.com. Figure 6.5 illustrates the synthetic absorption spectra of Na^{35}Cl and ^{39}K^{35}Cl at 300 K and 3000 K. The CDMS database contains 607 and 772 rotational lines for Na^{35}Cl and ^{39}K^{35}Cl, respectively. Comparisons with the CDMS lines are presented in Figure 6.6. As can be seen, the agreement is excellent for both frequency and intensity. In particular, predicted line intensities agree within 2 and 4 per cent for the NaCl and KCl isotopomers considered in CDMS, respectively.

Emission cross sections for Na^{35}Cl and ^{39}K^{35}Cl were simulated using the procedure described in Section 3.3 and Gaussian line-shape profiles with half-width = 0.01 cm^{-1}. The resulting synthetic emission spectra are compared to the experimental ones in Figure 6.7 and Figure 6.8. When making comparisons, one has to be aware of a number of experimental issues. The baseline in NaCl shows residual 'channelling': a sine-like baseline that often appears in Fourier transform spectra due to interference from reflections from parallel optical surfaces in the beam. For KCl, the spectrum is

Table 6.14: Extract from start of states file for $Na^{35}Cl$

i	E	g	J	v
1	0.000000	16	0	0
2	0.434501	48	1	0
3	1.303497	80	2	0
4	2.606971	112	3	0

i: State counting number;
E: State energy in cm^{-1};
g: State degeneracy;
J: State rotational quantum number;
v: State vibrational quantum number.

Table 6.15: Extract from start of states file for $^{39}K^{35}Cl$

i	E	g	J	v
1	0.0	16	0	0
2	0.256466	48	1	0
3	0.769393	80	2	0
4	1.538778	112	3	0

i: State counting number;
E: State energy in cm^{-1};
g: State degeneracy;
J: State rotational quantum number;
v: State vibrational quantum number.

Table 6.16: Extracts from the transitions file for $Na^{35}Cl$

i	f	A_{if}
2	1	7.21E-07
3	2	6.93E-06
4	3	2.50E-05
5	4	6.16E-05

i: Upper state counting number;
f: Lower state counting number;
A_{if}: Einstein A coefficient in s^{-1}.

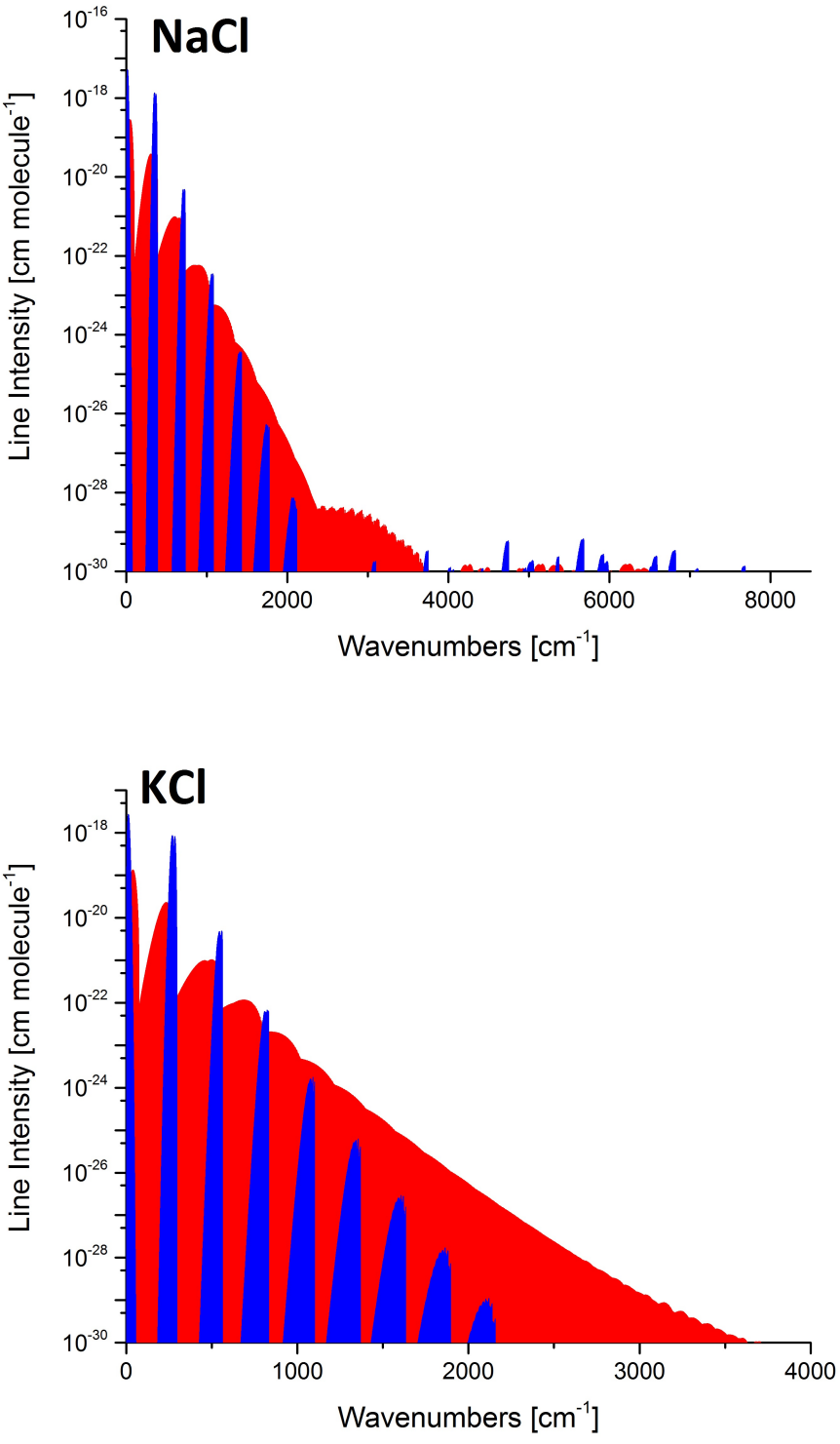

Figure 6.5: Absorption spectra of $Na^{35}Cl$ (upper) and $^{39}K^{35}Cl$ (lower) at 300 K (blue) and 3000 K (red).

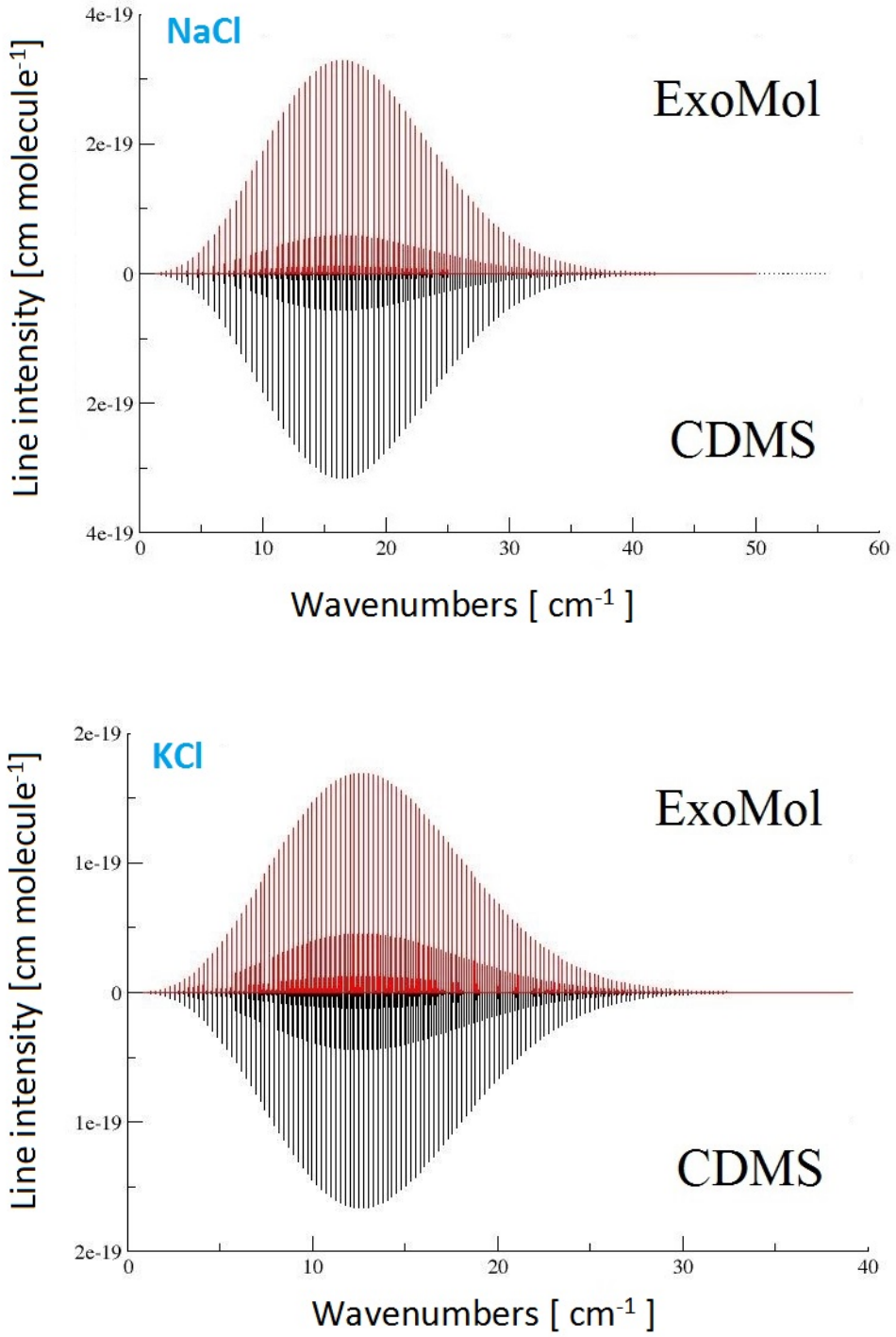

Figure 6.6: Absorption lines of $Na^{35}Cl$ (upper) and $^{39}K^{35}Cl$ (lower) at 300 K: ExoMol verses CDMS.

Table 6.17: Extracts from the transitions file for $^{39}K^{35}Cl$

i	f	A_{if}
2	1	1.89E-07
3	2	1.81E-06
4	3	6.55E-06
5	4	1.61E-05

i: Upper state counting number;
f: Lower state counting number;
A_{if}: Einstein A coefficient in s^{-1}.

very weak and the baseline, which has a large offset, was not properly adjusted to zero. Given these considerations, the comparisons must be regarded as satisfactory.

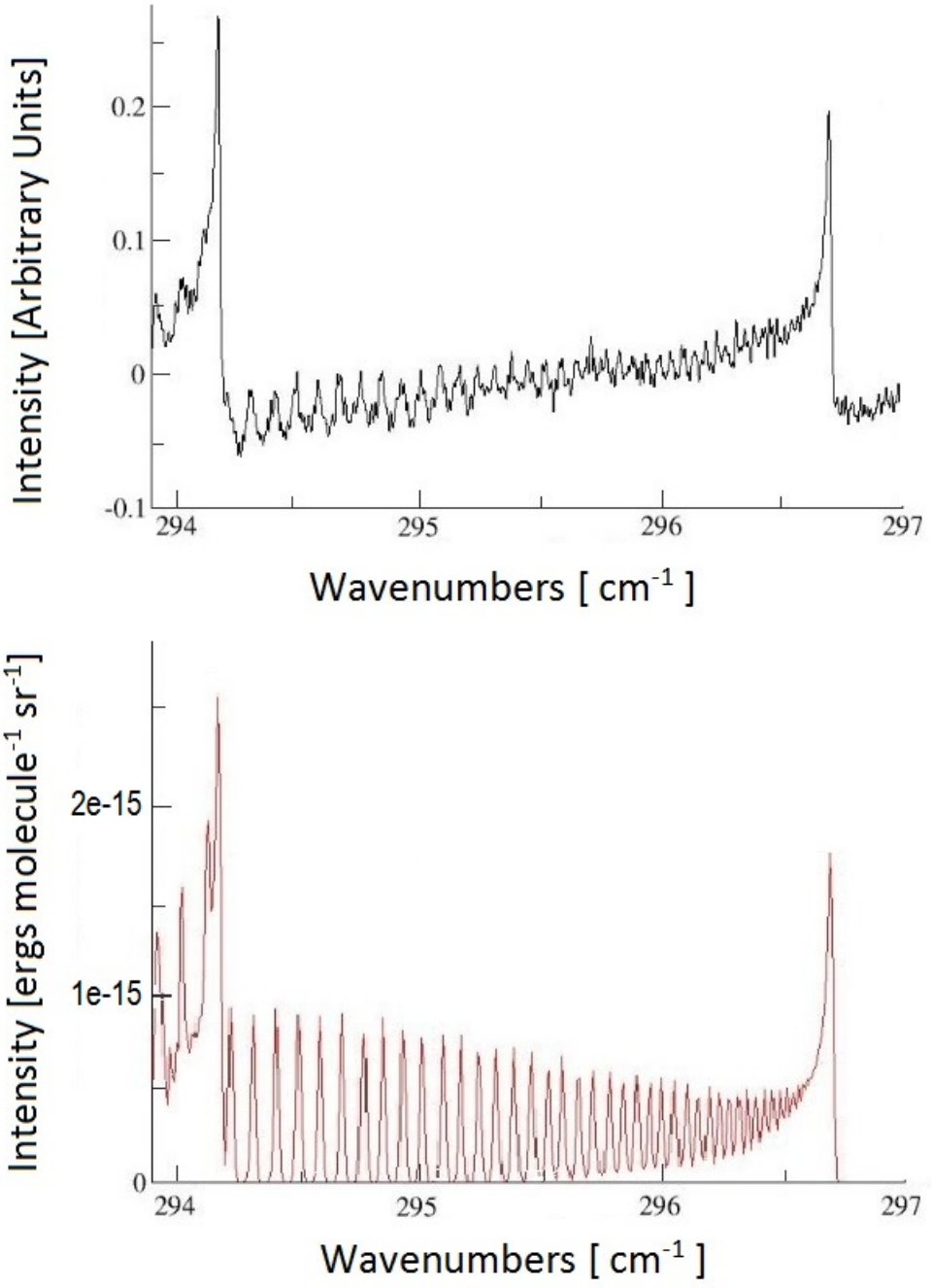

Figure 6.7: Observed (upper, Ram et al. (1997)) and simulated (lower, this work) emission spectra of $^{39}K^{35}Cl$.

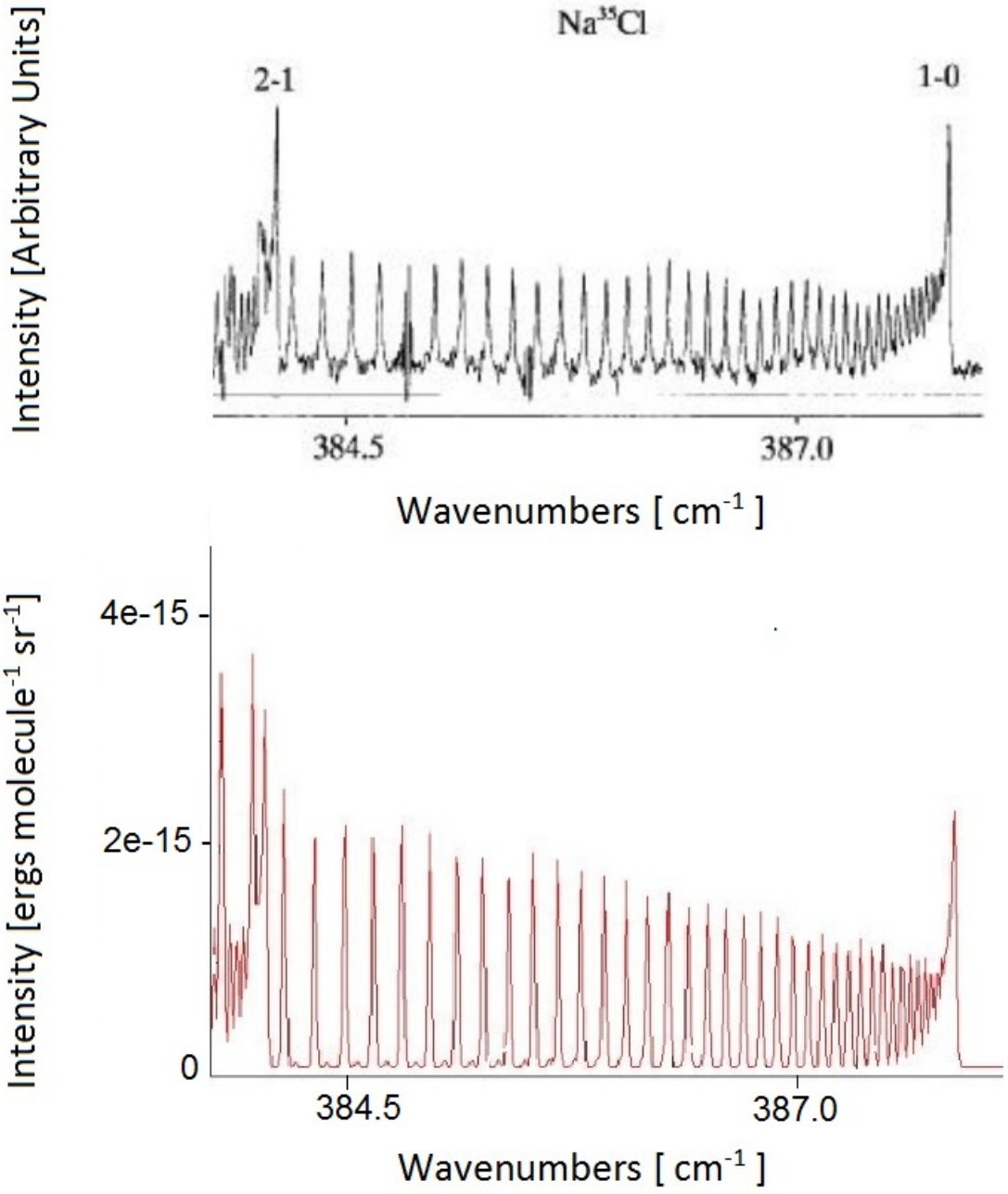

Figure 6.8: Observed (upper, Figure 2 in Ram et al. (1997)) and simulated (lower, this work) emission spectra of $Na^{35}Cl$.

6.2 Line Lists for Eight Isotopologues of CS

Line lists for all stable isotopologues of CS were computed by MSc student Ms Geethu Paulose using LEVEL (LeRoy (2007)). These calculations were able to predict ro-vibrational energies up to $v = 9$, and experimental frequencies, for $^{12}C^{32}S$ and $^{13}C^{32}S$ to within 0.02 cm^{-1} and 0.04 cm^{-1} respectively (see JnK columns in Table 6.18 and Table 6.19). The starting point for the calculations was a spectroscopic PEC determined by Coxon & Hajigeorgiou (1992), which had to be adapted for input into LEVEL as the analytical form employed by the authors was not implemented in the program. Consequently the results did not match the spectroscopic accuracy achieved by Coxon & Hajigeorgiou (1992).

The aim of this project was to refine the CS line lists, named JnK, using a method which takes advantage of the ExoMol format for representing molecular line lists (see Sections 2.1.2 and 3.1). As mentioned previously this includes a states file containing level energies and a transitions file detailing allowed energy level parings. The advantage of the format is it gives the option of replacing calculated energies with more refined or experimental energies such that, when the files are unpacked to produce the line list, more accurate line frequencies are computed, see Barber et al. (2014) for example.

6.2.1 Scaling Ro-vibrational Energies

The calculated ro-vibrational energies ($E^{\rm JnK}_{v,J}$) for all isotopologues may be refined using the vibrational ($J = 0$, $v \leq 20$) energies given in Coxon & Hajigeorgiou (1992) ($E^{\rm Cox}_{v,0}$) and the formula:

$$E^{\rm JnK-Cox}_{v,J} = \left(E^{\rm JnK}_{v,J} - E^{\rm JnK}_{v,0}\right) + E^{\rm Cox}_{v,0} \tag{6.1}$$

Ro-vibrational energies for $v > 20$ were shifted to maintain the energy level separations predicted by LEVEL according to:

$$E^{\rm JnK-Cox}_{v,J} = \left(E^{\rm JnK}_{v,J} - E^{\rm JnK}_{v-1,J}\right) + E^{\rm Cox}_{v-1,J} \tag{6.2}$$

After this energy scaling, vibrational energies to were predicted to the same spectroscopic accuracy achieved by Coxon & Hajigeorgiou (1992), however not all the line frequency predictions improved (see JnK-Cox columns in Table 6.19).

This is likely due to the fact experimental data available to Coxon & Hajigeorgiou (1992) was limited to $J \leq 41$ and $J \leq 28$ while Ram et al. (1995) and Uehara et al. (2015), the most recent experiments, assigned lines for J up to 113 and 86 for $^{12}C^{32}S$ and $^{13}C^{32}S$ respectively. Therefore the decision was made to substitute in experimental energies were possible.

6.2.2 Extracting Experimental Energies

Experimental energies were determined directly from frequencies measured by Ram et al. (1995) and Uehara et al. (2015) using the MARVEL technique (Furtenbacher

Table 6.18: A comparison of theoretically and experimentally derived vibrational term values for $^{12}C^{32}S$ and $^{13}C^{32}S$ in cm^{-1}.

T_v	Experiment	Calculated This Work	Obs-Calc This Work	Coxon & Harjigeorgion (1992)	
	(JnK-Exp)	(JnK)	(JnK)	(JnK-Cox)	(JnK-Cox)
		$^{12}C^{32}S$			
Uehara et al. (2015)					
T_1	1272.162085	1272.1690	-0.006915	1272.16214	-0.000055
T_2	2531.353715	2531.3486	0.005115	2531.35384	-0.000125
T_3	3777.597715	3777.5899	0.007815	3777.59800	-0.000285
T_4	5010.916850	5010.9087	0.008150	5010.91739	-0.000540
T_5	6231.333760	6231.3229	0.010860	6231.33456	-0.000800
T_6	7438.870820	7438.8584	0.012420	7438.87183	-0.001010
T_7	8633.550080	8633.5338	0.016280	8633.55125	-0.001170
Ram et al. (1995)					
T_8	9815.39254	9815.3752	0.0173	9815.39457	-0.00203
T_9	10984.42006	10984.4025	0.0176	10984.42297	-0.00291
		$^{13}C^{32}S$			
Uehara et al. (2015)					
T_1	1236.315929	1236.352358	-0.036429	1236.31591	0.000019
T_2	2460.388235	2460.378216	0.010019	2460.39043	-0.002195
T_3	3672.237852	3672.223355	0.014497	3672.24479	-0.006938
T_4	4871.88567	4871.883107	0.002563	-	-
T_5	6059.35246	6059.354654	-0.002194	-	-

Table 6.19: Comparison of predicted ro-vibrational frequencies (Calc), in cm^{-1}, with experimental line positions (Exp) measured by Ram et al. (1995) and Uehara et al. (2015) for $^{12}C^{32}S$ and $^{13}C^{32}S$.

J'	J''	v'	v''	Exp JnK-Exp	Calc JnK	Obs-Calc JnK	Calc JnK-Cox	Obs-Calc JnK-Cox
$^{12}C^{32}S$								
				Uehara et al. (2015)				
10	9	1	0	1287.847083	1287.854114	-0.007031	1287.847191	-0.000108
10	11	1	0	1253.542068	1253.549024	-0.006956	1253.542101	-0.000032
9	10	2	1	1242.440398	1242.428641	0.011757	1242.440739	-0.000341
11	10	2	1	1276.248067	1276.236290	0.011777	1276.248388	-0.000321
100	101	2	1	1040.852470	1040.848528	0.003942	1040.860626	-0.008156
20	21	6	5	1172.020927	1172.020128	0.000799	1172.021917	-0.000990
21	20	6	5	1237.819388	1237.818203	0.001185	1237.819992	-0.000604
78	79	6	5	1049.137636	1049.137625	0.000011	1049.139414	-0.001778
10	11	7	6	1176.836843	1176.836008	0.000835	1176.840042	-0.003199
15	14	7	6	1216.680436	1216.678641	0.001795	1216.682675	-0.002239
63	64	7	6	1072.087367	1072.088777	-0.001410	1072.092811	-0.005444
				Ram et al. (1995)				
102	103	1	0	1047.2868	1047.291040	-0.004240	1047.284117	0.002683
107	106	1	0	1371.8550	1371.852876	0.002124	1371.845953	0.009047
107	106	2	1	1357.5752	1357.576293	-0.001093	1357.588391	-0.013191
89	88	6	5	1296.2749	1296.274876	0.000024	1296.276665	-0.001765
89	88	7	6	1282.3246	1282.326279	-0.001679	1282.330313	-0.005713
25	26	8	7	1137.7464	1137.744640	0.001760	1137.746507	-0.000107
30	31	8	7	1128.3927	1128.390965	0.001735	1128.392832	-0.000132
52	53	8	7	1084.0478	1084.049553	-0.001753	1084.051420	-0.003620
59	58	8	7	1251.2061	1251.207909	-0.001809	1251.209776	-0.003676
25	26	9	8	1125.2391	1125.236731	0.002369	1125.237916	0.001184
28	27	9	8	1207.1842	1207.183263	0.000937	1207.184448	-0.000248
52	53	9	8	1071.8531	1071.854760	-0.001660	1071.855945	-0.002845
59	58	9	8	1237.6787	1237.676631	0.002069	1237.677816	0.000884
$^{13}C^{32}S$								
				Uehara et al. (2015)				
2	1	1	0	1239.369011	1239.405053	-0.036042	1239.368605	0.000406
79	80	1	0	1080.972174	1080.977506	-0.005332	1080.941058	0.031116
12	13	2	1	1203.322346	1203.275312	0.047034	1203.323884	-0.001538
70	71	2	1	1089.992782	1089.945856	0.046926	1089.994428	-0.001646
7	8	3	2	1199.383201	1199.376151	0.007050	1199.385462	-0.002261
53	52	3	2	1276.188741	1276.197650	-0.008909	1276.206961	-0.018220
6	7	4	3	1188.850787	1188.862540	-0.011753	1188.841105	0.009682
64	65	4	3	1080.169544	1080.175599	-0.006055	1080.154164	0.015380
14	13	5	4	1207.300671	1207.305740	-0.005069	1207.305740	-0.005069
45	46	5	4	1107.707636	1107.715903	-0.008267	1107.715903	-0.008267

Table 6.20: Comparison of predicted ro-vibrational frequencies (Calc), in cm^{-1}, with experimental line positions (Exp) measured by Burkholder et al. (1987) for $^{12}C^{33}S$ and $^{12}C^{34}S$.

J'	J''	v'	v''	Exp	Calc JnK	Obs-Calc JnK	Calc JnK-Cox	Obs-Calc JnK-Cox
$^{12}C^{33}S$								
3	2	1	0	1271.73537	1271.736018	-0.000648	1271.735366	0.000004
4	5	1	0	1258.72386	1258.724631	-0.000771	1258.723979	-0.000119
29	28	1	0	1308.72699	1308.728068	-0.001078	1308.727416	-0.000426
25	26	1	0	1221.09717	1221.098153	-0.000983	1221.097501	-0.000331
$^{12}C^{34}S$								
3	2	1	0	1266.78054	1266.775300	0.005240	1266.780744	-0.000204
4	5	1	0	1253.87137	1253.865751	0.005619	1253.871195	0.000175
35	34	1	0	1310.80236	1310.797693	0.004667	1310.803137	-0.000777
35	36	1	0	1197.09619	1197.091827	0.004363	1197.097271	-0.001081

et al. (2007)) which involves inverting transitions to extract experimental level energies. Energies for a vibrational band v' - v'' with experimental line positions of ν_P and ν_R for P and R branch lines respectively, are calculated using the relations:

$$E'_{v,J} = (E_{v-1,J-1})'' + \nu_R(J-1) \tag{6.3}$$

$$E''_{v,J} = (E_{v+1,J-1})'' + \nu_P(J) \tag{6.4}$$

Starting from the $J = 0$ energies derived by Uehara et al. (2015). Table 6.22 gives a subset of experimental line positions and extracted energies for the main isotopologue.

The process of building a list of experimentally derived energies can be likened to climbing a tree with P and R branches. Gaps in the branches were filled by calculated frequencies corrected for the obs. - calc. difference of the closest observed frequency.

Uehara et al. (2015) is the more accurate experimental study and thence energies extracted from these frequencies were used preferentially over those extracted from Ram et al. (1995) frequencies where possible. 733 energies were extracted in total for the main isotopologue and 341 energies for $^{13}C^{32}S$, see Table 6.23.

Table 6.21: Comparison of predicted rotational frequencies (Calc), in cm^{-1}, with experimental line positions (Exp) measured by Ahrens & Winnewisser (1999) for $^{12}C^{36}S$, $^{13}C^{33}S$ and $^{13}C^{34}S$.

J'	J''	v'	v''	Exp	Calc		Obs-Calc	
					JnK	JnK-Cox	JnK	JnK-Cox
$^{12}C^{36}S$								
6	5	0	0	9.507279		9.507297		-0.000018
22	21	1	1	34.561685		34.561709		-0.000024
$^{13}C^{33}S$								
6	5	0	0	9.173973		9.173971		0.000002
20	19	0	0	30.545844		30.545846		-0.000002
$^{13}C^{34}S$								
20	19	0	0	30.293201		30.293299		-0.000098
13	12	2	2	19.429173		19.429154		0.000019

Table 6.22: Subset of Energies Extracted from Experimental Line Positions (Uehara et al. (2015) or Ram et al. (1995) for v' - v'' = 1 - 0).

Experimental Frequencies				Upper			Extracted Energies Lower		
cm^{-1}	transition	cm^{-1}	transition	cm^{-1}	J	v	cm^{-1}	J	v
1270.527600	P(1)	1273.783	R(0)	0.000000	0	0	1272.162085	0	1
1268.882286	P(2)	1275.39176	R(1)	1.634485	1	0	1273.783	1	1
1267.223849	P(3)	1276.995263	R(2)	4.900714	2	0	1277.026245	2	1
1265.556631	P(4)	1278.580271	R(3)	9.802396	3	0	1281.895977	3	1
1263.873286	P(5)	1280.154752	R(4)	16.339346	4	0	1288.382667	4	1
1262.180748	P(6)	1281.717068	R(5)	24.509381	5	0	1296.494098	5	1
1260.476321	P(7)	1283.267829	R(6)	34.31335	6	0	1306.226449	6	1
1258.759888	P(8)	1284.806401	R(7)	45.750128	7	0	1317.581179	7	1
1257.032291	P(9)	1286.335021	R(8)	58.821291	8	0	1330.556529	8	1

Table 6.23: Summary of Energies Extracted from Experimental Frequencies.

v	Jmax	Total Extracted	Using Uehara et al. (2015)	Using Ram et al. (1995)
$^{12}C^{32}S$				
0	106	107	87	20
1	106	107	102	5
2	101	102	94	8
3	93	94	86	8
4	89	90	89	1
5	89	80	62	18
6	76	55	41	14
7	70	46	24	22
8	59	32	0	32
9	59	32	0	32
$^{13}C^{32}S$				
0	80	78	78	0
1	71	70	70	0
2	70	69	69	0
3	65	64	64	0
4	46	30	30	0
5	46	30	30	0

6.2.3 Manipulating the .states file

$^{12}C^{32}S$ and $^{13}C^{32}S$ energies for the experimental ranges were replaced with experimentally derived energies (Section 6.2.2). Ro-vibrational energies for (v, J) outside the experimental ranges were shifted to maintain the energy level separations predicted by LEVEL according to the following equations.

For $v < v_{\text{max}}^{\text{Exp}}$ and $J > J_{\text{max}}^{\text{Exp}}$:

$$E_{v,J}^{\text{JnK}-\text{Exp}} = \left(E_{v,J}^{\text{JnK}} - E_{v,0}^{\text{JnK}}\right) + E_{v,0}^{\text{Exp}} \tag{6.5}$$

For $v > v_{\text{max}}^{\text{Exp}}$:

$$E_{v,J}^{\text{JnK}-\text{Exp}} = \left(E_{v,J}^{\text{JnK}} - E_{v-1,J}^{\text{JnK}}\right) + E_{v-1,J}^{\text{JnK}-\text{Exp}} \tag{6.6}$$

The experimental frequencies for $^{12}C^{32}S$ and $^{13}C^{32}S$, by default, were reproduced almost exactly using this method. The largest residual is of the order 0.001 cm^{-1}. Hence the accuracy of the resulting line lists should be equal to the experimental accuracies, which are expected to be 0.012 cm^{-1} and 0.01 cm^{-1} for Ram et al. (1995) and Uehara et al. (2015) respectively.

For $^{12}C^{33}S$ and $^{12}C^{34}S$ an earlier experimental study, Burkholder et al. (1987), measured infra-red $v = 1 - 0$ absorption frequencies at 0.004 cm^{-1} unapodized reso-

lution. The Coxon refined energies, see Eqs. 6.1 and 6.2, reproduce these frequencies to very high precision (see Table 6.20), as would be expected considering they fitted to these frequencies. The Coxon refined energies also represent an improvement on the unrefined JnK energies (see Table 6.20), therefore we chose to employ them in our final line lists for these two isotopologues.

For the remaining isotopologues, with the exception of $^{13}C^{36}S$ which has not been observed experimentally, we have only measurements of rotational frequencies from Ahrens & Winnewisser (1999) to compare with. These are expected to have an accuracy of at least 0.00002 cm^{-1}. As can been seen in Table 6.21 the agreement is excellent. Due to our methods, unrefined JnK and Coxon refined energies predict the same rotational frequencies. However, since the Coxon refined energies improved ro-vibrational frequency predictions for other isotopologues, these are employed in the final line lists for the remaining four isotopologues.

An overview of the energy level content of the final 'hybrid' line lists is given in Table 6.24. Although the terms JnK, JnK-Cox and JnK-Exp are used in the text to refer to unrefined, Coxon refined and experimentally substituted energies respectively, the final line lists as provided on www.exomol.com are simply named JnK.

Table 6.24: Overview of sources of energy levels used in the JnK 'hybrid' line lists.

Isotopologue	Experimental Energies	Coxon Energies	Shifted Energies
$^{12}C^{32}S$	v $\leq$ 9, J $\leq$ 106	None	v $>$ 9, J $>$ 106 using Eq. 6.5 and Eq. 6.6
$^{12}C^{33}S$	None	v $\leq$ 7 using Eq. 6.1	v $>$ 7 using Eq. 6.2
$^{12}C^{34}S$	None	v $\leq$ 7 using Eq. 6.1	v $>$ 7 using Eq. 6.2
$^{12}C^{36}S$	None	v $\leq$ 7 using Eq. 6.1	v $>$ 7 using Eq. 6.2
$^{13}C^{32}S$	v $\leq$ 5, J $\leq$ 80	None	v $>$ 5, J $>$ 80 using Eq. 6.5 and Eq. 6.6
$^{13}C^{33}S$	None	v $\leq$ 3 using Eq. 6.1	v $>$ 3 using Eq. 6.2
$^{13}C^{34}S$	None	v $\leq$ 3 using Eq. 6.1	v $>$ 3 using Eq. 6.2
$^{13}C^{36}S$	None	v $\leq$ 3 using Eq. 6.1	v $>$ 3 using Eq. 6.2

6.2.4 High Overtone Intensities

The Normal Intensity Distribution Law (NIDL), whereby transition intensities decrease with increasing overtone in a linear fashion, is an approximation but one which provides a semi-quantitative prediction of higher overtone intensities based on lower overtone intensities (Medvedev et al. (2015)).

Medvedev et al. (2015) tested the original CS line lists by plotting the Einstein coefficients for all $\triangle v$ = 1 - 49 transitions with $J' = 1$ to the ground state in NIDL co-ordinates (Figure 6.9). This clearly showed unphysical intensity saturation above $\triangle v = 9$. The same effect can be seen in a plot of $\triangle v = x$ overtone against total overtone intensity (Figure 6.10). In response to this, all transitions with $\triangle v > 9$ were removed from the final CS line lists.

As the computation of unreliable high overtones intensities was shown by Medvedev et al. (2015) to be intrinsic to the numerical methods employed in line list production,

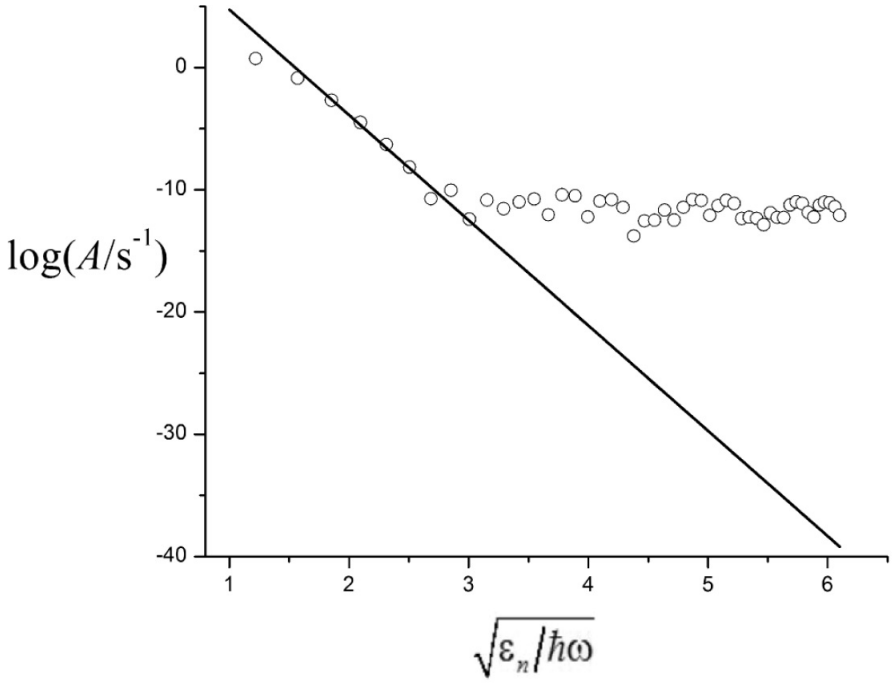

Figure 6.9: Einstein A coefficients plotted against NIDL coordinates for the $J = 0 \leftarrow J = 1$ transitions of overtones $\triangle v = 0$ - 49 predicted by LEVEL for CS. ω is the harmonic frequency and ε_n is the vibrational energy. Figure 3 in Medvedev et al. (2015).

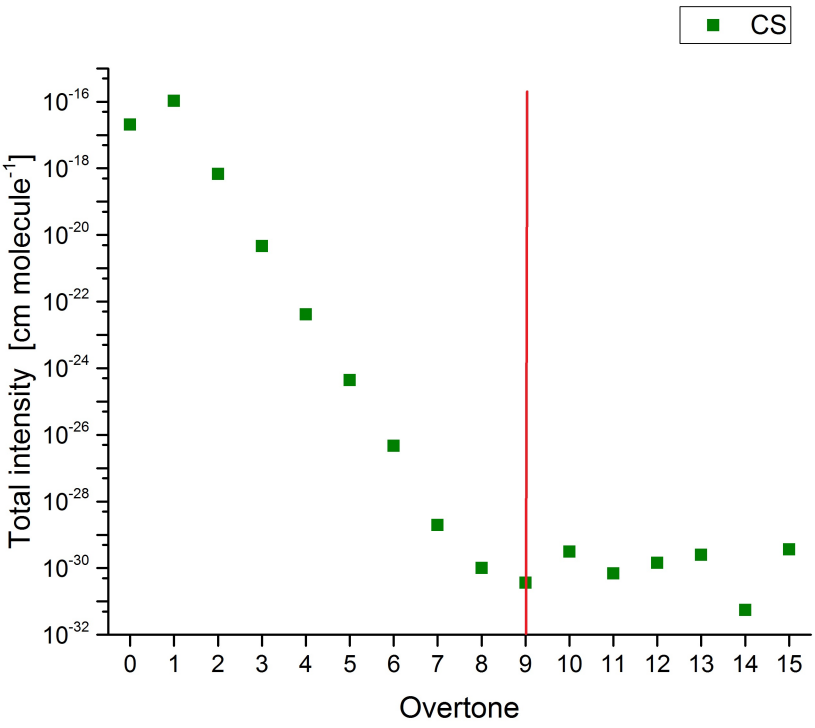

Figure 6.10: $\triangle v = x$ overtone vs. total overtone intensity (at 300 K) predicted by LEVEL for CS. The overtone beyond which transitions should be discarded is indicated by the red line.

it can be expected that the same effect manifests in other line lists. This was shown to be true for other ExoMol diatomic line lists computed using LEVEL, SiO, NaCl, KCl and PN. Figures 6.11 and 6.12 display the plots of $\triangle v = x$ overtone against total overtone intensity for these molecules. The overtone beyond which transitions should be discarded, and the number of lines remaining in the line lists after this removal, is summarised in Table 6.25.

Table 6.25: Overview of ExoMol line lists for which transition with $\triangle v > \triangle v_{sat}$ have been removed.

Isotopologue	$\triangle v_{sat}$	N_{lines} Old	N_{lines} New
$^{12}C^{32}S$	9	549,312	199,045
$^{12}C^{33}S$	9	550,244	199,917
$^{12}C^{34}S$	9	554,898	200,599
$^{12}C^{36}S$	9	560,733	201,944
$^{13}C^{32}S$	9	577,885	205,826
$^{13}C^{33}S$	9	581,375	206,622
$^{13}C^{34}S$	9	584,485	207,322
$^{13}C^{36}S$	9	590,320	209,071
$^{28}Si^{16}O$	5	1,784,964	254,675
$^{28}Si^{17}O$	5	1,818,923	254,649
$^{28}Si^{18}O$	5	1,852,656	259,371
$^{29}Si^{16}O$	5	1,993,414	279,077
$^{30}Si^{16}O$	5	1,890,039	264,605
$^{23}Na^{35}Cl$	7	4,734,567	702,271
$^{23}Na^{37}Cl$	7	4,763,324	731,046
$^{39}K^{35}Cl$	11	7,224,331	1,326,765
$^{39}K^{37}Cl$	11	7,224,331	1,326,765
$^{41}K^{35}Cl$	11	7,224,331	1,326,765
$^{41}K^{37}Cl$	11	7,224,331	1,326,765
$^{31}P^{14}N$	5	692,019	142,512
$^{31}P^{15}N$	5	743,114	193,607

Two problems that result in the saturation of high overtone intensities were identified by Medvedev and co-workers:

1. Inadequate numerical precision used in the calculations (Medvedev et al. (2015)),
2. Non-analytical representation of the DMC (Medvedev et al. (2016)).

LEVEL employs double precision arithmetic (LeRoy (2007)), and when the values of the transition moment become comparable with the double precision error ($\approx 10^{-16}$ a.u.) the corresponding intensities essentially represent numerical noise. Medvedev et al. (2015) demonstrated for CO that implementation of quadrupole precision resulted in more realistic high overtone intensities and no saturation is observed even up to the dissociation limit.

The DMCs of diatomics are typically represented on a grid for input to LEVEL (LeRoy (2007)). The user then specifies how interpolation between the points is to

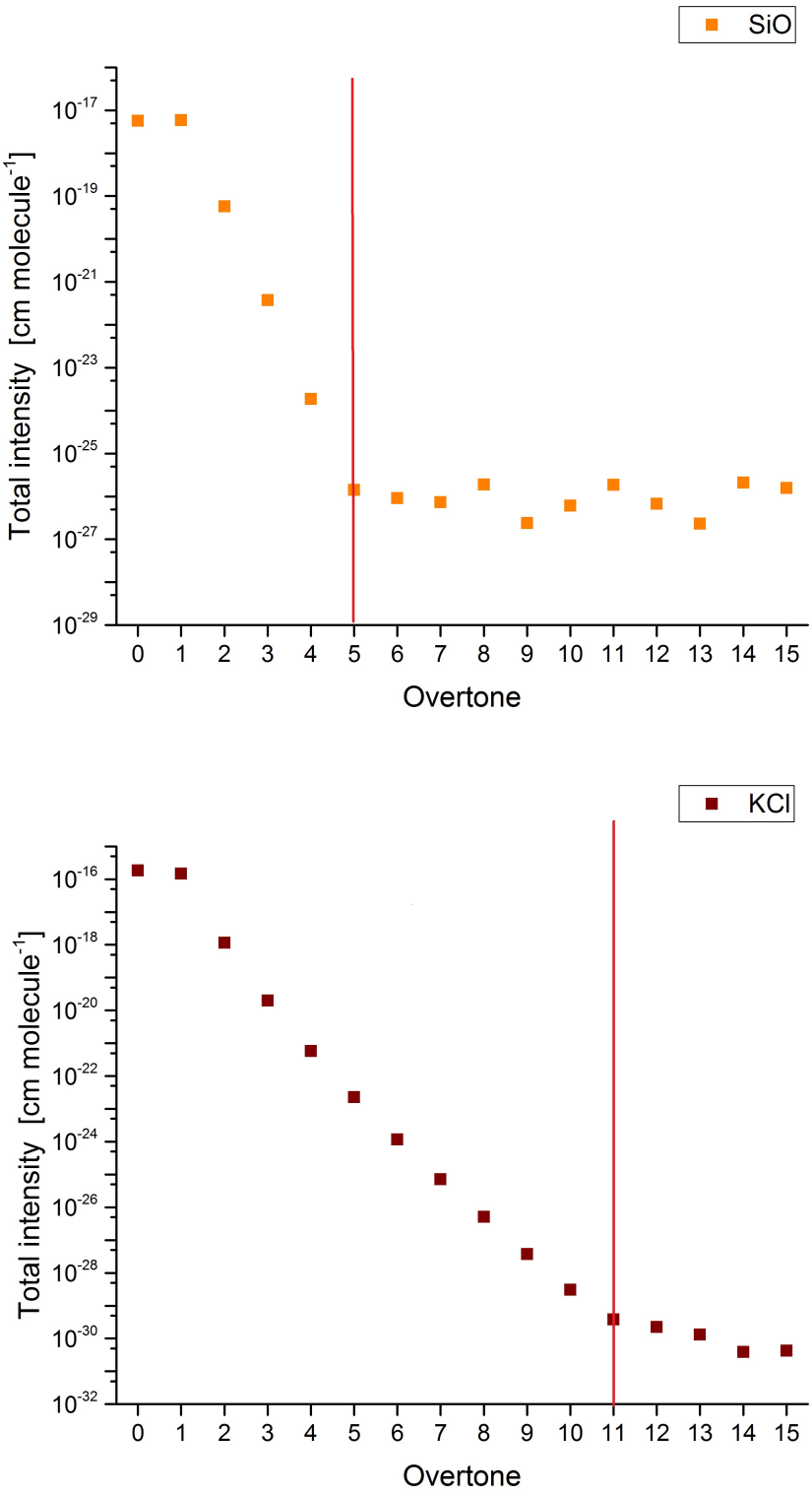

Figure 6.11: $\triangle v = x$ overtone vs. total overtone intensity (at 300 K) predicted by LEVEL for multiple ExoMol Diatomics. The overtone beyond which transitions should be discarded is indicated by the red lines.

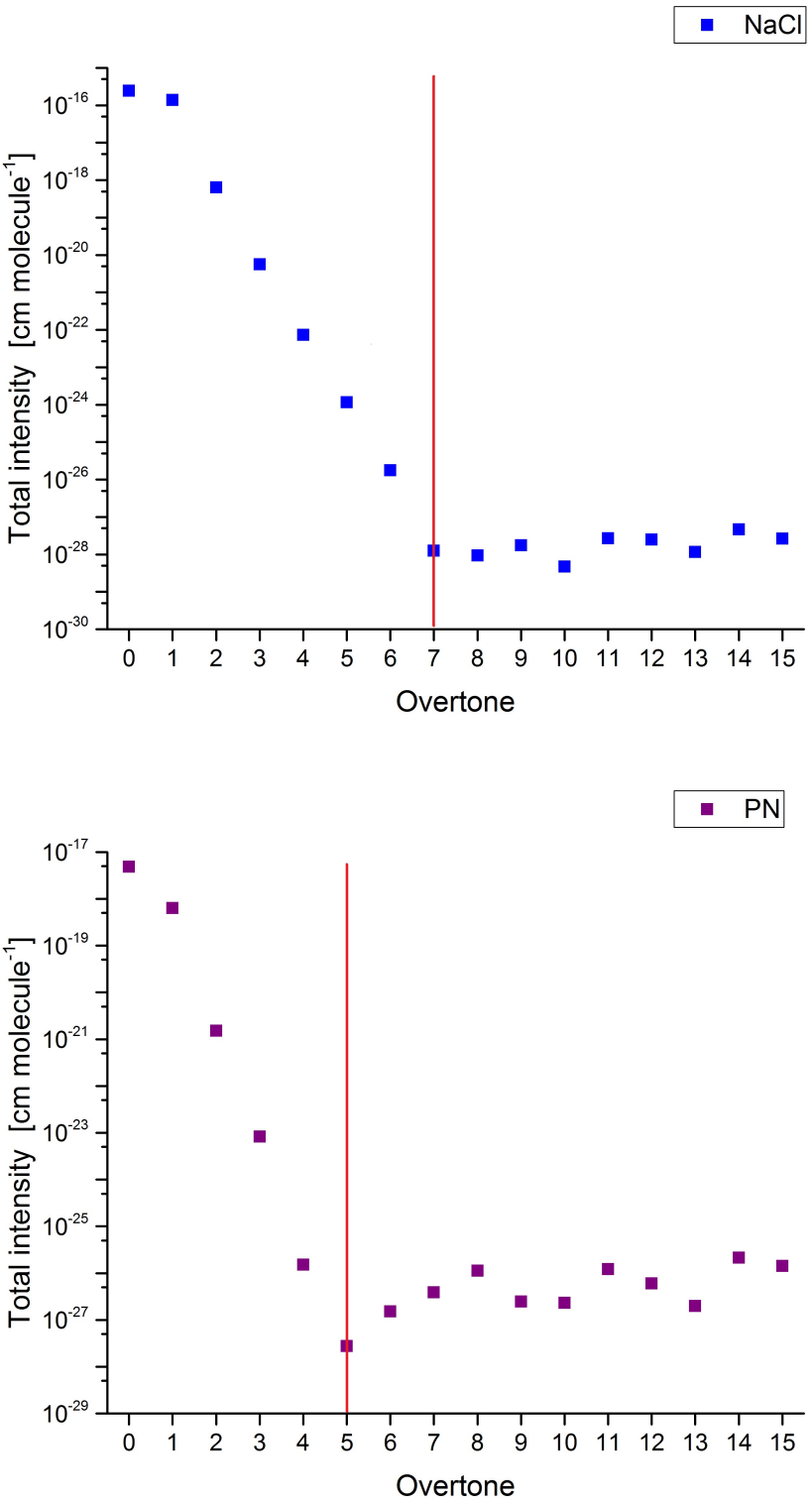

Figure 6.12: $\triangle v = x$ overtone vs. total overtone intensity (at 300 K) predicted by LEVEL for multiple ExoMol Diatomics. The overtone beyond which transitions should be discarded is indicated by the red lines.

be performed by the program, using piecewise polynomials or cubic splines (LeRoy (2007)). Medvedev et al. (2016) demonstrate for CO that an interpolated DMC results in saturation of high overtone intensities and only a DMC represented by an analytical function results in realistic intensities up to the dissociation limit.

The re-computation of diatomic intensities using quadrupole precision arithmetic and analytical DMCs is an avenue for future work. However, for the purposes of ExoMol, the high overtone transitions are all very weak and it is anticipated that their removal from the line lists will have little effect on practical applications.

6.3 Summary of Results

6.3.1 NaCl/KCl

The aim to produce more comprehensive line lists for the previously studied isotopologues of NaCl and KCl has been achieved. The first theoretical line list for ^{41}K^{37}Cl has also been computed. Laboratory frequencies are reproduced to sub-wavenumber accuracy. This accuracy should extend to all predicted transition frequencies up to at least $v = 8$ and $v = 12$ for NaCl and KCl respectively. New *ab initio* dipole moments and Einstein A coefficients are computed. For the transitions also considered by the previous theoretical study, the predicted intensities agree within 4 percent and 2 percent respectively for the parent isotopes at 300 K.

The results are line lists for the rotation-vibration transitions within the ground states of Na^{35}Cl, Na^{37}Cl, ^{39}K^{35}Cl, ^{39}K^{37}Cl, ^{41}K^{35}Cl and ^{41}K^{37}Cl, which should be accurate for a range of temperatures up to at least 2000 K. The line lists can be downloaded from CDS or from www.exomol.com.

The line lists have been truncated by removing transitions with $\Delta v \geq 8$ and $\Delta v \geq 12$ for NaCl and KCl respectively due to the numerical problem identified by Medvedev and co-workers with the intensities of high overtone transitions computed with LEVEL.

6.3.2 CS

In the present work improved line lists for all stable isotopologues of carbon monosulphide are produced. Calculated energies in the states file of the original line lists, calculated by Ms Geethu Paulose, were substituted with energies derived directly from experimental frequencies to match the experimental accuracy.

This accuracy should extend to all predicted transition frequencies up to at least $v = 9$ and $J = 106$ for ^{12}C^{32}S, and $v = 5$ and $J = 80$ for ^{13}C^{32}S, the experimental ranges. Based on comparisons with other experiments the frequencies for the remaining isotopologues should be predicted to sub-wavenumber accuracy at least for $v < 3$ and $J < 21$. Einstein A coefficients were taken from the original line lists.

The results are improved line lists for rotation-vibration transitions within the ground states of ^{12}C^{32}S, ^{12}C^{33}S, ^{12}C^{34}S, ^{12}C^{36}S, ^{13}C^{32}S, ^{13}C^{33}S, ^{13}C^{34}S and ^{13}C^{36}S,

which should be accurate for a range of temperatures up to at least 3000 K. The line lists can be downloaded from CDS or from www.exomol.com.

The line lists have been truncated by removing transitions with $\Delta v \geq 9$ due to the numerical problem identified by Medvedev and co-workers with the intensities of high overtone transitions computed with LEVEL.

Finally it is necessary to note that, although the current line lists are more comprehensive, for the purposes of high resolution radio astronomy and far infra-red studies of low temperature objects, the CDMS line lists are recommended.

Chapter 7

Validating Line Lists using Laboratory Measurements

The accuracy of spectral models is highly dependent on the quality of molecular line lists. The suitability of a theoretical line list for particular applications may be assessed by:

1. Taking laboratory measurements of the molecular spectrum for relevant physical conditions.
2. Using the line list to model the molecular spectrum for the experimental conditions.
3. Comparing the experimental and synthetic spectra.

The aim of this work was to validate high temperature line lists of HCl, NH_3, CH_4 and H_2CO for industrial spectral studies by comparison to high resolution FTIR spectra provided by Dr Alexander Fateev or measured as part of this work. Room temperature stick spectra for NH_3 are also compared to experimental line lists constructed by Prof Alain Campargue and Dr Serge Béguier to assess the accuracy of the line list for high wavenumber regions.

Section 7.1 gives an overview of the experimental spectra, those measured as part of this work are described in more detail in Section 7.1.1. Section 7.2 details the sources of theoretical molecular data and Section 7.3 discusses the comparisons.

7.1 Experimental Measurements

High resolution high temperature FTIR spectra of HCl (2000 - 6000 cm^{-1}), NH_3 (200 - 5500 cm^{-1}), CH_4 (200 - 7000 cm^{-1}) and H_2CO (200 - 6000 cm^{-1}) have been measured by or under the supervision of Dr Alexander Fateev. The individual spectra are described in Table 7.1.

Measurements for HCl and H_2CO were performed simply to test the quality of the current line lists for conditions relevant to industrial spectral studies. NH_3 (400 -

6000 cm^{-1}) and CH_4 spectra were measured at the highest resolution obtainable with the experimental set-up (0.09 cm^{-1}), and in some cases higher temperatures than the HCl and H_2CO spectra, so that detailed analyses could be carried out to provide new assignments and energy level information for both molecules (see Chapters 8 and 9). The 200 - 400 cm^{-1} NH_3 measurement campaign was undertaken as part of this work and is discussed in more detail in Section 7.1.1.

Table 7.1: Overview of FTIR spectra measured by or under the supervision of Dr Alexander Fateev. Conc is the molecule concentration per unit volume, l is the absorption path length and Res is the nominal spectral resolution. The intensities are either transmittance (T) or absorbance (A) which is calculated from the measured single beam spectra. In principle the measurements cover a wide spectral range (full coverage). In practice the signal level varies with wavenumber and the most useful information, where the signal to noise ratio is high and the spectral features are not saturated, is contained within a narrower region (chosen region).

Molecule	Full Coverage cm^{-1}	Chosen region cm^{-1}	Conc	T °C	P mbar	l cm	Res cm^{-1}	Type
HCl	2000 - 6000	2300 - 3800	3501 ppm	400	1003.9	33.25	0.5	T
			3501 ppm	500	1011.5	33.25	0.5	T
H_2CO	200 - 6000		9 %	500	1026.0	33.25	0.25	A
NH_3	200 - 2000	270 - 360	0.5 %	200	1014.2	33.25	2	A
			1 %	200	1014.3	33.25	2	A
			1 %	500	1014.0	33.25	2	A
			5.5 %	500	1014.0	33.25	0.25	A
	480 - 6000	500 - 2100	1 %	300	1020.3	33.25	0.09	A
			1 %	400	1023.1	33.25	0.09	A
			1 %	500	1010.0	33.25	0.09	A
			1 %	1027	1050.4	55.3	0.09	A
	480 - 6000	2100 - 5500	10 %	1027	1030.5	55.3	0.09	A
CH_4	200 - 7000	1000 - 6300	7%	700	1051.3	55.3	0.09	A
			30%	700	1085.1	55.3	0.09	A
			50%	700	1082.9	55.3	0.09	A
			1%	900	1061.8	55.3	0.09	A
			7%	900	1065.0	55.3	0.09	A
			50%	900	1043.3	55.3	0.09	A

Also available are experimental line lists for NH_3 in the regions 7400 - 8640 cm^{-1} and 9000 - 10400 cm^{-1} constructed by Prof Alain Campargue and c from pure NH_3 FTIR transmittance spectra available from the Kitt Peak archive. The spectra were measured at 25°C, 5 Torr ($\approx$ 7 mbar) and a nominal resolution of 0.01 cm^{-1} by Dr Catherine DeBergh in 1980. The path length is assumed to be 25 m (Campargue et al. (2015)).

7.1.1 200 - 400 cm^{-1} NH_3 measurements.

To gain experience in experimental techniques NH_3 measurements in the region 200 - 400 cm^{-1} were undertaken as part of this work. The experimental set-up is described in Section 4.1. KRS5 optical windows, that allow measurements down to 200 cm^{-1}, were installed on either end of the gas cell. As these windows had not been used before, there was no guarantee they would permit sufficient signal to reach the detector for measurements to be possible. A second complication was presented by a polythene filter that should protect the detector from excess visible and UV light. The filter had been damaged by an earlier experiment and there was no exact replacement. Therefore the technician proposed the use of a black polythene trash bag as a substitute. The experimental campaign over three days is described below. The experimental conditions are presented in Tables 7.2, 7.3 and 7.4 for 18-04-2016, 19-04-2016 and 20-04-2016 respectively.

The aim of this measurement campaign was first to measure the signal level at the detector with the KRS5 optical windows installed, and second to determine if good quality spectra for the region 200 - 400 cm^{-1} at the highest resolutions (0.25 or 0.09 cm^{-1}), required for a detailed analysis, could be measured within a reasonable time frame.

18-04-2016 (see Table 7.2)

Table 7.2: 18-04-2016 Measurement log: T is the temperature, P is the pressure, Res. is the nominal resolution, Acq. is the number of acquisitions (scans), BB indicates whether the Black Body source is ON or OFF and Signal is the reading at the detector.

T °C	P mbar	Res. cm^{-1}	Gas	BB (ON/OFF)	Acq.	Signal V	Notes
200	1014.3	2	Dry air only	ON	0.10	100	Trail using one layer of trash bag
200	1014.3	2	Dry air only	ON	0.40	100	Trail without trash bag (no filter)
200	1014.3	2	N_2 purge only	ON	0.41	100	Quick reference measurement N_2+BB
200	1014.2	2	N_2 purge only	OFF	0.23	100	Quick reference measurement N_2
200	1014.1	2	NH_3 (0.492%) + N_2	ON	0.42	100	Quick gas of interest measurement N_2+NH_3+BB
200	1014.3	2	NH_3 (0.492%) + N_2	OFF	0.20	100	Quick gas of interest measurement N_2+NH_3
200	1014.2	2	NH_3 (0.983%) + N_2	ON	0.42	100	Quick gas of interest measurement N_2+NH_3+BB
200	1014.3	2	NH_3 (0.983%) + N_2	OFF	0.20	100	Quick gas of interest measurement N_2+NH_3

Interpretation - Signal Level:

The first two measurements revealed that the substitute filter (trash bag) reduced the signal level significantly, hence the decision was made to take measurements without any filter. At 900°C, the temperature of the black body light source, the amount of visible and UV light reaching the detector should not be sufficient to damage it.

The maximum reading at the detector at 2 cm^{-1} nominal resolution was around 0.4 V. A strong signal would give a reading of around 1 - 2 V at the detector. This did not bode well for the pursuit of higher resolution measurements, where the signal level would be lower due to the effects described in Section 4.1. Another factor to consider is the contrast between the Black Body ON/OFF measurements. A factor of 2, observed here, is sufficient for measurements to be possible. Ideally a factor of 3 or 4 would be desired.

Interpretation - NH_3 absorption:

Measurements 3 - 6 did not reveal any NH_3 absorption in the region of interest (see Figure 7.1) so the concentration was increased for measurements 7 and 8. Unfortunately no NH_3 absorption in the region of interest was observed in these measurements either (see Figure 7.2). The decision was made to raise the temperature for the next day's experiments to increase the strength of the NH_3 absorption features. This would also increase the thermal emission from the cell which could impact the contrast between Black Body ON/OFF measurements.

19-04-2016 (see Table 7.3)

Table 7.3: 19-04-2016 Measurement log: T is the temperature, P is the pressure, Res. is the nominal resolution, Acq. is the number of acquisitions (scans), BB indicates whether the Black Body source is ON or OFF and Signal is the reading at the detector.

T °C	P mbar	Res. cm^{-1}	Gas	BB (ON/OFF)	Acq.	Signal V	Notes
500	1027.0	2	N_2 purge only	ON	0.4	200	Reference measurement N_2+BB
500	1027.0	2	N_2 purge only	OFF	0.2	200	Reference measurement N_2
500	1027.0	2	NH_3 (0.983%) + N_2	ON	0.4	200	Gas of interest measurement N_2+NH_3+BB
500	1027.0	2	NH_3 (0.983%) + N_2	OFF	0.2	200	Gas of interest measurement N_2+NH_3

Interpretation - NH_3 absorption:

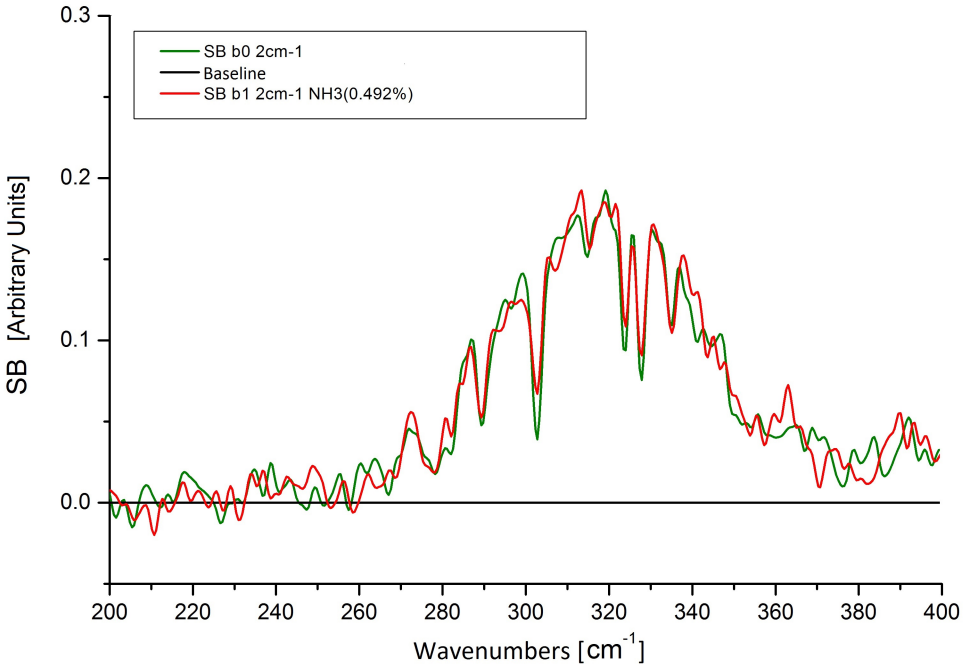

Figure 7.1: Single beam (SB) spectrum at 200 °C and 2 cm^{-1} nominal resolution of N_2 purge, b0, versus NH_3 (0.492 %), b1. Features due to b1 should be deeper than b0 if NH_3 absorption is detected. This is not observed.

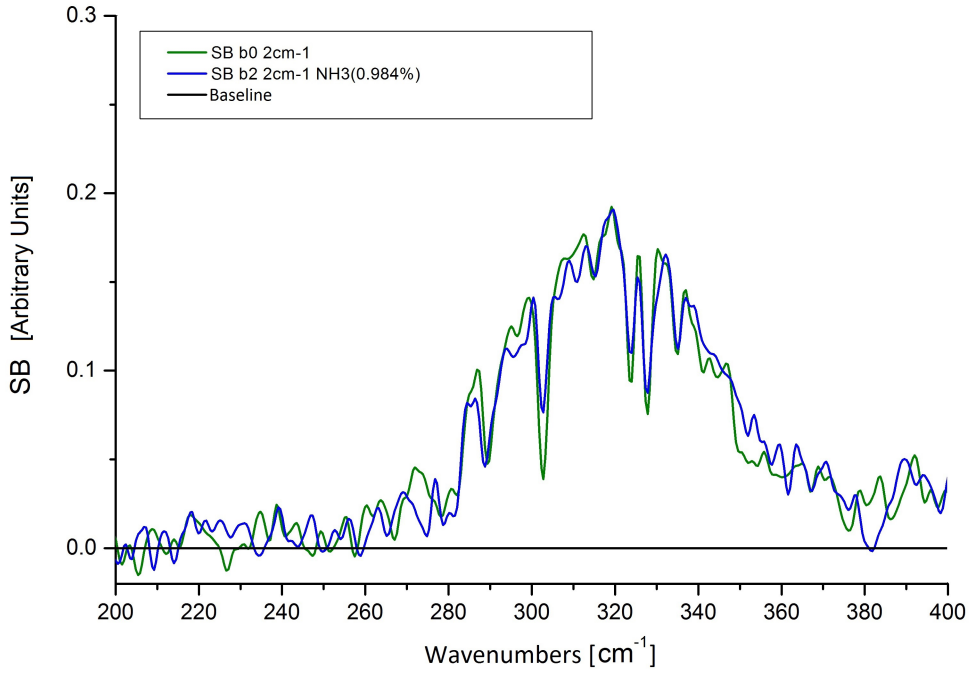

Figure 7.2: Single beam (SB) spectrum at 200 °C and 2 cm^{-1} nominal resolution of N_2 purge, b0, versus NH_3 (0.983 %), b2. Features due to b2 should be deeper than b0 if NH_3 absorption is detected. This is not observed.

As shown in Figure 7.3 absorption features are clearly observed in the region 280 - 350 cm^{-1}. To assess the quality of the measurements an absorbance spectrum was computed and is shown in Figure 7.4. A rough synthetic spectrum was generated to demonstrate that features in the region 280 - 350 cm^{-1} are due to NH_3 absorption. The signal level on the detector outside this region is very low, as indicated by the single beam spectra, which implies that reliable measurements will be contained within 280 - 350 cm^{-1}. The decision was made to perform higher resolution 0.25 cm^{-1} measurements at 500 °C in an attempt to resolve rotational structure which would be required for a detailed analysis.

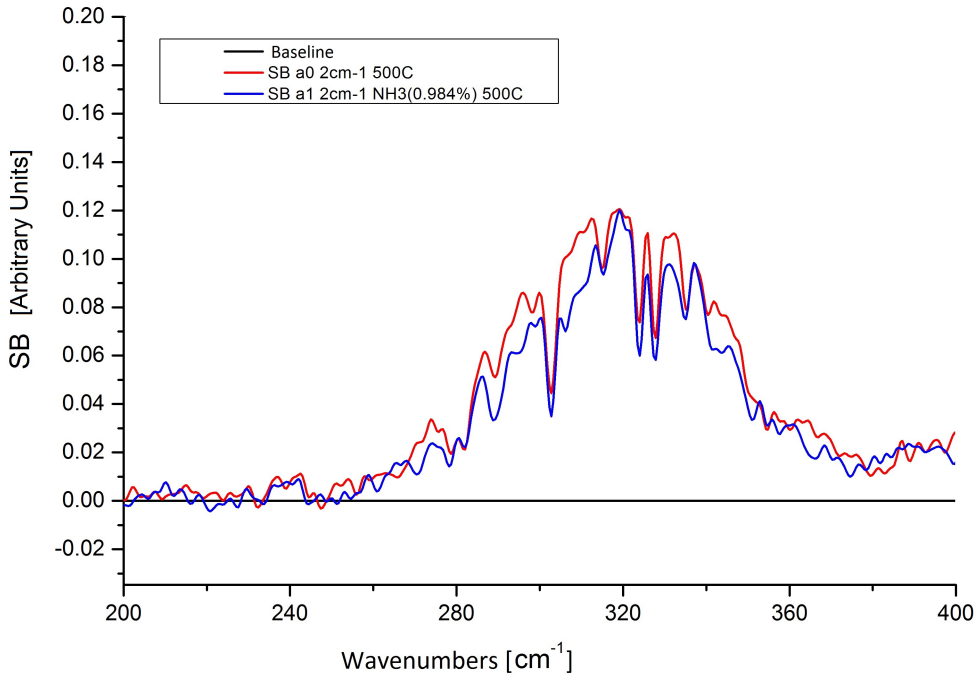

Figure 7.3: Single beam (SB) spectrum at 500 °C and 2 cm^{-1} nominal resolution of N_2 purge, a0, versus NH_3 (0.983 %), a1. Absorption features can be clearly seen between 280 and 320 cm^{-1}.

20-04-2016 (see Table 7.4)

Interpretation - NH_3 absorption:

The signal to noise level for the high resolution 0.25 cm^{-1} measurements was poor after 1000 acquisitions per spectra ($\approx$ 8 hours in total) as shown in Figure 7.5. The decision was made not to pursue more high resolution measurements as it is anticipated that the quantity of new information that could be derived from a detailed analysis of the

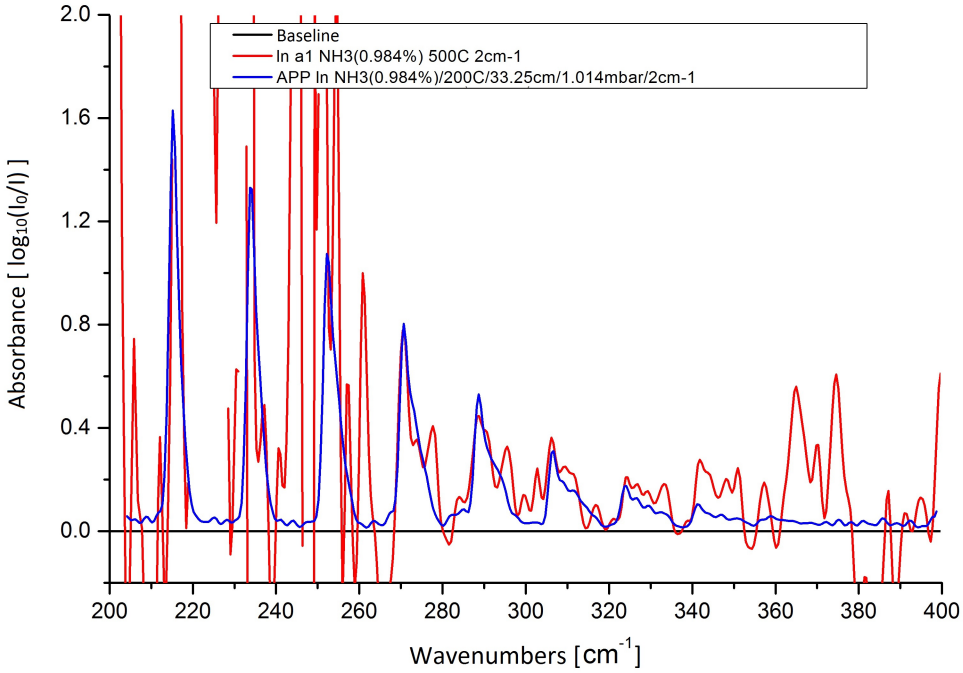

Figure 7.4: Absorbance spectrum at 500 °C and 2 cm^{-1} nominal resolution of NH_3 (5.5 %), a1, calculated from the single beam spectra in Figure 7.3. A rough synthetic spectrum, APP, is over-plotted to demonstrate that features between 280 and 350 cm^{-1} are due to NH_3 absorption.

Table 7.4: 20-04-2016 Measurement log: T is the temperature, P is the pressure, Res. is the nominal resolution, Acq. is the number of acquisitions (scans), BB indicates whether the Black Body source is ON or OFF and Signal is the reading at the detector.

T °C	P mbar	Res. cm^{-1}	Gas	BB (ON/OFF)	Acq.	Signal V	Notes
500	1027.0	0.25	N_2 purge only	ON	0.2	1000	Reference measurement N_2+BB
500	1027.0	0.25	N_2 purge only	OFF	0.1	1000	Reference measurement N_2
500	1027.0	0.25	NH_3 (5.5%) + N_2	ON	0.2	1000	Gas of interest measurement N_2+NH_3+BB
500	1027.0	0.25	NH_3 (5.5%) + N_2	OFF	0.1	1000	Gas of interest measurement N_2+NH_3

region 280 - 350 cm^{-1} would not justify the cost of time and resources. However the 2 cm^{-1} measurements can still be used for comparison in this work.

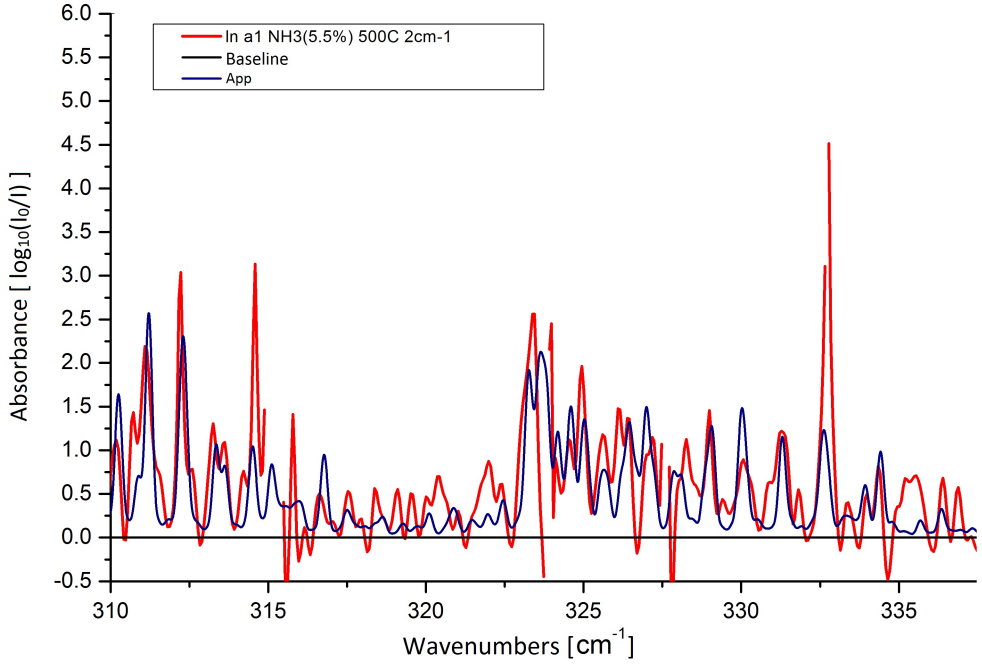

Figure 7.5: Absorbance spectrum at 500 °C and 0.25 cm^{-1} nominal resolution of NH_3 (0.983 %), a1, calculated from the single beam spectra measured on 20-04-2016. A rough synthetic spectrum, APP, is over-plotted in an attempt to identify features due to NH_3 absorption.

7.2 Theoretical Models

The sources of molecular data used to generate model transmittance or absorbance spectra in this work are summarised in Table 7.5. The synthetic spectra are calculated according to the method described in Section 4.2 for the experimental conditions detailed in Table 7.1. When generating cross sections (see Section 3.3) a Voigt line shape is assumed. The Doppler half width is calculated according to Eq. 3.32 and Lorentz half widths were estimated from the experimental spectra and with reference to measured widths compiled in the HITRAN database.

Li et al. (2013a,b) computed line lists for two isotopes of HCl using program LEVEL, a refined PEC and a semi-empirical DMC. They employed potential energy functions determined by Coxon & Hajigeorgiou (2015) in a direct potential fit to all available spectroscopic data to produce the refined PEC. The semi-empirical DMC was newly derived for their study. The line lists cover a spectral range of 0 - 35,000 cm^{-1} and include states up to $v = 17$ and $J = 40$.

Table 7.5: Overview of the molecular data used to simulate experimental spectra in this work.

Molecule	Line List	Partition Function	Cross sections generated by
HCl	Li et al. (2013a,b)	Fischer et al. (2003)	This work
H_2CO	AYTY Al-Refaie et al. (2015)	Al-Refaie et al. (2015)	Ahmed Al-Refaie
NH_3	BYTe Yurchenko et al. (2011a)	Sousa-Silva et al. (2014)	This work
CH_4	YT10to10 Yurchenko & Tennyson (2014)	Yurchenko & Tennyson (2014)	This work

The BYTe variational line list covers the spectral range 0 - 12,000 cm^{-1} and is expected to be fairly accurate for all temperatures up to 1500 K. It comprises of 1,138,323,251 transitions constructed from 1,373,897 energy levels lying below 18,000 cm^{-1}. It was computed using the NH3-2010 potential energy surface (PES) (Yurchenko et al. (2011b)), the TROVE ro-vibrational computer program (Yurchenko et al. (2007)) and a *ab initio* dipole moment surface (DMS) (Yurchenko et al. (2009)).

The variational line list for CH_4, YT10to10, contains 9.8 billion transitions between 0 - 12,000 cm^{-1} and should be complete for all temperatures up to 1500 K. The line list includes all transition to upper states with energies below 18,000 cm^{-1} and rotational excitation up to $J = 39$. It was computed using the TROVE ro-vibrational computer program (Yurchenko et al. (2007)), an *ab initio* DMS (Yurchenko et al. (2009)) and a new 'spectroscopic' PES determined by fitting an *ab initio* potential energy surface from Yurchenko et al. (2009) to experimental energies with $J = 0$, 1, 2, 3, 4.

AYTY, the computed line list for H_2CO, contains around 10.3 billion transitions for wavenumbers below 10,000 cm^{-1} and rotational excitations up to $J = 70$. The line list is applicable for temperatures up to 1500 K. The calculation employed the TROVE ro-vibrational computer program (Yurchenko et al. (2007)), an empirical PES from Yachmenev et al. (2011) and a newly computed *ab initio* DMS.

7.3 Comparisons

7.3.1 HCl

The 500 °C comparison for HCl is shown in Figure 7.6. As can been seen the agreement is excellent. All experimental line positions are reproduced within 0.01 cm^{-1} and experimental intensities are reproduced within 10 %. As an additional test the completeness of the line lists was assessed by summing the calculated energy levels to generate partition function values for a range of temperatures. The partition function

is at least 95% converged at 1500 K (≈ 1227 °C) and much better than this at lower temperatures. Therefore the line lists should be suitable for temperatures up to at least 1500 K.

7.3.2 H_2CO

Before the comparison is made it should be noted that the H_2CO measurements also contain features due to by-products of thermal decomposition, namely H_2O and CO. Figure 7.7 gives an overview of the experimental measurements, a CO band and H_2O features can be clearly identified around 2200 cm^{-1} and 3700 cm^{-1} respectively.

Figure 7.8 and Figure 7.9 illustrate the comparisons for H_2CO at 500 °C. Taking into account the presence of impurities, reproduction of line positions and overall band structure is excellent. The maximum shift in central position of spectral features is around 0.2 cm^{-1}. Overall the experimental intensities are reproduced within 10% with the exception of a few isolated features. These inconsistencies may be due to non-linear experimental effects that result in an under- or over-estimate of the molecular absorbance if the Lambert-Beer Law is assumed, rather than problems with the calculated intensities. Indeed comparisons with room temperature spectra presented in Al-Refaie et al. (2015) show very good intensity agreement.

7.3.3 NH_3

A comparison with the measurements made as part of this work is presented in Figure 7.10. Taking the experimental noise into account, the model provides a good description of the experimental spectrum.

Experimental versus theoretical spectra for the regions 500 - 2100, 2100 - 5500, 7400 - 8600 and 9000 - 10,000 cm^{-1}, are illustrated in Figure 7.11, Figure 7.12, Figure 7.13 and Figure 7.14 respectively. Overall there is good agreement. However, taking a closer look reveals shifts in line position that increase with wavenumber and problems with the reproduction of experimental intensities. The maximum shift in line position and the comparison with experimental intensities is summarised in Table 7.6.

Work towards a new, more accurate, hot NH_3 line list is currently being carried out as part of the ExoMol Project (Tennyson & Yurchenko (2012); Tennyson et al. (2016)).

7.3.4 CH_4

The CH_4 measurements cover four regions of CH_4 absorptions, 1000 - 2000, 2700 - 3300, 3900 - 4600 and 5800 - 6300 cm^{-1}. Comparisons for these four regions, at physical conditions that maximise the signal to noise without saturating spectral features in those regions, are presented in Figure 7.15, Figure 7.16, Figure 7.17 and Figure 7.18. For all regions the maximum shift in line position is less than 0.5 cm^{-1} and the experimental intensities are reproduced within 10 - 20 %.

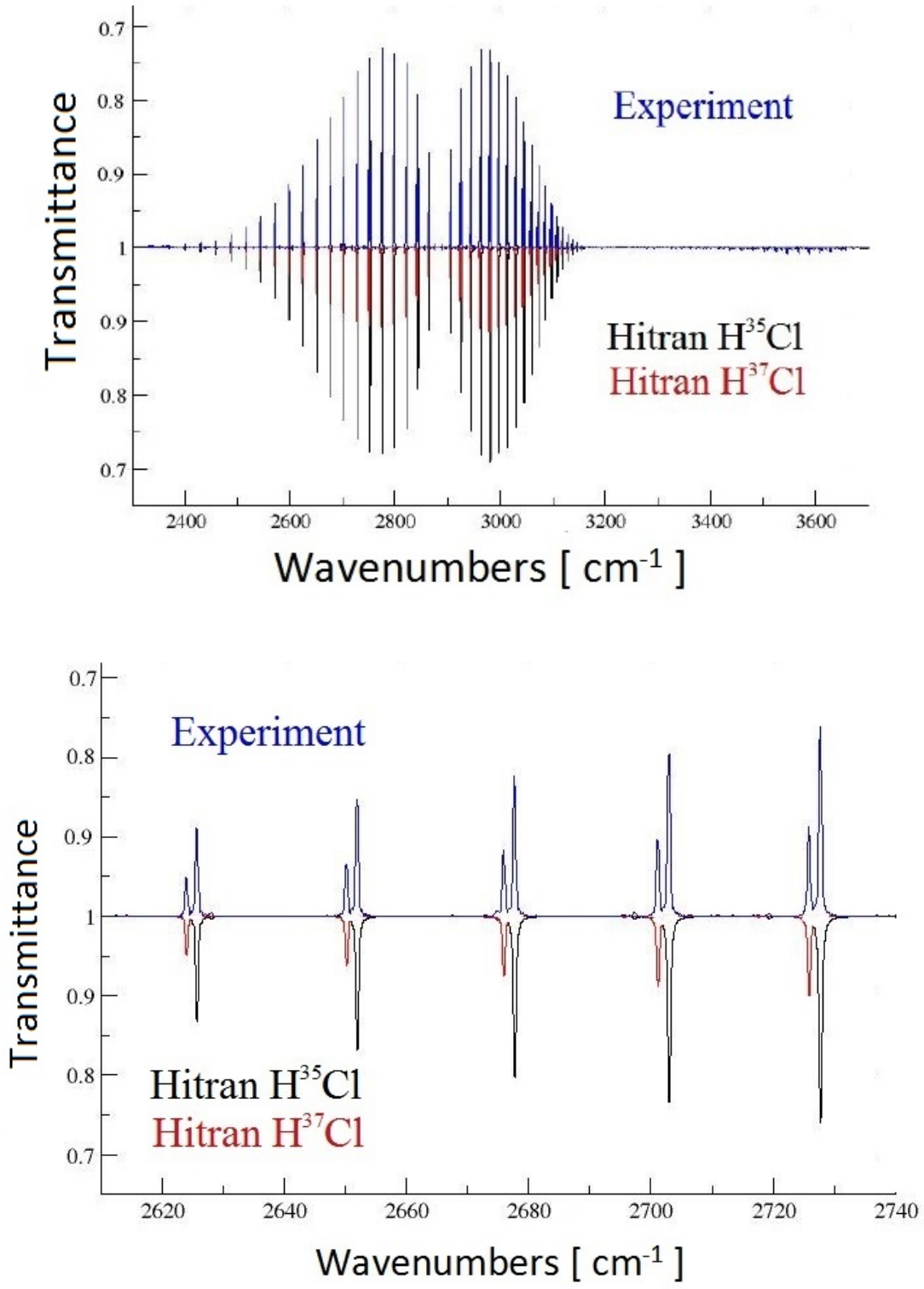

Figure 7.6: Transmittance spectra of HCl at 500 °C ($\sim$ 773 K) and 0.5 cm^{-1} nominal resolution: Li et al. (2013a,b) versus Experiment.

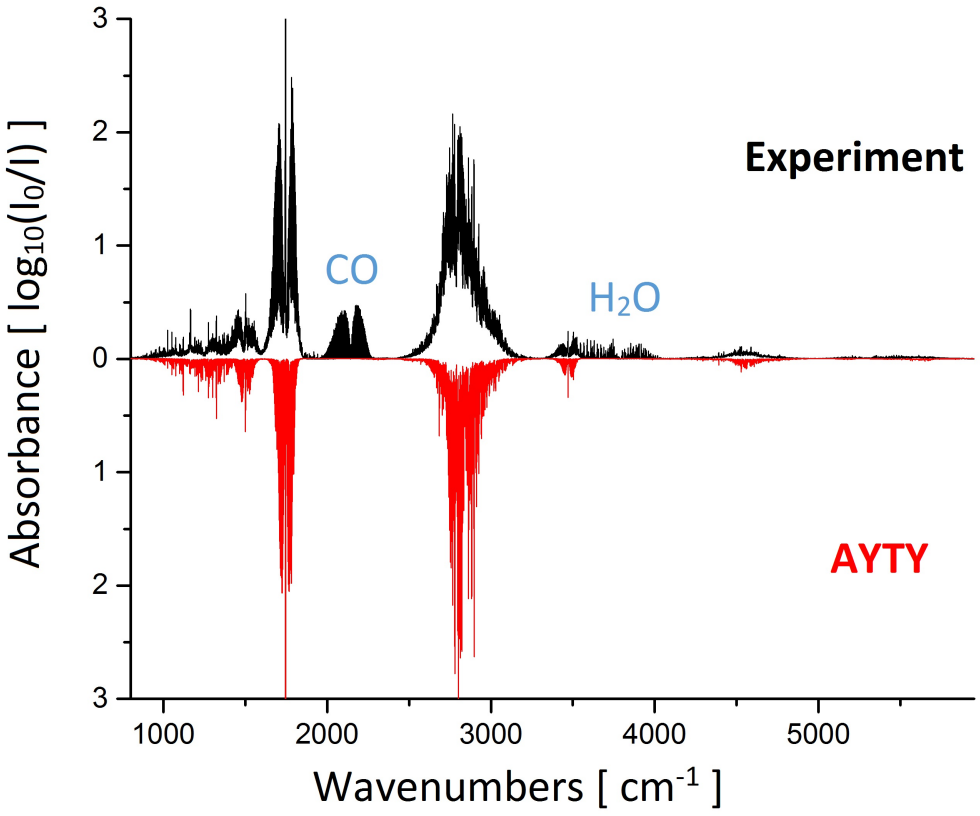

Figure 7.7: Overview of H_2CO spectrum at 500 °C ($\sim$ 773 K) and 0.25 cm^{-1} nominal resolution: AYTY versus Experiment.

Table 7.6: Summary of maximum shifts in line position $\Delta\tilde{v}$ and intensity comparison $\Delta I/I$ for BYTe versus experiment.

Region cm^{-1}	$\Delta\tilde{v}$ cm^{-1}	$\Delta I/I$ %
500 - 2100	0.5	10 - 30
2100 - 5500	2	10 - 30
7400 - 8600	3	20 - 55
9000 - 10,000	6	20 - 55

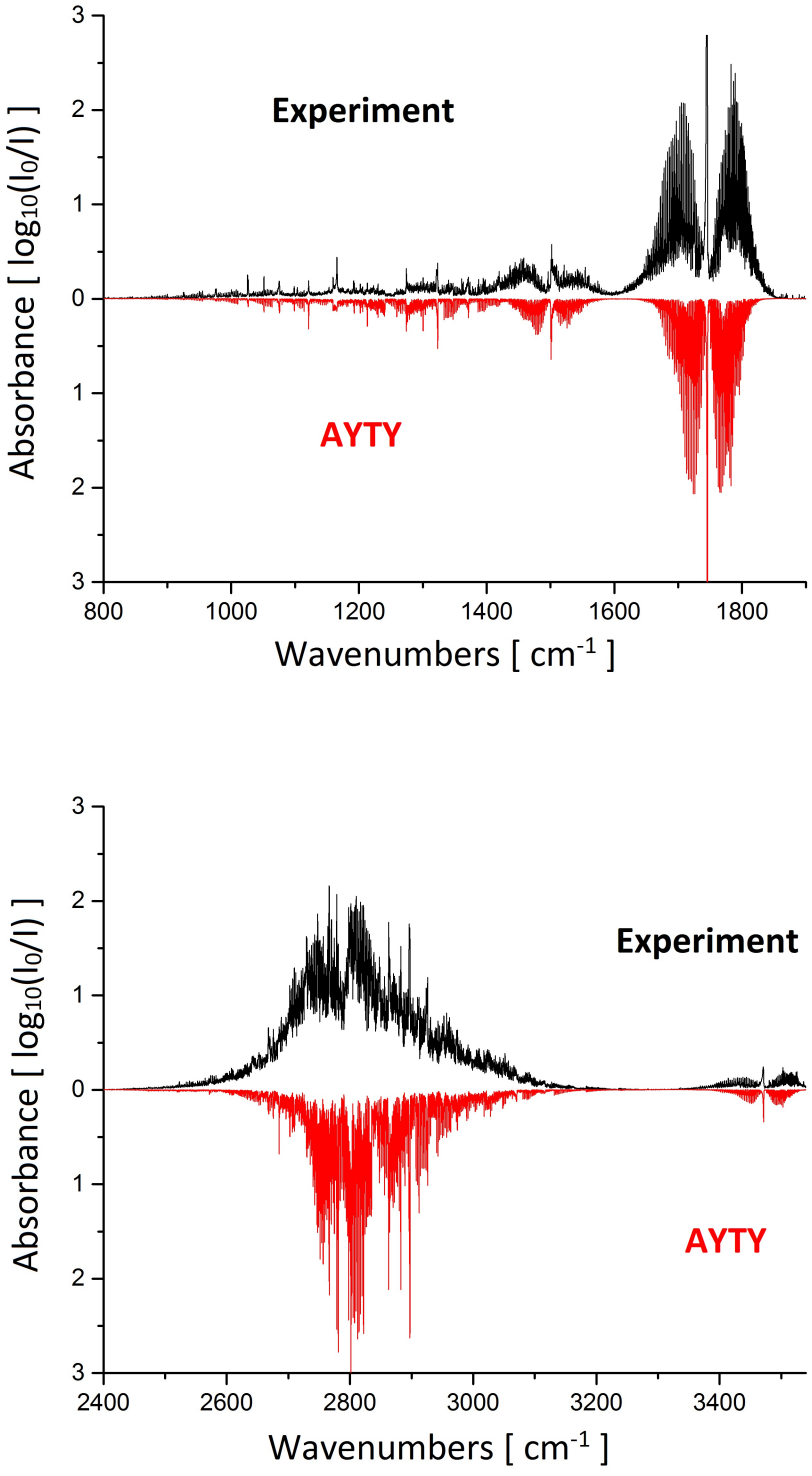

Figure 7.8: Absorbance spectra of H_2CO at 500 °C ($\sim$ 773 K) and 0.25 cm^{-1} nominal resolution in different regions: AYTY versus Experiment.

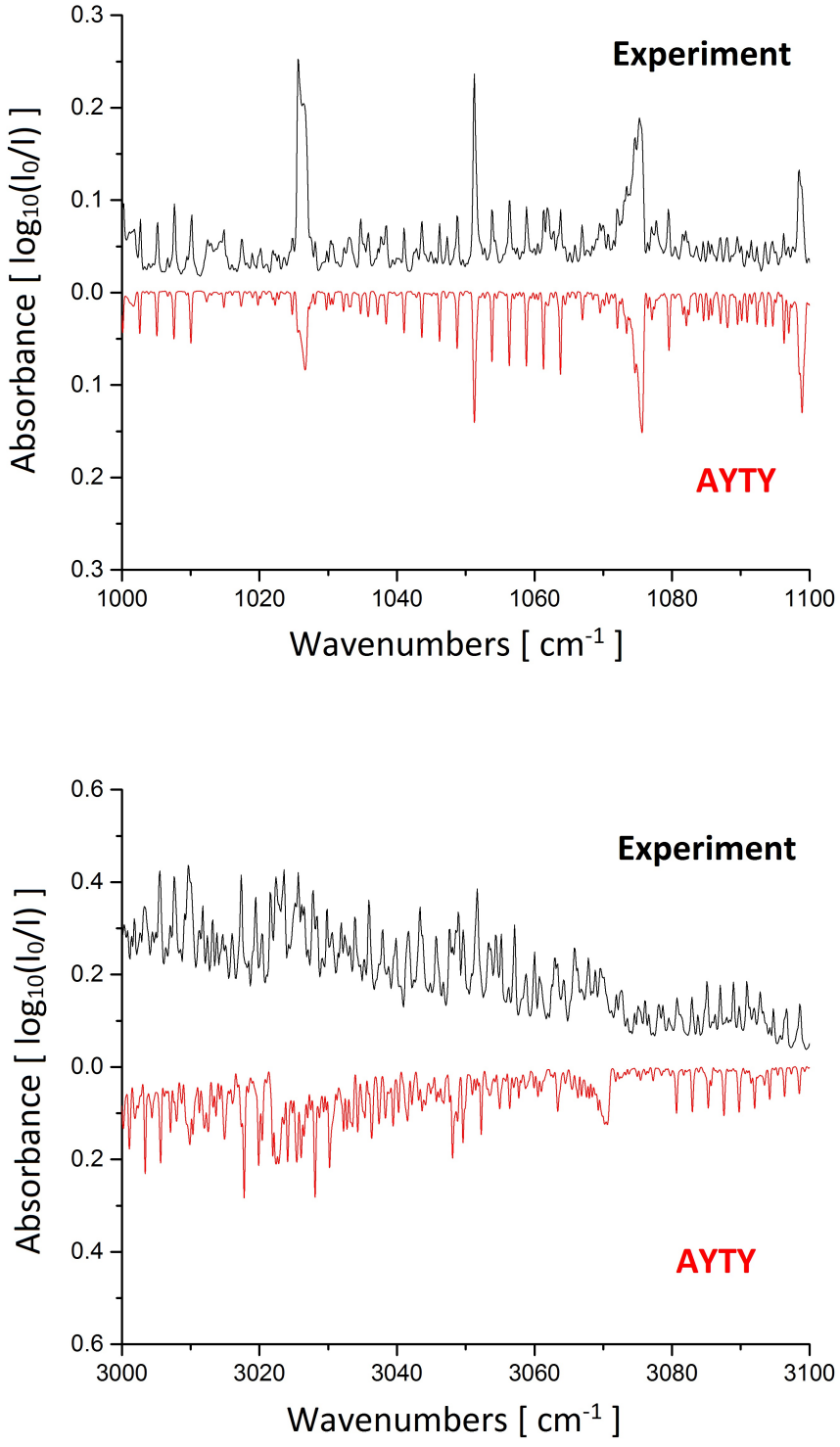

Figure 7.9: Zoomed absorbance spectra of H_2CO at 500 °C ($\sim$ 773 K) and 0.25 cm^{-1} nominal resolution in different regions: AYTY versus Experiment.

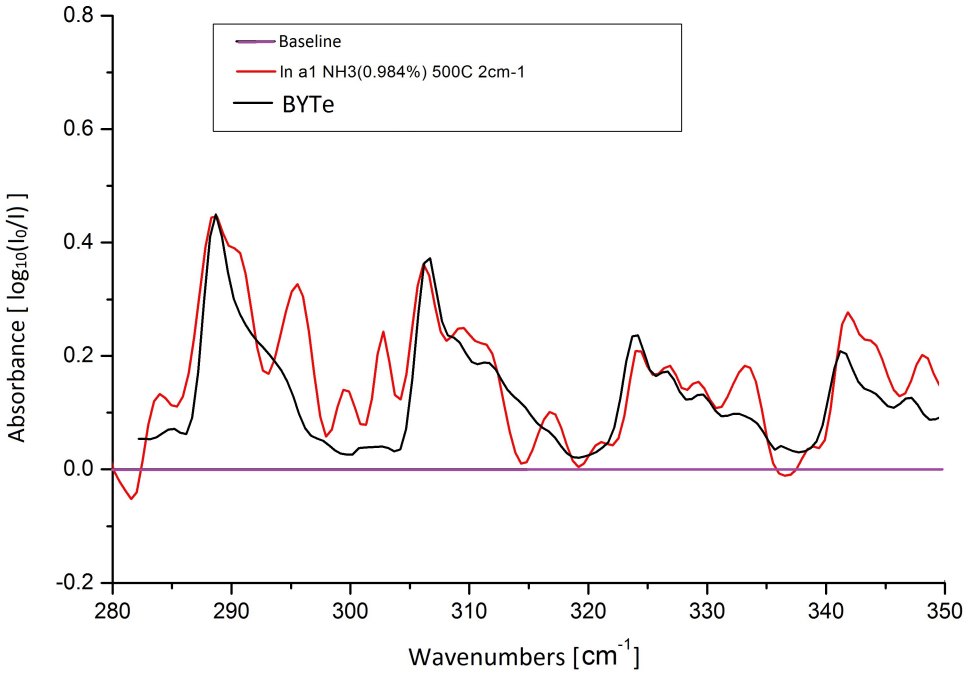

Figure 7.10: Absorbance spectra of NH_3 at 500 °C ($\sim$ 773 K) and 2 cm^{-1} nominal resolution in the region 200 - 400 cm^{-1}: BYTe versus Experiment.

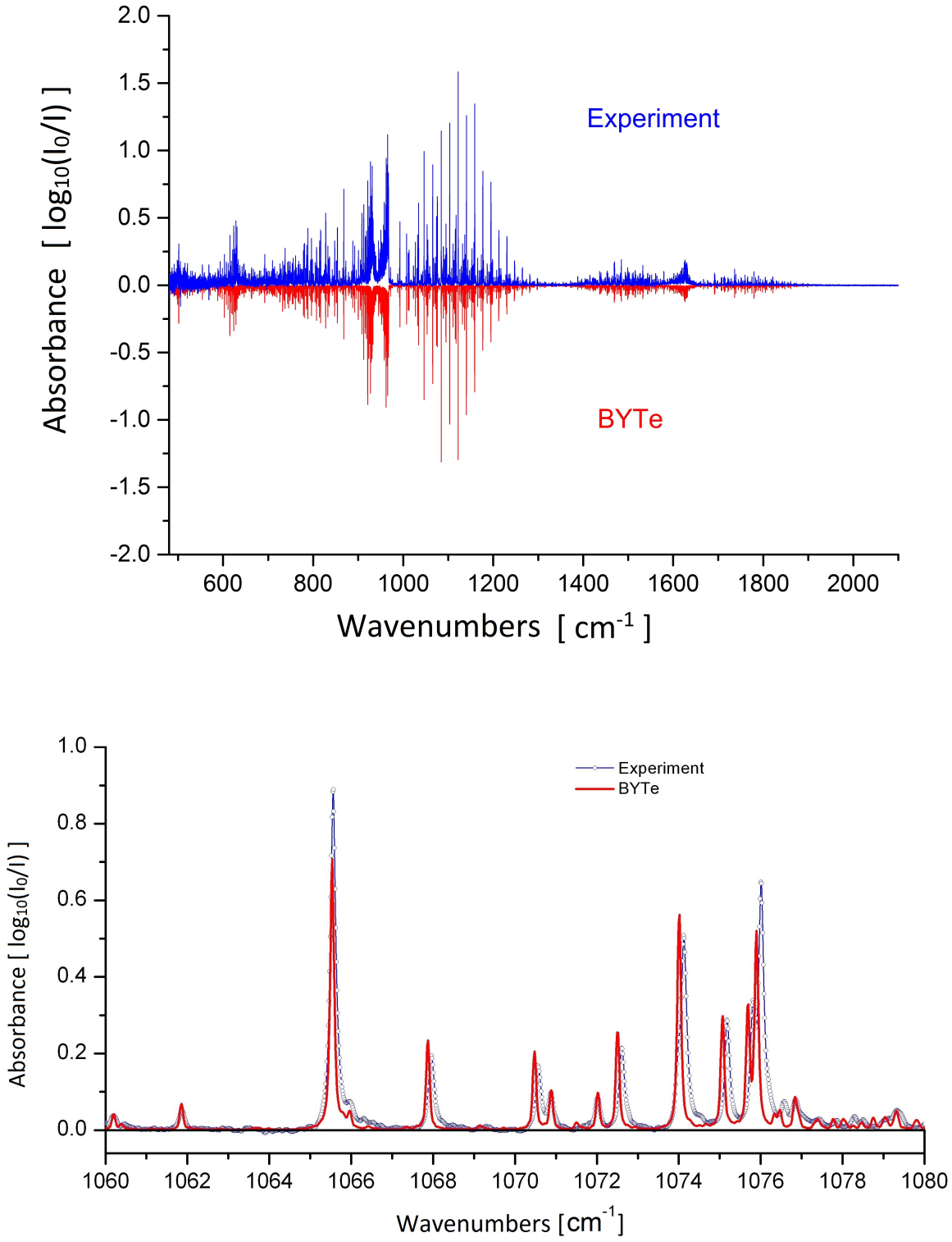

Figure 7.11: Absorbance spectra of NH_3 at 500 °C ($\sim$ 773 K) and 0.09 cm^{-1} nominal resolution in the region 500 - 2100 cm^{-1}(upper) and zoomed (lower): BYTe versus Experiment.

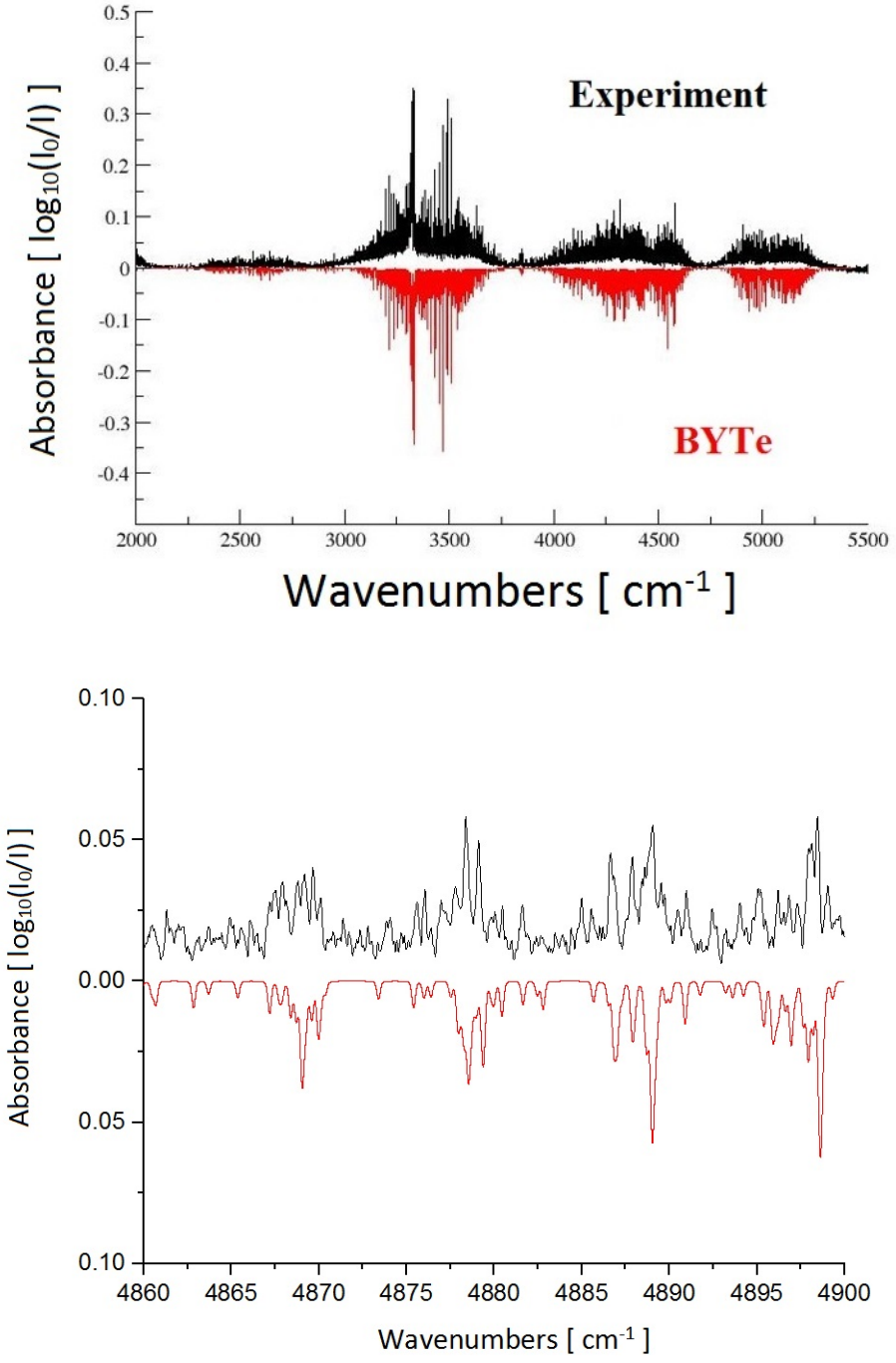

Figure 7.12: Absorbance spectra of NH_3 at 1027 °C ($\sim$ 1300 K) and 0.09 cm^{-1} nominal resolution in the region 2100 - 5500 cm^{-1}(upper) and zoomed (lower): BYTe versus Experiment.

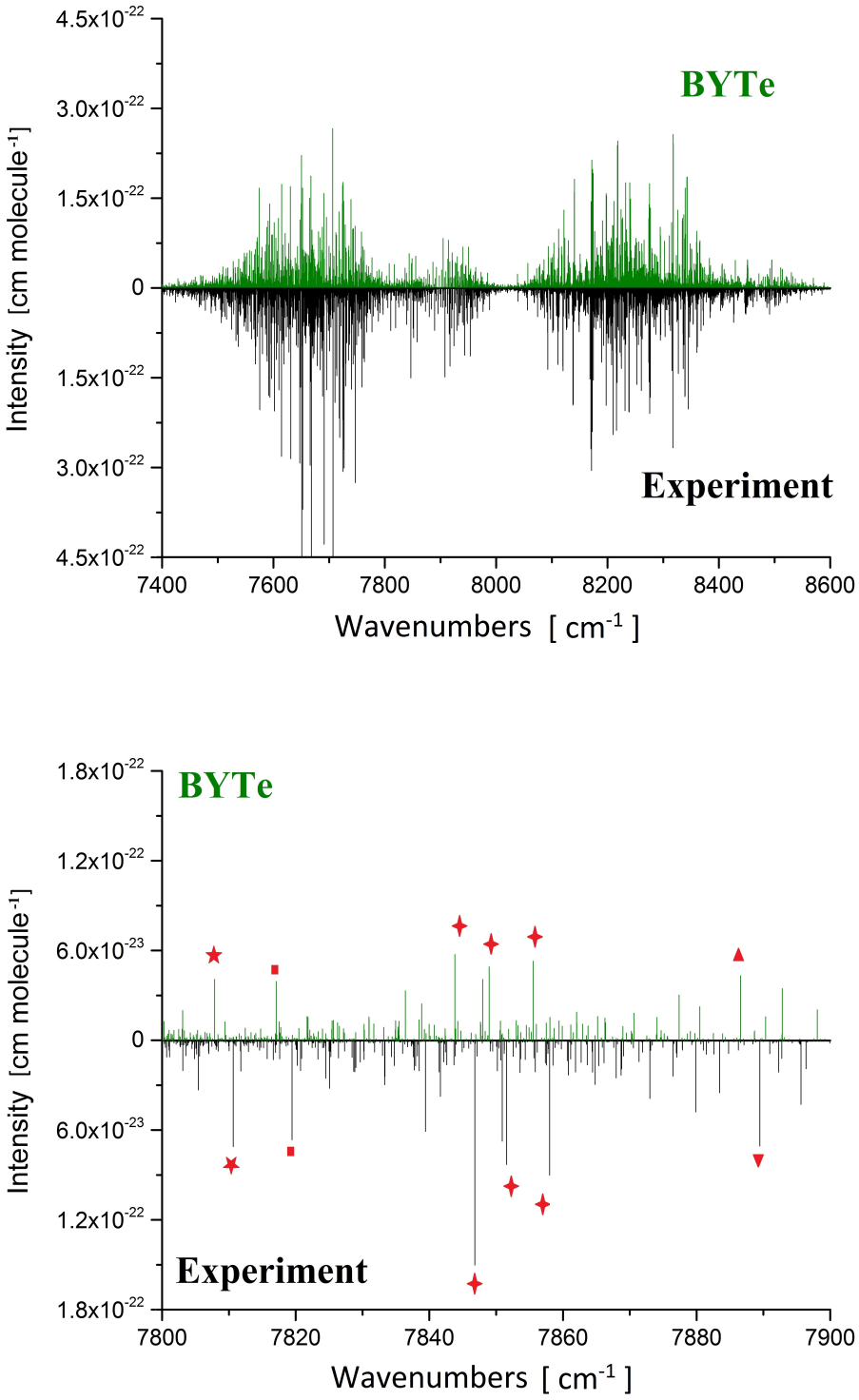

Figure 7.13: Stick spectra of NH_3 at 25 °C ($\sim$ 296 K) and 0.01 cm^{-1} nominal resolution in the region 7400 - 8600 cm^{-1}(upper) and zoomed (lower): BYTe versus Experiment.

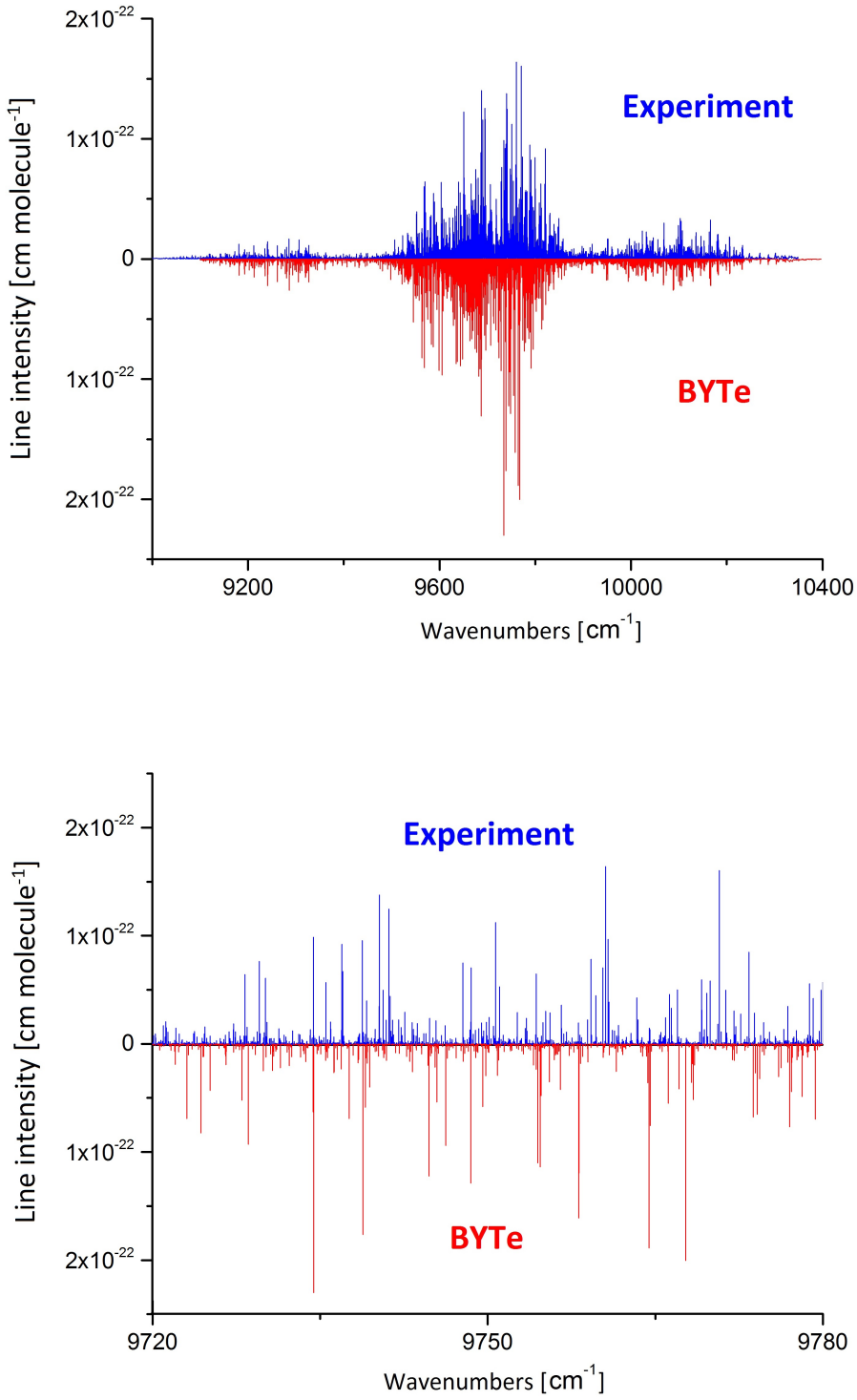

Figure 7.14: Stick spectra of NH_3 at 25 °C ($\sim$ 296 K) and 0.01 cm^{-1} nominal resolution in the region 9000 - 10000 cm^{-1}(upper) and zoomed (lower): BYTe versus Experiment.

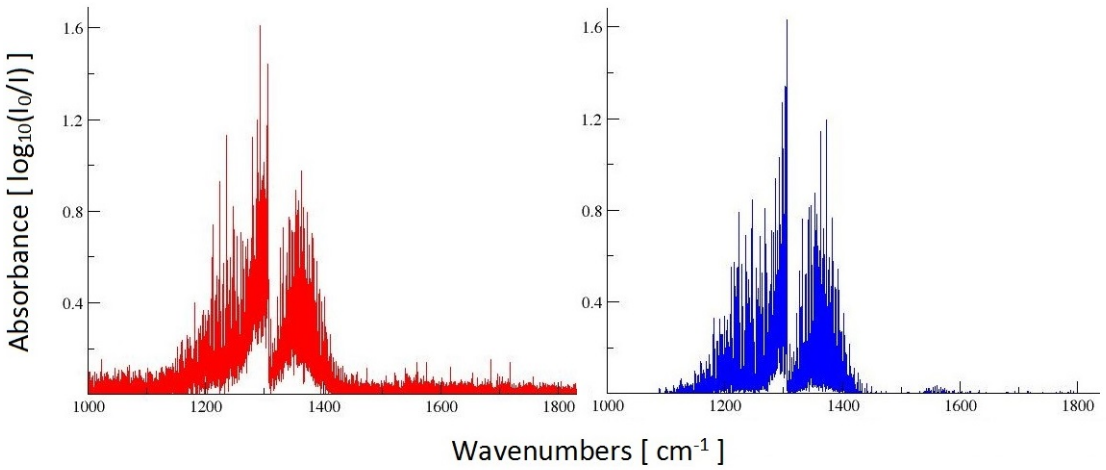

Figure 7.15: Absorbance spectra of CH_4 at 900 °C ($\sim$ 1173 K) and 0.09 cm^{-1} nominal resolution: YT10to10 versus Experiment.

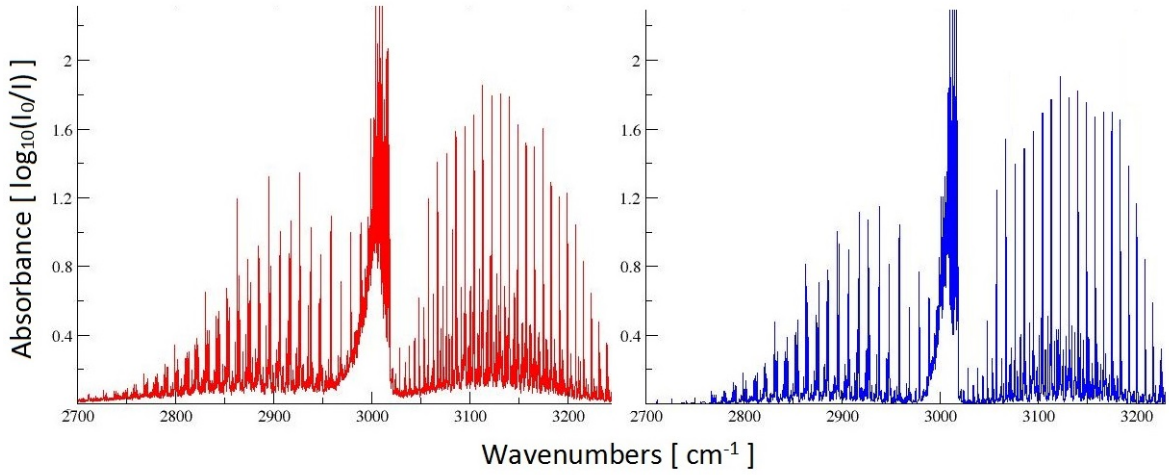

Figure 7.16: Absorbance spectra of CH_4 at 900 °C ($\sim$ 1173 K) and 0.09 cm^{-1} nominal resolution: YT10to10 versus Experiment.

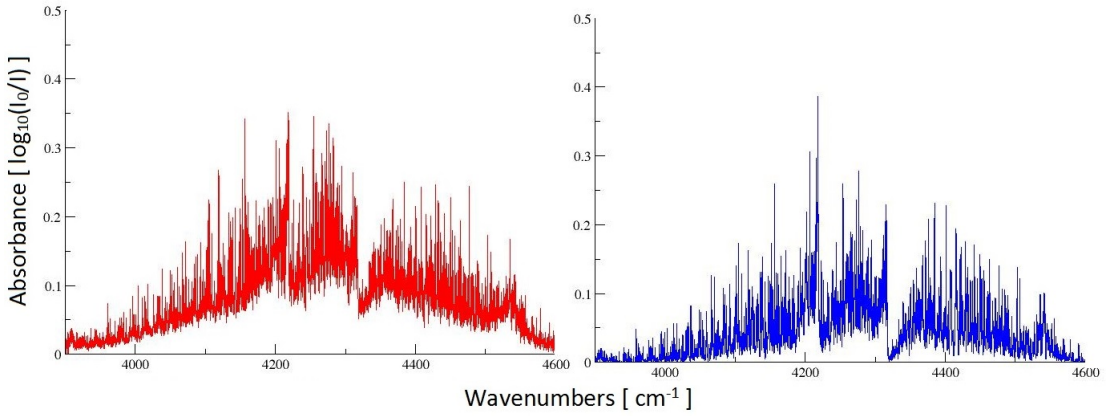

Figure 7.17: Absorbance spectra of CH_4 at 900 °C ($\sim$ 1173 K) and 0.09 cm^{-1} nominal resolution: YT10to10 versus Experiment.

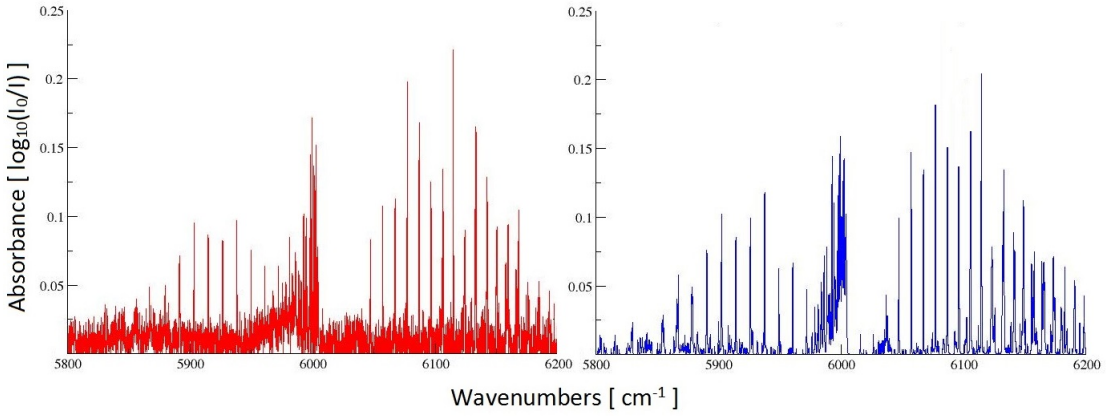

Figure 7.18: Absorbance spectra of CH_4 at 900 °C ($\sim$ 1173 K) and 0.09 cm^{-1} nominal resolution: YT10to10 versus Experiment.

7.4 Summary of Results

7.4.1 $HCl/H_2CO/CH_4$

This work has demonstrated that the current hot line lists for HCl, H_2CO and CH_4 due to Li et al. (2013a,b), Al-Refaie et al. (2015) and Yurchenko & Tennyson (2014) are suitable for use in industrial spectral studies. The line lists reproduce experimental line positions to sub-wavenumber accuracy and experimental line intensities within 10 - 20% overall.

7.4.2 NH_3

This work has shown that the accuracy of the current hot line list for NH_3 decreases with wavenumber for both line position and intensity. Work towards a new, more accurate, hot NH_3 line list is currently being carried out as part of the ExoMol Project (Tennyson & Yurchenko (2012); Tennyson et al. (2016)).

Chapter 8

Analysing Fourier Transform Infrared Spectra of Ammonia

The spectrum of NH_3 has many uses in both industry and astronomy, as discussed in Chapters 1 and 2. The applications cover a wide spectral range and include terahertz radiation, which is important for microwave and millimetre astronomy (see for example Mittleman (2013)) and infra-red radiation, which is used for *in situ* measurement of gas temperature and composition in smoke stacks (see for example van Ham et al. (1993) or Fateev (2015)).

A line list covering the spectral range 0 - 12,000 cm^{-1}, terahertz and infra-red, due to Yurchenko et al. (2011a) is currently available from ExoMol although it is known to have some problems, particularly at higher wavenumbers (see Chapter 7).

Work towards a new line list covering the spectral range 0 - 15,000 cm^{-1}, terahertz, infra-red and visible, is currently being carried out as part of the ExoMol project (Tennyson & Yurchenko (2012); Tennyson et al. (2016)). Part of the ExoMol methodology, described in Chapter 3, is the refinement of the potential energy surface to produce more accurate line positions by fitting to experimental frequencies. Therefore the new line list will benefit from new experimental line lists and assignments particularly for poorly characterised regions and hot bands.

The aim of this work was to analyse experimental measurements in four spectral regions, summarised in Table 8.1, by comparison to BYTe and experimental energies determined using the MARVEL procedure (Furtenbacher et al. (2007); Al Derzi et al. (2015)). This involves assigning quantum labels (see Section 3.4.1) to observed lines and using them to derive experimental energies. The projects can be separated into two categories, 'hot' dealing with high temperature measurements in previously analysed regions that include new transitions to highly excited states and 'cold' dealing with room temperature measurements in previously unanalysed regions significantly extending the range of experimental known vibrational and rotational energy levels. The 'hot' projects are aimed towards industrial spectral studies as Fateev (2015) has demonstrated that features in these regions can be used to extract NH_3 concentration from *in situ* measurements. The 'cold' projects provide the first results for two poorly characterised regions of the NH_3 spectrum. The regions are of present interest as there are peaks in NH_3 opacity in the spectra of cool stars at the corresponding

wavelengths (Canty et al. (2015)). Sections 8.1 and 8.2 describe and present results for the 'hot' projects in chronological order. Section 8.3 details and presents results for the first 'cold' project, while Section 8.4 discusses preliminary results for the second 'cold' project.

Table 8.1: Spectral regions of the NH_3 spectrum analysed in this work.

Region cm^{-1}	Temperature °C	Source of Measurements	Source of Line/Peak List
500 - 2100	$\leq$ 1027	Dr Alexander Fateev[a]	This work
2100 - 5500	$\leq$ 1027	Dr Alexander Fateev[a]	This work
7400 - 8640	21.5	Kitt Peak Archive[b]	Prof Alain Campargue[a]
9000 - 10,400	21.5	Kitt Peak Archive[b]	Prof Alain Campargue[a]

[a] Private communication;
[b] http://nsokp.nso.edu/archives.

8.1 500 - 2100 cm^{-1}

The first region to be analysed was 500 - 2100 cm^{-1}. Previous assignments for this region can be found in the HITRAN database (Rothman et al. (2013)) and the high temperature study Zobov et al. (2011).

Zobov et al. (2011) analysed high temperature emission spectra recorded by Hargreaves et al. (2011) and presented assignments for strong lines whose upper levels belong to vibrational states with band origins up to 2100 cm^{-1}. The present work is complementary to these previous works, providing assignments for high resolution absorption spectra of NH_3 up to 1027 °C (1300 K) in the region 500 - 2100 cm^{-1}. A proportion of these line assignments are new, of which some lines are also present but unassigned in the emission spectra. The notable advantage of the absorption measurements is the absolute intensity scale, as emission intensities are notoriously difficult to calibrate (Hargreaves et al. (2011, 2012b); Nassar & Bernath (2003)).

Initially measurements for temperatures up to 500 °C (773 K) were provided by Dr Alexander Fateev. A preliminary analysis was performed using BYTe alone to generate assignments, as MARVEL energy levels were not yet available. This analysis largely reproduced previous work, demonstrating that the assignment procedure gave results that were consistent with other studies and indicating that measurements at higher temperature were required to generate a significant quantity of new assignments. The final analysis, which included absorption spectra measured at 1027 °C (1300 K), is described in the following sections.

8.1.1 The Assignment Procedure

Taking the interpreted accuracy of BYTe and the resolution of the measurements into account (see Chapter 7), experimental and theoretical peaks were measured and

coupled using python scripts to produce an initial assignment list. In cases where multiple BYTe lines corresponded to a single peak, the peak was assigned to the strongest line.

At this point in the analysis MARVEL energy levels (Al Derzi et al. (2015)) became available and were subsequently used to test the initial assignment list. Assignments associated with energy levels already determined by experiment may be verified by comparing to the line position generated by subtracting upper and lower state energies.

Comparison with MARVEL line positions led to the identification of several 'problem' BYTe state energies. These energies disagreed with the experimentally derived energies to the extent that their use generated false assignments. In these cases the first step of the assignment procedure was repeated with MARVEL line positions and BYTe intensities to generate intrinsically verified 'trivial' assignments.

Any assignments that could not be verified but where not disproved by the comparison to MARVEL frequencies were kept as proposed assignments. The reliability of these assignments is discussed in the next section.

A list of all verified and proposed assignments, the final assignment list, was then compared to previous studies, namely those catalogued in the HITRAN database (Rothman et al. (2013)) and Hargreaves et al's high-temperature study (Zobov et al. (2011)).

8.1.2 Assignments

Out of 4309 measured experimental peaks 1967 lines have been assigned. The remaining peaks either did not correspond to a BYTe line within the set wavenumber (0.5 cm^{-1}) and intensity (30 %) thresholds or corresponded to multiple BYTe lines with roughly equal contribution to the total intensity such that it could not be confidently assigned. The partially assigned 1027 °C (1300 K) peak list is available from http://www.sciencedirect.com/science/article/pii/S002240731500271X. An extract is presented in Table 8.2.

The comparison with previous studies, namely the high temperature study of Zobov et al. (2011) and studies compiled in the HITRAN database (Rothman et al. (2013)), is shown in Table 8.4. Of the 851 newly assigned lines, 482 were also present, but unassigned, in Zobov et al. (2011).

Only 525 of the proposed assignments have the potential to provide new energy level information as, by definition, the upper and lower states of the MARVEL verified assignments are known experimentally. Hence this makes these proposed assignments the most interesting. For proposed assignments with an experimentally known lower energy state, energies for the upper state were computed using MARVEL lower energies and the line position of the strongest assigned transition to that state. These are available from http://www.sciencedirect.com/science/article/pii/S002240731500271X. An extract is presented in Table 8.3.

Lines were assigned to a large number of different bands including bending hot bands up to $5v_2$. While being unexpected this is not entirely surprising, as a detailed analysis of hot (1000 - 1500 °C / 1273 - 1773 K) H_2O spectra (Polyansky et al. (1997a);

Table 8.2: Extract from the partially assigned 1027 °C experimental peak list for 500 - 2100 cm^{-1}. Freq. is the central frequency of the experimental peak, Int. is the peak intensity in units of absorbance. The upper state and lower state labels are the 13 quantum numbers recommended by Down et al. (2013) (defined in Chapter 3). For the symmetries Grot, Gvib and Gtot (where G = Γ): 1 = A_1', 2 = A_2', 3 = E′, 4 = A_1'', 5 = A_2'' and 6 = E″. Entries in the last column indicate if the assignment is MARVEL verified (MV), included in the HITRAN database (HIT) or newly assigned by comparison to BYTe (NL).

#Freq.	Int.	Upper State													Lower State												
#cm^{-1}	log10	v1	v2	v3	v4	L3	L4	L	J	K	i	Grot	Gvib	Gtot	v1	v2	v3	v4	L3	L4	L	J	K	i	Grot	Gvib	Gtot	
500.1069	0.0869																											
500.3479	0.0857																											
500.5287	0.0545	0	3	0	0	0	0	0	3	2	0	3	1	3	0	2	0	0	0	0	0	3	2	1	3	5	6	MV
500.8301	0.0266	0	3	0	1	0	1	1	7	7	0	6	3	5	0	2	0	1	0	1	1	7	7	1	6	6	2	NL
500.9807	0.0510	0	0	0	1	0	1	1	7	4	1	3	6	5	0	1	0	0	0	0	0	8	3	1	4	5	2	HIT
501.1916	0.0430																											
501.2820	0.0462																											
501.4026	0.0601	0	2	0	0	0	0	0	12	8	1	3	5	6	0	2	0	0	0	0	0	11	8	0	3	1	3	NL
501.6135	0.2589	0	3	0	0	0	0	0	5	5	0	6	1	6	0	2	0	0	0	0	0	5	5	1	6	5	3	MV
501.8847	0.1593	0	3	0	0	0	0	0	1	1	0	6	1	6	0	2	0	0	0	0	0	1	1	1	6	5	3	MV
502.0956	0.1724																											
502.4271	0.1212	0	3	0	0	0	0	0	10	10	0	3	1	3	0	2	0	0	0	0	0	10	10	1	3	5	6	MV
502.6380	0.0628																											
502.7887	0.1292	0	3	0	0	0	0	0	11	11	0	6	1	6	0	2	0	0	0	0	0	11	11	1	6	5	3	MV
502.9393	0.0590	0	0	0	1	0	1	1	16	16	1	3	6	6	0	1	0	0	0	0	0	16	15	1	4	5	2	MV

Zobov et al. (1999, 2005)) produced similar results. Table 8.5 gives a summary of the observed bands including the number of lines assigned to each and, if the band was observed for the first time in this work, whether this number includes trivial assignments. For simplicity abbreviated vibrational labels ($v_1 v_2 v_3^{L_3} v_4^{L_4} i$) are used to identify bands in this table and only the highest value of the rotational quantum number J, assigned in this work for each band, is indicated. The full 26 quantum labels for each transition, 13 per vibration-rotation state as recommended by Down et al. (2013) (defined in Chapter 3), are given in the partially assigned peak list file.

The 1027 °C spectrum of certain previously observed bands, such as $2v_2$ and v_4^1, has some higher J transitions than previously reported. For these MARVEL energies were used to provide a guideline observed-calculated (obs. - calc.) difference to facilitate reliable line list (proposed) assignments beyond the known J values using the method of branches (Polyansky et al. (1997b)).

17 bands have been observed for the first time in this work, although some of the energy levels involved are experimentally known from measurements of other bands.

If many lines (> 10) were assigned to a new band, we were able to track obs. - calc. differences through the band. As these remain relatively stable we have confidence in our assignments. Furthermore if a subset of the assignments were trivial we were able to use the same technique as for previously observed bands to ensure our proposed assignments were sensible.

Line assignments in new bands for which only a few assignments could be made

Table 8.3: Extract from the file containing new derived experimental energy levels for 500 - 2100 cm^{-1}. Obs. is the experimentally derived energy (MARVEL lower energy + observed transition frequency) in cm^{-1}, Obs.-Calc. is the observed minus calculated (BYTe) energy difference in cm^{-1}. The given labels are the 13 quantum numbers recommended by Down et al. (2013) (defined in Chapter 3). For the symmetries Grot, Gvib and Gtot (where G = Γ): 1 = A_1', 2 = A_2', 3 = E′, 4 = A_1'', 5 = A_2'' and 6 = E″.

v1	v2	v3	v4	L3	L4	L	i	Gvib
0	2	0	0	0	0	0	0	1

J	K	Grot	Gtot	Obs.	Obs.-Calc.
9	5	6	6	2418.2968	0.10
10	5	6	6	2605.1391	0.07
12	11	6	6	2664.6221	0.21
15	14	3	3	3197.1329	0.25
18	17	6	6	3834.9822	0.25
19	17	6	6	4235.4715	0.31
17	10	3	3	4276.8671	0.28
18	10	3	3	4633.9065	0.34
17	4	3	3	4657.0740	0.33
17	2	3	3	4698.9488	0.31
17	1	6	6	4709.9507	0.34
21	18	2	2	4913.3960	0.40
21	16	3	3	5192.7277	0.38

are more tentative.

Table 8.4: Summary of NH_3 lines assigned in the region 500 - 2100 cm^{-1}

	Lines
Experimental	4309
HITRAN	1073
Zobov et al. (2011)	43
New trivial	326
New Line List	525
Total Assigned	1967

Table 8.5: Summary of observed bands in the region 500 - 2100 cm^{-1} in order of theoretical (BYTe) vibrational band centre (VBC = VBO' - VBO" where VBO = vibrational band origin) with abbreviated ($v_1 v_2 v_3^{L_3} v_4^{L_4} i$), vibrational labels and maximum upper and lower J rotational (J'_{max} and J''_{max} respectively) quantum number. N is the number of lines assigned to the band. If J_{max} in this work is higher than given in the literature, the previously known J_{max} is given in parentheses. iMV indicates a new band with trivial assignments. *VBO of 0^+ is set to 0.000000 cm^{-1} in line with the MARVEL study (Al Derzi et al. (2015)).

Band	**VBC**	**N**	**J′max**	**J″max**	**Note**
0^+ - 0^-	-0.793016*	1	28	27	
0^- - 0^+	0.793016	2	27	26	
$2v_2^+$ - $v_4^{1,-}$	254.80606	5	16	15	
$2v_2^-$ - $2v_2^+$	284.696502	14	19	18	
$(2v_2 + v_4^1)^-$ - $(2v_2 + v_4^1)^+$	313.043262	1	10	9	New Band
$(3v_2 + v_4^1)^-$ - $4v_2^-$	466.768801	1	9 (None)	8	New Band
$3v_2^+$ - $2v_2^-$	501.978729	58	23 (14)	23 (22)	
$(3v_2 + v_4^1)^+$ - $(2v_2 + v_4^1)^-$	504.649129	11	17 (None)	17	New Band
$3v_2^+$ - $3v_2^-$	511.366446	89	22 (13)	22 (14)	New Band iMV
$(3v_2 + v_4^1)^-$ - $(3v_2 + v_4^1)^+$	522.929054	13	16 (None)	16 (None)	New Band
$(3v_2 + v_4^1)^+$ - $4v_2^-$	544.263409	2	12 (None)	12 (7)	New Band
$4v_2^-$ - $(2v_2 + v_4^1)^-$	560.066366	4	10 (None)	10	New Band
$4v_2^+$ - $3v_2^-$	566.943220	72	21 (7)	21 (13)	New Band iMV

Continued on next page

Table 8.5 – continued from previous page

Band	VBC	N	J′max	J′max	Note
$4v_2^-$ - $4v_2^+$	599.680646	14	16 (None)	16 (7)	New Band
$(2v_2+v_4^1)^+$ - $(v_2+v_4^1)^-$	602.916749	34	17 (11)	17 (13)	
$(2v_2+v_4^1)^-$ - $3v_2^-$	606.552500	1	13	13	New Band
$2v_2^+$ - v_2^-	629.360589	120	24 (20)	24	
$5v_2^+$ - $4v_2^-$	633.065737	4	10 (None)	9 (7)	New Band
$v_4^{1,+}$ - v_2^-	658.157170	1	17	16	
$v_4^{1,-}$ - v_2^-	659.253867	50	21 (18)	20	
$5v_2^+$ - $(3v_2+v_4^1)^-$	688.482974	1	11 (None)	10 (None)	New Band
$2v_2^-$ - v_2^-	896.853859	2	16	15	
$(v_2+2v_4^0)^+$ - $2v_4^{0,-}$	898.073060	2	7	6	
$(v_2+v_4^1)^+$ - $v_4^{1,-}$	913.167342	68	19 (13)	18	
$(v_2+v_4^1)^+$ - $v_4^{1,+}$	914.264039	2	19 (13)	18	
$(2v_2+v_4^1)^-$ - $(v_2+v_4^1)^+$	915.960012	24	16	16 (13)	
$4v_2^+$ - $(v_2+v_4^1)^+$	922.721046	1	13 (7)	13	New Band
v_2^+ - 0^-	932.438362	208	24	23	
$(v_2+v_4^1)^+$ - $2v_2^+$	948.056868	14	18 (13)	18	
$2v_2^-$ - v_2^+	949.745375	158	23 (22)	23	
$(v_2+2v_4^2)^-$ - $2v_4^{2,+}$	952.951385	2	7	6	
$(v_2+v_4^1)^-$ - $v_4^{1,-}$	958.749640	2	14 (13)	13	
$(v_2+v_4^1)^-$ - $v_4^{1,+}$	959.846337	62	18 (13)	17	
v_2^- - 0^-	967.329878	2	15	14	
v_2^- - 0^+	968.122894	141	23	22	
$(v_2+v_3^1)^-$ - $v_3^{1,+}$	972.941917	4	8	8	
$(v_1+v_2)^-$ - v_1^+	983.959104	4	10	9	
$(v_2+v_3^1)^+$ - $v_3^{1,-}$	991.824695	2	9	8	
$3v_2^-$ - $v_4^{1,-}$	1267.97613	4	14	14	New Band iMV
$3v_2^-$ - $2v_2^+$	1301.041678	23	15 (13)	15	
$3v_2^+$ - v_2^-	1398.03582	32	18 (14)	18	
$(v_2+2v_4^0)^+$ - $(v_2+v_4^1)^+$	1575.075800	2	9 (8)	8	
$4v_2^+$ - $2v_2^-$	1580.288396	2	10 (7)	9	New Band iMV
$(v_2+2v_4^0)^-$ - $(v_2+v_4^1)^-$	1587.123794	1	6	6	
$2v_4^{0,+}$ - $v_4^{1,+}$	1589.719282	9	12	13	
$2v_4^{0,-}$ - $v_4^{1,-}$	1590.170082	6	12	13	
$(2v_2+v_4^1)^+$ - $2v_2^+$	1591.555915	7	19	18	New Band
$(v_2+2v_4^2)^+$ - $(v_2+v_4^1)^+$	1595.391899	9	17 (7)	16 (13)	
$2v_2^+$ - 0^-	1597.487235	23	18	18	
$(v_2+2v_4^2)^-$ - $(v_2+v_4^1)^-$	1607.009156	1	11 (8)	10	
$(v_2+v_4^1)^+$ - v_2^+	1608.105741	67	18 (13)	19	
$2v_4^{2,+}$ - $v_4^{1,+}$	1613.904108	20	14 (11)	15	

Continued on next page

Table 8.5 – continued from previous page

Band	VBC	N	J′max	J′max	Note
$2v_4^{2,-}$ - $v_4^{1,-}$	1614.198476	28	17 (13)	18	
$(v_2+v_4^1)^-$ - v_2^-	1617.999755	89	19 (13)	20	
$2v_4^{0,-}$ - $2v_2^+$	1619.266592	1	8	9	
$(2v_2+v_4^1)^-$ - $2v_2^-$	1619.902676	5	11	12	New Band
$v_4^{1,+}$ - 0^-	1625.485696	2	17	17	
$v_4^{1,+}$ - 0^+	1626.280064	247	20 (18)	20	
$v_4^{1,-}$ - 0^-	1626.582393	186	21 (18)	22	
$v_4^{1,-}$ - 0^+	1627.376761	1	6	7	
$2v_4^{2,-}$ - $2v_2^+$	1643.294986	2	14 (13)	13	
v_1^- - $v_4^{1,-}$	1709.695131	1	9	10	
v_1^+ - $v_4^{1,+}$	1701.788598	2	9	10	
$v_3^{1,+}$ - $v_4^{1,+}$	1817.344229	1	6	5	

8.2 2100 - 5500 cm^{-1}

Following on from the work in the region 500 - 2100 cm^{-1}, Dr Alexander Fateev increased the concentration of NH_3 in the high temperature (1027 °C / 1300 K) measurements to increase the strength of the spectrum above 2100 cm^{-1}. Previous assignments for this region can be found in the HITRAN database (Rothman et al. (2013)).

As the MARVEL energies were available from the beginning of this analysis it was possible to design a assignment procedure that employed them from the beginning. This is described in the next section.

It should be noted that experimental line lists in the region 2100 - 4000 cm^{-1}, constructed from high temperature (up to 1400 °C / 1673 K) emission spectra, are also available from Hargreaves et al. (2012b). Hargreaves and co-workers are in the process of improving and extending these line lists using high temperature absorption spectra. The revised line lists could be incorporated into the current analysis at a future date.

8.2.1 The Assignment Procedure

First a list of observable BYTe lines for the experimental conditions was compiled. For this purpose the absorbance of each line was approximated as:

$$A_{approx}^{BYTe} = \log_{10}\left[\frac{1}{\exp\left(-S_j^a lc\right)}\right] \tag{8.1}$$

where S_j^a is the absorption coefficient in cm/molecule, l is the path length in cm and c is the molecular concentration in cm^3 (see Chapter 3). Lines with $A_{approx} > 0.001$

were kept.

If both the upper and lower energies involved in a observable transition were known experimentally, the BYTe frequency was replaced by the MARVEL line position generated by subtracting upper and lower state energies. This hybrid line list shall henceforth be referred to as "BARVEL" (Mr. Philip Coles).

Taking the resolution of the measurements and the accuracy of BYTe intensities into account, experimental peaks and BARVEL line positions were coupled using python scripts to produce a 'trivial' assignment list. In cases where multiple BARVEL lines corresponded to a single peak, the peak was assigned to the strongest line.

Trivial assignments for the same vibrational band provide an expected obs. - calc. difference for all lines in that band. Lines present in the list of observable BYTe lines, but not in BARVEL, were shifted by this residual to make future assignments by the method of branches.

A list of all trivial and branch assignments, the final assignment list, was then compared to previous studies, namely those catalogued in the HITRAN database (Rothman et al. (2013)).

8.2.2 Assignments

Out of 3701 measured experimental peaks 2308 lines have been assigned. The remaining peaks either did not correspond to a BARVEL or BYTe line within the set wavenumber and intensity thresholds or corresponded to multiple BYTe lines with roughly equal contribution to the total intensity such that it could not be confidently assigned. 553 lines were previously assigned by studies included in the HITRAN database (see Table 8.6). The intention is to make the full 1027 °C (1300 K) peak list with assignments available as supplementary material to the article which will be submitted to JQSRT.

For branch assignments with an experimentally known lower energy state, energies for the upper state were computed using MARVEL energies and the line position of the strongest assigned transition to that state. The intention is to make these available as supplementary material to the article which will be submitted to JQSRT.

Table 8.6: Summary of NH_3 lines assigned in the region 2100 - 5500 cm^{-1}.

	Lines
Experimental	3701
HITRAN	553
New trivial	272
New branch	1483
Total Assigned	2308

As for the lower region (500 - 2100 cm^{-1}) lines were assigned to a large number of different bands. Table 8.5 gives a summary of the observed bands including the number of lines assigned to each and whether the band was observed for the first time

in this work. For simplicity abbreviated vibrational labels ($v_1 v_2 v_3^{L_3} v_4^{L_4} i$) are used to identify bands in this table and only the highest value of the rotational quantum number J, assigned in this work for each band, is indicated. If the observed $J_{\max}$ in this work is bigger that quoted in the literature, the previous $J_{\max}$ is also given. The full 26 quantum labels for each transition, 13 per vibration-rotation state as recommended by Down et al. (2013) (defined in Chapter 3), will be given in the partially assigned peak list file.

Table 8.7: Summary of observed bands in the region 2100 - 5500 cm^{-1} in order of theoretical (BYTe) vibrational band centre (VBC = VBO' - VBO" where VBO = vibrational band origin) with abbreviated ($v_1 v_2 v_3^{L_3} v_4^{L_4} i$), vibrational labels and maximum upper and lower J rotational ($J'_{\max}$ and $J''_{\max}$ respectively) quantum number. N is the number of lines assigned to the band. If $J_{\max}$ in this work is higher than given in the literature, the previously known $J_{\max}$ is given in parentheses. VBO of 0^+ is set to 0.000000 cm^{-1} in line with the MARVEL study (Al Derzi et al. (2015)).

Band	**VBC**	**N**	**J′max**	**J″max**	**Note**
$v_3^{1,+}$ - v_2^+	2475.497647	59	17 (12)	16	
$v_3^{1,+}$ - v_2^+	2511.549362	52	19 (12)	18	
$(v_2+v_3^1)^-$ - $2v_2^-$	2553.265251	14	16 (11)	15	New Band
$(v_2+v_3^1)^+$ - $2v_2^+$	2553.265251	6	9	9	New Band
$3v_2^-$ - 0^+	2895.528913	6	9	9	
$(v_1+2v_2)^+$ - $2v_2^-$	3120.685151	8	16 (11)	16	
$(v_2+2v_4^0)^+$ - v_2^+	3147.493257	1	8	8	New Band
$(v_2+2v_4^2)^+$ - v_2^+	3167.809542	19	18 (7)	19	New Band
$(2v_2+v_4^1)^+$ - 0^+	3189.043150	17	15 (11)	14	
$2v_4^{0,+}$ - 0^-	3215.206330	95	21 (12)	20	
$2v_4^{0,+}$ - 0^+	3215.999346	2	6	7	
$2v_4^{0,-}$ - 0^-	3216.753827	13	17 (12)	18	
$2v_4^{0,-}$ - 0^+	3217.546843	72	18 (12)	17	
$2v_4^{2,+}$ - 0^-	3239.391156	5	9	8	
$2v_4^{2,+}$ - 0^+	3240.184172	82	24 (13)	25	
$2v_4^{2,-}$ - 0^-	3240.782221	53	21 (13)	22	
$(v_2+2v_4^0)^-$ - v_2^-	3240.811833	1	7	8	New Band
$2v_4^{2,-}$ - 0^+	3241.575237	23	17 (13)	18	
$(v_2+2v_4^2)^-$ - v_2^-	3260.700195	8	16 (8)	17	New Band
$2v_1^+$ - $2v_4^{0,-}$	3296.581271	1	4	4	New Band
$(v_1+v_2)^+$ - v_2^-	3326.394745	62	22 (11)	22	
$(v_1+v_4^1)^+$ - $v_4^{1,-}$	3328.348603	19	14 (13)	15	New Band

Continued on next page

Table 8.7 – continued from previous page

Band	VBC	N	J′max	J′max	Note
$(v_1+v_4^1)^-$ - $v_4^{1,-}$	3329.511830	11	15 (12)	16	New Band
$(v_1+v_4^1)^-$ - $v_4^{1,+}$	3330.608526	10	13 (12)	14	New Band
v_1^+ - 0^-	3335.275646	158	21 (12)	21	
v_1^- - 0^+	3337.071892	155	21 (12)	21	
$(v_1+v_2)^-$ - v_2^+	3387.589404	85	19 (12)	19	
$v_3^{1,-}$ - 0^-	3443.194708	142	22 (12)	22	
$(v_3^1+v_4^1)^+$ - $v_4^{1,+}$	3443.598011	2	6	7	New Band
$v_3^{1,+}$ - 0^+	3443.624293	160	23 (12)	24	
$(v_2+v_3^1)^+$ - v_2^+	3448.802885	110	19 (12)	20	
$(v_2+v_3^1)^-$ - v_2^+	3467.322345	1	7	7	
$(v_2+v_3^1)^-$ - v_2^-	3503.010626	73	19 (11)	20	
$(2v_2+v_3^1)^-$ - $2v_2^-$	3470.631808	18	14 (7)	15	New Band
$(2v_2+v_3^1)^+$ - $2v_2^+$	3548.796752	74	21 (11)	22	New Band
$(2v_2+v_3^1)^+$ - v_2^+	4178.157341	89	18 (11)	17	New Band
$(v_1+v_2)^+$ - 0^-	4293.728372	11	12 (11)	12	
$(v_1+v_2)^-$ - 0^+	4320.027766	12	13 (12)	12	
$(v_2+v_3^1)^+$ - 0^+	4416.929641	123	19 (12)	18	
$(2v_2+v_3^1)^-$ - v_2^-	4420.377183	93	16 (7)	17	New Band
$(v_2+v_3^1)^+$ - 0^-	4434.655927	129	19 (11)	18	
$(v_1+v_4^1)^+$ - 0^+	4955.725364	100	18 (13)	18	
$(v_1+v_4^1)^-$ - 0^-	4956.095374	130	19 (12)	20	
$(v_3^1+v_4^1)^-$ - 0^-	5069.587870	3	9 (8)	9	
$(v_3^1+v_4^1)^+$ - 0^+	5069.878075	1	8	9	

17 bands have been observed for the first time in this work, although some of the energy levels involved are known from observations of other bands.

All trivial assignments are secure, as the MARVEL energies (and hence BARVEL frequencies) are known to very high accuracy (of the order 10^{-4} cm^{-1} for the energies). The accuracy of branch assignments depends on the determination of the obs. - calc. difference for a given vibrational band.

For previously observed bands or new bands with many (> 10) assignments the obs. - calc. difference can be tracked through the band. As this remains relatively stable we have confidence in our assignments.

New bands for which only a few lines could be assigned are more tentative.

8.3 7400 - 8640 cm^{-1}

At the 24th Colloquium on High Resolution Molecular Spectroscopy in Dijon (HRMS 2015) Prof Alain Campargue from Université Grenoble Alpes pointed out a room temperature near infra-red spectrum of NH_3 in the 5795 - 9682 cm^{-1} region available

from the Kitt Peak Archive. An overview of the spectrum is given in Figure 8.1. The spectrum was recorded by Dr Catherine de Bergh in 1980 and was recently used by Campargue et al. (2015) to identify residual NH_3 lines in their ultra-long pathlength water spectra.

There is an overall lack of detailed and accurate information for NH_3 transitions in the region 7000 - 15,000 cm^{-1}. The band model parameters of Irwin et al. (1999) cover the region 400 to 11000 cm^{-1}, but was intended for analysis at low spectral resolution so the measurements were obtained at a spectral resolution of only 0.25 cm^{-1} and not assigned. The 2012 edition of the HITRAN database (Rothman et al. (2013)), a major source of experimental data, contains no information for NH_3 above 7000 cm^{-1}. The critically reviewed and validated high resolution experiments employed in the recent MARVEL study (Al Derzi et al. (2015)), cover the region 0.7 - 17,000 cm^{-1} with a large gap between 7000 – 15,000 cm^{-1}.

The reason for the void between 7000 and 15,000 cm^{-1} is the complexity of the NH_3 spectrum making analysis of experimental spectra using the established method of fitting Hamiltonians tricky (Kleiner et al. (1995, 1999)). In the present work we take on this challenge by employing the same technique used previously (Zobov et al. (2011), this work see Sections 8.1 and 8.2) to study high temperature spectra, to study the room temperature Kitt Peak spectrum. The current analysis focuses on the region 7400 - 8640 cm^{-1} where the bulk of NH_3 lines are.

Prof Alain Campargue and Dr Serge Béguier agreed to a collaboration whereby they would construct a calibrated experimental line list with absolute intensities from the Kitt Peak spectrum to be assigned as part of this work. An overview of the experimental line list is presented in Figure 8.2, this includes 8468 lines with intensities ranging between about 5×10^{-25} and 5×10^{-22} cm/molecule. It is suspected that the retrieved intensity for the strongest experimental line ($I > 1 \times 10^{-21}$ cm/molecule) is at least an order of magnitude too strong. This is because the strongest BYTe lines are all of the order 1×10^{-22} cm/molecule which is consistent with the remaining strongest experimental lines. Fully assigned lines and partially assigned lines are separately highlighted in Figure 8.2; details of this distinction are discussed below and in Section 8.3.2.

Two key problems that presented themselves during the analysis were false positives and degenerate vibrational quantum labels. The density of lines in the region 7400 - 8600 cm^{-1} is high, notably for weak lines, meaning a simple search for combination differences using MARVEL energies and experimental frequencies would be plagued by false positives. To combat this, initial assignments were made to strong lines using BYTe as a starting point. Ensuring assignments to strong lines, and their combination difference partners, for the same vibrational band had consistent obs. - calc. differences gave confidence in the assignments, particularly when the derived upper state energies were supported by three or more transitions.

A downside of employing BYTe to initiate assignments is a number of vibrational bands do not have unique labels in BYTe. The decision was made to include assignments to such bands where possible but only supply rigorous labels (Γ_{tot} and J) for each assigned transition.

A rigorous or 'good' quantum number is related to a conserved physical quantity

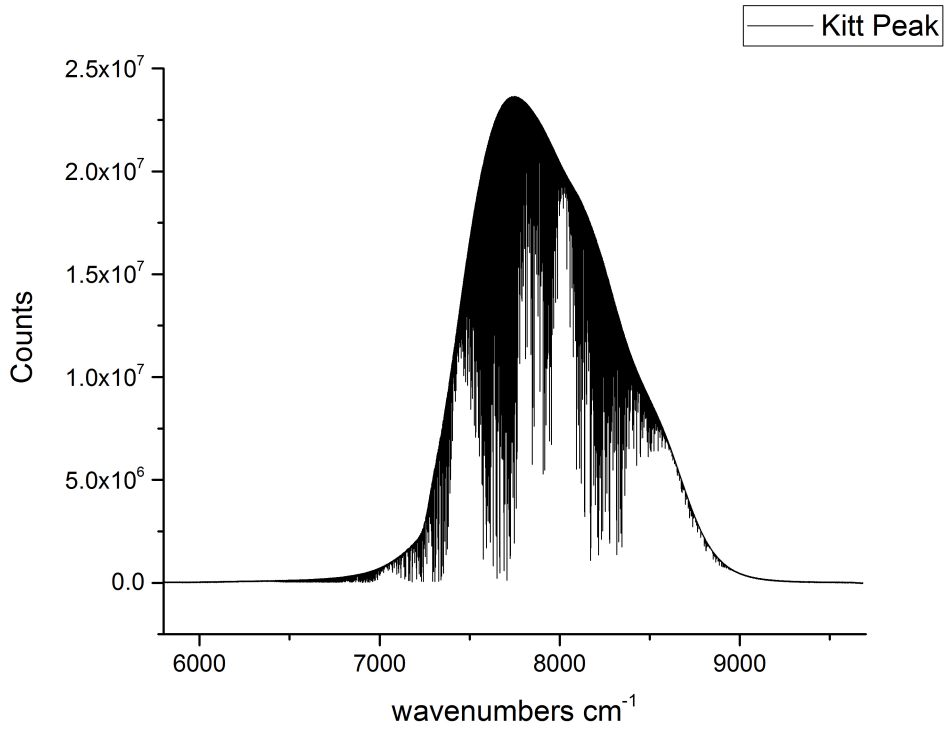

Figure 8.1: Overview of the NH_3 spectrum in the region 5795 - 9682 cm^{-1} measured by Dr. Catherine de Bergh in 1980.

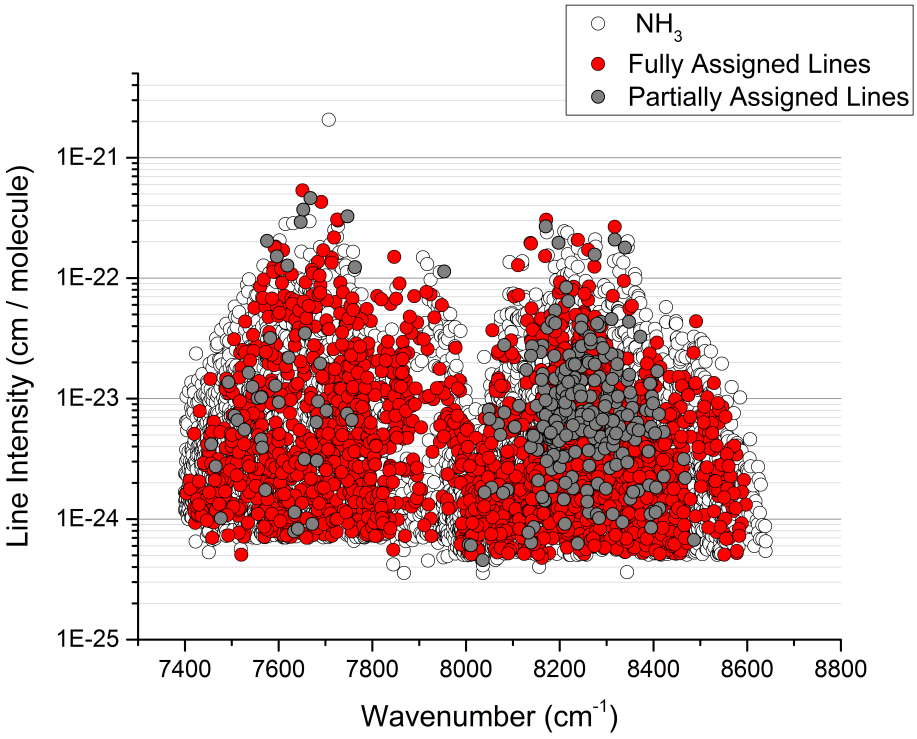

Figure 8.2: Overview of the NH_3 line list retrieved between 7400 and 8640 cm^{-1}. Fully assigned lines are highlighted in red, partially assigned lines are shaded in grey. Please refer to Section 8.3.2 for details.

(for example rotational angular momentum or total symmetry). In quantum mechanical terms, a rigorously good quantum number is associated with the eigenvalue of an operator that commutes with the exact molecular Hamiltonian (Field (2015)). Additional 'approximate' quantum numbers (for example vibrational normal mode labels), required to uniquely specify each energy level or eigenstate, are related to eigenvalues of an operator that does not commute with the exact molecular Hamiltonian (Field (2015)).

Some of these labelling problems may be resolved by the new ExoMol NH_3 line list (Dr Oleg Polyansky and Mr Philip Coles). The current analysis using BYTe is discussed below.

8.3.1 The Assignment Procedure

A list of observable BYTe lines for the experimental conditions was compiled. This list included all lines with an absorption intensity greater that 5×10^{-25} cm/molecule at 292.5 K (21.5 °C).

Tentative assignments were given to the strongest experimental lines by comparison with the strongest BYTe lines (see Figure 8.3). Combination difference partners for these tentative assignments were found in the list of observable BYTe lines and assigned to experimental lines where possible. In this case the BYTe intensity should be within 55% of the experimental intensity and have a residual (obs. - calc. difference) up to about 3 cm^{-1}. Upper state energies for resulting combination difference pairs (PQ, RQ or PR) or triplets (PQR) were calculated by adding the experimental line positions to the energy for the lower state associated with the transition. As all bands considered in this work go to the ground state and are limited to a rotational excitation of $J \leq 16$, these energies are known to very high accuracy (of the order 10^{-4} cm^{-1}) and are available from the recent MARVEL study (Al Derzi et al. (2015)). If the calculated upper energies agreed within 0.006 cm^{-1} for intermediate intensity unblended lines or 0.02 cm^{-1} for weak or blended lines these assignments were confirmed. Table 8.8 gives an subset of assignments confirmed by combination differences. In some cases the derived upper state energies were supported by more than three transitions.

Confirmed combination difference pairs and triplets for the same vibrational band provide an expected observed obs. - calc. difference for all lines in that band. This obs. - calc. difference was used to shift the BYTe line positions for vibrational bands with at least five combination difference pairs or triplets and hence make further assignments to those bands. This is the method of branches (Polyansky et al. (1997b)), which exploits the systematic behaviour of variational calculations that give an overall band shift but largely preserve the rotational structure. Table 8.9 gives a subset of assignments made using the method of branches.

The final assignment list is a compilation of all combination difference (CD) and branch (Br) assignments. Due to the inaccuracy of BYTe in the region 7400 - 8600 cm^{-1} (see Chapter 7) unconfirmed assignments made by simple line list comparison were discarded.

Table 8.8: A sample of the assigned transitions confirmed by combination differences. Abbreviated $(v_1 v_2 v_3^{L_3} v_4^{L_4})^i$ vibrational labels followed by rotational quantum numbers J and K are given below, full quantum assignments are provided in the experimental line list and energies files.

Obs.	Calc.	Upper Quanta	Lower Quanta	Type P/Q/R	Upper State Energy
cm^{-1}	cm^{-1}				cm^{-1}
7555.8782	7554.8133	$(v_1+v_2+v_3^1)^-$ 4 2	0^+ 5 0	P	7853.5211
7588.2929	7587.2278	$(v_1+v_2+v_3^1)^-$ 4 2	0^- 4 3	Q	7853.5204
7687.4314	7686.3683	$(v_1+v_2+v_3^1)^-$ 4 2	0^+ 3 0	R	7853.5209
7734.2821	7733.2204	$(v_1+v_2+v_3^1)^-$ 4 2	0^- 3 3	R	7853.5205
7766.8616	7765.7996	$(v_1+v_2+v_3^1)^-$ 4 2	0^- 5 3	P	7853.5206
7710.9095	7708.0570	$(v_2+2v_3^2)^+$ 6 1	0^+ 7 2	P	8250.7546
7837.5170	7834.6673	$(v_2+2v_3^2)^+$ 6 1	0^- 6 1	Q	8250.7549
7849.1070	7846.2574	$(v_2+2v_3^2)^+$ 6 1	0^+ 6 2	Q	8250.7551
7967.8183	7964.9705	$(v_2+2v_3^2)^+$ 6 1	0^+ 5 2	R	8250.7555
7519.4722	7517.1594	$(v_1+v_2+2v_4^2)^+$ 6 5	0^- 7 7	P	7894.5792
7537.0004	7534.6874	$(v_1+v_2+2v_4^2)^+$ 6 5	0^+ 6 4	Q	7894.5846
7655.9330	7653.6210	$(v_1+v_2+2v_4^2)^+$ 6 5	0^+ 5 4	R	7894.5856
8161.8067	8159.5253	$(v_1+3v_4^1)^-$ 8 5	0^+ 9 7	P	8872.6632
8321.9021	8319.6317	$(v_1+3v_4^1)^-$ 8 5	0^+ 7 1	R	8872.6608

Table 8.9: A sample of assignments made to vibrational band $(v_2 + 2v_3^2)^-$ using the method of branches. The expected Obs. - Calc. of 2.4 cm^{-1} was determined by averaging the residuals from 21 combination difference pairs and 20 combination difference triplets.

Obs. cm^{-1}	Calc. cm^{-1}	J′	K′	J″	K″	Type P/Q/R	Obs. - Calc. cm^{-1}
7833.3464	7833.3464	1	1	2	2	P	2.3824
7847.1197	7847.1197	0	0	1	1	P	2.3859
7704.1322	7704.1322	10	10	11	11	P	2.3772
7813.0536	7813.0536	8	5	8	4	Q	2.4110
7822.9094	7822.9094	7	4	7	3	Q	2.4245
7895.3264	7895.3264	10	8	10	9	Q	2.4227
8008.9997	8008.9997	12	11	11	10	R	2.4134
8010.4040	8010.4040	12	7	11	6	R	2.4159
8000.4518	8000.4518	11	9	10	8	R	2.3839

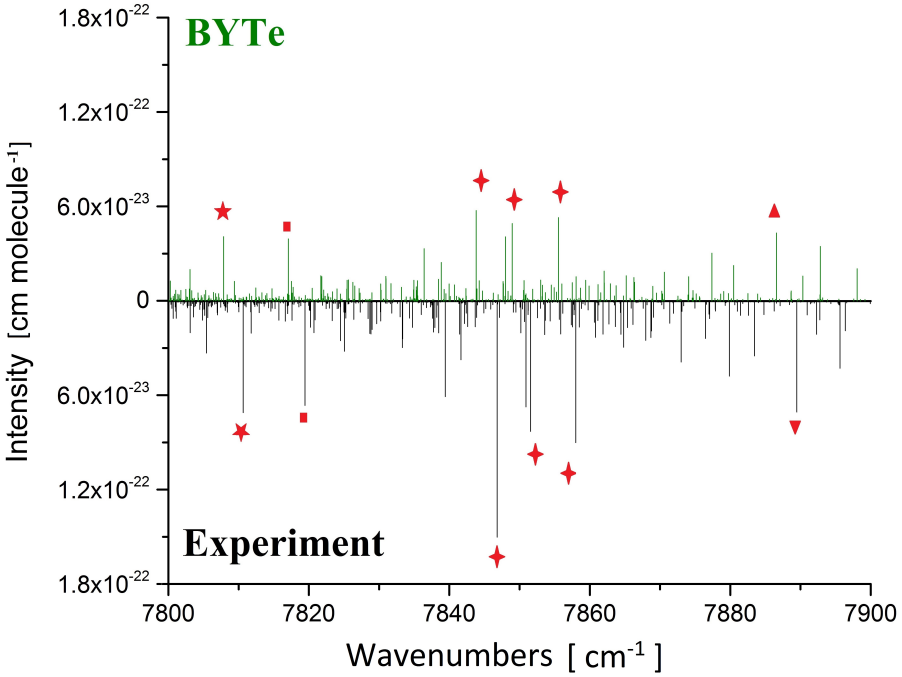

Figure 8.3: Comparison between experimental (black) and calculated BYTe (green) stick spectra at 21.5 °C for the range 7800 - 7900 cm^{-1}. Symbols indicate examples of tentative assignments made by line list comparison.

8.3.2 Assignments

All assignments, vibrational bands and experimental energies discussed below are new or observed for the first time in this work.

8468 experimental lines were retrieved in the region 7400 - 8600 cm^{-1}, in total 2474 of these have been assigned, 1343 by combination differences (CD) and 1131 by the method of branches (Br). 2170 assigned lines have unique upper and lower energy state quantum labels in BYTe. These are fully assigned with 26 quantum labels, 13 per rotation-vibration state as recommended by Down et al. (2013) (defined in Chapter 3). The additional 304 do not have unique upper state labels in BYTe hence only the rigorous quantum state labels (total angular momentum and total symmetry) can be trusted. These are partially assigned with 13 lower state labels, as recommended by Down et al. (2013), and 2 upper state labels, J and $\Gamma_{\rm tot}$. The 5994 unassigned experimental lines either did not have a CD partner or did not correspond to a shifted BYTe line for any of the vibrational bands analysed in this work. Most of these are weak lines that probably belong to other vibrational bands, perhaps hot bands, that have too few observed lines in the current experiment to be properly characterized. Around 1200 unassigned lines could be classified as strong or intermediate. These lines may belong to other bands not included in the present analysis, else the assignment of these lines may have been hampered by the uncertainty in experimental and theoretical intensities. The experimental line list with full or partial quantum labels for assigned lines is available from http://www.sciencedirect.com/science/article/pii/S0022285216300790. An extract is presented in Table 8.10.

Upper state energies were computed using MARVEL ground state energies and the line position of the strongest line assigned to that state. These are available from http://www.sciencedirect.com/science/article/pii/S0022285216300790 and summarised in Table 8.14 and Table 8.15. Extracts are presented in Table 8.11 and Table 8.12

Lines with full assignments belong to one of 15 different bands. Table 8.13 gives a summary of the observed bands including the number of lines assigned to each. The bands are listed in order of vibrational band origin (VBO) which is either the computed upper energy for the observed P(0) transition (E) or the BYTe prediction shifted by the average obs. - calc. difference for the band (B). For simplicity abbreviated vibrational labels $(v_1 v_2 v_3^{L_3} v_4^{L_4})^i$ are used to identify bands in this table. The full 26 quantum labels for each transition, 13 per vibration-rotation state as recommended by Down et al. (2013), are given in the experimental line list and energies files.

Lines with partial assignments belong to one of 6 different bands. In the absence of unique vibrational labels these bands are simply named Band 1 - 6. Line assignments and derived energies for these bands, totalling 304 and 223 respectively, are summarised in Table 8.15. Full lower and partial upper quantum labels for the assignments are given in the experimental line list and energies files. These bands are not the first observed ammonia bands for which the vibrational quantum numbers have yet to be determined (Coy & Lehmann (1986), Lehmann & Coy (1988)).

The CD assignments can be divided into two categories, those where the calculated

upper energies agree within 0.006 cm^{-1} and those where the calculated upper energies agree within 0.02 cm^{-1}.

The former can be considered secure, as the calculated upper energies consistently agree within the higher experimental uncertainty for given CD pair and triplets or groups of transitions sharing the same upper energy state.

In the latter case, the real transition(s) involved in the CD relation are obscured in the experimental spectrum by (a) stronger line(s). In other words the assigned line position is the nearest, rather than the true, peak-centre. Hence these are more tentative.

The accuracy of Br assignments depends on the determination of the obs. - calc. for a given vibrational band.

Strong bands with 10s of CD and Br assignments, such as $(v_2 + 2v_3^2)^-$, are well characterised and the stability of the obs. - calc. through the band can be clearly seen from the calculated energies in Table 8.11. Hence lines assigned to these bands by Br are reliable.

Weaker bands, such as $(2v_1 + v_4^1)^-$, are more tentative. Although the overall consistency of our CD and Br results gives us confidence in all our assignments.

Table 8.10: Extract from the partially assigned 21.5 °C experimental peak list for 7400 - 8640 cm^{-1}. Freq. is the experimental central peak frequency, Int. is the peak intensity in units of absorbance. The upper state and lower state labels are the 13 quantum numbers recommended by Down et al. (2013) (defined in Chapter 3). For the symmetries Grot, Gvib and Gtot (where G = Γ): 1 = A_1', 2 = A_2', 3 = E′, 4 = A_1'', 5 = A_2'' and 6 = E″. Partially assigned upper states are labelled with the 2 rigorous quantum numbers J and Gtot, and the band number = 1,2,3,4,5 or 6. Missing labels are indicated by the * symbol. The band number is given in place of the 'L' quantum number. Entries in the last column specify if the assignment was made by combination differences (CD) or the method of branches (Br).

#Freq.	Int.	Upper State													Lower State												
#cm^{-1}	cm/molecule	v1	v2	v3	v4	L3	L4	L	J	K	i	Grot	Gvib	Gtot	v1	v2	v3	v4	L3	L4	L	J	K	i	Grot	Gvib	Gtot	
7618.0026	7.72E-25	1	1	0	2	0	2	2	10	10	1	6	3	5	0	0	0	0	0	0	0	10	9	1	5	4	2	Br
7618.0239	2.11E-24																											
7618.4157	3.76E-24																											
7618.7748	1.27E-22	*	*	*	*	*	*	1	6	*	*	*	*	5	0	0	0	0	0	0	0	6	3	1	5	6	2	Br
7618.8596	5.56E-23	1	1	1	0	1	0	1	3	2	0	3	3	3	0	0	0	0	0	0	0	4	4	1	5	3	6	CD
7619.0285	2.18E-23	1	1	1	0	1	0	1	5	5	0	3	6	6	0	0	0	0	0	0	0	5	4	0	1	3	3	CD
7619.1295	1.06E-24																											
7619.8736	1.61E-23	1	1	0	2	0	2	2	3	2	1	6	3	5	0	0	0	0	0	0	0	3	3	1	5	4	2	Br
7619.9194	1.72E-24																											
7619.9351	3.79E-24																											
7620.1467	7.25E-25																											
7620.1939	5.67E-24																											
7620.2164	4.92E-23	1	1	1	0	1	0	1	1	0	0	3	2	3	0	0	0	0	0	0	0	2	1	0	1	6	6	CD

Table 8.11: Extract from the file containing new full assigned experimental energy levels for 7400 - 8640 cm^{-1}. Obs. is the experimentally derived energy (MARVEL lower energy + observed transition frequency) in cm^{-1}, Obs.-Calc. is the observed minus calculated (BYTe) energy difference in cm^{-1}. The given labels are the 13 quantum numbers recommended by Down et al. (2013) (defined in Chapter 3). For the symmetries Grot, Gvib and Gtot (where G = Γ): 1 = A_1', 2 = A_2', 3 = E′, 4 = A_1'', 5 = A_2'' and 6 = E″.

v1	v2	v3	v4	L3	L4	L	i	Gvib
0	1	2	0	2	0	2	1	6

J	K	Grot	Gtot	Obs.	Obs.-Calc.
0	0	1	6	7864.0831	2.39
1	1	6	3	7878.9339	2.38
1	1	6	2	7880.6680	2.49
1	0	2	6	7883.1046	2.40
2	2	3	5	7906.1076	2.36
2	2	3	6	7909.7019	2.41
2	1	6	3	7916.9634	2.40
2	1	6	2	7918.4108	2.45
2	0	1	6	7921.1359	2.36
3	3	4	3	7945.7676	2.52
3	2	3	5	7963.1252	2.38
3	2	3	6	7966.4671	2.55
3	1	6	3	7973.9760	2.41
3	1	6	2	7976.0707	2.44
3	0	2	6	7978.1535	2.46
4	4	3	6	7997.3836	2.33
4	3	4	3	8021.5926	2.36
4	2	3	5	8039.0949	2.40
4	2	3	6	8042.3156	2.45

Table 8.12: Extract from the file containing new partially assigned experimental energy levels for 7400 - 8640 cm^{-1}. Obs. is the experimentally derived energy (MARVEL lower energy + observed transition frequency) in cm^{-1}, Obs.-Calc. is the observed minus calculated (BYTe) energy difference in cm^{-1}. The given labels are the rigorous quantum numbers Gtot and J. For the symmetry Gtot (where G = Γ): 1 = A_1', 2 = A_2', 3 = E', 4 = A_1'', 5 = A_2'' and 6 = E''.

Band 1			
J	Gtot	Obs.	Obs.-Calc.
3	6	7616.4995	2.26
3	5	7661.9895	2.16
5	6	7666.6620	2.35
3	3	7678.0229	2.23
3	6	7689.9779	2.29
3	2	7701.4818	2.27
4	2	7709.3825	2.32
4	6	7735.7490	2.27
4	6	7738.9803	2.30
4	2	7757.1863	2.24
4	3	7759.7129	2.40
4	6	7771.3651	2.33
3	5	7771.8238	2.23
5	6	7840.3501	2.31
5	3	7856.3921	2.39
5	2	7857.7296	2.23
5	3	7875.7549	2.30

Table 8.13: Summary of fully assigned observed bands in the region 7400 - 8640 cm^{-1} in order of vibrational band origin (VBO) with abbreviated $(v_1 v_2 v_3^{L_3} v_4^{L_4} i)$ vibrational labels. N_{lines} is the total number of lines assigned to the band. CD and Br are the number of lines assigned using combination differences and the method of branches respectively. The VBO has been derived from the observed P(0) transition (E) or BYTe (B).

Band	VBO / cm^{-1}	N_{lines}	CD	Br
$(v_1 + v_2 + 2v_4^2)^+$	7572.9549 E	143	76	67
$(v_1 + v_2 + 2v_4^2)^-$	7603.1713 E	134	69	65
$(v_1 + v_2 + v_3^1)^+$	7656.8700 E	162	103	59
$(v_1 + v_2 + v_3^1)^-$	7673.84 B	135	72	63
$(v_2 + 2v_3^2)^+$	7854.3892 E	145	101	44
$(v_2 + 2v_3^2)^-$	7864.0831 E	152	106	46
$(2v_1 + v_4^1)^+$	8086.5926 E	64	12	52
$(2v_1 + v_4^1)^-$	8089.59 B	63	14	49
$(v_1 + v_3^1 + v_4^1)^+$	8174.7017 E	224	135	89
$(v_1 + v_3^1 + v_4^1)^-$	8177.4358 E	217	120	97
$(v_1 + 3v_4^1)^+$	8253.7494 E	159	109	50
$(v_1 + 3v_4^1)^-$	8257.5341 E	152	91	61
$(v_1 + 2v_2 + 2v_4^2)^+$	8266.3284 E	120	73	47
$(2v_3^2 + v_4^1)^+$	8463.2901 E	151	54	97
$(2v_3^2 + v_4^1)^-$	8463.8719 E	149	55	94

Table 8.14: Summary of fully assigned new NH_3 experimental energies above 7000 cm^{-1} with abbreviated $(v_1 v_2 v_3^{L_3} v_4^{L_4} i)$ vibrational labels and maximum rotational quantum numbers J_{max} and K_{max}. N_E is the total number of experimentally derived energies for the band. Obs. - Calc. gives the average experimental minus BYTe energy difference for the band in cm^{-1}.

Band	N_E	J_{max}	K_{max}	Obs.-Calc.
$(v_1 + v_2 + 2v_4^2)^+$	104	14	14	2.3
$(v_1 + v_2 + 2v_4^2)^-$	99	14	14	3.0
$(v_1 + v_2 + v_3^1)^+$	101	16	16	0.6
$(v_1 + v_2 + v_3^1)^-$	92	15	15	1.0
$(v_2 + 2v_3^2)^+$	85	15	15	2.9
$(v_2 + 2v_3^2)^-$	88	14	14	2.4
$(2v_1 + v_4^1)^+$	58	13	13	1.2
$(2v_1 + v_4^1)^-$	56	14	13	1.3
$(v_1 + v_3^1 + v_4^1)^+$	151	15	15	-1.9
$(v_1 + v_3^1 + v_4^1)^-$	105	16	16	-0.6
$(v_1 + 3v_4^1)^+$	101	14	14	2.3
$(v_1 + 3v_4^1)^-$	104	14	13	2.2
$(v_1 + 2v_2 + 2v_4^2)^+$	81	11	11	1.5
$(2v_3^2 + v_4^1)^+$	123	13	13	2.4
$(2v_3^2 + v_4^1)^-$	121	12	12	2.2

Table 8.15: Summary of partially assigned lines, and new NH_3 experimental energies above 7000 cm^{-1} derived from them, with arbitrary band name and maximum rotational quantum numbers J_{max}. N_E is the total number of experimentally derived energies for each band. N_{lines} is the total number of lines assigned to the band. CD and Br are the number of lines assigned using combination differences and the method of branches respectively. Obs. - Calc. gives the average experimental minus BYTe energy difference for the band in cm^{-1}. Range gives the approximate span of the band in cm^{-1}. The VBO has been derived from the observed P(0) transition (E) or BYTe (B).

Band	Range (approx.)	VBO / cm^{-1}		N_{lines}	CD	Br	N_E	J_{max}	Obs.-Calc.
1	7450 - 8000	7491.18	B	36	18	18	27	8	2.3
2	8000 - 8450	8282.30	B	63	30	33	46	11	-1.9
3	8000 - 8450	8283.5189	E	69	24	45	56	11	-0.6
4	8000 - 8400	8211.24	B	52	35	17	34	9	2.3
5	8100 - 8400	8212.04	B	50	21	29	39	10	2.2
6	8050 - 8400	8281.65	B	34	25	9	21	9	1.5

8.4 9000 - 10,400 cm^{-1}

Following on from the work in the region 7400 - 8640 cm^{-1} Prof Alain Campargue and Dr Serge Béguier agreed to construct a calibrated experimental line list with absolute intensities from another Kitt Peak spectrum. This spectrum was also measured by Dr. Catherine de Bergh in 1980 and covers the region 7497 - 11,524 cm^{-1}. An overview of the spectrum and experimental line list is given in Figure 8.4 and Figure 8.5 respectively. The line list contains 12,063 lines with intensities ranging between about 1×10^{-25} and 5×10^{-22} cm/molecule.

As expressed before, there is a lack of detailed and accurate information for NH_3 transitions between 7000 and 15,000 cm^{-1}. Hence all assignments, vibrational bands and experimental energies identified in or derived from the Kitt Peak spectrum will be new or observed for the first time.

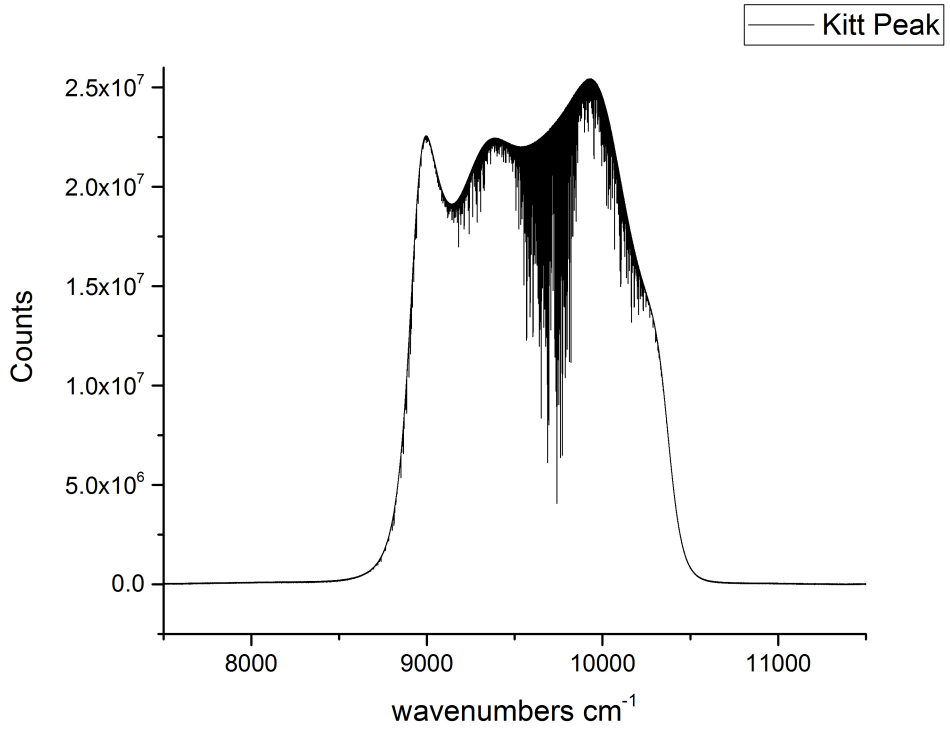

Figure 8.4: Overview of the NH_3 spectrum in the region 7497 - 11,524 cm^{-1} measured by Dr. Catherine de Bergh in 1980.

It is expected that the analysis of this spectrum will present the same challenges as the lower region with perhaps a little more difficulty introduced by the lower accuracy of BYTe above 9000 cm^{-1}. The next section describes assignments made to the strongest band in the region 9000 - 10,400 cm^{-1}, $(2v_1 + v_3^1)^+$. Generating assignments for other vibrational bands, including the second strongest $(2v_1 + v_3^1)^-$, is future work.

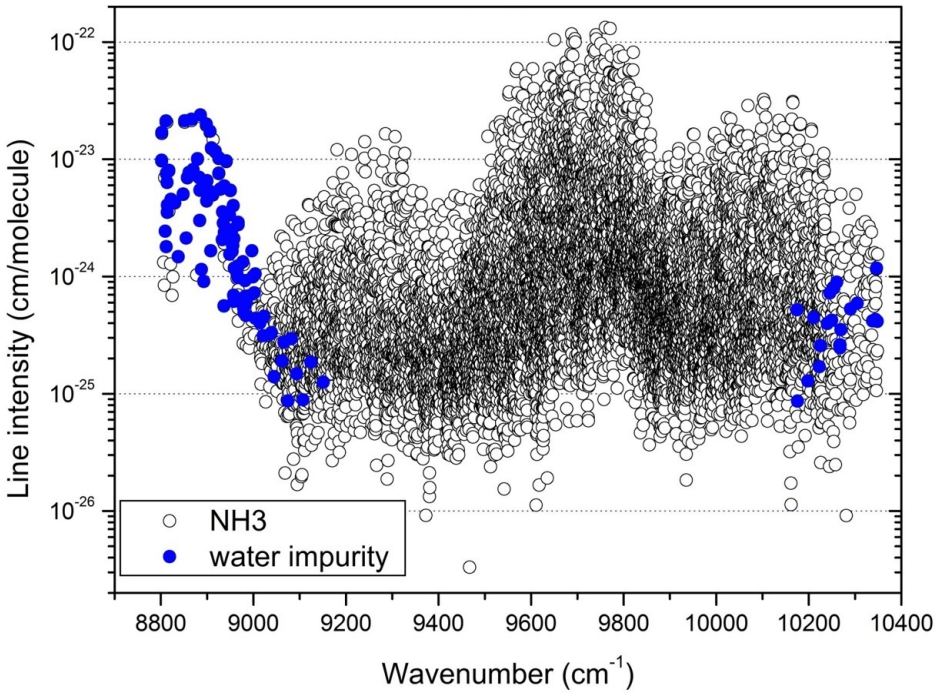

Figure 8.5: Overview of the NH_3 line list retrieved between 9000 and 10,400 cm^{-1}. H_2O impurity lines used for wavenumber calibration are highlighted in blue.

8.4.1 Preliminary Work

The assignment process for the region 7400 - 8640 cm^{-1} described in Section 8.3.1 is employed here. The only difference being the residuals (observed minus calculated difference) for assignments will be up to about 7 cm^{-1} to account for the lower accuracy of BYTe in the region 9000 - 10,400 cm^{-1}.

The current focus is on the strongest band $(2v_1 + v_3^1)^+$. The strongest BYTe lines in the region 9000 - 10,400 cm^{-1} belong to this band, which can be tentatively assigned to the strongest experimental lines. A sample of tentative assignments, with their combination difference partners, is shown in Table 8.16.

Assuming these assignments are correct, and adopting the average residual for the band 6.5 cm^{-1}, a further 176 assignments can be made to symmetric $2v_1 + v_3^1$, 56 by combination differences and 120 by the method of branches.

Table 8.16: A sample of tentative assignments and their combination difference partners for $(2v_1 + v_3^1)^+$. Abbreviated $(v_1 v_2 v_3^{L_3} v_4^{L_4})^i$ vibrational labels followed by rotational quantum numbers J and K are given below.

Obs.	Calc.	Obs. - Calc.	Upper Quanta	Lower Quanta	Type P/Q/R	Upper State Energy
cm^{-1}	cm^{-1}	cm^{-1}				
9562.52054	9555.78800	6.73254	$(2v_1 + v_3^1)^+$ 4 4	0^+ 5 3	P	9827.03827
9661.70647	9654.97512	6.73135	$(2v_1 + v_3^1)^+$ 4 4	0^+ 4 3	Q	9827.03863
9741.17597	9734.44569	6.73028	$(2v_1 + v_3^1)^+$ 4 4	0^+ 3 3	R	9827.03865
9760.89550	9754.52034	6.37516	$(2v_1 + v_3^1)^+$ 5 4	0^+ 4 3	R	9926.22766
9661.70647	9655.33322	6.37325	$(2v_1 + v_3^1)^+$ 5 4	0^+ 5 3	Q	9926.22420
9621.88922	9615.07482	6.81440	$(2v_1 + v_3^1)^+$ 6 4	0^- 7 6	P	10045.11332
9661.79607	9654.98384	6.81223	$(2v_1 + v_3^1)^+$ 6 4	0^+ 6 3	Q	10045.11562
9780.59722	9773.78791	6.80931	$(2v_1 + v_3^1)^+$ 6 4	0^+ 5 3	R	10045.11495
9583.29036	9577.11438	6.17598	$(2v_1 + v_3^1)^+$ 4 2	0^- 5 1	P	9877.25871
9682.35439	9676.17816	6.17623	$(2v_1 + v_3^1)^+$ 4 2	0^- 4 1	Q	9877.26071
9761.72139	9755.54914	6.17225	$(2v_1 + v_3^1)^+$ 4 2	0^- 3 1	R	9877.25804

8.5 Summary of Results

8.5.1 NH_3: Hot

High resolution absorption measurements of NH_3 in the region 500 - 2100 cm^{-1} at atmospheric pressure and temperatures of 300, 400, 500 and 1027 °C, and in the region 2100 - 5500 cm^{-1} at atmospheric pressure and 1027 °C, have been analysed.

A comparison between the measurements and BYTe shows in general good agreement though there are some shifts in line position (up to 0.5 cm^{-1} for the lower region and 2 cm^{-1} for the higher region) and BYTe has some difficulty reproducing strong line intensities. Work towards a new NH_3 line list is currently being carried out as part of the ExoMol project (Tennyson & Yurchenko (2012); Tennyson et al. (2016)).

Where results are presented below these refer to the region 500 - 2100 cm^{-1} and 2100 - 5500 cm^{-1} in that order.

The use of BYTe and MARVEL has allowed the assignment of 1967 and 2308 lines. 1116 and 553 lines were previously assigned, 1073 and 553 by studies included in the HITRAN database and an additional 43 by high temperature study (Zobov et al. (2011)) for the lower region. 851 and 1755 lines have been assigned for the first time in this work, for the lower region 482 were also present but unassigned in the spectra analysed by Zobov et al. (2011). The 326 and 272 new assignments verified by MARVEL line positions, also known as trivial assignments, are secure as the accuracy of MARVEL energies is of the order 10^{-4} cm^{-1}. Of the 525 and 1483 proposed or branch assignments, those associated with bands which have verified assignments in this work or numerous assignments should be reliable because the observed minus calculated differences remain relatively stable within a given band. The remaining assignments should also be valid, as the methods used in this work have proven effective at generating valid assignments and reproducing previous work. However caution is advised on the basis that the accuracy of BYTe does not rule out miss-assignments.

The NH_3 spectrum between 500 - 2100 cm^{-1} has now been comprehensively studied using both hot emission (Zobov et al. (2011)) and hot absorption (this work) spectra. The region 2100 - 5500 cm^{-1} has been studied using hot absorption spectra. New line lists for the region due to Hargreaves and co-workers, partially constructed from hot emission spectra, could be incorporated into the current analysis when they become available.

8.5.2 NH_3: Cold

Presented is an analysis of a 35 year old room temperature spectrum of NH_3 in the region 7400 – 8600 cm^{-1}.

A comparison between the measurements and BYTe shows in general good agreement but there are shifts in line position of up to 3 cm^{-1} throughout the region and experimental line intensities are only reproduced within 20 - 55 % at best. Work towards a new, more accurate, hot NH_3 line list is currently being carried out as part of the ExoMol Project (Tennyson & Yurchenko (2012); Tennyson et al. (2016)).

The use of BYTe and MARVEL has allowed the assignment of 2474 lines, 1343 by combination differences and a further 1131 by the method of branches. In total 1692 new experimental energies between 7000 - 9000 cm^{-1} have been derived. Assignments associated with strong bands with tens of combination difference and branch assignments should all be reliable, as these bands are well characterised and have stable observed minus calculated differences throughout the band. The remaining assignments should also be safe, as all results from the two assignment procedures have

proven very consistent, though these are more tentative. A similar analysis for the region 9000 - 10,400 cm^{-1} is ongoing, preliminary assignments made to the strongest band are presented in this work. As for the lower region experimental line intensities are only reproduced within 20 - 55 % at best, though there are shifts in line position of up to 7 cm^{-1} in the higher region.

Chapter 9

The Infrared Spectrum of Methane

As a potential biosignature (Marais et al. (2004)), a global warming species (Rhoderick & Dorko (2004)) and a key component in many gaseous environments, including the atmospheres of cool stars (see for example Canty et al. (2015)) and Titan (see for example Karkoschka (1998)), CH_4 is a molecule many seek to understand. However both the experimental and theoretical study of CH_4 spectra present a challenge due to its dense and complex nature (see Chapter 2 and references therein).

Many experimental studies (see Table 9.2) have provided detailed information such as line positions, intensities and experimental energies accompanied with quantum labels to aid the understanding of the polyatomic spectrum. Unfortunately not all these studies are consistent due to the variable use of limited quantum label sets. The ExoMol line list for CH_4, YT10to10 (Yurchenko & Tennyson (2014)), employs 30 quantum labels to describe each transition, 15 per energy level, while the majority of assigned measurements (compiled in Table 9.2) provide only 14, 7 per energy level. These seven are not sufficient to uniquely identify every spectral line.

The first CH_4 project started as part of this work aims to compile all available assigned high resolution experimental measurements for CH_4, match each line to a unique set of quantum labels and hence derive an accurate self-consistent list of accurate experimental energy levels. In other words perform a MARVEL analysis (see Section 4.4.1). Some vital components of this work, performing a literature review and extracting data for example, are simple enough to be taught to undergraduate or even high school students. This presents an ideal opportunity to give budding scientists, in this case Year 12/13 pupils, a chance to contribute to original academic research.

The 'A' in MARVEL stands for 'Active' as with time new experimental data will become available and be included in the MARVEL database to produce an updated, and hopefully more extensive, list of energies.

The second CH_4 project started as part of this work aims to provide new information for excited states of CH_4 through analysis of high temperature FTIR spectra provided by Dr Alexander Fateev. This project shall require the MARVEL energies generated by the first project to aid assignment.

Section 9.1 describes the CH_4 MARVEL project that, with contribution from five secondary school students, results in an accurate compilation of experimental energy

levels. Section 9.2 describes the planned analysis of hot FTIR absorption spectra of CH_4 in the region 1000 - 6300 cm^{-1}.

9.1 Compilation of Experimental Energy Levels (MARVEL/ORBYTS)

In the spring of 2016 the education program associated with the Twinkle Space mission (EduTwinkle) launched a pilot of ORBYTS (Original Research By Young Twinkle Students). ORBYTS pairs PhD students and early career post-docs with groups of secondary school students, together they perform original research and work towards a peer-reviewed publication.

The pilot is focused on molecular astrophysics, and each group is responsible for performing, or at least starting, a MARVEL analysis for one molecule of astronomical interest. The current molecules being considered are CH_4 (this work), TiO (Dr. Laura McKemmish) and C_2H_2 (Ms Katy Chubb).

As part of this work I supervised 'Team Methane' at Highams Park School with support from the ORBYTS representative at the school Dr. Clara Sousa-Silva. The team consisted of five AS/A-level students Miss Menghan Liu, Mr Tom Farnell, Mr Alex Goring, Miss Megan Sturgeon and Miss Georgia White. The stages of the project can be summarised as follows:

1. **Task 1 - Astronomical and Earthly context**: Research CH_4 detections and uses of its spectra on Earth and in space.

2. **Task 2 - Research experimental data**: Collect all articles describing high resolution experimental measurements of CH_4 spectra.

3. **Task 3 - Assess experimental data**: Determine which experimental sources collated in Task 2 will be utilised in MARVEL by assessing uncertainties, availability of the experimental data and provision of upper and lower energy state labels.

4. **Task 4 - Digitising data**: Extract experimental data from Tables or supplementary material to create MARVEL input files. The input files should contain frequencies, uncertainties, upper and lower energy state labels and a reference code for every measured transition.

5. **Task 5 - MARVEL analysis**: Input files from Task 4 will be analysed using MARVEL. One by one the input files will be combined to generate a master file. Any inconsistencies between datasets will be handled here.

6. **Task 6 - Result validation**: Output MARVEL energies can be compared to values from the literature where available. So called 'Magic Numbers' may be introduced to link, and hence provide absolute energies for, the three principle spectroscopic networks of CH_4, ortho, para and meta, if required.

7. **Task 7 - Preparing documentation**: Results from the MARVEL analysis shall be presented in Tabular form. This shall include a Table detailing which experimental sources were used and how many transitions from each source were validated, and a Table summarising the number of energies and vibrational band origins derived.

8. **Task 8 - Prepare research article**: Collate all relevant information and Tables to construct a research article on the project. This article will be submitted to JQSRT.

The aim was to involve the students in as many parts of the project as possible, and to produce at least a subset of final results that will be included in the peer reviewed article. Due to the large volume of CH_4 experimental data (see Table 9.2) and complications posed by quantum labels (described in Section 9.1.3) a large portion of Task 5 and beyond will be completed now the ORBYTS pilot has concluded. Progress for Tasks 1 - 6 is discussed below. Tasks 7 - 8 are future work.

9.1.1 Task 1: Astronomical and Earthly context

CH_4 is present in many environments and its spectrum has many uses. To give some examples, the molecule is found in:

1. The Earth's atmosphere (Goldberg (1950))
2. Industrial emissions (Kirchgessner et al. (1997))
3. Cool star atmospheres (Canty et al. (2015))
4. Comet comae (Gibb et al. (2003))
5. Solar system giant planets (Karkoschka (1998))

and its spectrum can be used to:

1. Search for alien life (Marais et al. (2004))
2. Monitor global warming (Rhoderick & Dorko (2004))
3. Classify stars (Leggett et al. (2000))
4. Characterise planets (Swain et al. (2008))
5. Detect illegal farming (Cara et al. (2005))

Therefore there is plenty of motivation to collect, review and validate all the high resolution experimental information available for CH_4 and use it to derive experimental quality ro-vibrational energy levels using MARVEL. Particular sources of interest to the ORBYTS students will be included in the introduction of the research article. These are summarised in Table 9.1.

Table 9.1: References and information identified by the ORBYTS students to be included in the introduction of the CH_4 MARVEL research article.

Reference	Details
Swain et al. (2008)	First observation of CH_4 in an extrasolar planet (HD189733 b).
Karkoschka (1998)	Presence of CH_4 in the spectra of Jovian planets and Titan.
Allen et al. (2013)	On the direct measurement of industrial CH_4 emission.
Leggett et al. (2000)	Distinguishing between L and T type dwarfs using CH_4 absorption.

9.1.2 Task 2 & 3: Experimental data

The collation and review of CH_4 experimental sources for a MARVEL analysis had already been started by summer students Mr Richard Stones and Mr Saajan Sujanani a few years prior to the start of the ORBYTS project. This included research articles up to 2009. Hence the aim for the purposes of ORBYTS was to ensure this previous complication was complete and identify new experimental sources for the years 2010 - 2016.

Experimental sources to be included in the MARVEL analysis are listed in Table 9.2 with their main characteristics. Table 9.3 details experimental sources that will not be included in the current MARVEL analysis and the reason why.

Comments on data sources:

(IIa) 92PuWe: The highly sensitive double resonance spectroscopy technique is employed to measure weak rotational lines of CH_4 in the v_3 band.
(IIb) 85OlAnBaRo: Reports pure rotational Q-branch lines of the vibrational ground state, measured with a pulsed microwave Fourier transform spectrometer. The method is particularly suited to the observation of rotational transitions of non-polar molecules.
(IIc) 87HiLoChDe: Applies a conventional Stark spectrometer to detect four weak rotational transitions resulting from the distortion electronic dipole moment.
(IId) 10BoPiRoBr: High accuracy pure rotational line position are obtained using high intensity synchrotron radiation combined with an FTIR spectrometer at the AILES beamline of SOLEIL.
(IIe) 12SaAuPiRo: Following the work of 10BoPiRoBr, this paper presents measurements of, and N_2/self pressure broadened widths for, 181 pure rotational lines.
(IIf) 93HiBaBrGa: Performs high temperature (850 K) measurements in the dyad region and identifies a number of hot vibrational bands.

Table 9.2: Data sources to be used and their characteristics for $^{12}CH_4$. For comments marked 'II + letter' please refer to the text. Sources that have been analysed in MARVEL to date are marked [A].

Reference	Source Tag	Range cm^{-1}	No. Trans.	T K	Comments
[A]Pursell & Weliky (1992)	92PuWe	0.39 - 0.58	15		IIa
[A]Oldani et al. (1987)	85OlAnBaRo	0.27 - 0.60	27	292	IIb
[A]Holt et al. (1973)	73HoGeOz	0.26 - 0.47	4	292	$v_4 - v_4$
[A]Hilico et al. (1987)	87HiLoChDe	4 - 9	14		IIc
[A]Boudon et al. (2010)	10BoPiRoBr	50 - 500	188	296	IId
Sanzharov et al. (2012)	12SaAuPiRo	50 - 290	181	296	IIe
Hilico et al. (1993)	93HiBaBrGa	1260 - 1275	45	850	IIf
[A]Pinson & Dupre-Maquaire (1979)	79PiDu	1259 - 1305	136	300	v_4
[A]Restelli & Cappellani (1979)	79ReCa	1292 - 1307	111	295	v_4
[A]Bronnikov et al. (1998)	98BrKaRuFi	1260 - 1333	351		IIg
[A]Champion et al. (1989)	89ChHiWeBr	1200 - 1400	44	296	IIh
[A]Hilico et al. (1992)	92HiLoBr	1382 - 1599	248	297	$v_3 - v_3$, $v_3 + v_3$
[A]Hilico et al. (1985)	85HiLoBr	1568 - 1932	413	296	$v_3 - v_4$
Martinez et al. (1997)	97MaBeSaCh	2869 - 2873	21		$2v_1 - v_1$
Owyoung et al. (1978)	78OwPaMc	2916 - 2918	39		v_4
Santos et al. (1992)	92SaCaDoRo	2916 - 2918	44	77, 296	v_1
Bermejo et al. (1992)	92BeSaCa	2911 - 2921	83	296, 500	v_1, $v_2 + v_4$
de Martino et al. (1983a)	83DeFrPrb	2920 - 2980	6		$v_3 - 2v_3$
Menard-Bourcin et al. (2000)	00MeDoMeBo	2942 - 2982	8		IIi
Boursier et al. (2006)	06BoMeMa	2931 - 2996	198		IIj
Pine (1992)	92Pine	3012 - 3019	66	296	IIk
Dang-Nhu et al. (1979)	79DaPiRo	2937 - 3067	30		IIl
de Martino et al. (1983b)	83DeFrPr	3034 - 3068	4		$2v_3$
Fejard et al. (2000)	00FeChJoBr	2884 - 3149	258	296	
Bobin & Fox (1973)	73BoFo	2840 - 3167	361		v_3
Tarrago et al. (1975)	75TaDaPoGu	2850 - 3200	277		IIm
Huth et al. (1981)	81HuBrToBr	2400 - 3200	705	296	$v_2 + v_3$
Grigoriev et al. (2002)	02GrFiToCh	3182 - 3224	92		IIn
Husson et al. (1972)	72HuPoVaAm	4136 - 4288	182		$v_1 + v_4$
Predoi-Cross et al. (2005)	05PrBrMaBr	4100 - 4635	1432	298	IIo
Hilico et al. (1980)	80HiDeChGu	4400 - 4650	886	296	$v_3 + v_4 - v_4$
Brown & Rothman (1982)	82BrRo	4136 - 4666	1800	296	IIp
[A]Albert et al. (2009)	09AlBaBoBr	0 - 4800	9300	78	IIq
Daumont et al. (2013)	13DaNiThRe	4600 - 4887	1014	290, 296	IIr
Robert et al. (2001)	01RoHiLoCh	4909 - 5272	189		$4v_4$
Nikitin et al. (2014)	14NiThReDa	4800 - 5300	2725		IIs
Georgoes et al. (1998)	98GeHeHiRo	5577 - 6077	22	17	IIt
Bobin (1972)	72Bo	5890 - 6107	82		$2v_3$
Rank et al. (1960)	60RaEaSkWi	5983 - 6115	107		$2v_3$
Zolot et al. (2013)	13ZoGiBaSw	5870 - 6130	611		IIu
Nikitin et al. (2016)	16NiReTaKa	6539 - 6800	2443	80	IIv
Hipper & Quack (2001)	01HiQu	7478 - 7553	23	296	$v_2 + 2v_3$
Pierre et al. (1980)	80PiHiDeMa	9000 - 9156	45	149	$3v_3$
Campargue et al. (1995)	95CaPeJo	11245 - 11313	10		IIw
Boraas et al. (1994)	94BoLiRe	11120 - 11325	30	15	$3v_1 + v_3$
Campargue et al. (1991)	91CaChSt	13702 - 13806	20		IIx

Table 9.3: Data sources not included in the current MARVEL analysis and their characteristics for $^{12}CH_4$.

Reference	Source Tag	Range cm^{-1}	No. Trans	T K	Comments
Margolis (1988)	88Margolis	5500 - 6180	2000	296	unassigned
Margolis (1990)	90Margolis	5500 - 6150	1600	296	unassigned
Brown (1988)	88Brown	3700 - 4136	1900	297	unassigned
Nassar & Bernath (2003)	03NaBe	2000 - 6400	26821	1273	unassigned
Béguier et al. (2015)	15BeLiCa	9523 - 10435	7212	296	empirical
Hargreaves et al. (2012a)	12HaBeMi	960 - 5000	12000	1673	unassigned

(IIg) 98BrKaRuFi: This paper investigates non-equilibrium distribution of vibrationally excited methane in a supersonic jet and records high resolution spectra in the 8 μm region. Many vibrational bands are observed.
(IIh) 89ChHiWeBr: Presents an analysis of the v_2/v_4 dyad of $^{12}CH_4$ and $^{13}CH_4$ using new infra-red measurements combined with existing microwave data.
(IIi) 00MeDoMeBo: Investigate the ro-vibrational energy transfer processes occurring in CH_4 upon inelastic collisions using time-resolved double resonance measurements.
(IIj) 06BoMeMa: The pump-probe technique is used to excite methane molecules to selected levels and observe numerous transitions in the pentad, tetracontad and triacontad regions.
(IIk) 92Pine: Retrieved Self-, N_2-, O_2-, H_2-, Ar and He pressure broadening parameters for Q-branch lines in the v_3 band.
(IIl) 79DaPiRo: Measured spectral intensities in the v_3 band for $^{12}CH_4$ and $^{13}CH_4$.
(IIm) 75TaDaPoGu: Derived ground state energies through observation of forbidden v_3 transitions.
(IIn) 02GrFiToCh: Determined line parameters and shapes for R branch lines of the v_3 band of CH_4 broadened by helium pressure.
(IIo) 05PrBrMaBr: Derived self-broadening coefficients from a multis-pectrum analysis of $^{12}CH_4$ from 4100 - 4635 cm^{-1}.
(IIp) 82BrRo: Positions and intensities are measured for some 1800 absorptions, around 25% of these are unassigned.
(IIq) 09AlBaBoBr: The authors combine new cold (78 K) measurements and data from several other sources to perform a global analysis in the region 0 - 4800 cm^{-1}.
(IIr) 13DaNiThRe: Presents new assignments for the octad band system of $^{12}CH_4$.
(IIs) 14NiThReDa: Studies CH_4 absorption in the region 4800 - 5300 cm^{-1} with long path-length (1603 m) spectra, the resulting experimental line list is partially assigned.
(IIt) 98GeHeHiRo: Recorded absorption spectra of jet cooled $^{12}CH_4$ and assigned lines to several vibrational bands.
(IIu) 13ZoGiBaSw: Employs a dual frequency comb to measure Doppler-limiting spectra of CH_4 and C_2H_2.
(IIv) 16NiReTaKa: Provides assignments for a subset of lines in the WKLMC experimental line list constructed by Campargue et al. (2013).

(IIw/IIx) 91CaChSt/95CaPeJo: Both studies measure high overtone transitions of methane in a supersonically cooled jet.

9.1.3 Task 4 & 5: MARVEL

A MARVEL input file contains four types of information, frequencies, uncertainties, labels and references. The frequency is the measured line position in units cm^{-1}. Some research articles, particularly for rotational transitions, record line position in alternative units, for example MHz. In which case the line position is converted to cm^{-1} (by dividing the frequency in Hz by the speed of light in cm/s, see Table 2) before use. The uncertainty is self explanatory though not always specified in the research articles. In cases where the uncertainty in line position is not known, the resolution of the measurements divided by two is assumed to represent the uncertainty. Labels are quantum labels identifying the upper and lower energy levels associated with a measured transition, see discussion below. Each line in the MARVEL input file is given a reference string, constructed out of the source tag (see Table 9.2), spin state (ortho/meta/para) and line number. For example `79ReCa_meta.1` is the first meta transition from the 79ReCa (Restelli & Cappellani (1979)) dataset.

Methane Quantum Labels: As mentioned earlier YT10to10 employs 15 quantum labels per energy level, these are:

$$v_1 \;\; v_2 \;\; v_3 \;\; v_4 \;\; L_2 \;\; L_3 \;\; L_4 \;\; M_3 \;\; M_4 \;\; J \;\; K \;\; \Gamma_{\text{rot}} \;\; \Gamma_{\text{vib}} \;\; \Gamma_{\text{tot}} \;\; N_{J,\Gamma_{\text{tot}}}$$

as defined in Section 3.1.4. The most common quantum number set employed by experimental works is:

$$v_1 \;\; v_2 \;\; v_3 \;\; v_4 \;\; J \;\; \Gamma_{\text{tot}} \;\; n$$

where n is a counting number. A number of works also provide Γ_{vib}.

MARVEL is agnostic to the choice of quantum label set, in fact the set could be comprised entirely of counting numbers if one so desired. However since the intention is to employ the results alongside variational line list YT10to10 in the second CH_4 project (Section 9.2) it seems sensible to use the same quantum label set.

For the purposes of constructing MARVEL inputs from the sources tabulated in Table 9.2, the 7 label 'experimental' set is employed. Inconsistencies between datasets are handled by adjusting the counting number n. Once validated, the resulting MARVEL energies can be reassigned using the 15 label 'YT10to10' set, by comparison to computed YT10to10 energies.

The CH_4 spectroscopic network has three principle components, ortho, para and meta, as transitions between the three spin states are forbidden (although some have been observed Yi et al. (1970)). As such a MARVEL analysis for each spin state can be performed separately, with the ortho, para and meta master files being combined

at the end of the analysis to produce the final list of energies. An extract from the meta master file is given in Table 9.4.

Thus far 2074, 517 and 631 transitions from 12 experimental sources have been analysed in MARVEL, resulting in 984, 268 and 343 energies for ortho-, para- and meta-CH_4 respectively. The results are visualised in Figure 9.1, Figure 9.2 and Figure 9.3. These network plots were generated using Gephi. Gephi is an open source visualisation program for graphs and networks (Gephi Consortium (2016)). The nodes (coloured circles) represent energy levels while the edges (coloured arrows) represent transitions. Other than looking pretty these plots highlight the size and connectivity of networks within the principle components and can indicate the location of 'hubs', sites of high density links. For example the meta component (Figure 9.1) currently contains 1 spectroscopic network and 23 floating components, and energies in the spectroscopic networks are bound to the network by up to 5 links (transitions). As more data is added to the master file the networks will likely grow and link up to some of the floating components.

Table 9.4: Extract from the meta-CH_4 MARVEL input. Pos. is the line position, Unc. is the uncertainty in line position and Ref. is the reference tag 10BoPiRoBr_meta.N where N is the line number.

Pos. cm^{-1}	Unc. cm^{-1}	v_1'	v_2'	v_3'	v_4'	n'	J'	Γ'_{tot}	v_1''	v_2''	v_3''	v_4''	n''	J''	Γ''_{tot}	Ref.N
182.92118	0.001	0	0	0	1	3	11	A2	0	0	0	1	2	10	A1	10BoPiRoBr_meta.35
185.14892	0.001	0	0	0	0	1	18	A2	0	0	0	0	1	17	A1	10BoPiRoBr_meta.36
185.81261	0.001	0	0	0	0	1	18	A1	0	0	0	0	1	17	A2	10BoPiRoBr_meta.37
195.41070	0.001	0	0	0	0	1	19	A2	0	0	0	0	1	18	A1	10BoPiRoBr_meta.38
195.69065	0.001	0	0	0	0	1	19	A1	0	0	0	0	2	18	A2	10BoPiRoBr_meta.39
208.57552	0.001	0	0	0	1	2	11	A2	0	0	0	1	1	10	A1	10BoPiRoBr_meta.40
210.08444	0.001	0	0	0	1	3	11	A1	0	0	0	1	1	10	A2	10BoPiRoBr_meta.41
214.27081	0.001	0	1	0	0	1	2	A2	0	0	0	1	1	2	A1	10BoPiRoBr_meta.42
234.60288	0.001	0	0	0	1	3	12	A2	0	0	0	1	1	11	A1	10BoPiRoBr_meta.43
251.65046	0.001	0	0	0	1	4	13	A2	0	0	0	1	1	12	A1	10BoPiRoBr_meta.44
259.42717	0.001	0	0	0	1	3	14	A1	0	0	0	1	1	13	A2	10BoPiRoBr_meta.45

9.1.4 Task 6: Validation and Re-assignment

To ensure correct energies in an absolute sense are computed for each principle component (ortho/meta/para) of the CH_4 spectroscopic network so called 'Magic Numbers' can be introduced to the final all inclusive master file. These are 'fake' transitions linking the roots of each higher energy network (ortho/para) to the ground state (meta, which has zero energy by definition). For CH_4 this may not be required as 'forbidden' transitions between spin states have been observed (Yi et al. (1970)).

However for the purposes of validating the current output 'Magic numbers' 10.48176 cm^{-1} (ortho-meta) and 31.44246 cm^{-1} (para-meta) resulting from an effective Hamiltonian (EH) fit (V. Boudon, private communication) were introduced. The MARVEL energies are compared to experimental energies determined previously from a EH fit

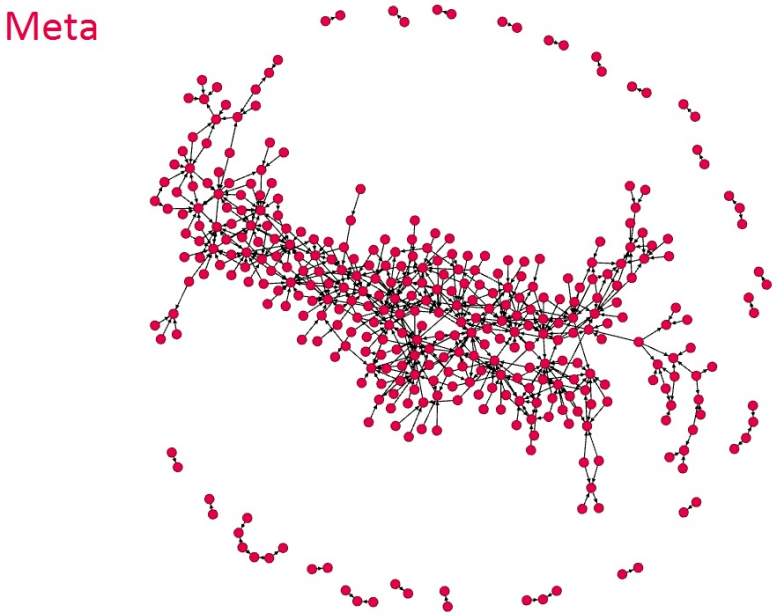

Figure 9.1: Visualisation of the meta-CH_4 spectroscopic network. This contains 1 network and 23 floating components.

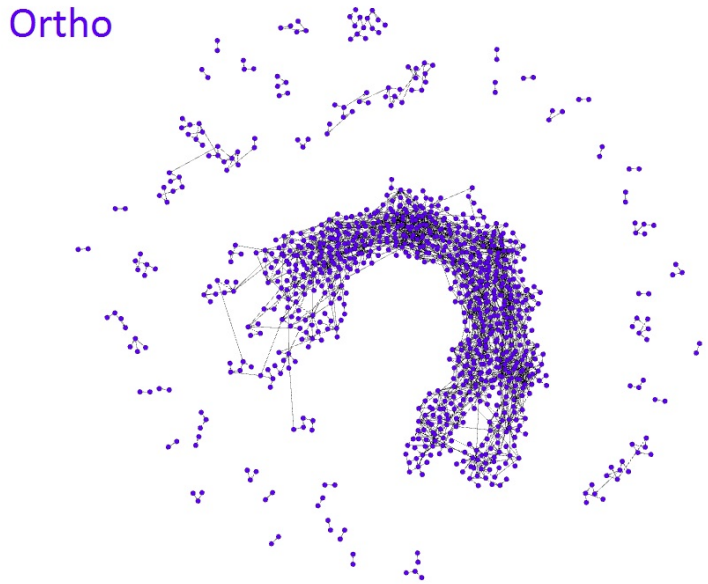

Figure 9.2: Visualisation of the ortho-CH_4 spectroscopic network. This contains 5 networks and 38 floating components.

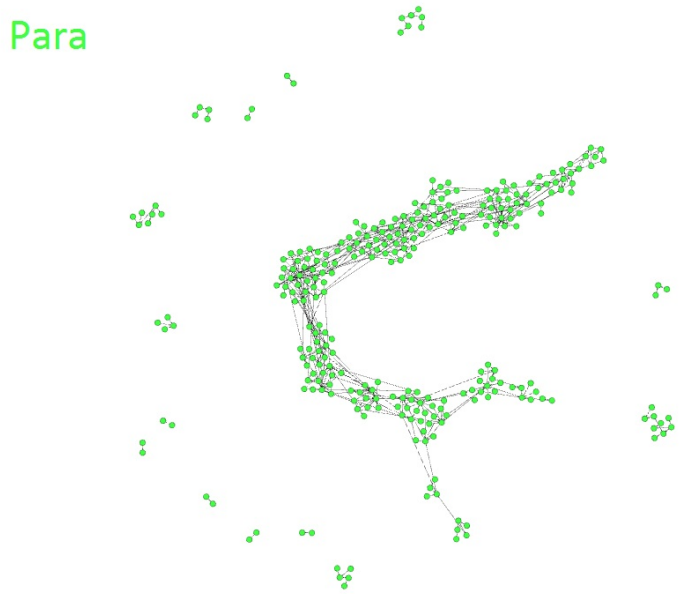

Figure 9.3: Visualisation of the para-CH_4 spectroscopic network. This contains 1 network and 14 floating components.

(V. Boudon, private communication). All energies agree within the respective uncertainties, a sample of comparisons is presented in Table 9.5. Also shown here is the YT10to10 assignment generated by matching the experimental energy to a calculated energy (within ≈ 1 cm^{-1}) and 'experimental' labels (v_1 v_2 v_3 v_4 J Γ_{tot}) to equivalent YT10to10 labels.

9.2 Analysis of Hot Fourier Transform Infrared Spectra

As discussed in Chapter 7, an extensive FTIR measurement campaign was carried out by Dr Alexander Fateev on the hot absorption spectrum of CH_4 in the region 200 - 7000 cm^{-1}, with the most useful information contained within 1000 - 6300 cm^{-1}. The varying temperature and concentrations used in the measurements allows the signal to noise and strength (avoiding saturation) for different regions of the spectrum to be optimised.

The CH_4 spectrum is often characterised in terms of polyads, groups of states or transitions which have similar energies or frequencies (Boudon et al. (2006)).

Four polyad regions are present in the current spectra which will be the focus of the planned analysis. These are the dyad, 1000 - 2000 cm^{-1} (Figure 9.4), pentad 2700 - 3300 cm^{-1} (Figure 9.5), octad 3700 - 4600 cm^{-1} (Figure 9.6) and tetradecad 5800 - 6300 cm^{-1} (Figure 9.7). Wavenumber ranges quoted here are with respect to the

Table 9.5: Validation of MARVEL output by comparison of MARVEL energies and previously determined experimental energies (V. Boudon, private communication). YT10to10 assignments are presented on the right. For the symmetries $\Gamma_{\rm vib}$, $\Gamma_{\rm rot}$ and $\Gamma_{\rm tot}$: 1 = A_1, 2 = A_2, 3 = E, 4 = F_1 and 5 = F_2. $N_{J,\Gamma_{\rm tot}}$ for all these states equals 1.

MARVEL cm^{-1}	Experiment cm^{-1}	v_1	v_2	L_2	v_3	L_3	M_3	v_4	L_4	M_4	J	K	$\Gamma_{\rm vib}$	$\Gamma_{\rm rot}$	$\Gamma_{\rm tot}$
689.8857	689.8861	0	0	0	0	0	0	0	0	0	11	2	3	1	3
690.0391	690.0396	0	0	0	0	0	0	0	0	0	11	6	3	1	3
1880.5813	1880.5823	0	0	0	0	0	0	1	1	1	10	3	5	5	3
1416.5539	1416.5534	0	0	0	0	0	0	0	0	0	16	2	3	1	3
1593.0442	1593.0446	0	0	0	0	0	0	0	0	0	17	2	3	1	3
1778.2040	1778.2049	0	0	0	0	0	0	0	0	0	18	18	3	1	3
1975.0141	1975.0146	0	0	0	0	0	0	0	0	0	19	18	3	1	3
1988.3197	1988.3236	0	0	0	0	0	0	1	1	1	11	3	5	5	3

current experimental measurements and may not reflect the full extent of the polyad. The spectrum of methane is very dense, around five times more dense than the NH_3 spectrum, hence the subwavenumber accuracy of the variational line list YT10to10, although more than enough for certain applications, will make reliable assignment by line list comparison difficult. The methods employed to take on this challenge will be:

1. Estimating the lower energy using the experimental peak intensity at both temperatures (see Section 4.4) to limit the number of possible 10t0 lines per experimental peak.

2. Combining MARVEL frequencies (computed from the MARVEL energies, Section 9.1) with YT10to10 intensities to generate 'trivial' assignments and initiate assignment by the method of branches (see Section 4.3.3).

9.2.1 Preliminary Work

To determine what information may be derived from the analysis, a list of observable YT10to10 lines for the experimental conditions is constructed for each polyad. The vibrational bands in each region are summarised in Table 9.6, Table 9.7, Table 9.8 and Table 9.9. For simplicity, and due to the lack of use of 'L', 'M' and 'K' labels in experimental works, abbreviated vibrational labels (v_1 v_2 v_3 v_4) are used to identify bands in these tables and only the highest value of the rotational quantum number, J, is indicated. Full YT10to10 quantum numbers will be employed during the actual assignment process. If the band has been measured previously, $J_{\rm max}$ from the literature is also specified. Clearly there is sufficient potential new information to justify pursuing a detailed analysis.

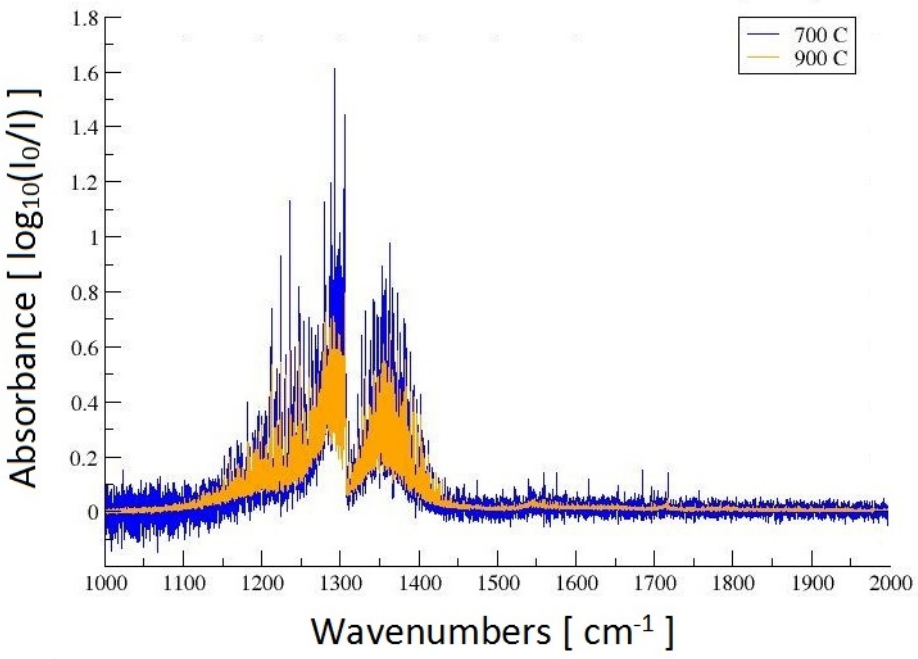

Figure 9.4: Overview of 7% CH_4 experimental measurements for the dyad at 700/900 °C.

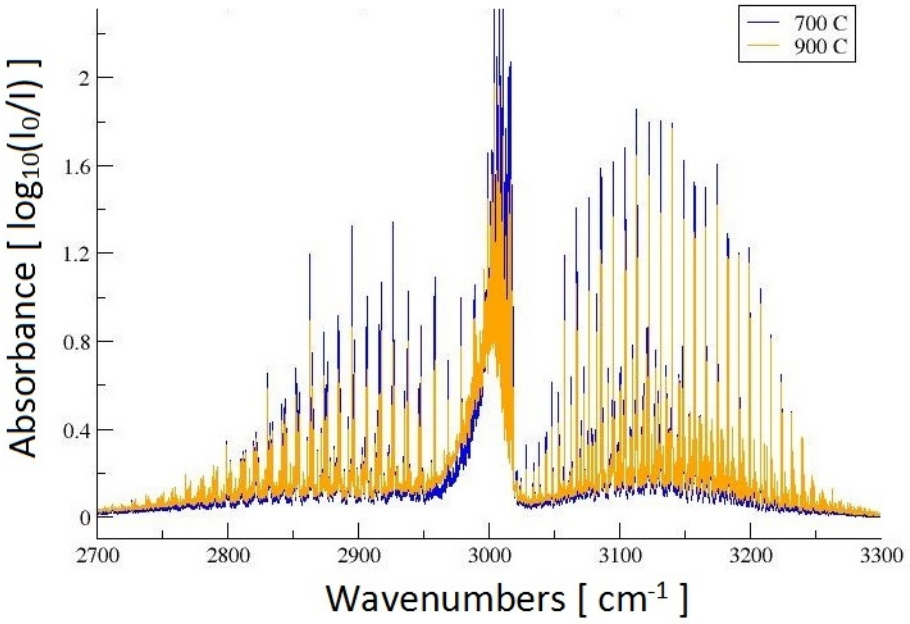

Figure 9.5: Overview of 7% CH_4 experimental measurements for the pentad at 700/900 °C.

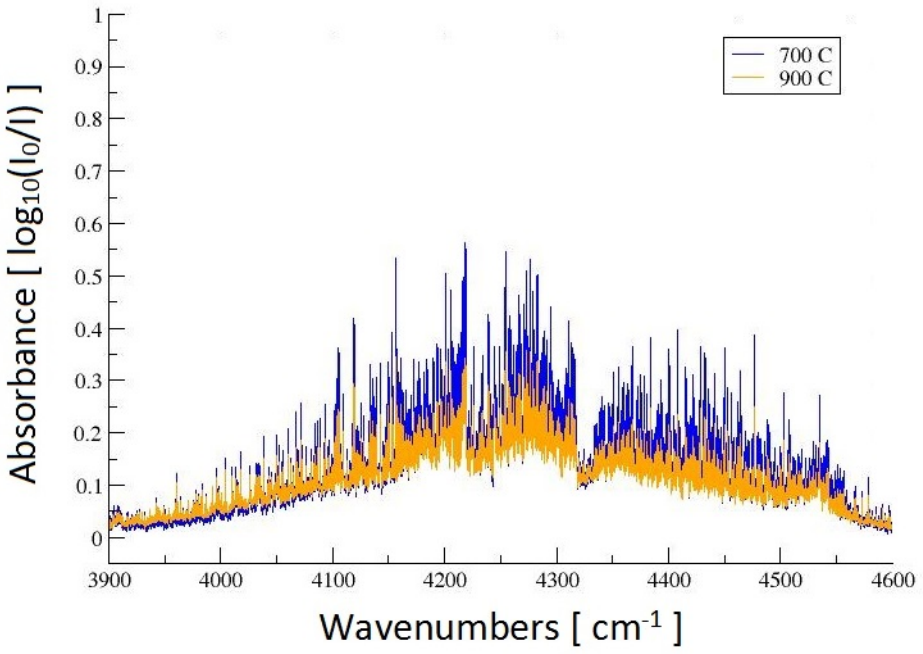

Figure 9.6: Overview of 50% CH_4 experimental measurements for the octad at 700/900 °C.

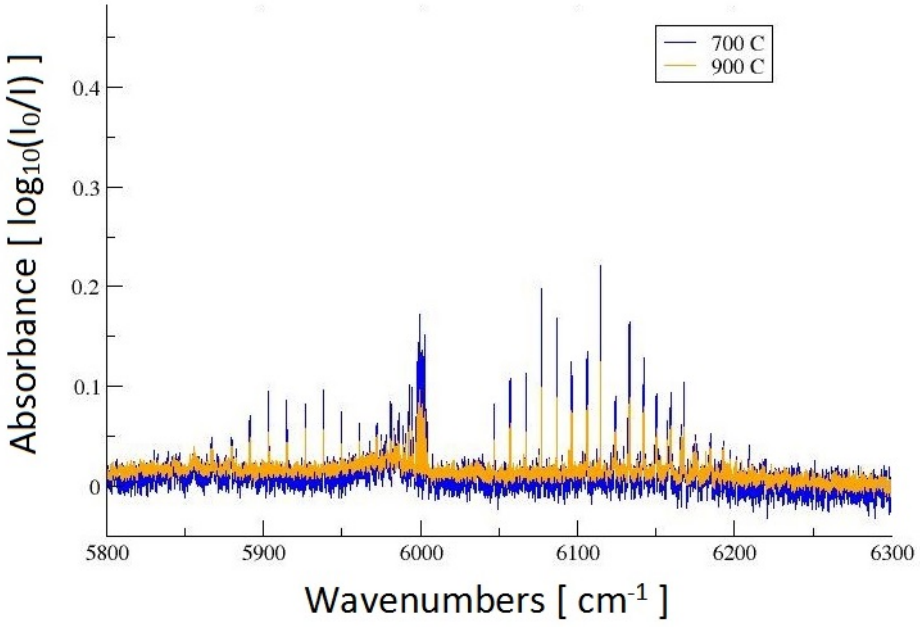

Figure 9.7: Overview of 50% CH_4 experimental measurements for the tetradecad at 700/900 °C.

Table 9.6: Summary of observable vibrational bands in the dyad of CH_4 at 700/900 °C. $J_{max}^{YT10to10}$ is the highest observable rotational excitation in the current experiment based on YT10to10. J_{max}^{obs} is the highest previously observed rotational excitation. NB indicates a potential new band.

Band	$J_{max}^{YT10to10}$	Comment
v_4	28	$J_{max}^{obs} = 22$
$2v_4$ - v_4	26	$J_{max}^{obs} = 11$
$3v_4$ - $2v_4$	22	$J_{max}^{obs} = 10$
$4v_4$ - $3v_4$	15	$J_{max}^{obs} = 9$
v_2	23	$J_{max}^{obs} = 22$
$2v_2$ - v_2	19	$J_{max}^{obs} = 13$
v_3 - v_4	13	$J_{max}^{obs} = 14$
v_3 - v_2	15	$J_{max}^{obs} = 13$
v_1 - v_2	18	$J_{max}^{obs} = 13$
$(v_2 + v_4)$ - v_2	21	$J_{max}^{obs} = 8$
$(2v_2 + v_4)$ - $2v_2$	8	$J_{max}^{obs} = 6$
$(v_1 + v_4)$ - v_1	11	NB
$(v_3 + v_4)$ - v_3	11	$J_{max}^{obs} = 5$
$(v_2 + 2v_4)$ - $(v_2 + v_4)$	18	$J_{max}^{obs} = 6$
$(v_1 + v_4)$ - $(v_2 + v_4)$	12	NB

9.3 Summary of Results

A MARVEL analysis of the infra-red spectrum of $^{12}CH_4$ has been started. To date 3222 transitions from 12 experimental sources have been analysed resulting in 1595 experimental energies below 5000 cm^{-1}. The current analysis will be expanded in the near future to include transitions measured by a further 34 experimental sources. On completion the resulting energies shall be reassigned using YT10to10 quantum numbers and employed in the analysis of hot CH_4 spectra in the region 1000 - 6300 cm^{-1}.

Table 9.7: Summary of observable vibrational bands in the pentad of CH_4 at 700/900 °C. $J_{max}^{YT10to10}$ is the highest observable rotational excitation in the current experiment based on YT10to10. J_{max}^{obs} is the highest previously observed rotational excitation. NB indicates a potential new band.

Band	$J_{max}^{YT10to10}$	Comment
v_3	20	$J_{max}^{obs} = 23$
$2v_2$	14	$J_{max}^{obs} = 24$
$v_1 + v_4$	17	$J_{max}^{obs} = 22$
$2v_3$ - v_3	17	$J_{max}^{obs} = 7$
$2v_1$ - $(v_2 + v_4)$	10	NB
$(v_3 + v_4)$ - v_4	21	$J_{max}^{obs} = 11$
$(v_2 + v_3)$ - v_2	21	$J_{max}^{obs} = 16$
$(v_2 + 2v_4)$ - v_4	20	$J_{max}^{obs} = 16$
$(v_1 + v_4)$ - v_4	22	$J_{max}^{obs} = 16$
$(v_3 + 2v_4)$ - $2v_4$	22	NB
$(2v_2 + v_4)$ - v_4	21	$J_{max}^{obs} = 17$
$(2v_3 + v_4)$ - $2v_2$	18	NB
$(2v_2 + 2v_4)$ - $2v_4$	14	NB
$(v_1 + 2v_4)$ - $2v_4$	16	NB
$(v_2 + 3v_4)$ - $2v_4$	15	NB
$(v_1 + v_2 + v_4)$ - $2v_4$	14	NB
$(v_2 + v_3 + v_4)$ - v_1	11	NB
$2v_3$ - $(v_2 + v_4)$	17	NB
$(v_1 + v_3)$ - $(v_2 + v_4)$	16	NB
$(3v_2 + v_4)$ - $(v_2 + v_4)$	11	NB
$(v_1 + v_2 + v_4)$ - $(v_2 + v_4)$	13	NB
$(v_2 + v_3 + v_4)$ - $(v_2 + v_4)$	20	NB

Table 9.8: Summary of observable vibrational bands in the octad of CH_4 at 700/900 °C. $J_{max}^{YT10to10}$ is the highest observable rotational excitation in the current experiment based on YT10to10. J_{max}^{obs} is the highest previously observed rotational excitation. NB indicates a potential new band.

Band	$J_{max}^{YT10to10}$	Comment
$v_1 + v_4$	17	$J_{max}^{obs} = 16$
$v_3 + v_4$	21	$J_{max}^{obs} = 16$
$v_2 + v_3$	13	$J_{max}^{obs} = 18$
$v_2 + 2v_4$	9	$J_{max}^{obs} = 15$
$2v_2 + v_4$	12	$J_{max}^{obs} = 13$
$(v_3 + 2v_4)$ - v_4	15	NB
$(v_1 + 2v_4)$ - v_4	14	NB

Table 9.9: Summary of observable vibrational bands in the tertradecad of CH_4 at 700/900 °C. $J_{max}^{YT10to10}$ is the highest observable rotational excitation in the current experiment based on YT10to10. J_{max}^{obs} is the highest previously observed rotational excitation.

Band	$J_{max}^{YT10to10}$	Comment
$2v_3$	12	$J_{max}^{obs} = 10$

Chapter 10

Pressure Dependent Cross Sections for τ - REx

One of the aims of this work was to collaborate with the exoplanet group at UCL on the development of a new spectral retrieval code τ-REx (Waldmann et al. (2015a,b)). In particular the goal was to ensure accurate and optimal use of the ExoMol line lists for modelling the transmission or emission spectra of extrasolar planets within the code.

The core virtue of ExoMol is to compute all allowed transitions, or as many as is computational feasible, that could influence the molecular spectrum at high temperatures, typically 1500 K or higher. It has been proven that the completeness of a line list can significantly influence atmospheric models at these temperatures (see for example Yurchenko et al. (2014)). Therefore one of the objectives of the τ-REx project was to implement the most complete opacity data available in the atmospheric models, in other words the ExoMol line lists where possible.

It was immediately apparent that the direct implementation of the full line lists was simply impractical due to their sheer size. Fortunately Hill et al. (2013) had already proposed a method to combat the data handling issues associated with the line lists, by representing the molecular absorptions as cross sections. Table 10.1 compares dataset sizes for three ExoMol molecules. Here a line list refers to a file with a four column entry for every computed line of the molecule: line position, line intensity, thermal broadened width, pressure broadened width. These properties are required to model the molecular spectrum for a single temperature and pressure. Cross section refers to a file with a two column entry for every wavenumber bin: central wavenumber, cross section. The size of the cross section file is dependent on the total number of wavenumber bins and hence the grid on which the cross sections are generated. ExoMol currently provides cross sections on a grid with a spacing of $\Delta\tilde{\nu}$= 0.01 cm^{-1} which corresponds to a spectral resolution of R $\approx 10^5 - 10^6$ at $\lambda < 10\mu m$. As Table 10.1 demonstrates the saving on disk space alone is considerable.

For the τ-REx project the decision was made to construct a library of pre-computed high resolution ($\Delta\tilde{\nu} = 0.01$ cm^{-1}) cross sections for a fixed range of temperatures and pressures. A routine could then be written to retrieve cross sections at required resolution, temperature and pressure from the library using binning or

Table 10.1: Comparison of line list versus cross section dataset size for three ExoMol molecules

Molecule	Number of ExoMol Lines	Line list file size	Cross section file size (for $\Delta\tilde{\nu} = 0.01$ cm^{-1})
KCl	1,326,765	∼2 GB	32 MB
H_2O	505,806,202	∼40 GB	73 MB
CH_4	9,819,605,160	∼13 TB	70 MB

interpolation procedures respectively.

This approach has two main advantages. Firstly, assuming that the cross sections are computed on a fine enough grid to preserve their spectroscopic features, cross sections can provide an ideal solution to the data handling problems posed by large line lists. Secondly, pre-computing the cross sections means the routine for inputting molecular data to the retrieval code can remain the same while the method or data used to compute the cross sections is revised or updated as required.

The generation of cross sections involves a series of numerical considerations which can impact the results. Even subtly dissimilar choices here can lead to a different answer. The method employed by ExoMol to compute pressure dependent cross sections is currently under review and is likely to change in the near future to incorporate more accurate and efficient techniques for evaluating line shapes. In addition, the source of line lists or pressure broadening parameters used to compute the cross sections may also change as more accurate or complete theoretical or experimental work becomes available. This could involve a change in the format of the input line list, for example from HITRAN to ExoMol format.

Prior to this work, all ExoMol cross sections were calculated at zero pressure. This was mostly due to the lack of pressure broadening information relevant to current spectroscopically accessible extrasolar planetary atmospheres (Hill et al. (2013)). Present atmospheric observations are most sensitive to hot giant planets with H_2/He atmospheres (Hedges & Madhusudhan (2016)), yet broadening of molecular lines by H_2/He pressure has been the subject of relatively few studies, particularly at high temperatures (see Chapter 11). However it has been shown that pressure broadening may be significant in extrasolar planetary atmospheres, particularly at long wavelengths (Tinetti et al. (2012)), meaning the current cross sections are not sufficient.

The provision of temperature-, pressure- and broadening species dependent cross sections would be computationally demanding. Also the reliability of these cross sections for molecules with little or no data on broadening by appropriate species would be highly questionable. As such only the computation of temperature- and pressure-dependent cross sections for key molecular species in a mixed H_2/He environment are pursued for the time being, provided suitable pressure broadening information is available. However it should be noted that some super-Earth's and mini-Neptune's are expected to have atmospheres that are not H_2-dominated, and instead have water-rich, oxygen-rich or even hydrocarbon-rich atmospheres (Hu & Seager (2016)). To

compute cross sections suitable for modelling these atmospheres broadening by other species and self broadening, in particular for the case of water-rich atmospheres, would have to be taken into account.

At present ExoMol will supply H_2/He pressure dependent cross sections for H_2O, CO, CO_2, NH_3 and CH_4. H_2O, CO, CO_2 and CH_4 have all been detected in the atmospheres of extrasolar giant planets (see Swain et al. (2010) and references therein). NH_3 is also expected to be important due to its presence in the atmosphere of solar system planets (see for example Sudarsky et al. (2003)) and cool stars (see for example Canty et al. (2015)).

The aim of this work was to compute H_2/He pressure dependent cross sections for H_2O, CO, CO_2 and NH_3. The temperature range considered is 300 - 2000 K for H_2O and 300 - 1500 K for CO, CO_2 and NH_3. The pressure range considered is 0.001 - 10 bar for all molecules. CH_4 cross sections will generated by Dr. Segery Yurchenko. Section 11.1 describes a series of numerical tests used to inform the cross section computation method employed by this work. Section 11.2 discusses the results for the case study H_2O, the molecule with the most complete H_2/He pressure broadening dataset, and Section 11.3 presents the results for CO_2, CO, and NH_3.

10.1 Generating Cross Sections: Numerical Considerations

Generation of pressure dependent cross sections requires the following numerical considerations which impact both computational time and accuracy:

1. **Importance Sampling:** Whether a cut-off in intensity can be applied to reduce the computation time for large line lists without significant loss of opacity.

2. **Profile evaluation width:** To what extent should a Voigt profile be evaluated considering the computational cost and the non-physical behaviour of the far wings.

3. **Profile grid resolution:** What grid spacing is required to adequately sample the contribution from each profile.

4. **Pressure broadening parameters:** Does the use of an approximate set of parameters significantly alter the resulting cross sections.

5. **Temperature - pressure grid:** At which temperatures and pressures should cross sections be computed to minimise interpolation errors.

The impact of the above factors on the cross sections is investigated in the following sections by running test calculations for H_2O, the molecule with the most complete H_2/He pressure broadening dataset. H_2O was also the test case for a similar investigation carried out by Hedges & Madhusudhan (2016).

10.1.1 Importance Sampling

As noted previously, high temperature line lists can contain several billion entries. Consequently the generation of cross sections, which involves line-by-line calculations, can be very computationally expensive, particularly if one attempts to explore a broad parameter space.

One method of tackling this problem is to evaluate only the most significant lines. Lines with an integrated absorption intensity, $S(T)_j^a$ (see Eq.(3.27) in Chapter 3), greater than some threshold, $S_{cut}^a(T)$, at the relevant temperature are included in the calculation while lines with $S(T) < S_{cut}(T)$ are discarded.

$S_{cut}^a(T)$ can be a fixed value for all lines selected to reduce computation time with (ideally) minimal effect on the accuracy. For example Hedges & Madhusudhan (2016) and Sharp & Burrows (2007) applied fixed cut-offs of 1×10^{-30} cm/molecule and 1×10^{-40} cm/molecule respectively when sampling a line list for H_2O. Or $S_{cut}^a(T)$ can be wavenumber dependent. Rothman et al. (2013) and Rothman et al. (2010) for example split the H_2O spectrum into wavenumber domains to take into account the radiation field at very low wavenumbers whilst reducing the disk storage required for the remainder of the line list.

Rothman et al. (2010) domains:

$$S_{cut}(T) = \frac{S_{crit}}{\tilde{\nu}_{crit}} \tanh\left(\frac{c_2\tilde{\nu}}{2T}\right) \quad \text{for} \quad 0 < \tilde{\nu} \leq 5000 \text{ cm}^{-1} \tag{10.1}$$

$$S_{cut}(T) = S_{crit} \quad \text{for} \quad 5000 < \tilde{\nu} \leq 7000 \text{ cm}^{-1} \tag{10.2}$$

$$S_{cut}(T) = \frac{S_{crit}}{3} \quad \text{for} \quad \tilde{\nu} > 7000 \text{ cm}^{-1} \tag{10.3}$$

where $S_{crit} = 3 \times 10^{-27}$ cm/molecule and $\tilde{\nu}_{crit} = 2000$ cm^{-1}.

Rothman et al. (2013) domains:

$$S_{cut}(T) = \frac{S_{crit}\tilde{\nu}}{\tilde{\nu}_{crit}} \tanh\left(\frac{c_2\tilde{\nu}}{2T}\right) \quad \text{for} \quad 0 < \tilde{\nu} \leq 2000 \text{ cm}^{-1} \tag{10.4}$$

$$S_{cut}(T) = S_{crit} \quad \text{for} \quad \tilde{\nu} > 2000 \text{ cm}^{-1} \tag{10.5}$$

where $S_{crit} = 1 \times 10^{-29}$ cm/molecule and $\tilde{\nu}_{crit} = 2000$ cm^{-1}.

In this work the effect of applying different thresholds $S_{cut}^a(T)$ (see first column of Table 10.2 or Table 10.3) on the calculated cross section is investigated for different wavenumber regions of the H_2O spectrum. Tests are performed for the temperature extremes of the current parameter space. At 300 K, applying an intensity threshold is expected to result in a significant reduction in computation time, as comparatively few lines influence the total opacity. At 2000 K, many lines with a small $S(T)_j^a$ could add up to an appreciable amount of opacity hence the $S_{cut}^a(T)$ that results in

minimal change in the total opacity may be different than for lower temperatures. The following procedure is carried out for each test:

1. The BT2 line list is sampled at the relevant temperature, lines with $S(T) < S_{cut}(T)$ are discarded.

2. $S(T)_j^a$ for remaining lines is summed for the whole wavenumber region to give a representative value of the total retained opacity.

3. The reduced line list is used to compute a set of zero pressure cross sections using a grid spacing of 0.01 cm^{-1}. The computation time is noted.

Figure 10.1 illustrates a zero pressure cross section for H_2O at 300 K and 2000 K for a 0.01 cm^{-1} grid spacing. One may immediately deduce that the impact of $S_{cut}^a(T)$ will vary with spectral region as $\sigma_{max}(T)$ for a given region can change by orders of magnitude. Representative results of the importance sampling tests are presented in Table 10.2 and Table 10.3.

As expected, for both temperatures, the $S_{cut}^a(T)$ that results in no (to 10 decimal places) or negligible ($< 10^{-6}$) change in $\Sigma\ S(T)_j^a$ varies with spectral range and temperature. To ensure negligible loss of opacity over all temperatures considered, cut-offs of 1×10^{-33} cm/molecule for $\tilde{\nu} < 10,000$ cm^{-1} and 1×10^{-36} cm/molecule for $\tilde{\nu} > 10,000$ cm^{-1} are required.

The computational saving of applying these cut-offs at 300 K is dramatic, the calculation can be more than 100 times faster, while at 2000 K the saving is small, only a few percent. However, when considering a broad parameter space, it can still be worthwhile to apply the cut-offs at high temperatures as a small reduction in time required per cross section calculation can add up to hours or days.

In the current work the line lists are sampled with multiple cut-offs to speed up the cross sections whilst ensuring negligible ($< 10^{-6}$) loss of opacity. The optimal cut-offs were determined from cross section calculations. For the molecules considered in this work these cut-offs are summarised in Table 10.4. Note that cut-offs have already been applied to the CO (Li et al. (2015)) and CO_2 (Tashkun & Perevalov (2011)) line lists.

10.1.2 Voigt evaluation width

In theory the Voigt profile (Eq. (3.33) in Section 3.2.2), employed to model the joint contributions from thermal and collision broadening, is infinite in extent and, provided only very weak interactions between molecules occur, a good description of the broadened line shape. In reality computing a Voigt profile out to the extremes of the wavenumber range considered for every line in impractical, and physically inaccurate (Hartmann et al. (2008); Tennyson et al. (2014); Thomas & Stamnes (1999)). Realistic collision perturbations result in collisional narrowing, line mixing, asymmetry and shift of the profile with respect to its unperturbed centre (Hartmann et al. (2008); Thomas & Stamnes (1999)). Fortunately the core and near wings of a pressure broadened line remain predominately Lorentzian in nature, even under severe conditions.

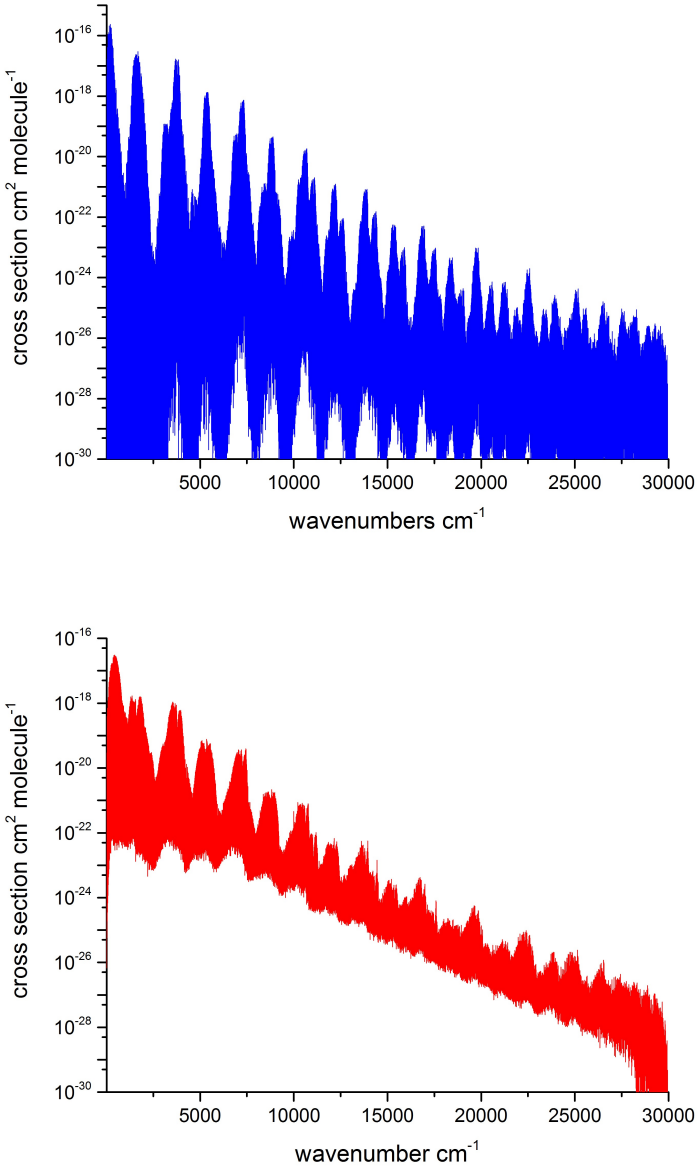

Figure 10.1: Overview of H_2O spectrum at 300K (upper) and 2000 K (lower).

Table 10.2: Results of importance sampling test performed on the regions 10 - 250 cm^{-1}, 8500 - 9000 cm^{-1} and 20,000 - 30,000 cm^{-1} at 300 K. For the summed intensity, $\Sigma\ S(T)_j^a$, digits that differ from the 'all lines included' case are highlighted in red. t is computation time required using 1 core at 2.8 GHz.

S_{cut} (fixed) cm/molecule	Region 1	$\Sigma\ S(T)_j^a$ cm/molecule Region 2	Region 3
None	$1.8966628120 \times 10^{-17}$	$1.9980548977 \times 10^{-20}$	$8.4330042577 \times 10^{-24}$
1×10^{-50}	$1.8966628120 \times 10^{-17}$	$1.9980548977 \times 10^{-20}$	$8.4330042577 \times 10^{-24}$
1×10^{-40} [a]	$1.8966628120 \times 10^{-17}$	$1.9980548977 \times 10^{-20}$	$8.4330042577 \times 10^{-24}$
1×10^{-36} [b]	$1.8966628120 \times 10^{-17}$	$1.9980548977 \times 10^{-20}$	$8.433004\mathbf{1319} \times 10^{-24}$
1×10^{-33}	$1.8966628120 \times 10^{-17}$	$1.998054897\mathbf{4} \times 10^{-20}$	$8.43\mathbf{29352920} \times 10^{-24}$
1×10^{-30} [b],[c]	$1.8966628120 \times 10^{-17}$	$1.99805\mathbf{47819} \times 10^{-20}$	$8.4\mathbf{027955280} \times 10^{-24}$
1×10^{-29} [d]	$1.896662\mathbf{818} \times 10^{-17}$	$1.99805\mathbf{39998} \times 10^{-20}$	$8.\mathbf{2432380860} \times 10^{-24}$
1×10^{-27} [e]	$1.89666\mathbf{27966} \times 10^{-17}$	$1.99\mathbf{79986493} \times 10^{-20}$	$\mathbf{5.4420528000} \times 10^{-24}$
S_{crit} (variable S_{cut}) cm/molecule	Region 1	Region 2	Region 3
1×10^{-29} [d]	$1.8966628120 \times 10^{-17}$	-	-
1×10^{-27} [e]	$1.896662\mathbf{816} \times 10^{-17}$	-	-

S_{cut} (fixed) cm/molecule	Region 1	t seconds Region 2	Region 3
None	37	1266	1653
1×10^{-50}	0.4	91	1644
1×10^{-40} [a]	0.05	12	669
1×10^{-36} [b]	0.02	5	265
1×10^{-33}	0.01	2	103
1×10^{-30} [b],[c]	0.005	0.8	21
1×10^{-29} [d]	0.004	0.6	8
1×10^{-27} [e]	0.002	0.3	0.4
S_{crit} (variable S_{cut}) cm/molecule			
1×10^{-29} [d]	0.004	-	-
1×10^{-27} [e]	0.006	-	-

[a] Sharp & Burrows (2007);
[b] Shillings et al. (2011);
[c] Hedges & Madhusudhan (2016);
[d] Rothman et al. (2013);
[e] Rothman et al. (2010).

Table 10.3: Results of importance sampling test performed on the regions 10 - 250 cm^{-1}, 8500 - 9000 cm^{-1} and 20,000 - 30,000 cm^{-1} at 2000 K. For the summed intensity, $\Sigma\ S(T)_j^a$, digits that differ from the 'all lines included' case are highlighted in red. t is computation time required using 1 core at 2.8 GHz.

S_{cut} (fixed) cm/molecule	Region 1	$\Sigma\ S(T)_j^a$ cm/molecule Region 2	Region 3
None	$7.5044569745 \times 10^{-18}$	$4.1202213944 \times 10^{-20}$	$1.9609699223 \times 10^{-23}$
1×10^{-50}	$7.5044569745 \times 10^{-18}$	$4.1202213944 \times 10^{-20}$	$1.9609699223 \times 10^{-23}$
1×10^{-40} [a]	$7.5044569745 \times 10^{-18}$	$4.1202213944 \times 10^{-20}$	$1.9609699223 \times 10^{-23}$
1×10^{-36} [b]	$7.5044569745 \times 10^{-18}$	$4.1202213944 \times 10^{-20}$	$1.9609699\mathbf{205} \times 10^{-23}$
1×10^{-33}	$7.504456973\mathbf{6} \times 10^{-18}$	$4.120221\mathbf{3634} \times 10^{-20}$	$1.9609\mathbf{463615} \times 10^{-23}$
1×10^{-30} [b],[c]	$7.5044\mathbf{59112} \times 10^{-18}$	$4.120\mathbf{1078008} \times 10^{-20}$	$1.\mathbf{8954524889} \times 10^{-23}$
1×10^{-29} [d]	$7.5044\mathbf{05908} \times 10^{-18}$	$4.1\mathbf{192232984} \times 10^{-20}$	$1.\mathbf{6459567019} \times 10^{-23}$
1×10^{-27} [e]	$7.504\mathbf{3114641} \times 10^{-18}$	$4.\mathbf{0979575848} \times 10^{-20}$	$\mathbf{4.1537944000} \times 10^{-24}$
S_{crit} (variable S_{cut}) cm/molecule	Region 1	Region 2	Region 3
1×10^{-29} [d]	$7.5044569\mathbf{194} \times 10^{-18}$	-	-
1×10^{-27} [e]	$7.50445\mathbf{316081} \times 10^{-18}$	-	-

S_{cut} (fixed) cm/molecule	Region 1	t seconds Region 2	Region 3
None	37	1266	1653
1×10^{-50}	37	1266	1653
1×10^{-40} [a]	37	1266	1653
1×10^{-36} [b]	35	1248	1637
1×10^{-33}	26	1114	1408
1×10^{-30} [b],[c]	7	492	277
1×10^{-29} [d]	3	230	60
1×10^{-27} [e]	1	28	1
S_{crit} (variable S_{cut}) cm/molecule			
1×10^{-29} [d]	17	-	-
1×10^{-27} [e]	5	-	-

[a] Sharp & Burrows (2007);
[b] Shillings et al. (2011);
[c] Hedges & Madhusudhan (2016);
[d] Rothman et al. (2013);
[e] Rothman et al. (2010).

Table 10.4: Summary of intensity cut-offs employed in the calculation of the current cross sections.

Molecule	Region cm^{-1}	S_{cut} cm/molecule
H_2O	10 - 10,000	1×10^{-33}
	10,000 - 30,000	1×10^{-36}
NH_3	10 - 9,000	1×10^{-33}
	9,000 - 12,000	1×10^{-35}
CO	10 - 8500	None
CO_2	250 - 8300	None

It is the far wings that are distorted, resulting in a reduction of absorption intensity (Thomas & Stamnes (1999)).

Hence for both computational and physical reasons it is common practice to apply a cut-off at some distance from the line centre, after which the profile in no longer evaluated (see for example Amundsen et al. (2014); Hedges & Madhusudhan (2016); Sharp & Burrows (2007); Grimm & Heng (2016)). This distance may be fixed for every line (Sharp & Burrows (2007)) or be adaptive with the temperature and/or pressure line width (Amundsen et al. (2014); Hedges & Madhusudhan (2016); Grimm & Heng (2016)). A special case applies to H_2O if the water continuum is to be included. Here all lines have to be cut-off at 25 cm^{-1} (Clough et al. (1989)).

The point at which the Voigt cut-off should be applied is not well understood (Hedges & Madhusudhan (2016)), nor is the choice of cut-off typically backed up with any sound physical reason (Grimm & Heng (2016)). Hedges & Madhusudhan (2016) performed comparative tests to investigate the influence of different methods on the resulting cross sections. The authors compared two methods, a pressure adaptive fixed cut-off (Sharp & Burrows (2007)) and a cut-off evaluated per line as a multiple of Lorentzian half-widths (Grimm & Heng (2016)), to their approach, a cut-off evaluated per line as a multiple of effective Voigt half-widths. The effective Voigt half-width was defined as:

$$\gamma_V \approx 0.5346\gamma_L \sqrt{0.2166\gamma_L^2 + \gamma_G^2} \tag{10.6}$$

Hedges & Madhusudhan found that both the fixed cut-off method and Lorentzian half-width analysis resulted in significant ($> 40\%$) opacity loss at the low end of the pressure range (P < 0.01 bar) compared to the Voigt half-width analysis.

To avoid this loss of opacity the current work also adopts an approach that adapts with both temperature and pressure, although for simplicity the cut-off is defined as a multiple of thermal broadened half-width α_j and pressure broadened half-width γ_j. $\gamma_G = \alpha_j$, $\gamma_L = \gamma_j$ and $\gamma_V < (\alpha_j + \gamma_j)$ for comparison to Hedges & Madhusudhan.

In this work the effect of applying a Voigt cut-off at fac * $(\alpha + \gamma)$ for different values of fac (see Table 10.5) on the calculated cross section and computation time is

investigated. The following procedure is carried out for each test:

1. The BT2 line list is sampled using the intensity cut-off scheme described in Section 11.1.1 for a set wavenumber interval and temperature (for example 10000 - 10050 cm^{-1} and 300 K).

2. The reduced line list is used to compute a set of cross sections using a grid spacing of 0.01 cm^{-1} for a set pressure (for example 1 bar) and a Voigt cut-off of fac * $(\alpha + \gamma)$ from the line centre. The computation time is noted.

3. The cross sections are summed to give representative values of the total computed opacity.

Representative results for the profile evaluation width tests are presented in Table 10.5. The summed cross section for the 'None' case may be an overestimate of the total opacity due to the effects discussed above, but it is used here to put an upper limit on the opacity loss due to applying a cut-off. Without knowing the true contribution to opacity from the wings, it appears that a factor of 200 provides a suitable compromise between computation time and incorporating opacity from the wings.

Table 10.5: Results of profile evaluation width tests for the region 10000 - 10050 cm^{-1}, 300 K and 1 bar. The Voigt cut-off is defined as factor $\times(\alpha + \gamma)$ from the centroid in both directions. Digits that differ from the 'Voigt evaluated out to the extent of the wavenumber region' case are highlighted in red. x % is the percentage difference in summed cross section compared to the 'None' case. y× speed up is the factor difference in computation time compared to the 'None' case. t is computation time required using 1 core at 2.8 GHz.

Cut-off Factor	Summed cross section cm^2/molecule		t s	
None	$1.3881604367 \times 10^{-18}$		1055	
500	$1.38\mathbf{79038468} \times 10^{-18}$	(- 0.02 %)	681	(∼ 1.5× speed up)
200	$1.38\mathbf{70341269} \times 10^{-18}$	(- 0.08 %)	273	(∼ 4× speed up)
100	$1.38\mathbf{55795770} \times 10^{-18}$	(- 0.2 %)	160	(∼ 6.5× speed up)
50	$1.38\mathbf{27170808} \times 10^{-18}$	(- 0.4 %)	102	(∼ 10× speed up)

An alternative approach to truncating the Voigt profile for physical reasons is to apply a correction to the far wings to reduce their contribution. The far wings may be modified by a function, for example an exponential (Birnbaum (1979); Edwards & Strow (1991)) to give sub- or super- Lorentzian behaviour (Thomas & Stamnes (1999)). Though again at what distance from the centroid this correction should be applied is unknown and the actual shape of the far wings is difficult to estimate (Hedges & Madhusudhan (2016)). Investigating the effects of sub- or super-Lorentzian far wing shapes on the cross sections, particularly in sparse regions, is

an avenue for further work. The computational implications will also have to be considered.

Another option involves 'folding' the opacity from the far wings back into the line centre. This method ensures no opacity is missed but can overestimate the core absorption (Hedges & Madhusudhan (2016)).

For current purposes an unmodified Voigt profile is employed and evaluated out to 200 $\times(\alpha_j + \gamma_j)$ either side of the centroid. This should adequately sample the contribution from the wings in a manner that adapts with both pressure and temperature.

10.1.3 Profile grid resolution

In order to adequately sample the contribution from each broadened line the Voigt profile most be computed on a grid finer than the width of the profile. In the words of Sharp & Burrows (2007) *"when the profiles are much narrower than the grid intervals on average most will fall between grid points and only the far wings are sampled, or missed completely"*.

Hill et al. (2013) employed a staggered wavenumber grid for zero pressure cross sections (see Table 10.9 in Section 11.2). This takes into account the wavenumber dependence of the thermal broadened widths.

In this work the suitability of this grid for the pressure dependent cross sections is assessed using the following method:

1. A cross section for each wavenumber domain (see Table 10.6) is computed using the Hill et al. (2013) grid and a finer and courser grid, though no courser than the intended final resolution $\Delta\tilde{\nu} = 0.01$ cm^{-1}. The computation times are noted.

2. The cross sections are summed and multiplied by the grid spacing to give representative values of the total computed opacity.

As demonstrated by the representative results presented in Table 10.6, the difference in summed cross sections between the finer and Hill et al. grids is very small, while the coarser grid results in a more substantial loss of opacity for the 100 - 1000 cm^{-1} region. Therefore the Hill et al. grid appears to provide a suitable compromise between computational expense and opacity retention.

Hedges & Madhusudhan proposed a more computationally efficient grid resolution, a pressure adaptive grid, than the staggered grid employed by this work. However they did comment that the pressure adaptive grid resulted in a small loss of opacity ($\sim 2\%$) compared to the staggered grid at the high end of the pressure range (P $\sim$ 10 bar). Hence the current work will adopt the staggered grid of Hill et al. (2013).

10.1.4 Pressure Broadening Parameters

For cases where pressure broadening parameters are not included with the line lists, line shape studies have resorted to estimating them from other sources (see for example Amundsen et al. (2014)). This is typically the case for broadening by H_2 and He as

Table 10.6: Results of profile grid resolution tests for the regions 10 - 100 cm^{-1}, 100 - 1000 cm^{-1}, 1000 - 10,000 cm^{-1} and 10,000 - 30,000 cm^{-1}, 300 K and 0.001 bar when the line shapes are anticipated to be at their narrowest for the current parameter space. x % is the percentage difference in summed cross section compared to the Hill et al. grid. t is computation time required using 1 core at 2.8 GHz.

Grid	Grid Spacing cm^{-1}	Summed cross section cm^2/molecule	t seconds
10 - 100 cm^{-1}			
Finer	10^{-6}	$3.4650820035 \times 10^{-18}$ (+ 3.4×10^{-6} %)	40
Hill et al.	10^{-5}	$3.4650818846 \times 10^{-18}$	4
Courser	10^{-4}	$3.4653156180 \times 10^{-18}$ (+ 6.7×10^{-3} %)	0.4
100 - 1000 cm^{-1}			
Finer	10^{-5}	$2.11433618697 \times 10^{-17}$ (- 7.8×10^{-6} %)	60
Hill et al.	10^{-4}	$2.11433633896 \times 10^{-17}$	6
Courser	10^{-3}	$2.09978997135 \times 10^{-17}$ (- 0.6 %)	0.6
1000 - 10000 cm^{-1}			
Finer	10^{-4}	$4.38191905802 \times 10^{-20}$ (- 4.2×10^{-8} %)	50
Hill et al.	10^{-3}	$4.38191905986 \times 10^{-20}$	5
Courser	10^{-2}	$4.38191906422 \times 10^{-20}$ (+ 9.9×10^{-8} %)	0.5
10000 - 30000 cm^{-1}			
Finer	10^{-3}	$1.35239648391 \times 10^{-20}$ (+ 2.0×10^{-7} %)	1823
Hill et al.	10^{-2}	$1.35239648668 \times 10^{-20}$	182

there is currently no database that provides parameters for these broadeners systematically (Fortney et al. (2016)), although both the HITRAN and ExoMol databases are starting to incorporate them (Wilzewski et al. (2016); Tennyson et al. (2016), this work see Chapter 11).

One could map available measured or calculated values to a line list then employ a model to 'fill in the gaps'. This is the method employed by HITRAN to populate their pressure broadening parameter datasets and is what the new `.broad` files developed for the ExoMol database (see Chapter 11) are intended to be used for. Indeed it should be the preferred approach as it ensures that accurate parameters are being utilised where available and that no molecule line is left without parameters.

However several line shape studies employ a model for all lines. For example Amundsen et al. (2014) complied all available H_2 and He pressure broadening parameters as a function of J'' for several molecules then modelled the dependence on J'' as a linear function using a least-squares fit.

For use in this work Prof. Nina Lavrentieva calculated H_2O-H_2 and H_2O-He Lorentzian half-widths for BT2 lines in the range 500 - 10,000 cm^{-1} with an intensity that exceeds 1×10^{-30} cm/molecule in the temperature range 300 - 2000 K, around 4 million lines. This dataset will henceforth be referred to as NLAD.

Hedges & Madhusudhan (2016) compared line-by-line and mean treatment of the pressure broadening parameters for H_2O in air and found the median difference to be around 20 % at worst (for 500 K, 0.1 atm).

In this work the effect of line-by-line (NLAD) verses J'' averaged and mean treatment of the broadening parameters on the cross sections is investigated for H_2O in H_2. The sampled BT2 line list for which NLAD parameters were determined is used to compute cross sections with:

1. Line-by-line NLAD parameters.
2. J'' averaged parameters: derived by compiling NLAD parameters for each J'' and finding the mean.
3. Constant parameters for all lines: derived by averaging all parameters from the NLAD dataset.

Then the difference between the cross sections is determined as:

$$\delta\sigma^{\%} = \left(\frac{|\sigma_{NLAD} - \sigma_{J''/mean}|}{\sigma_{NLAD}} \right) \times 100 \tag{10.7}$$

The median difference in the 0.01 cm^{-1} cross section for the worst case (500 K, 0.1 bar) was $\sim$ 10% for J'' averaged and $\sim$ 30% for mean treatment of the pressure broadening parameters. The $\sim$ 10% difference introduced by J'' averaged difference is representative of the typical uncertainty in pressure broadening parameters (see Chapter 11) hence, although not ideal, this approximation is not entirely unreasonable. The $\sim$ 30% difference introduced by the mean treatment is more considerable hence this approach should be avoided if possible.

The current work employs the NLAD pressure broadening parameters dataset for H_2O and J'' averaged values for other molecules derived from available sources.

10.1.5 Temperature - Pressure grid

The disadvantage of using cross sections is that they are inflexible, suitable for only the temperature and pressure for which they were computed.

Hill et al. (2013) presented interpolation procedures for the zero pressure cross sections which resulted in a maximum interpolation residual of 2% (linear Eq. (3.36) Chapter 3) or 1.68 % (exponential Eq. (3.38) Chapter 3) using a temperature grid with steps of 100 K below 1000 K and 200 K above 1000 K.

The aim is to at least match this interpolation residual by selecting a suitably spaced pressure grid. At present this is a work in process.

The pressure grid points presented in Table 10.7 combined with linear interpolation (Eq. (3.41) Chapter 3) results in residuals below 2.6% for the region 6000 - 30,000 cm^{-1} for all pressures. However, below 6000 cm^{-1} for low pressures and below 1000 cm^{-1} for high pressures, there are spikes in interpolation residual ($> 10\%$) for individual wavenumber bins, notably in the wings of strong features. The wings of strong lines add appreciable amounts of opacity to wavenumber bins where there previously was negligible opacity in an non-linear fashion. In reality this effects only a small fraction of the bins ($< 0.7\%$) and changes the total cross section in the region 10 - 6000 cm^{-1} by less than 2×10^{-3} % at worst, hence this should have negligible effect on practical applications.

The current work employs the temperature grid of Hill et al. (2013) and the pressure grid determined here (see Table 10.7). The maximum interpolation residual for the temperature grid, using the more accurate interpolation scheme, is below 2%. The maximum interpolation residual for the pressure grid, for all but a small fraction of bins, is 2.6%.

Table 10.7: Pressure grid for the cross sections.

Pressure (bar)			
0.001	0.003	0.005	0.01
0.02	0.04	0.08	0.1
0.3	0.6	0.9	1.0
1.2	1.5	2.0	2.5
3.0	4.0	5.0	6.0
8.0	10.0		

10.2 Water

H_2O has been used to investigate the influence of various numerical considerations on the 0.01 cm^{-1} cross sections. Then current choices are as follows:

1. **Importance sampling:** wavenumber dependent cut-offs, see Table 10.4.
2. **Profile evaluation width:** A cut-off that adapts with the thermal and pressure broadened line width, namely 200 * $(\alpha_j + \gamma_j)$.

3. **Profile grid resolution:** The staggered wavenumber grid of Hill et al. (2013).

4. **Pressure broadening parameters:** Calculated NLAD parameters (H_2O) or averaged J'' values (CO, CO_2, NH_3).

5. **Temperature - pressure grid:** Temperature grid of Hill et al. (2013), pressure grid described in Section 11.1.5.

These were used in the generation of the cross sections described below and in Section 11.3. The tests indicate that the largest source of uncertainty in the pressure dependent cross sections is introduced by the sparse and approximate nature of current H_2/He pressure broadening parameter datasets. Clearly more accurate and comprehensive parameters would be desired in future.

Pressure dependent absorption cross sections for H_2O in a mixed H_2/He environment (85/15%) are calculated on a fixed temperature and pressure grid (see Table 10.8) using the BT2 line list, the Vidler & Tennyson (2000) partition function, pressure broadening parameters determined by Prof. Nina Lavrentieva and Dr. Anna Dudaryonok, and the method described in Section 3.3. However, no attempt is made to include contributions to the opacity from the water vapour continuum or water dimer absorption.

The cross sections were calculated between 10 and 30,000 cm^{-1} using the staggered wavenumber grid given in Table 10.9 and then binned to a common grid spacing of 0.01 cm^{-1}. Each region was calculated to overlap with its neighbours by at least 1 cm^{-1} to avoid discontinuities when they are binned to a common grid spacing (Hill et al. (2013)). The suitability of this grid for pressure dependent cross sections has been demonstrated (see Section 11.2.3).

Cross sections are provided for 12 temperatures and 22 pressures between 300 - 2000 K and 0.001 - 10 bar respectively (see Table 10.8). This temperature - pressure grid was chosen to minimise interpolation residuals (see Section 11.2.5). A cross section at intermediate conditions may be obtained by first interpolating on the temperature grid then interpolating on the pressure grid (see Eqs. (3.36-3.42) in Chapter 3.3 and discussion in Section 10.1.5).

Calculated cross sections for a range of temperatures at a single pressure and a range of pressures at a single temperature are shown in Figures 10.2 and 10.3. A change in temperature predominately influences the shape of the cross section (Figure 10.2) while a change in pressure results in a redistribution of opacity (Figure 10.3).

τ-REx uses facial recognition software to pre-select molecules likely to be present in the observed spectra then employs several minimization routines to retrieve temperature, pressure and mixing ratios. A change in temperature has a strong influence on the whole H_2O spectrum, while a change in pressure predominately influences the H_2O spectrum below 10,000 cm^{-1}. This characteristic could be used to break degeneracies when trying to distinguish between a change in temperature verses pressure.

Table 10.8: Temperatures and pressures at which H_2O cross sections are calculated

Temperature (K)			
300	400	500	600
700	800	900	1000
1200	1400	1600	1800
2000			
Pressure (bar)			
0.001	0.003	0.005	0.01
0.02	0.04	0.08	0.1
0.3	0.6	0.9	1.0
1.2	1.5	2.0	2.5
3.0	4.0	5.0	6.0
8.0	10.0		

Table 10.9: Summary of the grid spacings for the cross sections calculated in different wavenumber regions

Wavenumber range cm^{-1}	Grid spacing cm^{-1}
10 - 100	10^{-5}
100 - 1000	10^{-4}
1000 - 10,000	10^{-3}
10,000 - 30,000	10^{-2}

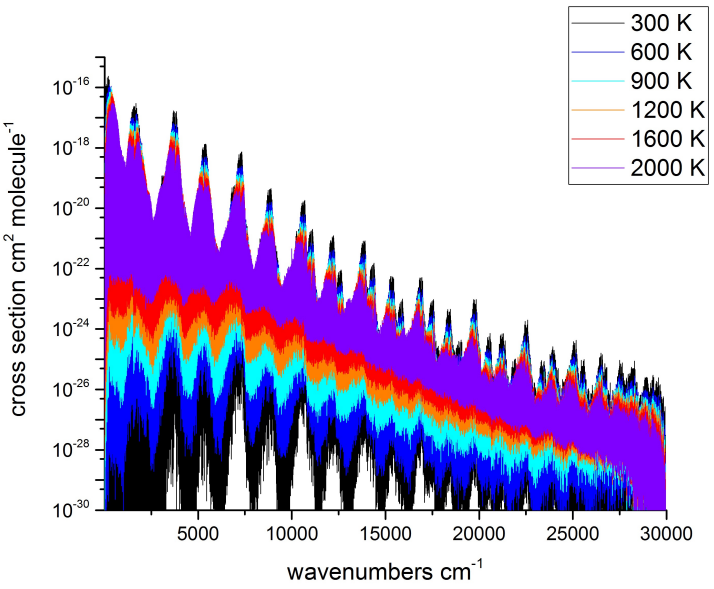

Figure 10.2: H_2O cross sections in a mixed H_2-He (85/15%) environment calculated at 0.01 bar and temperatures in the range 300 - 2000K.

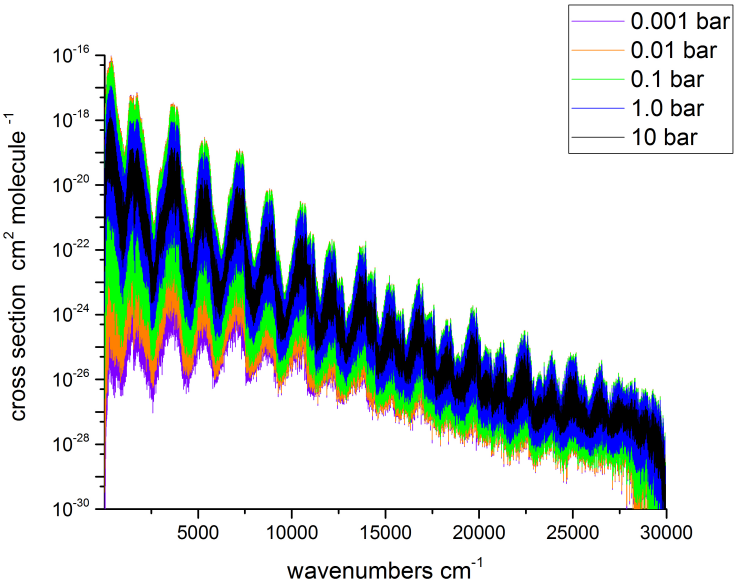

Figure 10.3: H_2O cross sections in a mixed H_2-He (85/15%) environment calculated at 1000 K and pressures in the range 0.001 - 10 bar.

10.3 Other Molecules

Pressure dependent absorption cross sections for NH_3, CO and CO_2 in a mixed H_2/He environment (85/15%) are calculated on a fixed temperature and pressure grid (see Table 10.12) using the line lists and partition functions summarised in Table 10.10, J'' averaged pressure broadening parameters derived from sources summarised in Table 10.11, and the method described in Section 3.3.

Table 10.10: Line list and partition functions used to calculate cross sections.

Molecule	Line list	Partition function	Wavenumber coverage of cross sections
NH_3	Yurchenko et al. (2011a)	Sousa-Silva et al. (2014)	10 - 12,000
CO	Li et al. (2015)	Fischer et al. (2003)	10 - 8500
CO_2	Tashkun & Perevalov (2011)	Fischer et al. (2003)	250 - 8300

The cross sections were calculated using the staggered wavenumber grid given in Table 10.9 and then binned to a common grid spacing of 0.01 cm^{-1} in accordance with the H_2O cross sections.

Calculated cross sections for a range of temperatures at a single pressure and a

Table 10.11: Sources of pressure broadening parameters

Molecule	Broadener	Source
NH_3	H_2	Pine et al. (1993)
		Hadded et al. (2001)
		Sharp & Burrows (2007)
		Wilzewski et al. (2016)
	He	Pine et al. (1993)
		Hadded et al. (2001)
		Sharp & Burrows (2007)
		Wilzewski et al. (2016)
CO	H_2	Regalia-Jarlot et al. (2005)
		Moal & Severin (1986)
		Faure et al. (2013)
	He	BelBruno et al. (1982)
		Mantz et al. (2005)
CO_2	H_2	Padmanabhan et al. (2014)
	He	Abrams (1974)
		Pack (1979)

Table 10.12: Temperatures and pressures at which H_2O cross sections are calculated

Temperature (K)			
300	400	500	600
700	800	900	1000
1200	1400	1500	
Pressure (bar)			
0.001	0.003	0.005	0.01
0.02	0.04	0.08	0.1
0.3	0.6	0.9	1.0
1.2	1.5	2.0	2.5
3.0	4.0	5.0	6.0
8.0	10.0		

range of pressures at a single temperature are shown in Figures 10.4, 10.6 and 10.8 and Figures 10.5, 10.7 and 10.9.

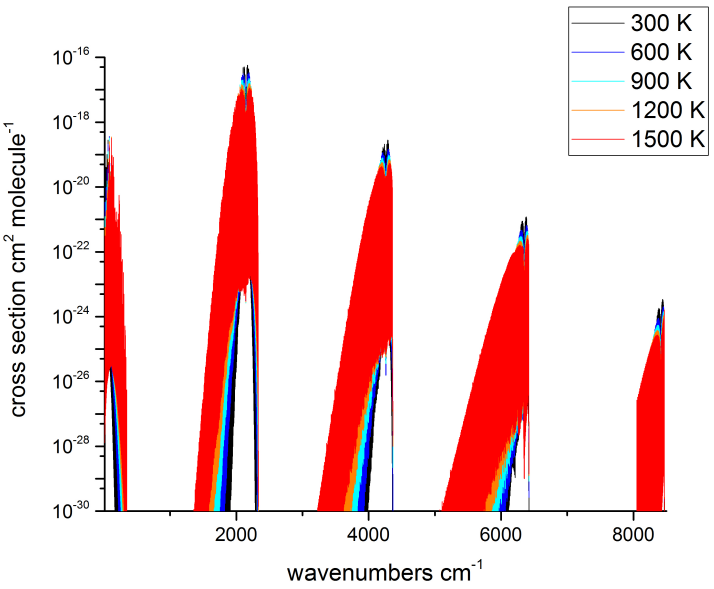

Figure 10.4: CO cross sections in a mixed H_2-He (85/15%) environment calculated at 0.01 bar and temperatures in the range 300 - 2000K.

10.4 Summary of Results

Pressure dependent cross sections for H_2O, CO, CO_2 and NH_3 have been computed for a range of temperatures and pressures relevant to extrasolar planetary atmospheres. The cross sections are sufficient for use in current extrasolar planetary spectral studies. Improvements in the cross section computation method and treatment of pressure broadening should be pursued for more high resolution studies.

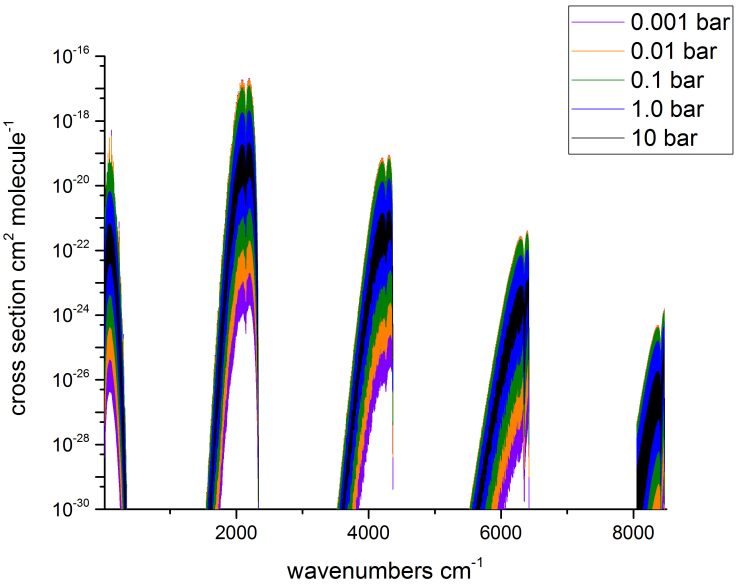

Figure 10.5: CO cross sections in a mixed H_2-He (85/15%) environment calculated at 1000 K and pressures in the range 0.001 - 10 bar.

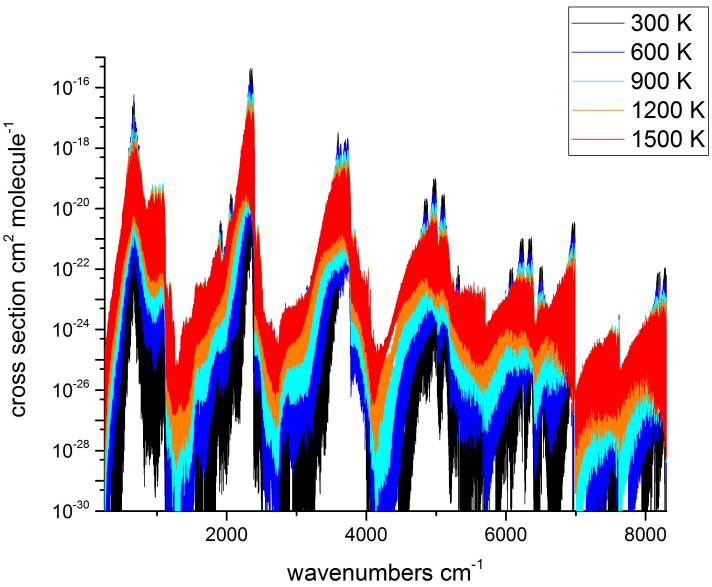

Figure 10.6: CO_2 cross sections in a mixed H_2-He (85/15%) environment calculated at 0.01 bar and temperatures in the range 300 - 2000K.

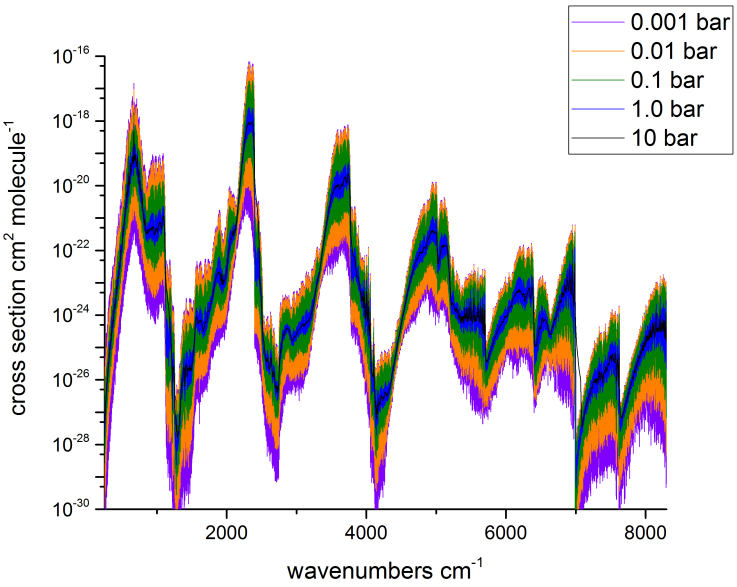

Figure 10.7: CO_2 cross sections in a mixed H_2-He (85/15%) environment calculated at 1000 K and pressures in the range 0.001 - 10 bar.

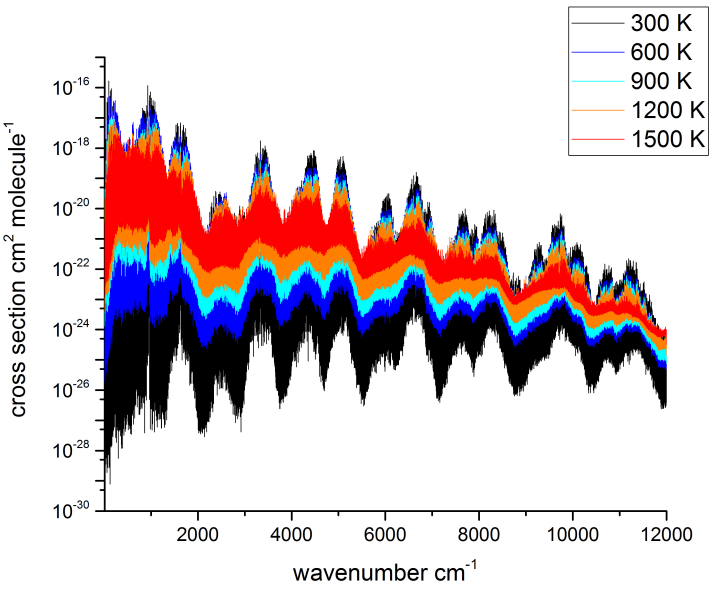

Figure 10.8: NH_3 cross sections in a mixed H_2-He (85/15%) environment calculated at 0.01 bar and temperatures in the range 300 - 2000K.

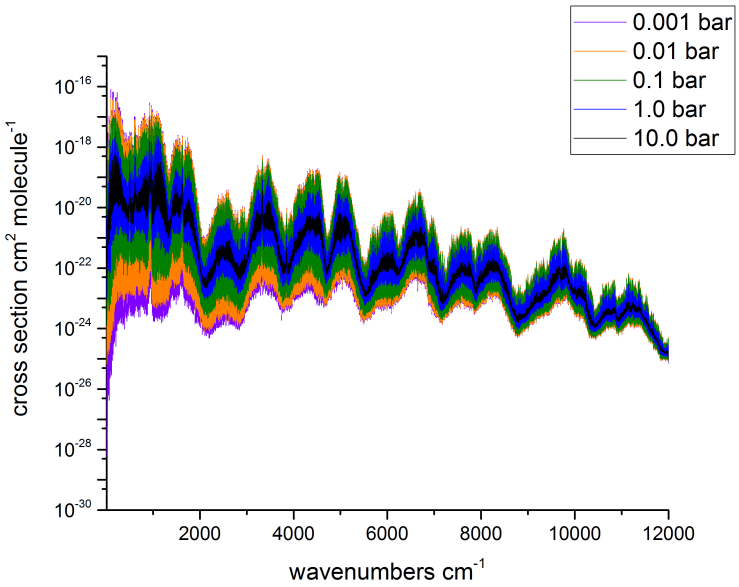

Figure 10.9: NH_3 cross sections in a mixed H_2-He (85/15%) environment calculated at 1000 K and pressures in the range 0.001 - 10 bar.

Chapter 11

Implementing Pressure Broadening in the ExoMol Database

Prior to this work the ExoMol database did not include information on the pressure broadening of molecular lines. The focus of the database was to provide comprehensive lists of transitions for molecules expected to be of importance in the atmospheres of planets (Tennyson & Yurchenko (2012); Tennyson et al. (2013)), although the data was often used to compute partition functions, cross sections and other properties. Now the scope of the database is being extended to systematically provide this additional data and other supplementary data in order to maximise the usefulness of the line lists (Tennyson et al. (2016)). A major new feature is the inclusion, albeit at a fairly crude level, of pressure broadening parameters.

Although the need to implement pressure broadening in models of current low resolution (R $\leq$ 100) extrasolar planetary atmospheric measurements is arguable (Tinetti et al. (2012); Hedges & Madhusudhan (2016)), Hedges & Madhusudhan (2016) have demonstrated that the treatment of pressure broadening in models of medium (R $\leq$ 5000) to high (R $\approx 10^5$) resolution measurements can significantly influence the resulting spectra. Such resolutions will be obtainable with upcoming space missions and large ground based facilities including the James Webb Space telescope (JWST R $\simeq$ 1000-3000, Barstow et al. (2015)) and the European Extremely Large Telescope (E-ELT R $\simeq$ 100,000, Snellen (2013)).

In addition the data from ExoMol is not exclusively being used to study extrasolar planets, and the inclusion of pressure broadening information in high resolution (R $>$ 100,000) spectral models, such as those used to extract molecular concentrations from *in situ* gas measurements in industrial environments, is imperative (see Chapter 7).

The aim of this work was to incorporate pressure broadening parameters into the ExoMol database. In this context pressure broadening parameters refers to the Lorentzian half width γ (see Section 3.2.2) and its temperature dependence expressed as an exponent n (defined in Section 11.2.1).

The availability of these parameters varies with species and broadener. In any case there are no individual values available for every molecular line and often parameters have only been measured or calculated for a small fraction of transitions.

The method adopted by the HITRAN database to construct complete pressure broadening datasets, is to assemble all the data available for each molecule-broadener pair considered, and then use the collected data to create semi-empirical models to fill in the gaps (Rothman et al. (2013); Wilzewski et al. (2016); Gordon et al. (2007)). Using this approach the database provides pressure broadening parameters for every HITRAN line of the molecule under study.

The ExoMol line lists are larger, in some cases orders of magnitude larger, than the HITRAN line lists. For this reason following the HITRAN approach would not be ideal nor, considering the sparsity of data in many cases, particularly reliable. Therefore, rather than pre-determine values for every molecular line and increase the size of the line lists, a separate pressure broadening parameters (`.broad`) file to be included with the line lists was developed as part of this work.

Each `.broad` file will present available measurement, calculated and empirically or semi-empirically determined pressure broadening parameters in a compact form. This file, which will make use of trends in pressure broadening parameters as a function of molecule dependent quantum numbers, can then be combined with a semi-empirical temperature-pressure model to generate a Lorentzian half width for every ExoMol line of the molecule under study.

Sources of pressure broadening parameters are reviewed in Section 11.1. The temperature, pressure, broadening species and quantum number dependence of pressure broadening parameters is discussed in Section 11.2. Finally the `.broad` file specification for inclusion in the new extended ExoMol format is presented in Section 11.3, along with examples for H_2O and CS.

11.1 Sources of Pressure Broadening Parameters

There are three types of pressure broadening parameters available from the literature:

1. Experimental: Measured Lorentzian half widths
2. Calculated: Theoretically determined Lorentzian half widths
3. Empirical/Semi-empirical: Lorentzian half widths and temperature exponents derived from models fitted to experimental values

Retrieval of Lorentzian half widths from measured spectra involves fitting profiles (Lorentzian or Voigt) to molecular lines to extract the line widths that best reproduce the observations (see Zeninari et al. (2004) for example). Intuitively this technique favours strong, isolated lines. Hence measurements of Lorentzian half widths for weak lines or at high temperature, when the molecular spectra becomes more dense, can be tricky to obtain. On top of this the broad spectral, temperature and pressure parameter space makes exhaustive coverage by laboratory measurement difficult (Lynch et al. (1996)).

Theoretical *ab initio* calculations can help fill in the gaps (Lynch et al. (1996)). However the complex dependence of Lorentzian half widths on the energy level structure of interacting species, intermolecular forces and physical conditions makes their

accurate theoretical determination non-trivial. The calculations are particularly time consuming and require empirical tuning which can only be performed for the limited spectral, temperature and pressure ranges covered by laboratory measurements (Lynch et al. (1996)). Methods in use include the complex Robert-Bonamy formalism, very computational expensive but capable of providing accuracy of up to 1-5% (Lynch et al. (1996)), which has been used to calculate Lorentzian half widths for certain vibrational bands of H_2O broadened by N_2 and CO_2 by Lynch et al. (1996) and Gamache et al. (1997) for example. More approximate methods include the simplified Robert-Bonamy approach (Starikov & Laventieva (2006)), the J′J″ dependence technique (Voronin et al. (2010a, 2012)) and the random phase approximation (Faure et al. (2013)), developed to reduce computation time whilst still providing reasonable accuracy ($\simeq$ 10 - 30%).

Lorentzian half widths derived from semi-empirical or empirical models are also available. Experimental line widths may be fitted to an empirical expression, for example Brown & Peterson (1994) fitted the measured Lorentzian half widths of NH_3 to a polynomial function of rotational quantum numbers J'' and K''. J is the total rotational angular momentum while K is the projection of J onto the molecular axis. Alternatively experimental line widths may be used to refine a semi-empirical model like the technique developed by Bykov et al. (2004). Based on approximations proposed by Anderson (1949), the theoretical expression for the half width used by the method contains a small correction factor which is determined by fitting to experimental data (Bykov et al. (2004); Lavrentieva et al. (2014b)).

Temperature exponents are derived for different molecular lines by fitting Lorentzian half widths measured or calculated at a range of temperatures to an equation, typically a simple power law (Amundsen et al. (2014); Faure et al. (2013); Wilzewski et al. (2016); Ngo et al. (2012), see Eq. (11.1) in Section 11.2.1).

For this work, a data set of H_2 and He pressure broadening parameters for H_2O in the temperature range 500 – 2000 K have been computed by Prof Nina Lavrentieva and Dr Anna Dudaryonok from Tomsk University in Russia using semi-empirical methods, see Lavrentieva et al. (2014b,a). In principle parameters were computed for every H_2O line of importance in the ExoMol BT2 line list in the spectral range 500 - 10,000 cm^{-1} for these temperatures. In practice, the vibrational dependence of the pressure broadening parameters was neglected and the results can hence be represented in a more compact form as a function of rotational quantum numbers (see Section 11.3).

Table 11.1 lists the main sources of pressure broadening parameters identified for key molecule-broadener species currently being considered by ExoMol, and specifies whether the source primarily provides measured, theoretical or empirical/semi-empirical parameters.

Air-broadening and self-broadening parameters are readily available from the HITRAN database for many molecular species (Gordon et al. (2007)) so in the absence of other sources those are taken from HITRAN 2012 (Rothman et al. (2013)). In gas giants H_2 and He are the major broadeners. There is no systematic source of parameters for these broadeners at present (Fortney et al. (2016)), although the HITRAN database is starting to include these parameters (Wilzewski et al. (2016)), so each

system is treated on a case-by-case basis.

Table 11.1: Sources of pressure broadening parameters for key molecule-broadener species currently being considered by ExoMol. Entries marked * were extracted from HITRAN (Rothman et al. (2013); Wilzewski et al. (2016)).

Molecule - Broadener	**Reference**	**Methodology**
H_2O - H_2	Lavrentieva et al. (2014b)	Semi-empirical
	Lavrentieva et al. (2014a)	Semi-empirical
	Steyert et al. (2004)	Measured
	Brown & Plymate (1996)	Measured
	Brown et al. (2005)	Measured
	Gamache et al. (1996)	Theoretical
	Dick et al. (2009)	Measured
	Faure et al. (2013)	Theoretical
	Langlois et al. (1994)	Measured
	Dutta et al. (1993)	Measured
	Zeninari et al. (2004)	Semi-empirical
	Drouin & Wiesenfeld (2012)	Theoretical
	Golubiatnikov (2005)	Measured
	Lucchesinia et al. (2000)	Measured
H_2O - He	Lavrentieva et al. (2014b)	Semi-empirical
	Lavrentieva et al. (2014a)	Semi-empirical
	Petrova et al. (2016)	Measured
	Petrova et al. (2013)	Measured
	Petrova et al. (2012)	Measured
	Solodov & Starikov (2009)	Measured
	Solodov & Starikov (2008)	Measured
	Godon & Bauer (1988)	Measured
	Lazarev et al. (1995)	Measured
	Poddar et al. (2010)	Measured
	Claveau et al. (2001)	Measured
	Claveau & Valentin (2009)	Measured
	Steyert et al. (2004)	Measured
	Lucchesinia et al. (2000)	Measured
	Golubiatnikov (2005)	Measured
	Gamache et al. (1996)	Theoretical
	Dick et al. (2009)	Measured
	Dutta et al. (1993)	Measured
	Zeninari et al. (2004)	Semi-empirical
H_2O - Air*	Mérienne et al. (2003)*	Measured

Continued on next page

Table 11.1 – continued from previous page

Molecule - Broadener	Reference	Methodology
	Gamache & Hartmann (2004)*	Semi-empirical
	Gasster et al. (1988)*	Measured
	Payne et al. (2008)*	Measured
	Gamache (2005)*	Semi-empirical
	Gamache & Laraia (2009)	Semi-empirical
H_2O - H_2O*	Mérienne et al. (2003)*	Measured
	Gamache & Hartmann (2004)*	Semi-empirical
	Markov (1994)*	Measured
	Golubiatnikov et al. (2008)*	Measured
	Cazzoli et al. (2008)*	Semi-empirical
CH_4 - H_2	Pine (1992)	Measured
	Margolis (1993)	Measured
	Fox et al. (1988)	Measured
	Strong et al. (1993)	Measured
CH_4 - He	Pine (1992)	Measured
	Varanasi & Chudamani (1990)	Measured
	Gabard et al. (2004)	Measured
	Grigoriev et al. (2001)	Semi-empirical
	Fox et al. (1988)	Measured
CH_4 - Air*	Predoi-Cross et al. (2006)*	Measured
	Smith et al. (2009a)*	Measured
	Brown et al. (2003)*	Semi-empirical
	Antony et al. (2008)	Theoretical
CH_4 - CH_4^*	Predoi-Cross et al. (2005)*	Measured
	Smith et al. (2009b)*	Measured
	Brown et al. (2003)*	Semi-empirical
NH_3 - H_2^*	Pine et al. (1993)*	Measured
	Hadded et al. (2001)*	Measured
	Sharp & Burrows (2007)*	Semi-empirical
NH_3 - He*	Pine et al. (1993)*	Measured
	Hadded et al. (2001)*	Measured
	Sharp & Burrows (2007)*	Semi-empirical
NH_3 - Air*	Brown & Peterson (1994)*	Measured
NH_3 - NH_3^*	Brown & Peterson (1994)*	Measured
PH_3 - H_2	Bouanich et al. (2004)	Semi-empirical
	Levy et al. (1993)	Measured
	Sergent-Rozey et al. (1988)	Measured
	Salem et al. (2004)	Measured
	Pickett et al. (1981)	Measured
	Levy et al. (1994)	Measured
PH_3 - He	Salem et al. (2005)	Measured
	Levy et al. (1993)	Measured

Continued on next page

Table 11.1 – continued from previous page

Molecule - Broadener	Reference	Methodology
	Sergent-Rozey et al. (1988)	Measured
	Pickett et al. (1981)	Measured
	Levy et al. (1994)	Measured
PH_3 - Air*	Butler et al. (2006)*	Measured
	Kleiner et al. (2003)*	Semi-empirical
PH_3 - PH_3^*	Butler et al. (2006)*	Measured
	Kleiner et al. (2003)*	Semi-empirical
H_2CO - H_2	Nerf (1975)	Measured
H_2CO - He	Nerf (1975)	Measured
H_2CO - N_2	Jacquemart et al. (2010)	Semi-empirical
H_2CO - H_2CO*	Jacquemart et al. (2010)*	Semi-empirical
HCN - H_2	Mehrotra et al. (1985)	Measured
HCN - He	Mehrotra et al. (1985)	Measured
HCN - Air*	Yang et al. (2008)*	Measured
	Devi et al. (2004)*	Semi-empirical
	Rinsland et al. (2004)*	Semi-empirical
HCN - HCN*	Devi et al. (2004)*	Semi-empirical
	Devi et al. (2003)*	Semi-empirical
CS - Air*	Blanquet et al. (1999)*	Semi-empirical
CS - CS*	Misago et al. (2009)*	Semi-empirical

11.2 Trends in Pressure Broadening Parameters

11.2.1 Temperature and Pressure Dependence

The Lorentzian half width of a spectral line depends on both pressure and temperature and the relationship is often approximated as (Amundsen et al. (2014); Faure et al. (2013); Wilzewski et al. (2016); Ngo et al. (2012)):

$$\gamma(T,P) = \gamma_{\text{ref}} \times \left(\frac{T_{\text{ref}}}{T}\right)^n \times \left(\frac{P}{P_{\text{ref}}}\right). \tag{11.1}$$

where T_{ref} is the reference temperature, P_{ref} is the reference pressure, γ_{ref} is the Lorentzian half width at reference temperature and pressure and n is the temperature exponent. In this work $T_{\text{ref}} = 296$ K and $P_{\text{ref}} = 1$ bar.

As mentioned in the previous section, n for different molecular lines is typically derived by fitting Lorentzian half widths measured or calculated for a range of temperatures to Equation (11.1).

Equation (11.1) describes the overall trend of a decrease in Lorentzian half width with an increase in temperature and a increase in Lorentzian half width with an increase in pressure. These trends are illustrated in Figures 11.1 and 11.2 for H_2O (tem-

perature dependence) and O_2 (pressure dependence). It has been noted by Wilzewski et al. (2016) that the power law representing temperature dependence only works well within relatively narrow temperature intervals and, ideally, the temperature dependence of Lorentzian half widths should be described by three or four exponents valid for different temperature intervals.

An example of this is practice can be found in work performed by Thibault et al. (2008) for C_2H_2. Line widths determined at different temperatures (between 77 - 2000 K) from a combined theoretical and experimental study were fitted to two power laws of the form Equation (11.1), one valid for T $<$ 296 K and one valid for T $>$ 296 K, as an acceptable fit could not be achieved for the whole temperature range.

One might suggest that, since a simple power law of the form Equation (11.1) cannot describe the full temperature range of interest ($\simeq$ 296 - 3000 K for this work), an alternative model should be developed. Unfortunately, for most molecules, there are very little data on the temperature dependence of Lorentzian half widths so neither a multi-exponent power law nor an alternative model can be characterised at present. Therefore, like HITRAN (Wilzewski et al. (2016)), ExoMol shall employ Equation (11.1) with a single temperature exponent for the time being.

Concerning the linear pressure dependence, this has been observed up to 3 atm ($\approx$ 3 bar) for H_2O broadening by He pressure (Petrova et al. (2016, 2013, 2012)). Equation (11.1) is therefore assumed to hold, at least approximately, for the pressure range of interest ($\simeq$ 0.001 - 10 bar for this work). Of course this needs to be experimentally verified.

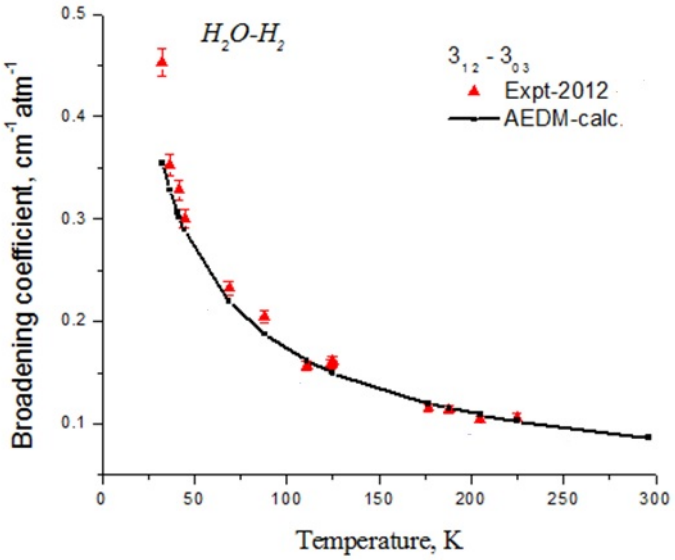

Figure 11.1: Temperature dependence of H_2 Lorentzian half widths for 12 lines of H_2O between 25 - 300 K. Red symbols represent measurements, the black line represents the best fit power law model (Lavrentieva et al. (2014b)).

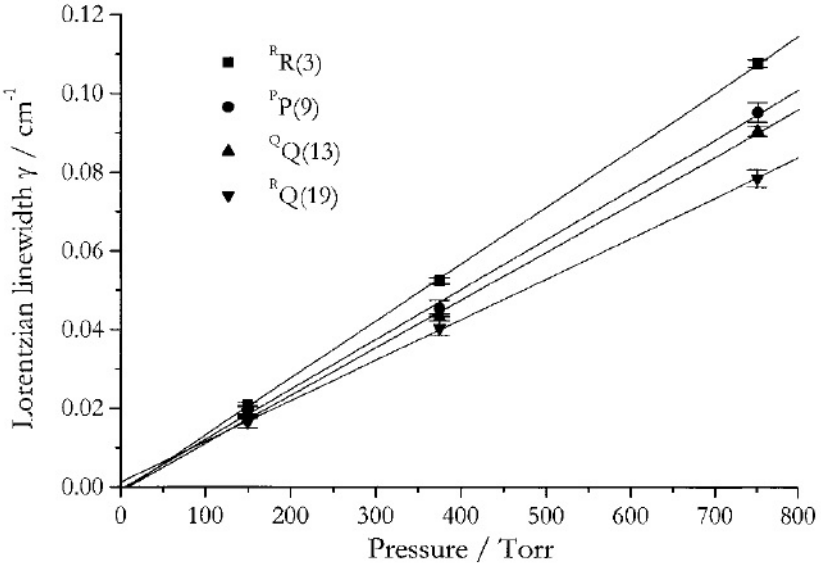

Figure 11.2: Pressure dependence of N_2 Lorentzian half widths for 4 lines of O_2 between 100 and 800 Torr. Symbols represent measurements, the straight line represents the best fit linear model (Newman et al. (2000)).

11.2.2 Rotational Quantum Number Dependence

It is common for Lorentzian half widths to be measured or calculated for one or a few vibrational bands in order to investigate trends in line broadening coefficients due to rotational structure (see for example Brown & Peterson (1994); Pine et al. (1993)). These parameters are the presented with rotational assignments (see for example Pine et al. (1993)) or fitted to a function of rotational quantum numbers (see for example Brown & Peterson (1994)).

Figure 11.4 and 11.3 illustrate the dependence of Lorentzian half widths on rotational quantum numbers for CO (representing a diatomic) and H_2O (representing a polyatomic). Plotted on Figure 11.3 are three types of widths for H_2O: (1) Measured values (green points) have dependence on rotational quantum numbers J (upper and lower), K_a and K_c (upper and lower), (2) values for different K_a and K_c are averaged to give Lorentzian half widths as a function of J'-J'' (blue points), this highlights dependence within P, Q and R branches and (3) values for different J' are averaged to give Lorentzian half widths as a function of J'' only (orange points). For CO, Figure 11.4, the J'' averaged values are practically indistinguishable from the measured values, so only the measured values are shown.

As can be seen for H_2O, and is certainly true for CO, J'' averaged widths describe the general trend of decreasing Lorentzian half width with increasing rotational quantum number, tending to a constant value for the highest rotational quantum numbers. This is a very basic model similar to that used by line width studies Amundsen et al. (2014), Burrows et al. (1997) and Voronin et al. (2010a) to solve the problem of

missing data for the bulk of molecular lines.

ExoMol will employ this model to ensure that a semi-empirical Lorentzian half width can be derived for every spectral line, even if no detailed information for that line exists in the literature.

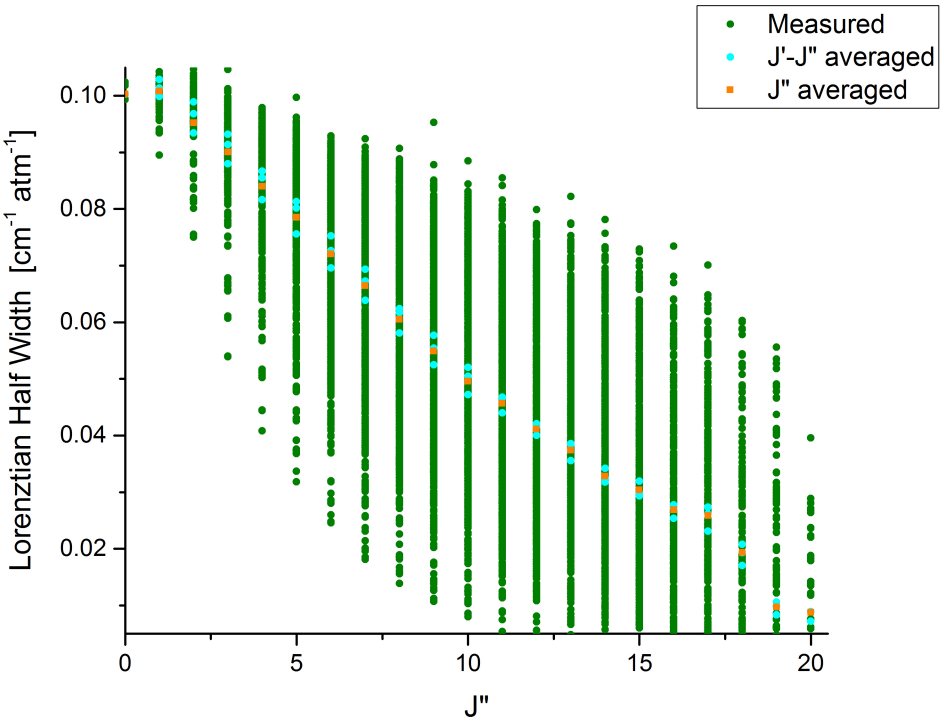

Figure 11.3: Dependence of H_2O Lorentzian half widths on rotational quantum numbers for a single vibrational band. Green points show measured values, blue points show $J' - J''$ averaged values and orange points show J'' averaged values.

11.2.3 Vibrational Quantum Number Dependence

The vibrational dependence of Lorentzian half widths is often neglected to remove a layer of complexity (see for example Lavrentieva et al. (2014b); Wilzewski et al. (2016)). The argument being that the rotational dependence of the Lorentzian half width is much stronger (Lavrentieva et al. (2014b)) or that vibrational dependence is not observed in the available measurements (Wilzewski et al. (2016); Ngo et al. (2012)) and hence can be assumed to be negligible.

However vibrational dependence has been observed for particular molecule-broadener systems (see for example Cottaz et al. (2001); Kleiner et al. (2003)) and some attempts have been made to include this dependence in particular datasets. For example, in the case of NH_3-NH_3, it was observed by Cottaz et al. (2001) that select transitions in vibrational bands with similar vibrational quantum numbers differed by a roughly

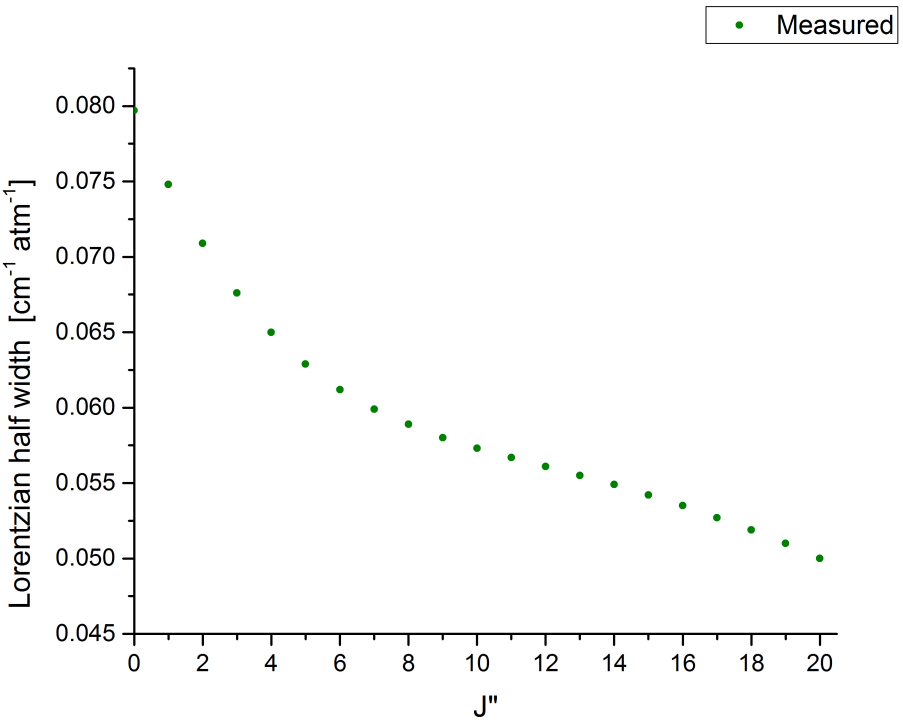

Figure 11.4: Dependence of CO Lorentzian half widths on rotational quantum numbers for a single vibrational band. Green points show measured values.

constant factor. The effect was approximated in the HITRAN database by deriving this factor for each observed band with respect to the strongest band, and then using the factor to scale the computed widths for the strongest band to obtain widths for the other bands (Kleiner et al. (2003)). Another example, for H_2O-He Petrova and co-workers performed detailed measurements for several vibrational bands and derived an analytical expression that described the broadening coefficients as a function of vibrational and rotational quantum numbers and temperature (Petrova et al. (2016, 2013, 2012)).

ExoMol will supply measured, calculated or empirically derived widths with vibrational assignments where available, but will not attempt to fill in any gaps using scaling factors.

11.2.4 Broadening Species Dependence

The calculation of absorption cross sections assuming different broadening gases can produce significantly different results (Wilzewski et al. (2016); Hedges & Madhusudhan (2016)).

The strength of a broadener depends on intermolecular (in particular dipole-dipole) interactions between the broadener and molecular species. In general for the foreign broadening species currently being considered by ExoMol (Wilzewski et al. (2016); Rothman et al. (2013)):

$$\text{air} \approx N_2 > H_2 > He \tag{11.2}$$

While the position of self broadening in the hierarchy depends on the molecule in question. For example in the case of H_2O (Hedges & Madhusudhan (2016)):

$$H_2O > \text{air} \approx N_2 > H_2 > He \tag{11.3}$$

Where multiple molecular-broadener datasets for the same molecule but different broadeners is desired, one approach is to measure, or compile measurements of, the same molecular lines broadened by different species. These can then be used to determine scaling factors for the individual broadeners. Wilzewski et al. (2016) utilized this approach when constructing H_2, He and CO_2 broadened datasets for SO_2. For the SO_2-H_2 and SO_2-He systems, multiple experimental datasets and an empirical model were available to build the datasets. However, for the SO_2-CO_2 system only one line had been measured experimentally. The authors used the scaling factor between this value and the corresponding H_2 broadened width to scale all H_2 broadening coefficients, resulting in a new CO_2 broadened dataset.

Where no data for a particular molecule-broadener system exists, one may use the broadener scaling factors for a similar molecule.

ExoMol will supply pressure broadening parameters for molecule-broadener systems of interest if data is available from the literature. In addition a default value of Lorentzian half width and temperature exponent will be included in the isotopologue definitions files to be used for cases where no information is available.

11.2.5 Default Values

Where no data on the pressure broadening of a particular molecule exists at all, one may adopt the broadening parameters of a similar molecule. For example, one could assume that the pressure broadening parameters for SO_3-broadener systems will be approximately the same as for SO_2-broadener systems. The current version of the HITRAN database (Rothman et al. (2013)) gives a single value of 0.07 cm^{-1}/atm for all the SO_3-air Lorentzian half widths. This approximately represents the average of all SO_2-air Lorentzian half widths.

An alternative for the temperature exponent is to use the classical value of 0.5 as a default (Rothman et al. (1987)).

ExoMol will employ such considerations when choosing default values to include in the isotopologue definitions files.

11.3 The `.broad` File

Measured, theoretical and empirical/semi-empirical parameters from the literature are presented with their respective full or partial quantum number assignments. Additional semi-empirical parameters are determined by compiling all experimental and theoretical parameters as a function of J'', the total rotational quantum number of the lower level of the transition, and computing an average value for each J''. To avoid introducing additional error, no extrapolation is attempted beyond the $J''_{\rm max}$ for which data are available, the parameters are simply assumed to be constant from this point. Constructing the pressure broadening parameters file in this way ensures that parameters are provided for every spectral line.

As the quantum numbers are molecule dependent and each file may contain pressure broadening parameters with different sets of quantum number simultaneously, a labelling system was devised to specify the quantum number sets for each molecule.

These quantum number sets are explicitly defined in the isotopologue definitions file, and are the same for each isotopologue of the same molecule. Also provided here are default and $J''_{\rm max}$ values of the Lorentzian half width and temperature exponent. The isotopologue definitions file, described in Tennyson et al. (2016), is a new addition to the ExoMol format and gives information on what ExoMol provides for a particular isotopologue and describes how the data can be used. The description for the pressure broadening section of the isotopologue definitions file is reproduced below.

"If $N_{\rm broad} = 0$ this simply contains default values of Lorentzian half width γ_L and temperature exponent n_L. If $N_{\rm broad} > 0$ this section has the following structure. The broadener is defined first, immediately followed by the associated file name, $J_{\rm max}$, and the asymptotic values of the Lorentzian half width γ_L and temperature exponent n_L for the a0 quantum number set. N_Q quantum number sets are explicitly defined by a label (e.g. a0) that corresponds to codes in the broadener file, the number of lines in the broadener file with that code and the number of quantum numbers in that set. After this each additional quantum number is also described (the total angular momentum quantum number of the lower state, J'', is compulsory). The quantum numbers relate

to the quanta defined in the states section (see Tennyson et al. (2016)) *followed by either a prime or double prime."*

The labelling system referred to above uses two alphanumeric characters, a letter followed by a number, allowing for up to 216 quantum number sets to be defined per molecule. This is more than sufficient, so far the largest number of quantum number sets defined for a single molecule (CH_4) is 10. The highest order approximation represented in the `.broad` file, J'' only dependence, is labelled 'a0', indicating that zero quantum numbers are specified in addition to the compulsory quantum number J''. The second highest order approximation, J'-J'' dependence, is labelled 'a1', indicating that one quantum number is specified in addition to the compulsory quantum number J'' and so forth. The label for pressure broadening parameters with 10+ specified quantum numbers in addition to J'' will begin with a different letter. For example, measured pressure broadening parameters for H_2O with 12 quantum number assignments (including J'') have been given the label 'b2'.

Although, as portrayed above, an attempt was made to make the labels understandable, in truth they are completely arbitrary and their interpretation unnecessary as they are explicitly defined in the isotopologue definitions file.

The data structure of the `.broad` is as follows. The first four fields of the file are mandatory for all records, see Table 11.2. This includes one quantum number, J'', which is always known and hence guarantees that at least a semi-empirical Lorentzian half width (γ_{ref}) and temperature dependence, represented by exponent n (see Eq. (11.1) in Section 11.2.1), can be generated for every molecular line. Additional upper and lower state labels, which give molecule and quantum number dependent behaviour, follow the compulsory fields. These are given in the definitions file along with the maximum J'' for which approximate parameters have been generated, J''_{max}, and the respective values of Lorentzian half width and temperature exponent, γ_{max} and n_{max}. When $J'' > J''_{\text{max}}$, γ_{max} and n_{max} should be used for the Lorentzian half width and temperature exponent respectively.

The `.broad` file has a hierarchical structure; values of γ_{ref} and n with full quantum assignments are presented first, followed by values with partial quantum assignments, then finally values with J'' dependence only. This represents the preferential order in which the values of γ_{ref} and n should be used. This hierarchical structure is demonstrated in Table 11.4 where a portion of the H_2O-H_2 `.broad` file is presented.

Once a suitable γ_{ref} and n have been identified, the Lorentzian half width of a spectral line at temperature T and pressure P using Eq. (11.1) (see Section 11.2.1).

A separate `.broad` file is supplied for each molecule-broadener system and the broadener is specified in the file name. Example .broad files for CS-Air and H_2O-H_2 are given in Table 11.3 and Table 11.4. In the example for H_2O-H_2, pressure broadened parameters provided by Prof. Nina Lavrentieva are represented by the 'a3' block. For particular molecule-broadener systems where no pressure broadening information is available, the default values of γ_{ref} and n given in the isotopologue's definition file may be used.

Table 11.2: Specification of the mandatory part of the pressure broadening parameters file.

Field	Fortran Format	C format	Description
code	A2	%2s	Code identifying quantum number set following J''
γ_{ref}	F6.4	%6.4f	Lorentzian half width at reference temperature and pressure in cm^{-1}/bar
n	F6.3	%6.3f	Temperature exponent
J''	I7/F7.1	%7d/%7.1f	Lower J-quantum number integer/half-integer

Table 11.3: File `12C-32S__air.broad`: Air `.broad` file for $^{12}\mathrm{C}^{32}\mathrm{S}$: portion of the file (upper part); field specification (lower part).

a0	0.0860	0.096	0
a0	0.0850	0.093	1
a0	0.0840	0.091	2
a0	0.0840	0.089	3
a0	0.0830	0.087	4
...			
a0	0.0720	0.067	35
a0	0.0720	0.066	36
...			

Field	Fortran Format	C format	Description
code	A2	%2s	Code identifying quantum number set following J''*
γ_{ref}	F6.4	%6.4f	Lorentzian half width at reference temperature and pressure in cm^{-1}/bar
n	F5.3	%5.3f	Temperature exponent
J''	I7	%7d	Lower J-quantum number

*Code definition:
a0 = no additional quantum numbers specified.

Table 11.4: `1H2-16O__H2.broad`: H_2O - H_2 broad file: portion of the file (upper part); field specification (lower part).

```
...
b2  0.0356  0.300   9   8   1   9   0   8   0   0   0   0   1   0
b2  0.0522  0.300   9   8   1   9   0   8   0   0   0   1   0   0
b2  0.0521  0.300   7   8   1   6   1   7   0   0   0   0   0   1
...
a5  0.0600  0.546   3   4   0   3   1   4
a5  0.0618  0.551   3   4   2   1   1   4
a5  0.0569  0.525   2   3   2   1   3   0
...
a3  0.0724  0.600   1   2   1   0
a3  0.0907  0.640   2   1   1   0
a3  0.0846  0.600   3   2   1   2
...
a1  0.0301  0.268   14  15
a1  0.0291  0.230   15  16
a1  0.0282  0.218   16  17
...
a0  0.0242  0.165   24
a0  0.0239  0.160   25
a0  0.0236  0.150   26
...
```

Field	Fortran Format	C format	Description
code	A2	%2s	Code identifying quantum number set following J''*
γ_{ref}	F6.4	%6.4f	Lorentzian half width at reference temperature and pressure in cm^{-1}/bar
n	F5.3	%5.3f	Temperature exponent
J''	I7	%7d	Lower J-quantum number
J'	I7	%7d	Upper J-quantum number
K''_a	I2	%2d	Lower rotational quantum number
K''_c	I2	%2d	Lower rotational quantum number
K'_a	I2	%2d	Upper rotational quantum number
K'_c	I2	%2d	Upper rotational quantum number
v''_1	I2	%2d	Lower vibrational quantum number
v''_2	I2	%2d	Lower vibrational quantum number
v''_3	I2	%2d	Lower vibrational quantum number
v'_1	I2	%2d	Upper vibrational quantum number
v'_2	I2	%2d	Upper vibrational quantum number
v'_3	I2	%2d	Upper vibrational quantum number

*Code definitions:
b2 = J', K''_a, K''_c, K'_a, K'_c, v''_1, v''_2, v''_3, v'_1, v'_2, v'_3;
a5 = J', K''_a, K''_c, K'_a, K'_c;
a3 = J', K''_a, K'_a;
a1 = J';
a0 = no additional quantum numbers specified.

11.4 Summary of Results

Pressure broadening parameters are now included in the ExoMol database in the form of `.broad` files. Each file provides calculated or measured parameters where available and a model for determining parameters for other lines for a single molecule-broadener system. The files can be used to generate a complete, if mostly approximate, pressure broadening dataset for each molecule-broadener system considered.

Chapter 12

Summary and Conclusions

The following results have been presented in Chapters 6 to 11:

1. New comprehensive line lists for all stable isotopologues of NaCl and KCl.
2. Improved line lists for all stable isotopologues of CS.
3. Validation of current hot line lists for HCl, H_2CO and CH_4 for industrial spectral studies.
4. Demonstration that improvements to the current hot line list for NH_3 are required.
5. 5080 new line assignments and 3151 new experimental energies for NH_3 in the region 500 - 11,000 cm^{-1}.
6. Preliminary results from the analysis of a room temperature NH_3 spectrum in the region 9000 - 10,400 cm^{-1}.
7. Preliminary results from a MARVEL analysis that shall result in a self-consistent compilation of accurate experimental energies for CH_4.
8. Pressure dependent cross sections for H_2O, CO, CO_2 and NH_3 computed for a range of temperatures and pressures relevant to extrasolar planetary atmospheres.
9. A new file type to be included with the ExoMol format, the `.broad` file, that shall be used to provide pressure broadening parameters with the ExoMol line lists.

12.1 Concluding Remarks

The data requirements and challenges related to data usage of the projects described in Chapters 6 to 10 were used to inform the implementation of pressure broadening in the ExoMol database (Chapter 11) as follows.

First it is necessary to select a line shape that models the pressure broadening of molecular lines, for which parameters can be provided. Voigt profiles are in widespread use and are easily computed, they are therefore used to represent pressure broadening effects in ExoMol.

It was immediately apparent that for many molecule-broadener systems relevant to ExoMol, pressure broadening information was not comprehensive. The pressure dependent parameters for the majority of ExoMol lines would thence be generated from a model.

Once available calculated and measured parameters for a molecule were complied, and the appropriate model or models identified to fill in the gaps, it would be a straightforward task to extract or generate pressure broadening parameters for every ExoMol line. This is the HITRAN approach to constructing pressure broadening parameter datasets. However some ExoMol line lists, such as YT10to10 (CH_4), already present data handling issues due to their sheer size. Adding columns of pressure broadening parameters to the transitions files would exacerbate this problem, for little gain, considering the sparsity of accurate information.

This challenge related to data usage led to the decision that the pressure broadening parameters would be integrated into the compact ExoMol format as a new file type, the `.broad` file. Each molecule could have a number of associated `.broad` files, one per broadener, as the completeness of pressure broadening datasets varies with broadener.

Industrial spectral studies are carried out at high resolution and physical conditions under which pressure broadening has a significant influence on the observed spectra. Therefore the retrieval of molecular concentrations, the desired information, using theoretical models could be hampered by inaccurate line width data.

Accurate measured and calculated pressure broadening parameters where available should be included in the `.broad` files to meet this data requirement.

Extrasolar planetary spectral retrieval is hindered by incomplete molecular data. It has been demonstrated that the millions or billions of lines calculated by ExoMol add up to a significant amount of opacity at high temperatures relevant to favourable targets (Yurchenko et al. (2014)). Pressure, as implied by the cross section calculations, has the effect of redistributing this opacity and hence can have a strong impact on the observed spectrum.

A model that guarantees a complete pressure broadening dataset can be generated, should be included in the `.broad` file to meet this data requirement.

To include the two types of pressure broadening parameters, accurate (measured or calculated) and approximate (model generated), a hierarchical structure was devised based on quantum number dependence. Accurate parameters would come with an assignment pertaining to a particular transition, for which the parameters have been measured, or a small collection of transitions with similar quantum numbers, for which the parameters have been observed or are predicted to be the same. Approximate parameters would be associated with at least one quantum number which is known for every molecular transition (for example J''). Every molecular transition with the same value of that quantum number (for example $J'' = 1$), for which accurate parameters have not been measured or calculated, would be assumed to have the

same (approximate) parameters.

The resulting `.broad` file (see Chapter 11) meets the data requirements for both industrial and extrasolar planetary spectral studies, whilst not significantly increasing the size of the current line lists.

The files also provide the necessary pressure broadening information for other applications with similar data requirements. For example, the interpretation of brown dwarf atmospheres requires complete pressure broadening datasets, as they are similar to extrasolar planetary atmospheres, but also accurate data for strong features, as it is possible to obtain high resolution measurements of brown dwarf atmospheres.

This work also represents a successful collaboration between academia and industry. Chloride containing molecules, H_2CO, NH_3, CH_4, elevated temperatures and ambient pressure are common to both industrial and extrasolar planetary applications. Indeed *"it is surprising how similar smoke stacks and hot extrasolar planetary atmospheres are"* (Prof Jonathan Tennyson). Hence, as demonstrated here, work to provide, improve or validate data for those molecules and conditions is beneficial to both parties. The new NaCl/KCl line lists presented here, or existing H_2CO/HCl/CH_4 line lists validated here, can be used to identify and extract information from molecular features in smoke stack or extrasolar planetary atmospheric spectra. Work on the NH_3 spectrum has provided new information that should be useful for fitting the new PES and validating the resulting line list. The line list could then be used in the same manner expressed above. Implementing pressure broadening in the ExoMol database will allow users to generate pressure dependent spectra from the ExoMol line lists without the need to seek parameters elsewhere. This is vital for industrial spectral studies and arguably important for current extrasolar planet spectral studies. Clearly for both applications one must be wary of the accuracy of the pressure broadening dataset, as this can introduce an appreciable uncertainty in the calculated spectra (Chapter 10).

Finally this work has utilised and, following work by Zobov and co-workers, further demonstrated the power of variational line lists for analysing complex polyatomic spectra. Methods employed here could be applied to other molecules.

12.2 Future Work

Clearly the project which requires the most future work is pressure broadening. Firstly, the Voigt line shape is widely used to model the combined thermal and pressure broadening, though is it known to be only an approximate solution and some decisions on its evaluation are made for computational rather than physical reasons. The influence of employing more complex line shapes in the calculations of the cross sections on the resulting spectra needs to be investigated. The second issue, and perhaps the more critical one, is the availability of accurate pressure broadening parameters. Tests performed in this work imply that the largest uncertainty in the cross sections is introduced by the choice of pressure broadening dataset. There is a need for more experimental or detailed theoretical work, particularly for broadening by hydrogen and helium. Also the assumed temperature and pressure dependence of

the line widths needs more thorough investigation. A linear dependence on pressure appears to be a reasonable assumption around ambient pressure, though there is no evidence that this is true for much higher pressures. The simple power law describing temperature dependence has been shown to only work well within narrow temperature ranges. Measurements of pressure broadened line widths for higher pressures and a wide range of temperatures for a number of molecule-broadener systems is required to develop and verify realistic models describing the temperature and pressure dependence of line widths.

For KCl, NaCl, CS and other ExoMol diatomics improvements in the computation and validation of line intensities could be pursued. It has been suggested that the use of a point-wise dipole moment and double rather than quadrupole precision, as is typically used in the computation of diatomic line intensities, can result in a gross overestimation of high overtone intensities. Hence implementing a functional from of the dipole and increasing the precision used in the computation of Einstein A coefficients could rectify this problem. For the validation of line intensities new experimental work is required, specifically the measurement of absolute intensities.

Significant contributions have been made to the understanding of the NH_3 spectrum, in particular above 7000 cm^{-1}. Future work will include completion of the analysis in the region 9000 - 10,400 cm^{-1} and could include extensions of the other analyses. For example the new NH_3 line list could be employed to assign more lines in the region 7400 - 8600 cm^{-1} and potentially resolve some of the labelling problems in this region. In addition it is worthwhile mentioning that more room temperature spectra for NH_3, measured by Dr Catherine de Bergh in 1980, is available from the Kitt Peak Archive. These spectra cover spectral ranges around 6500, 15,000 and 18,000 cm^{-1}. The first region could be analysed using BYTe or the new NH_3 line list, the second region would require the new line list as BYTe coverage stops at 12,000 cm^{-1} while the last region is beyond the reach of current theoretical works.

Finally for CH_4, future work shall include completion of the MARVEL project and analysis of high temperature spectra in the region 1000 - 6300 cm^{-1}. It may also be possible to analyse other experimental works in various regions of the CH_4 spectrum which are currently unassigned.

Bibliography

Abrams R. L., 1974, Appl. Phys. Lett., 25, 609

Ahrens V., Winnewisser G., 1999, Z. Naturforsch, 54a, 131

Al Derzi A. R., Furtenbacher T., Yurchenko S. N., Tennyson J., Császár A. G., 2015, J. Quant. Spectrosc. Radiat. Transf., 161, 117

Al-Refaie A. F., Polyansky O. L., I. R., Ovsyannikov, Tennyson J., Yurchenko S. N., 2016, Mon. Not. R. Astron. Soc., 461, 1012

Al-Refaie A. F., Yurchenko S. N., Yachmenev A., Tennyson J., 2015, Mon. Not. R. Astron. Soc., 448, 1704

Albert S., Bauerecker S., Boudon V., Brown L. R., Champion J.-P., Loëte M., Nikitin A., Quack M., 2009, Chem. Phys., 356, 131

Alberti M., Weber R., Mancini M., Fateev A., Clausen S., 2015, J. Quant. Spectrosc. Radiat. Transf., 157, 14

Allen D. T. et al., 2013, Proc. Natl. Acad. Sci., 110, 17768

Amundsen D. S., Baraffe I., Tremblim P., Manners J., Hayek W., Mayne N. J., Acreman D. M., 2014, Astron. Astrophys., 564, A59

Anderson P. W., 1949, Phys. Rev., 76, 647

Antony B. K., Niles D. L., Wroblewski S. B., Humphrey C. M., Gabard T., Gamache R. R., 2008, J. Mol. Spectrosc., 251, 268

Atkins P. W., de Paula J., 2006, Physical Chemistry 8th Edition. Oxford University Press, England

Azzam A. A. A., Yurchenko S. N., Tennyson J., Naumenko O. V., 2016, Mon. Not. R. Astron. Soc., 460, 4063

Bailey J., 2014, Publ. Astron. Soc. Aust., 31, 43

Barber R. J., Strange J. K., Hill C., Polyansky O. L., Mellau G. C., Yurchenko S. N., Tennyson J., 2014, Mon. Not. R. Astron. Soc., 437, 1828

Barber R. J., Tennyson J., Harris G. J., Tolchenov R. N., 2006, Mon. Not. R. Astron. Soc., 368, 1087

Barman T. S., Konopacky Q. M., Macintosh B., Marios C., 2015, Astrophys. J., 804, 61

Barstow J. K., Aigrain S., Irwin P. G. J., Kendrew S., Fletcher L. N., 2015, Mon. Not. R. Astron. Soc., 448, 2546

Barton E. J., Yurchenko S. N., Tennyson J., 2013, Mon. Not. R. Astron. Soc., 434, 1469

Batalha N. M. et al., 2013, Astrophys. J. Suppl., 204, 24

Bean J. L., Désert J.-M., Seifahrt A., Madhusudhan N., Chilingarian I., Homeier D., Szentgyorgyi A., 2013, Astrophys. J., 771, 108

Bean J. L., Kempton E. M.-R., Homeier D., 2010, Nature, 468, 669

Béguier S., Liu A. W., Campargue A., 2015, J. Quant. Spectrosc. Radiat. Transf., 166, 6

BelBruno J. J., Gelfand J., Radigan W., Verges K., 1982, J. Mol. Spectrosc., 94, 336

Bell S., Ng T., Suggitt C., 1972, J. Mol. Spectrosc., 44, 267

Bermejo D., Santos J., Cancio P., 1992, J. Mol. Spectrosc., 156, 303

Bilalbegovic G., Baranovic G., 2015, Mon. Not. R. Astron. Soc., 446, 3118

Birnbaum G., 1979, J. Quant. Spectrosc. Radiat. Transf., 21, 597

Blanquet G., Walrand J., Bouanich J.-P., 1999, J. Mol. Spectrosc., 198, 408

Bobin B., 1972, Journ. Phys., 33, 345

Bobin B., Fox K., 1973, Journ. Phys., 34, 571

Bogey M., Demuynck C., Destombes J., 1981, Chem. Phys. Lett., 81, 256

Bogey M., Demuynck C., Destombes J., 1982, J. Mol. Spectrosc., 95, 35

Boraas K., Lin Z., Reilly J. P., 1994, J. Chem. Phys., 100, 7916

Born M., Oppenheimer J. R., 1927, Annalen der Physik, 389, 20

Bouanich J.-P., Salem J., Aroui H., Walrand J., Blanquet G., 2004, J. Quant. Spectrosc. Radiat. Transf., 84, 195

Boucher O., Friedlingstein P., Collins B., Shine K. P., 2009, Envrio. Res. Lett, 4, 044007

Boudon V., Pirali O., Roy P., Brubach J.-B., Manceron L., Auwera J. V., 2010, J. Quant. Spectrosc. Radiat. Transf., 111, 1117

Boudon V., Rey M., Loëte M., 2006, J. Quant. Spectrosc. Radiat. Transf., 98, 394

Boursier C., Menard J., Marquette A., Menard-Boucin F., 2006, J. Mol. Spectrosc., 237, 104

Bracewell R. N., 2000, The Fourier Transform and Its Applications 3rd Edition. McGraw-Hill, New York

Brandt A. R. et al., 2014, Science, 343, 733

Brewer L., Brackett E., 1961, Chem. Phys. Rev., 61, 425

Bronnikov D. K., Kalinin D. V., Rusanov V. D., Filimonov Y. G., Selivanov Y. G., Hilico J. C., 1998, J. Quant. Spectrosc. Radiat. Transf., 60, 1053

Brown L. R., 1988, Appl. Optics, 27, 3275

Brown L. R., Benner D. C., Champion J. P., Devi V. M., Fejard L., Gamache R. R., et al., 2003, J. Quant. Spectrosc. Radiat. Transf., 82, 219

Brown L. R., Benner D. C., Devi V. M., Smith M. A. H., Toth R. A., 2005, J. Mol. Struct., 742, 111

Brown L. R., Peterson D. B., 1994, J. Mol. Spectrosc., 168, 593

Brown L. R., Plymate C., 1996, J. Quant. Spectrosc. Radiat. Transf., 56, 263

Brown L. R., Rothman L. S., 1982, Appl. Optics, 21, 2425

Brown L. R. et al., 2013, J. Quant. Spectrosc. Radiat. Transf., 201

Bunker P. R., 1968, J. Mol. Spectrosc., 28, 422

Burkholder J. B., Lovejoy E., Hammer P. D., Howard C. J., 1987, J. Mol. Spectrosc., 124, 450

Burrows A. et al., 1997, Astrophys. J., 491, 856

Butler R. A. H., Sagui L., Kleiner I., Brown L. R., 2006, J. Mol. Spectrosc., 238, 178

Bykov A., Lavrentieva N. N., Sinitsa L., 2004, Mol. Phys., 102, 1706

Cacciani P., Cermák P., Cosléou J., El Rohm J., Hovorka J., Khelkhal M., 2014, Mol. Phys., 112, 2476

Campargue A., Chenevier M., Stoeckel F., 1991, Chem. Phys. Lett., 183, 153

Campargue A., Leshchishina O., Wang L., Mondelain D., Kassi S., 2013, J. Mol. Spectrosc., 291, 16

Campargue A., Mikhailenko S. N., Lohan B. G., Karlovets E. V., Mondelain D., Kassi S., 2015, J. Quant. Spectrosc. Radiat. Transf., 157, 135

Campargue A., Permogorov D., Jost R., 1995, J. Chem. Phys., 102, 5910

Canty J. I. et al., 2015, Mon. Not. R. Astron. Soc., 450, 454

Cara S. D., Houzé M., Jayet P.-A., 2005, Enviromental and Resource Economics, 32, 551

Caris A., Lewen F., Müller H. S. P., Winnewisser G., 2002, Z. Naturforsch, 57a, 663

Caris A., Lewen F., Müller H. S. P., Winnewisser G., 2004, J. Molec. Struct., 695, 243

Carnegie P. A., 2011, Breen Energy and Headwaters Resources Announce Agreement to Market Gas Phase Ammonia Slip Mitigation Technology. Breen Energy News

Cazzoli G., Puzzarini C., Buffa G., Tarrini O., 2008, J. Quant. Spectrosc. Radiat. Transf., 109, 2820

Cermák P., Hovorka J., Veis P., Cacciani P., Cosléou J., Romh J. E., Khelkhal M., 2014, J. Quant. Spectrosc. Radiat. Transfer, 137, 13

Cernicharo J., Guelin M., 1987, Astron. Astrophys., 183, L10

Champion J. P., Hilico J. C., Wenger C., Brown L. R., 1989, J. Mol. Spectrosc., 133, 256

Claveau C., Henry A., Hurtmans D., Valentin A., 2001, J. Quant. Spectrosc. Radiat. Transf., 68, 273

Claveau C., Valentin A., 2009, Mol. Phys., 107, 1417

Clough S. A., Kneizys F. X., Davis R. W., 1989, Atmospheric Research, 23, 229

Clouser P. L., Gordy W., 1964, Phys. Rev. A, 134, 863

Coppola C. M., Lodi L., Tennyson J., 2011, Mon. Not. R. Astron. Soc., 415, 487

Cossart D., Horani M., Rostas J., 1977, J. Mol. Spectrosc., 67, 283

Cottaz C., Tarrago G., Kleiner I., Brown L. R., 2001, J. Mol. Spectrosc., 209, 30

Coxon J. A., Hajigeorgiou P. G., 1992, Chem. Phys., 167, 327

Coxon J. A., Hajigeorgiou P. G., 2015, J. Quant. Spectrosc. Radiat. Transf., 151, 133

Coy S. L., Lehmann K. K., 1986, J. Chem. Phys., 84, 5239

Crawford F. H., Shurcliff W. A., 1934, Phys. Rev., 45, 860

Croll B., Albert L., Jayawardhana R., Kempton E. M.-R., Fortney J. J., Murray N., Neilson H., 2011, Astrophys. J., 736, 78

Crossfield I. J. M., 2015, Publ. Astron. Soc. Pac., 127, 941

Dang-Nhu M., Pine A. S., Robiette A. G., 1979, J. Mol. Spectrosc., 77, 57

Daumont L. et al., 2013, J. Quant. Spectrosc. Radiat. Transf., 116, 101

de Martino A., Frey R., Pradere F., 1983a, Chem. Phys. Lett., 100, 329

de Martino A., Frey R., Pradere F., 1983b, Chem. Phys. Lett., 95, 200

Devi V. M., Benner D. C., Smith M. A. H., Rinsland C. P., Sharpe S., Sams R. L., 2003, J. Quant. Spectrosc. Radiat. Transf., 82, 319

Devi V. M., Benner D. C., Smith M. A. H., Rinsland C. P., Sharpe S., Sams R. L., 2004, J. Quant. Spectrosc. Radiat. Transf., 87, 339

Dick M. J., Drouin B. J., Pearson J. C., 2009, J. Quant. Spectrosc. Radiat. Transf., 110, 619

Down M. J., Hill C., Yurchenko S. N., Tennyson J., Brown L. R., Kleiner I., 2013, J. Quant. Spectrosc. Radiat. Transf., 130, 260

Drouin B., Wiesenfeld L., 2012, Phys. Rev. A, 86, 022705

Dutta J. M., Jones C. R., Goyette T. M., Lucia F. C., 1993, Icarus, 102, 232

Edwards D. P., Strow L. L., 1991, J. Geophys. Res., 96, 20

Encrenaz T., 1990, Reports on Progress in Physics, 53, 793

Engel E. A., Doss N., Harris G. J., Tennyson J., 2005, Mon. Not. R. Astron. Soc., 357, 471

EPA, 2014a, Methane Emissions. United States Enviromental Protection Agency, http://www.epa.gov/airquality/oilandgas/methane.html Last updated on 27/08/2015

EPA, 2014b, Nitrogen Oxides. United States Enviromental Protection Agency, http://www.epa.gov/oaqps001/nitrogenoxides/ Last updated on 15/08/2014

EPA, 2015, Inventory of U.S. Greenhouse Gas Emissions and Sinks: 1990-2013. Tech. rep., United States Environmental Protection Agency, ePA 430-R-15-004

Evseev V., Fateev A., Clausen S., 2012, J. Quant. Spectrosc. Radiat. Transf., 113, 2222

F. Ochsenbein, P. Bauer, J. Marcout, 2000, Astron. Astrophys. Suppl., 143, 23

Fateev A., 2015, in Spectroscopy of Exoplanets, Cumberland Lodge, Windsor, 24-26 July 2015

Fateev A., Clausen S., 2008, Online non-contact gas analysis. Tech. rep., Technical University of Denmark, contract no.: Energinet.dk no. 2006 1 6382.

Fateev A., Clausen S., 2012, in 22nd UCL Astrophysics Colloquium: Opacities in Cool Stars and Exoplanets, Cumberland Lodge, Windsor, 2-5 June 2012

Faure A., Wiesenfeld L., Tennyson J., Drouin B. J., 2013, J. Quant. Spectrosc. Radiat. Transf., 116, 79

Fejard L., Champion J. P., Jouvard J. M., Brown L. R., 2000, J. Mol. Spectrosc., 201, 83

Field R. W., 2015, Spectra and Dynamics of Small Molecules: Alexander von Humboldt Lectures. Springer International Publishing, Switzerland

Fischer J., Gamache R. R., Goldman A., Rothman L. S., Perrin A., 2003, J. Quant. Spectrosc. Radiat. Transf., 82, 401

Fortney J. J. et al., 2016, arXiv:1602.06305v2 [astro-ph.EP]

Fox K., Jennings D. E., Stern E. A., Hunnard R., 1988, J. Quant. Spectrosc. Radiat. Transf., 39, 473

Fré R. D., Vanderreudt I., Swaans W., 2004, Formaldehyde measurement in emissions from press board and bonded fibre production. Tech. rep., CEM-2004

Fu Q., Liou K. N., 1992, J. Atmos. Sci., 49, 2139

Furtenbacher T., Császár A. G., 2012, J. Quant. Spectrosc. Radiat. Transf., 113, 929

Furtenbacher T., Császár A. G., Tennyson J., 2007, J. Mol. Spectrosc., 245, 115

Gabard T., Grigoriev I. M., Grigorovich N. M., Tonkov M. V., 2004, J. Mol. Spectrosc., 225, 123

Gamache R. R., 2005, J. Mol. Spectrosc., 229, 9

Gamache R. R., Hartmann J.-M., 2004, Can. J. Chem., 82, 1013

Gamache R. R., Laraia A. L., 2009, J. Mol. Spectrosc., 257, 116

Gamache R. R., Lynch R., Brown L. R., 1996, J. Quant. Spectrosc. Radiat. Transf., 56, 471

Gamache R. R., Lynch R., Plateaux J. J., Barbe A., 1997, J. Quant. Spectrosc. Radiat. Transf., 57, 485

Gasster S. D., Townes C. H., Goorvitch D., Valero F. P. J., 1988, J. Opt. Soc. Am. B, 5, 593

Georgoes R., Herman M., Hilico J. C., Robert O., 1998, J. Mol. Spectrosc., 187, 13

Giannini E., Lunine J. I., 2013, Rep. Prog. Phys., 76, 056901

Gibb E. L., Mumma M. J., Russo N. D., DiSanti A. A., Magee-Sauer K., 2003, Icarus, 165, 391

Giese T. J., York D. M., 2004, J. Chem. Phys., 120, 7939

Godon M., Bauer A., 1988, Chem. Phys. Lett., 147, 189

Goldberg L., 1950, Astrophys. J., 113, 567

Golubiatnikov G., Koshelev M., Krupnov A., 2008, J. Quant. Spectrosc. Radiat. Transf., 109, 1828

Golubiatnikov Y. G., 2005, J. Mol. Spectrosc., 230, 196

Gordon I. E. et al., 2007, J. Quant. Spectrosc. Radiat. Transf., 108, 389

Gottlieb C. A., Myers P. C., Thaddeus P., 2003, Astrophys. J., 588, 655

Griffiths P. R., de Haseth J. A., 2007, Fourier Transform Infrared Spectrometry, 2nd Edition. John Wiley and Sons Ltd, England

Grigoriev I. M., Filippov N. N., Tonkov M. V., Champion J. P., 2002, J. Quant. Spectrosc. Radiat. Transf., 74, 431

Grigoriev I. M., Filippov N. N., Tonkov M. V., Gabard T., Le Doucen R., 2001, J. Quant. Spectrosc. Radiat. Transf., 69, 189

Grimm S. L., Heng K., 2016, Astrophys. J., 808, 182

Grosch H., Fateev A., Nielsen K. L., Clausen S., 2013, J. Quant. Spectrosc. Radiat. Transf., 130, 392

Hadded S., Arouli H., Orphal J., Bouanich J.-P., Hartmann J.-M., 2001, J. Mol. Spectrosc., 210, 275

Hargreaves R. J., Beale C. A., Michaux L., Irfan M., Bernath P. F., 2012a, Astrophys. J., 757, 46

Hargreaves R. J., Li G., Bernath P. F., 2011, Astrophys. J., 735, 111

Hargreaves R. J., Li G., Bernath P. F., 2012b, J. Quant. Spectrosc. Radiat. Transf., 113, 670

Harris G. J., Larner F. C., Tennyson J., Kaminsky B. M., Pavlenko Y. V., Jones H. R. A., 2008, Mon. Not. R. Astron. Soc., 390, 143

Hartmann J.-M., Boulet C., Robert D., 2008, Collisional Effects on Molecular Spectra. Elsevier, Oxford

Hebert A. J., Lovas F. J., Melendres C. A., Hollowell C. D., StoryJr T. L., StreetJr K., 1968, J. Chem. Phys., 48, 2824

Hedges C., Madhusudhan N., 2016, Mon. Not. R. Astron. Soc., 458, 1427

Herzberg G., 1950, Molecular Spectra and Molecular Structure Volume I - Spectra of Diatomic Molecules. D. Van Nostrand Company Inc, New Jersey

Herzberg G., 1991, Molecular Spectra and Molecular Structure Volume II - Infrared and Raman Spectra of Polyatomic Molecules. Krieger Publishing Company, Florida

Hilico J. C., Baronov G. S., Bronnikov D. K., Gavrikov S. A., Nikolaev I. I., Rusanov V. D., Filimonov Y. G., 1993, J. Mol. Spectrosc., 161, 435

Hilico J. C., Degni J., Champion J. P., Guelachvili G., 1980, J. Mol. Spectrosc., 81, 277

Hilico J. C., Loete L., Champion J. P., Destomes J. L., Bogey M., 1987, J. Mol. Spectrosc., 122, 381

Hilico J. C., Loete M., Brown L. R., 1985, J. Mol. Spectrosc., 111, 119

Hilico J. C., Loete M., Brown L. R., 1992, J. Mol. Spectrosc., 152, 229

Hill C., Yurchenko S. N., Tennyson J., 2013, Icarus, 226, 1673

Hipper M., Quack M., 2001, J. Chem. Phys., 116, 6045

Hollas J. M., 2004, Modern Spectroscopy 4th Edition. John Wiley and Sons Ltd, England

Hollis M. D. J., Tessenyi M., Tinetti G., 2014, Comp. Phys. Comm., 185, 695

Holt C. W., Gerry M. C. L., Ozier I., 1973, Phys. Rev. Lett., 31, 1033

Honig A., Mandel M., Stitch M. L., Townes C. H., 1954, Phys. Rev., 93, 953

Horiai K., Fujimoto T., Nakagawa K., Uehara H., 1988, Chem. Phys. Lett., 147, 133

Hu R., Seager S., 2016, Astrophys. J., 784, 63

Huang X., Schwenke D. W., Lee T. J., 2011a, J. Chem. Phys., 134, 044320

Huang X., Schwenke D. W., Lee T. J., 2011b, J. Chem. Phys., 134, 044321

Huber K. P., Herzberg G., 1979, Molecular Spectra and Molecular Structure IV. Constants of Diatomic Molecules. Van Nostrand Reinhold Company, New York

Hund F., 1927, Z. Physik, 40, 742

Husson N., Poussigue G., Valentin A., Amiot C., 1972, Phys. Rev. A, 7, 267

Huth R., Brown L. R., Toth R., Brault J. W., 1981, J. Mol. Spectrosc., 86, 170

Irwin A. W., 1981, Astrophys. J. Suppl., 45, 621

Irwin P. G. J., Calcutt S. B., Sihra K., Taylor F. W., Weir A. L., Ballard J., Johnston W. B., 1999, J. Quant. Spectrosc. Radiat. Transf., 62, 193

Irwin P. G. J. et al., 2008, Icarus, 109, 1136

Jacquemart D., Laraia A., Tchana F. K., Gamache R. R., Perrin A., Lacome N., 2010, J. Quant. Spectrosc. Radiat. Transf., 111, 1209

Jacquinet-Husson N. et al., 2011, J. Quant. Spectrosc. Radiat. Transf., 112, 2395

Johnson S. G., 2012, Faddeeva Package: complex error functions. C++ open-source code, http://uk.mathworks.com/matlabcentral/fileexchange/38787-faddeeva-package–complex-error-functions (Updated 17 Dec 2012)

Karkoschka E., 1998, Icarus, 133, 134

Kear R. W., 2007, J. Appl. Chem., 5, 237

Kewley R., Sastry K. V. L. N., Winnewisser M., Gordy W., 1963, J. Chem. Phys., 39, 2856

Kim E., Yamamoto S., 2003, J. Mol. Spectrosc., 219, 296

Kirchgessner D. A., Lott R. A., Cowgill R. M., Harrison M. R., Shires. T. M., 1997, Chemosphere, 35, 1365

Kleiner I., Brown L. R., Tarrago G., Kou Q. L., Picque N., Guelachvili G., Dana V., Mandin J. Y., 1999, J. Mol. Spectrosc., 193, 46

Kleiner I., Tarrago G., Brown L. R., 1995, J. Mol. Spectrosc., 173, 120

Kleiner I. et al., 2003, J. Quant. Spectrosc. Radiat. Transf., 82, 293

Knight G., 2008, Selective Catalytic Reduction Technology for the Control of Nitrogen Oxide Emissions from Coal-Fired Boilers. DIANE Publishing, U.S.

Knutson H. A., Benneke B., Deming D., Homeier D., 2014, Nature, 505, 66

Kreidberg L. et al., 2014, Nature, 505, 66

Langlois S., Birbeck T. P., Hanson R. K., 1994, J. Mol. Spectrosc., 167, 272

Lavrentieva N. N., Dudaryonok A. S., Ma Q., 2014a, Proceedings of SPIE., 92920M, 1

Lavrentieva N. N., Voronin B. A., Naumenko O. V., Bykov A. D., Fedorova A. A., 2014b, Icarus, 236, 38

Lazarev V. V., Ponomarev Y. N., Sumpf B., Fleischmann O., Waschull J., Kronfeldt H., Stroinova V. N., 1995, J. Mol. Spectrosc., 173, 177

Leeuw F. H., Wachem R., Dymanus A., 1970, J. Chem. Phys., 53, 981

Leggett S. K. et al., 2000, Astrophys. J., 536, L35

Lehmann K. K., Coy S. L., 1988, J. Chem. Soc. Faraday Trans. II, 84, 1389

LeRoy R. J., 2007, LEVEL8.0: A Computer Program for Solving the Radial Schrödinger Equation for Bound and Quasibound Levels. University of Waterloo, Chemical Physics Research Report

LeRoy R. J., 2011, Equilibrium Structure of Molecules. Taylor and Francis, London, pp. 159–293

LeRoy R. J., Seto J. Y., Huang Y., 2006, DPotFit1.1: A Computer Program for Fitting Diatomic Molecule Spectral Data to Potential Energy Functions. University of Waterloo, Chemical Physics Research Report

Levy A., Lacome N., Tarrago G., 1993, J. Mol. Spectrosc., 157, 172

Levy A., Lacome N., Tarrago G., 1994, J. Mol. Spectrosc., 166, 20

Li C., Deng L., Zhang J., Qiu X., Wei J., Chen Y., 2013, J. Mol. Spectrosc., 284, 29

Li G., Gordan I. E., Rothman L. S., Tan Y., Hu S.-M., Kassi S., Campargue A., Medvedev E. S., 2015, Astron. Astrophys. Suppl., 216, 15

Li G., Gordon I., Hajigeorgiou P. G., Coxon J. A., Rothman L. S., 2013b, J. Quant. Spectrosc. Radiat. Transf., 130, 284

Li G., Gordon I., LeRoy R. J., Hajigeorgiou P. G., Coxon J. A., Bernath P. F., Rothman L. S., 2013a, J. Quant. Spectrosc. Radiat. Transf., 121, 78

Line M. R. et al., 2013, Astrophys. J., 775, 137

Liou K. N., 2002, An Introduction to Atmospheric Radiation 2nd Edition. Elsevier Science, USA

Lodi L., Yurchenko S. N., Tennyson J., 2015, Mol. Phys., 113, 1559

Lovas F., Krupenie P., 1974, J. Phys. Chem. Ref. Data, 3, 245

Lucchesinia A., Gozzini S., Gabbanini C., 2000, Eur. Phys. J. D, 8, 223

Lynch R., Gamache R. R., Neshyba S. P., 1996, J. Chem. Phys., 105, 5711

Madhusudhan N., Agundez M., Moses J. I., Hu Y., 2016, Space Science Reviews, in review

Madhusudhan N., Knutson H., Fortney J. J., Barman T., 2014, Protostars and Planets VI - Exoplanetary Atmospheres in Part III, University of Arizona Press, p. 739

Mandell A. W., Haynes K., Sinukoff E., Madhusudhan N., Burrows A., Deming D., 2013, Astrophys. J., 779, 128

Mantz A. W., Devi V. M., Benner D. C., .et al, 2005, J. Molec. Struct., 742, 99

Marais D. J. D. et al., 2004, Astrobiology, 2, 153

Margolis J. S., 1988, Appl. Optics, 27, 4038

Margolis J. S., 1990, Appl. Optics, 29, 2295

Margolis J. S., 1993, J. Quant. Spectrosc. Radiat. Transf., 50, 431

Markov V., 1994, J. Mol. Spectrosc., 164, 233

Martinez R. Z., Bermejo D., Santos J., Champion J. P., Hilico J. C., 1997, J. Chem. Phys., 107, 4864

Matsuo T., Trau W. A., Hattori M., Tamura M., 2011, Astrophys. J., 729, 50

Mayor M., Queloz D., 1995, Nature, 378, 355

McKemmish L. K., Yurchenko S. N., Tennyson J., 2016, Mon. Not. R. Astron. Soc., in press

Medvedev E. S., 2012, J. Chem. Phys., 137, 174307

Medvedev E. S., Meshkov V. V., Stolyarov A. V., Gordan I. E., 2015, J. Chem. Phys., 143, 154301

Medvedev E. S., Meshkov V. V., Stolyarov A. V., Ushakov V. G., Gordon I. E., 2016, J. Mol. Spectrosc., in press

Mehrotra S. C., Mäder H., de Vreede J. P. M., Dijkerman H. A., 1985, Chem. Phys., 93, 115

Menard-Bourcin F., Doyenette L., Menard J., Boursier C., 2000, J. Phys. Chem. A, 104, 5444

Mérienne M.-F. et al., 2003, J. Quant. Spectrosc. Radiat. Transf., 82, 99

Miles T., Miles T. J., Baxter L., Bryers R., Jenkins B., Oden L., 1995, Alkali deposits found in biomass power plants: a preliminary investigation of their extent and nature. National Renewable Energy Labratory, Golden, CO

Misago F., Lepére M., Bouanich J.-P., 2009, J. Mol. Spectrosc., 254, 16

Mittleman D., 2013, Sensing with Terahertz Radiation. Springer-Verlag, Berlin Heidelberg

Moal M. F. L., Severin F., 1986, J. Quant. Spectrosc. Radiat. Transf., 35, 145

Mockler R. C., Bird G. R., 1955, Phys. Rev., 98, 1837

Mohr P. J., Newell D. B., Taylor B. N., 2014, arXiv:1507.07956 [physics.atom-ph]

Montgomery M., Jensen S. A., Borg U., Biede O., Vilhelmsen T., 2010, Materials and Corrosion, 61, 9999

Müller H. S. P., Schlöder F., Stutzki J., Winnewisser G., 2005, J. Mol. Spectrosc., 742, 215

Muñoz A. G., Isaak K. G., 2015, Proc. Natl. Acad. Sci. USA, 112, 13461

Nassar R., Bernath P., 2003, J. Quant. Spectrosc. Radiat. Transf., 82, 279

Neale L., Miller S., Tennyson J., 1996, Astrophys. J., 464, 516

Nerf R. B. J., 1975, J. Mol. Spectrosc., 58, 451

Neveu M., Kim H.-J., Benner S. A., 2013, Astrobiology, 13, 391

Newman S. M., Orr-Ewing A. J., Newman D. A., Ballard J., 2000, J. Chem. Phys., 104, 9467

Ngo N. H., Tran H., Gamache R. R., Hartmann J. M., 2012, Phil. Trans. R. Soc., 370, 2495

Nielson N. P., Frandsen F. J., Dam-Johansen K., Baxter L. L., 2000, Progress in Energy and Combustion Science, 26, 283

Nikitin A. et al., 2015, J. Quant. Spectrosc. Radiat. Transf., 154, 63

Nikitin A., Rey M., Tashkun S., Kassi S., Mondelain D., Campargue A., Tyuterev V., 2016, J. Quant. Spectrosc. Radiat. Transf., 168, 207

Nikitin A., Thomas X., Régalia L., Daumont L., Rey M., Tashkun S., Tyuterev V., Brown L., 2014, J. Quant. Spectrosc. Radiat. Transf., 138, 116

Nisbet E. G., Dlugokencky E. J., Bousquet P., 2014, Science, 343, 493

NIST, 2009, NIST Special Publication 330: The International System of Units (SI). Barry N. Taylor and Ambler Thompson, Editors

NSO, 2004, NSO Digital Library. Can be accessed from http://diglib.nso.edu/

Oldani M., Andrist M., Bauder A., Robiette A. G., 1987, J. Mol. Spectrosc., 122, 381

Owyoung A., Patterson C. W., McDowell R. S., 1978, Chem. Phys. Lett., 59, 156

Pack R. T., 1979, J. Chem. Phys., 70, 3424

Padmanabhan A., Tzanetakisa T., Chanda A., Thomson M. J., 2014, J. Quant. Spectrosc. Radiat. Transf., 133, 81

Pater I., Lissauer J. J., 2013, Planetary Sciences 2nd Edition. Cambridge University Press

Patrascu A. T., Tennyson J., Yurchenko S. N., 2015, Mon. Not. R. Astron. Soc., 449, 3613

Paulose G., Barton E. J., Yurchenko S. N., Tennyson J., 2015, Mon. Not. R. Astron. Soc., 454, 1931

Pavlyuchko A. I., Yurchenko S. N., Tennyson J., 2015, Mon. Not. R. Astron. Soc., 452, 1702

Payne V., Delamere J., Cady-Pereira K., Gamache R., Moncet J.-L., Mlawer E., Clough S., 2008, IEEE Transactions on Geoscience and Remote Sensing, 46, 3601

Peach G., 1981, Advances in Physics, 30, 367

Petrova T. M., Solodov A. M., Solodov A. A., Starikov V. I., 2012, Mol. Phys., 110, 1493

Petrova T. M., Solodov A. M., Solodov A. A., Starikov V. I., 2013, J. Quant. Spectrosc. Radiat. Transf., 129, 241

Petrova T. M., Solodov A. M., Solodov A. A., Starikov V. I., 2016, J. Mol. Spectrosc., 321, 50

Pickett H., Poynter R. L., Cohen E. A., Delitsky M. L., Pearson J. C., Müller H. S. P., 1998, J. Quant. Spectrosc. Radiat. Transf., 60, 883

Pickett H. M., Poynter R. L., Cohen E. A., 1981, J. Quant. Spectrosc. Radiat. Transf., 26, 197

Pierre G., Hilico J., Bergh C. D., Maillard J., 1980, J. Mol. Spectrosc., 82, 379

Pine A. S., 1992, J. Chem. Phys., 97, 773

Pine A. S., Markov V. N., Buffa G., Tsrrini O., 1993, J. Quant. Spectrosc. Radiat. Transf., 50, 337

Pineiro A. L., Tipping R. H., Chackerian Jr C., 1987, J. Mol. Spectrosc., 125, 91

Pinson P., Dupre-Maquaire J., 1979, J. Mol. Spectrosc., 78, 170

Poddar P., Mitra S., Hossain M. M., Biswas D., Ghosh P. N., Ray B., 2010, Mol. Phys., 108, 1957

Polyansky O. L., Zobov N. F., Tennyson J., Lotoski J. A., Bernath P. F., 1997a, J. Mol. Spectrosc., 184, 35

Polyansky O. L., Zobov N. F., Viti S., Tennyson J., Bernath P. F., Wallace L., 1997b, Astrophys. J., 489, L205

Pont F., Gilliland R. L., Knutson H., Holman M., Charbonneau D., 2008, Mon. Not. R. Astron. Soc. Lett., 393, L6

Predoi-Cross A., Brawley-Tremblay M., Brown L. R., Devi V. M., Benner D. C., 2006, J. Mol. Spectrosc., 236, 201

Predoi-Cross A., Brown L. R., Malathy-Devi V., Brawley-Tremblay M., Benner D., 2005, J. Mol. Spectrosc., 232, 231

Pursell C. J., Weliky D. P., 1992, J. Mol. Spectrosc., 97, 773

Ram R. S., Bernath P. F., Davis S. P., 1995, J. Mol. Spectrosc., 173, 146

Ram R. S., Dulick M., Guo B., Zhang K.-Q., Bernath P. F., 1997, J. Mol. Spectrosc., 183, 360

Rank D. H., Eastman D. P., Skorinko G., Wiggins T. A., 1960, J. Mol. Spectrosc., 1, 78

Regalia-Jarlot L., Thomas X., von der Heyden P., Barbe A., 2005, J. Quant. Spectrosc. Radiat. Transf., 91, 121

Restelli G., Cappellani F., 1979, J. Mol. Spectrosc., 78, 161

Rey M., Nikitin A. V., Babikovb Y. L., Tyutereva V. G., 2016a, J. Mol. Spectrosc., in press

Rey M., Nikitin A. V., Campargue A., Kassi S., Mondelain D., Tyuterev V. G., 2016b, Phys. Chem. Chem. Phys., 18, 176

Rey M., Nikitin A. V., Tyuterev V. G., 2014, Astrophys. J., 789

Rhoderick G. C., Dorko W. D., 2004, Environ. Sci. Technol., 38, 2685

Rice S., Klemperer W., 1957, J. Chem. Phys., 27, 573

Rinsland C. P., Devi V. M., Benner D. C., Smith M. A. H., Sharpe S., Sams R. L., 2004, J. Quant. Spectrosc. Radiat. Transf., 82, 343

Rivlin T., Lodi L., Yurchenko S. N., Tennyson J., Le Roy R. J., 2015, Mon. Not. R. Astron. Soc., 451, 5153

Robert O., Hilico J. C., Loëte M., Champion J. P., r. Brown L., 2001, J. Mol. Spectrosc., 209, 14

Rothman L. S. et al., 1987, Appl. Optics, 26, 4058

Rothman L. S. et al., 2013, J. Quant. Spectrosc. Radiat. Transf., 130, 4

Rothman L. S. et al., 2010, J. Quant. Spectrosc. Radiat. Transf., 111, 2139

Rothman L. S. et al., 2005, J. Quant. Spectrosc. Radiat. Transf., 96, 139

Salem J., Bouanich J.-P., Walrand J., Aroui H., Blanquet G., 2004, J. Mol. Spectrosc., 228, 23

Salem J., Bouanich J.-P., Walrand J., Aroui H., Blanquet G., 2005, J. Mol. Spectrosc., 232, 247

Santos J., Cancio P., Domenech J. L., Rodrigues J., 1992, Laser Chem., 12, 53

Sanzharov M., Auwera J. V., Pirali O., Roy P., Brubach J.-B., Manceron L., Gabard T., Boudon V., 2012, J. Quant. Spectrosc. Radiat. Transf., 113, 1874

Sauval A. J., Tatum J. B., 1984, Astrophys. J. Suppl., 56, 193

Schaefer L., Lodders K., Fegley B., 2012, Astrophys. J., 755, 41

Schmidt T. O. B. et al., 2016, Astron. Astrophys., accepted

Seager S., 2008, Exoplanet Atmospheres: Physical Processes. Princeton University Press

Selsis F., Wordsworth R. D., Forget F., 2011, Astron. Astrophys., 532, A1

Sergent-Rozey M., van Thanh N., Rossi I., Lacome N., Levy A., 1988, J. Mol. Spectrosc., 131, 66

Sharp C. M., Burrows A., 2007, Astrophys. J. Suppl., 168, 140

Shi D. H., Li W. T., Zhang X. N., Sun J. F., Liu Y. F., Zhu Z. L., Wang J. M., 2011, J. Mol. Spectrosc., 266, 27

Shillings A. J. L., Ball S. M., Barber M. J., Tennyson J., Jones R. L., 2011, Atmos. Chem. Phys., 11, 4273

Smith M. A. H., Benner D. C., Predoi-Cross A., Malathy Devi V., 2009a, J. Quant. Spectrosc. Radiat. Transf., 110, 639

Smith M. A. H., Benner D. C., Predoi-Cross A., Malathy Devi V., 2009b, J. Quant. Spectrosc. Radiat. Transf., 111, 1152

Snellen I., 2013, EPJ Web of Conferences, 47, 110011

Snellen I. A. G., de Mooij E. J. W., Albrecht S., 2009, Nature, 459, 543

Sochi T., Tennyson J., 2010, Mon. Not. R. Astron. Soc., 405, 2345

Solodov A. M., Starikov V. I., 2008, Opt. Spectrosc., 105, 14

Solodov A. M., Starikov V. I., 2009, Mol. Phys., 104, 43

Sousa-Silva C., Al-Refaie A. F., Tennyson J., Yurchenko S. N., 2015, Mon. Not. R. Astron. Soc., 446, 2337

Sousa-Silva C., Hesketh N., Yurchenko S. N., Hill C., Tennyson J., 2014, J. Quant. Spectrosc. Radiat. Transf., 142, 66

Starikov V. I., Laventieva N. N., 2006, Collisional Line Broadening and Shifting of Atmospheric Species. Publishing House of IAO DB RAS, Tomsk (in Russian)

Stark G., Yoshino K., Smith P. L., 1987, J. Mol. Spectrosc., 124, 420

Staudt J. E., 2000, Measureing Ammonia Slip from Post Combustion NOx Reduction System. Andover Technology Partners, ICAC Forum

Steyert D. W., Wang W., Sirota J., Donahue N. M., Reuter D. C., 2004, J. Quant. Spectrosc. Radiat. Transf., 83, 183

Strong K., Taylor F. W., Calcutt S. B., Remedios J. J., Ballard J., 1993, J. Quant. Spectrosc. Radiat. Transf., 50, 363

Sudarsky D., Burrows A., Hubeny I., 2003, Astrophys. J., 588, 1121

Sung K., Brown L. R., Huang X., Schwenke D. W., Lee T. J., Coy S. L., Lehmann K. K., 2012, J. Quant. Spectrosc. Radiat. Transf., 113, 1066

Swain M. R. et al., 2010, Nature, 463, 637

Swain M. R. et al., 2009a, Astrophys. J., 704, 1616

Swain M. R., Vasisht G., Tinetti G., 2008, Nature, 452, 329

Swain M. R., Vasisht G., Tinetti G., Bouwman J., Chen P., Yung Y., Deming D., Deroo P., 2009b, Astrophys. J. Lett., 690, L114

Tarrago G., Dang-Nhu M., Poussigue G., Guelachvili G., Amiot C., 1975, J. Mol. Spectrosc., 57, 246

Tashkun S., Perevalov V., 2011, J. Quant. Spectrosc. Radiat. Transf., 112, 1403

Tennyson J., 2011, Astronomical Spectroscopy, 2nd Edition. World Scientific Publishing, London

Tennyson J. et al., 2014, Pure Appl. Chem., 86, 1931

Tennyson J., Hill C., Yurchenko S. N., 2013, AIP Conference Proceedings, 1545, 186

Tennyson J., Kostin M. A., Barletta P., Harris G. J., Polyansky O. L., Ramanlal J., Zobov N. F., 2004, Comp. Phys. Comm., 163, 85

Tennyson J., Yurchenko S. N., 2012, Mon. Not. R. Astron. Soc., 425, 21

Tennyson J. et al., 2016, J. Mol. Spectrosc., in press

Thibault F., Corretja B., Viel A., Bermejo D., Martinez R. Z., Bussery-Honvault B., 2008, Phys. Chem. Chem. Phys., 10, 5419

Thomas G. E., Stamnes K., 1999, Radiative Transfer in the Atmosphere and Ocean. Cambridge University Press

Tinetti G., Tennyson J., Griffiths C. A., Waldmann I., 2012, Phil. Trans. Royal Soc. London A, 370, 2749

Tinetti G. et al., 2007, Nature, 448, 169

Todd T. R., 1977, J. Mol. Spectrosc., 66, 162

Todd T. R., Olson W. B., 1979, J. Mol. Spectrosc., 74, 190

Tsiaras A. et al., 2016, Astrophys. J., 820, 99

Uehara H., Horiai K., Konno T., Miura K., 1990, Chem. Phys. Lett., 169, 599

Uehara H., Horiai K., Nakagawa K., Fujimoto T., 1989, J. Mol. Spectrosc., 134, 98

Uehara H., Horiai K., Sakamoto Y., 2015, J. Mol. Spectrosc., 313, 19

Underwood D. S., Tennyson J., Yurchenko S. N., Huang X., Schwenke D. W., Lee T. J., Clausen S., Fateev A., 2016a, Mon. Not. R. Astron. Soc., 459, 3890

Underwood D. S., Yurchenko S. N., Tennyson J., Al-Refaie A. F., Clausen S., Fateev A., 2016b, Mon. Not. R. Astron. Soc., in press

van Ham J., Janssen L. J. H. M., Swart R. J., 1993, in Proceedings of an International Symposium (The Netherlands, 13-15 December 1993)

Vandaele A. C. et al., 2008, J. Geophys. Res., 113, E00B23

Varanasi P., Chudamani S., 1990, J. Quant. Spectrosc. Radiat. Transf., 43, 1

Vidler M., Tennyson J., 2000, J. Chem. Phys., 113, 9766

von Newman J., Wigner E. P., 1929, Z. Physik, 30, 467

Voronin B. A., Lavrentieva N. N., Lugovskoy A. A., Bykov A. D., Starikov V. I., Tennyson J., 2012, Atmos. Ocean. Opt., 25, 27

Voronin B. A., Lavrentieva N. N., Mishina T. P., Chesnokova T. Y., Barber M. J., Tennyson J., 2010a, J. Quant. Spectrosc. Radiat. Transf., 111, 2308

Voronin B. A., Tennyson J., Tolchenov R. N., Lugovskoy A. A., Yurchenko S. N., 2010b, Mon. Not. R. Astron. Soc., 402, 492

Wachem R., Dymanus A., 1967, J. Chem. Phys., 46, 3749

Waldmann I. P., Tinetti G., Barton E. J., Yurchenko S. N., Tennyson J., 2015a, Astrophys. J., 802, 107

Waldmann I. P., Tinetti G., Barton E. J., Yurchenko S. N., Tennyson J., 2015b, Astrophys. J., 813, 13

Warmbier R., Schneider R., Sharma A. R., Braams B. J., Bowman J. M., Hauschildt P. H., 2009, Astron. Astrophys., 495, 655

Watson J. K. G., 2003, J. Mol. Spectrosc., 326-328, 11

Werner H. J., Knowles P. J., Lindh R., Manby F. R., Schütz M., 2010, MOLPRO, a package of ab initio programs. See http://www.molpro.net

Western C. M., 2016, J. Quant. Spectrosc. Radiat. Transf., in press

Wilzewski J. S., Gordon I., Kochanov R. V., Hill C., Rothman L. S., 2016, J. Quant. Spectrosc. Radiat. Transf., 168, 193

Winkel R. J., Davis S. P., Pecyner R., Brault J. W., 1984, Can. J. Phys., 62, 1414

Wolszczan A., Frail D. A., 1992, Nature, 355, 145

Woodman J. H., Trafton L., Owen T., 1977, Icarus, 32, 314

Yachmenev A., Yurchenko S. N., Thiel P. J. W., 2011, J. Chem. Phys., 134, 11

Yadin B., Vaness T., Conti P., Hill C., Yurchenko S. N., Tennyson J., 2012, Mon. Not. R. Astron. Soc., 425, 34

Yamada C., Hirota E., 1979, J. Mol. Spectrosc., 74, 203

Yang C., Buldyreva J., Gordon I. E., Rohart F., Cuisset A., Mouret G., Bocquet R., Hindle F., 2008, J. Quant. Spectrosc. Radiat. Transf., 109, 2857

Yang T., Kai X., Li R., Sun Y., He Y., 2014, Energy Sources A, 36, 15

Yi P., Khosla A., Ramsey N. F., 1970, Phys. Rev. Lett, 24, 12

Yorke L., Yurchenko S. N., Lodi L., Tennyson J., 2014, Mon. Not. R. Astron. Soc., 445, 1383

Yurchenko S. N., 2015, J. Quant. Spectrosc. Radiat. Transf., 152, 28

Yurchenko S. N., Amundsen D. S., Tennyson J., 2016a, Astron. Astrophys.

Yurchenko S. N., Barber R. J., Tennyson J., 2011a, Mon. Not. R. Astron. Soc., 413, 1828

Yurchenko S. N., Barber R. J., Tennyson J., Thiel W., Jensen P., 2011b, J. Mol. Spectrosc., 268, 123

Yurchenko S. N., Barber R. J., Yachmenev A., Thiel W., Jensen P., Tennyson J., 2009, J. Phys. Chem. A, 113, 11845

Yurchenko S. N., Blissett A., Asari U., Vasilios M., Hill C., Tennyson J., 2016b, Mon. Not. R. Astron. Soc., 456, 4524

Yurchenko S. N., Tennyson J., 2014, Mon. Not. R. Astron. Soc., 440, 1649

Yurchenko S. N., Tennyson J., Bailey A., Hollis M. D. J., Tinetti G., 2014, PNAS, 111, 9379

Yurchenko S. N., Thiel W., Jensen P., 2007, J. Mol. Spectrosc., 245, 126

Zeninari V., Parvitte B., Courtois D., Lavrentieva N. N., Ponomarev Y. N., Durry G., 2004, Mol. Phys., 102, 1697

Zhang L., Steinmanus C., Eastmond D. A., Xin X. K., Smith M. T., 2009, Mutation Research, 681, 150

Zobov N. F., Polyansky O. L., Tennyson J., Lotoski J. A., Colarusso P., Zhang K.-Q., Bernath P. F., 1999, J. Mol. Spectrosc., 193, 118

Zobov N. F. et al., 2011, J. Mol. Spectrosc., 269, 104

Zobov N. F., Shirin S. V., Polyansky O. L., Tennyson J., Coheur P.-F., Bernath P. F., Carleer M., Colin R., 2005, Chem. Phys. Lett., 414, 193

Zolot A. M., Giorgetta F. R., Baumann E., Swann W. C., Coddington I., Newbury N. R., 2013, J. Quant. Spectrosc. Radiat. Transf., 118, 26